EXPERIMENTAL INVESTIGATION ON MULTIFLUID, MULTIPHASE FLOW PHENOMENA FOR COMPUTER CODE VALIDATION

A Dissertation

by

SE RO YANG

Submitted to the Office of Graduate and Professional Studies of
Texas A&M University
in partial fulfillment of the requirements for the degree of

DOCTOR OF PHILOSOPHY

Chair of Committee,	Yassin A. Hassan
Committee Members,	Maria D. King
	William H. Marlow
	Rodolfo Vaghetto
Head of Department,	John E. Hurtado

May 2019

Major Subject: Nuclear Engineering

ABSTRACT

Thermal hydraulics in nuclear engineering including multifluid, multiphase flow phenomena is indispensable because it is the most crucial mechanism of energy transfer in the current conventional nuclear plants, and it also governs some of the important operational conditions and safety margins of nuclear plants. In this study, two independent subjects of multifluid and multiphase flow closely related to the reactor building transient response of the next generation nuclear plant and conventional boiling water reactors are experimentally investigated.

The first part covers the transient response of helium-air binary gas mixture flow to characterize the next generation nuclear plant (NGNP) high temperature gas cooled reactor (HTGR) reactor building (RB) response to hypothetical depressurized loss of forced convection (D-LOFC) accident scenario. 1/28 down-scaled experimental facility is designed and fabricated based on the scaling analysis of simplified NGNP HTGR RB model. The transient responses of pressure, temperature and oxygen concentration for three hypothetical D-LOFC accident scenarios on the facility are measured and analyzed. Characteristics of air ingress into reactor building during the corresponding accident scenarios are analyzed quantitatively and qualitatively. The experimental results suggest an increment in the flow area of the flow path between the reactor cavity and steam generator cavity in the NGNP HTGR conceptual design. The boundary and initial conditions of the experimental work are adopted to establish computer simulation cases for generation of thermal hydraulic information in containment (GOTHIC) code. The reported validation of the GOTHIC simulation results against the experimental results presents consistency in general.

The second part deals with the steam-air mixture flow in subcooled water pool to investigate direct contact condensation (DCC) of steam jet with various steam mass flow rate. The DCC process is important in modern boiling water reactors (BWRs) since the RB containment of BWRs employs a pressure suppression chamber as a major safety feature which utilize the DCC process. Steady state gas injection rate, gas temperature, and pool temperature are measured, and their effects on the DCC process are analyzed. A new correlation of heat transfer coefficient is suggested

based on the experimental results. The effect of non-condensable gas on heat transfer characteristics is discussed. A novel method of temperature field measurement using backlight aided planar laser induced fluorescence (PLIF) for two-phase flow is developed. Instantaneous velocity and temperature fields during the DCC process near the condensing region are measured by simultaneous particle image velocimetry (PIV) and developed PLIF. Improvement of the DCC closure model in computational fluid dynamics (CFD) code is discussed.

The application of the current study is not limited to the nuclear thermal-hydraulics computer code validation, but can be extended to general research of multifluid, multiphase flow phenomena.

DEDICATION

This dissertation is respectfully dedicated to my mother and father

Kotsbhat Choi and Joon Cheol Yang,

To my loving wife Beth Hyoshin Nam

And to my precious daughter Eliana Ensuh Yang.

CONTRIBUTORS AND FUNDING SOURCES

Contributors

This work was supervised by a dissertation committee consisting of Professors Yassin Hassan, William Marlow, and Rodolfo Vaghetto of the Department of Nuclear Engineering and Professor Maria King of the Department of Mechanical Engineering.

All work for the dissertation was completed by the student, under the advisement of the dissertation committee and Dr. Thien Nguyen of the Department of Nuclear Engineering.

Funding Sources

A part of this study is based upon work supported by the Department of Energy [National Nuclear Security Administration] under Award Number [DE-NE0008324] in cooperation with AREVA Federal Service LLC (AFS), Ultra Safe Nuclear Corporation (USNC) and AREVA Inc. This report was prepared as an account of work sponsored by an agency of the United States Government. Neither the United States Government nor any agency thereof, nor any of their employees, makes any warranty, express or implied, or assumes any legal liability or responsibility for the accuracy, completeness, or usefulness of any information, apparatus, product, or process disclosed, or represents that its use would not infringe privately owned rights. Reference herein to any specific commercial product, process, or service by trade name, trademark, manufacturer, or otherwise does not necessarily constitute or imply its endorsement, recommendation, or favoring by the United States Government or any agency thereof. The views and opinions of authors expressed herein do not necessarily state or reflect those of the United States Government or any agency thereof.

TABLE OF CONTENTS

Page

LIST OF FIGURES

FIGURE Page

LIST OF TABLES

TABLE Page

1. INTRODUCTION AND SCOPE

1.1 Importance of Thermal-hydraulic Research in Nuclear Engineering Field and Computer based Simulations

Ever since work directed by Fermi succeeded to reach the criticality of the Chicago Pile #1 (CP-1), the very first fission controlled reactor in the world, nuclear power engineers have been endeavoring to design safer and more efficient nuclear plants. Because the most effective way to harness the nuclear fission reaction as a useful form of energy currently by use thermodynamic cycles, thermal-hydraulics is indispensable subject to study in nuclear plant design.

Especially, thermal-hydraulic stability margin such as departure from nucleate boiling (DNB) condition is one of the key factors to determine the operational conditions and design limits of the nuclear plant for its safe operation in the case of conventional light water reactors (LWRs). Furthermore, thermal efficiency of the power cycle is governed by the thermal-hydraulic characteristics of design elements.

However, despite the importance of studying thermal-hydraulics, it is not easy to research further from what we have already learned through the previous generations. The main difficulties of research in thermal-hydraulics include the scale, complexity, and non-linearity of the phenomena.

First of all, the scales of the nuclear thermal-hydraulic phenomena are broad, and the geometric scale is extreme in particular. Even though it is possible to scale down the domain of the phenomena by thermal-hydraulic similarity, at least one set of full scale experiment is necessary to evaluate the distortions in length and time scales caused by the scaling. Secondly, the phenomena involve with complex multiphase mass, momentum, and energy transfer system, and it is still very hard to solve the problem analytically. Even though a set of nuclear thermal-hydraulic problem could be solved numerically, verification and validation of the results must be conducted. Furthermore, non-linearity of the system makes hard to predict the phenomena, and the turbulence nature of the phenomena induces chaotic or stochastic behavior (Francesco D'Auria, 2017). Those are the main

reasons that make the nuclear thermal-hydraulic research difficult and expensive.

Computer based simulations are part of an effort to cut down the overall cost of thermal-hydraulic research. The U.S. Nuclear Regulatory Commission (USNRC), the power utilities, and foreign organizations employ various advanced computer simulations to investigate the reactor system thermal-hydraulic behavior during realistic and hypothetical transient scenarios, especially for loss of coolant accidents (LOCAs) and system transients in LWRs (USNRC, 2018). However, those computer simulations require verification and validation to guarantee the applicability and accuracy of the results even though the governing equations of the simulations are strictly derived from the law of physics due to the truncation error of the computation and the solver characteristics caused by the numerical scheme. Furthermore, some of the empirical closure models developed previously should be validated by the state-of-the-art advanced measurement techniques and would be updated if necessary.

Since most of the parameters and the coefficients in the empirical closure models are specifically tuned for several conventional designs, it is common that the calculational results show inaccurate predictions as expected for newly designed systems. In fact, many researchers try to improve the accuracy and applicability of the conventional closure models and correlations from the results of verification and validation of the computer code with existing or newly developed experimental database. It is mainly because more accurate predictions would give us tighter margins in engineering and design processes compared to that of idealized and oversimplified systems, which could result in more efficient design. Furthermore, successful utilization of the computer simulation in design optimization processes will save huge net costs in comparison with the experimental approach. It should be also noted that the successfully coupled numerical simulation of neutronics and thermal-hydraulics of the nuclear power plant would provide many advantages to investigate the safe operational conditions and accident scenarios without worry of radioactive contamination.

1.2 Scope of the Present Study

The main objective of the present study is to provide extended experimental database of multi-fluid, multiphase flow phenomena using the state-of-the-art measurement techniques for computer code validation. In particular, this study investigates the helium-air binary gas mixture flow transient and the direct contact condensation of steam-air mixture jet in subcooled water pool. The results of helium-air flow transient can be applied to characterize the next generation nuclear plant (NGNP) high temperature gas cooled reactor (HTGR) reactor building (RB) response to depressurized loss of forced convection (D-LOFC) accident scenario. Application of steam-air condensation can be extended to characterize the boiling water reactor (BWR) suppression pool response in the case of loss of coolant accident (LOCA) scenario.

Both cases are focusing on the transient thermal-hydraulic phenomena in between the reactor vessel system and the reactor containment building during specific accident scenarios of the conventional and next generation nuclear plant. Since the transient response during the accident provides the most crucial information including the temperature and pressure fluctuations to determine the corrective actions before the accident propagates to catastrophic disasters such as core melt down or massive radioactive release to environment due to the damaged reactor containment, integrated understandings of the transient response for both global and local thermal-hydraulic phenomena are vital.

Since the present study deals with two different flow phenomena, this thesis is organized in two parts. The first part covers the helium-air binary gas mixture flow transient in the case of the specific hypothetical D-LOFC accident scenarios in NGNP HTGR. This part focuses on the global transient response of NGNP HTGR RB to the accident scenarios. Thermal-hydraulic phenomena of buoyancy driven flow (gravity current) and diffusion of binary gas mixture are investigated. Design and fabrication of the experimental facility based on the scailing analysis are described. Transient responses of pressure, temperature and oxygen concentration for corresponding scenarios are measured and analyzed.

The second part is more fundamental and focuses on local phenomena which obviously af-

fects global transient response. The direct contact condensation of steam jet with various steam mass flow rate is studied, which is the major heat removal and pressure suppression mechanism in conventional BWRs during the accident scenarios such as turbine trip or LOCA. The effect of non-condensable gas in heat transfer rate is discussed. Flow conditions are selected from the steam condensation regime map. Steady state gas injection flowrate, gas temperature, and pool temperature are measured. Improvement of the existing heat transfer coefficient model is discussed, and a new heat transfer correlation based on the thermal hydraulic characteristics is proposed. A novel method of temperature field measurement using backlight aided planar laser induced fluorescence (PLIF) for two-phase flow is developed.Instantaneous velocity and temperature fields during the DCC process near the condensing region are measured by the state-of-the-art technique using flow visualization as particle image velocimetry (PIV) and developed PLIF.

The application of the current study is not limited to the nuclear thermal-hydraulics computer code validation, but can be extended to general research of multifluid, multiphase flow phenomena.

2. PART I. HELIUM-AIR BINARY GAS MIXTURE FLOW: NGNP HTGR REACTOR BUILDING RESPONSE TO DEPRESSURIZATION EVENT*

2.1 Background: NGNP HTGR Reactor Building Concept

High-temperature gas-cooled reactors (HTGRs) proposed in the United States for next generation nuclear plants (NGNPs), such as the steam-cycle modular helium reactor (SC-MHR), employ vented low-pressure containment (VLPC) as their reactor building (RB) design, also known as confinement, as opposed to conventional leak-tight RB containments for light water reactors (LWRs) (M. Richards, 2012). Figure 2.1 shows the different reactor building (RB) design philosophies between the NGNP HTGR conceptual design and conventional PWR design.

The conventional PWR has a leak tight containment design. In the case of Loss-of-coolant-accident (LOCA), emergency core cooling system (ECCS) will be activated, and the discharged steam from the break will be condensed into water and recirculated through the containment sump. On the contrary, NGNP HTGR VLPC RB design allows to release the exceeding pressure to the atmosphere through vent path if depressurized loss of forced convection (D-LOFC) occurred.

Even though the VLPC design can mitigate pressure build-up inside the RB and provides the advantage of controlling fission product release (EPRI 2005, T. Wilson *et al*. 2012), it is also possible that the buoyancy and diffusion driven reversal flow of atmospheric air coming into the RB and eventually coming into the reactor pressure vessel (RPV), which may result in oxidation of the fuel elements and other nuclear grade graphite components. The in-core graphite oxidation would weaken the core structure and possibly produce extra heat in the core (Areva NP Inc. 2008, S. Ball *et al*. 2008). This reversal atmospheric air inflow is called air ingress.

Many studies on air ingress into RPV have been conducted and reported by various researchers,

*Part of this work is reprinted with permission from "Experimental study on 1/28 scaled NGNP HTGR reactor building test facility response to depressurization event" by Se Ro Yang, Ethan Kappes, Thien Nguyen, Rodolfo Vaghetto, Yassin Hassan, 2018, Annals of Nuclear Energy, Vol. 114, pp. 154-164, and "Numerical analysis of 1/28 scaled NGNP HTGR reactor building facility response to depressurization event using GOTHIC, by Mustafa Alper Yildiz, Se Ro Yang, Rodolfo Vaghetto, Yassin A. Hassan, 2018, Annals of Nuclear Energy, Vol. 119, pp. 46-65, Copyrights [2017, 2018] by Elsevier Ltd.

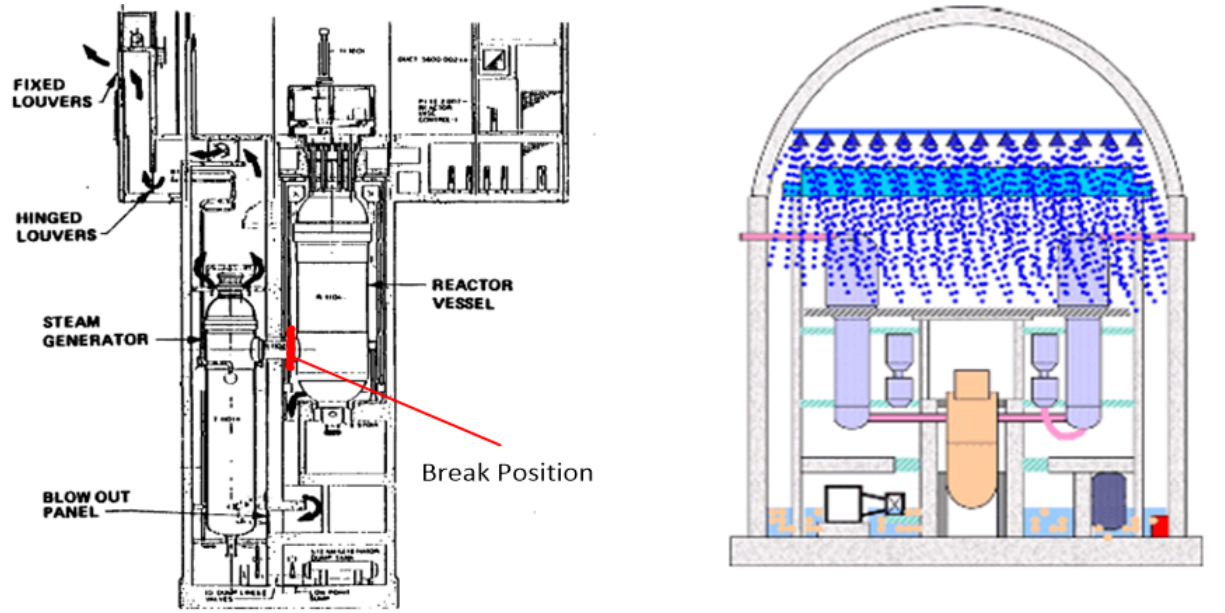

Figure 2.1: The difference between confinement and containment of NGNP HTGR and PWR (Ball & Wichner, 1992, Maneke, 1988, USNRC)[1]

both experimentally and numerically (H. Haque 2008, M. Hishida *et al.* 1999, J. Kim *et al.* 2016, D. Gould *et al.* 2017, Z. Chen *et al.* 2017). However, current air ingress studies focus only on air ingress into the RPV under the assumption of 100% air inside the RB compartments. Because air ingress into the RPV is strongly dependent on the behavior of the air/helium mixture within the RB as time-dependent boundary conditions (T. Wilson *et al.* 2012), it is necessary to investigate the characteristics of air ingress into the RB through the vent and leak path following depressurization, to predict and assess the characteristics and consequences of air ingress into RPV accurately. The Ultra Safe Nuclear Corporation (USNC) defines the three stages of a hypothetical D-LOFC event as blowdown (depressurization), air refill, and air ingress, based on the current NGNP conceptual design. Figure 2.2 provides a schematic representation of the three phases described by the USNC (S. Yang *et al.* 2017).

It should be noted that the D-LOFC resulting from breaks in the helium pressure boundary

[1]Figure credits: HTGR - S. J. Ball & R. P. Wichner (1992), Maneke (1988), LWR - USNRC

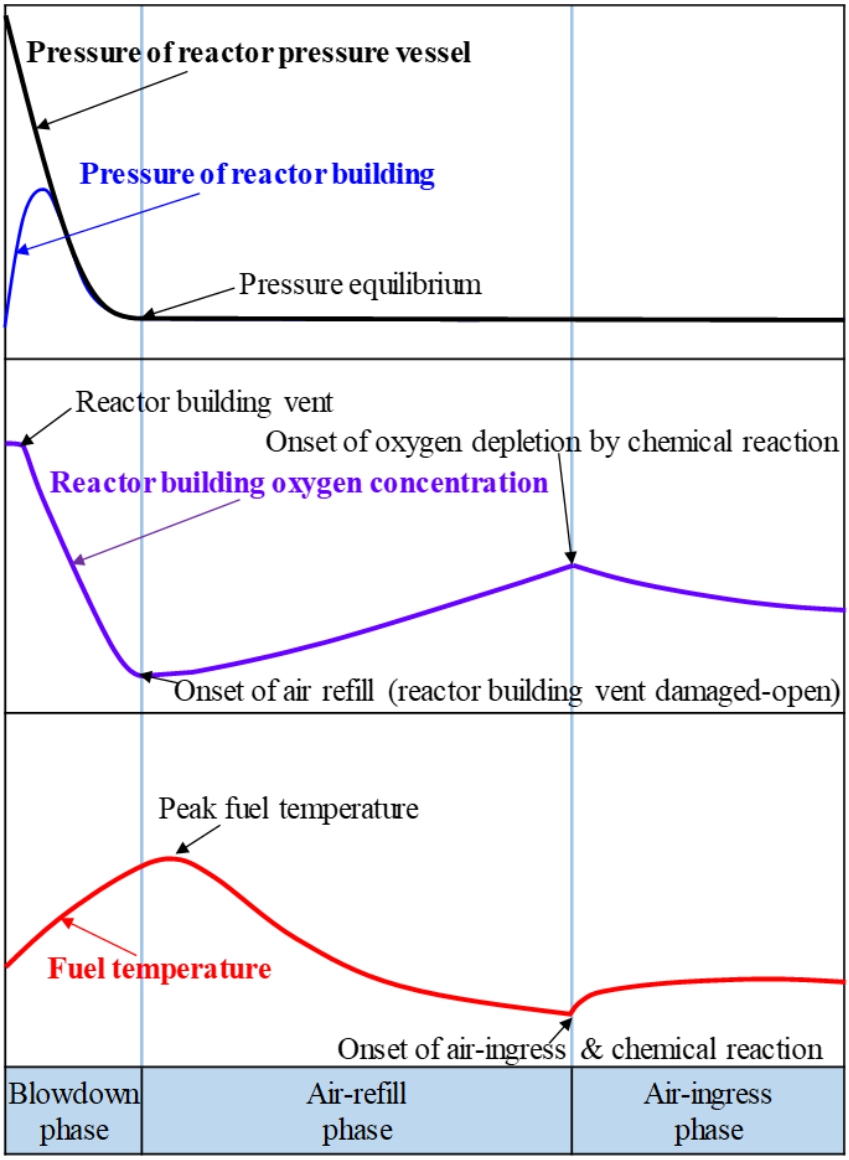

Figure 2.2: Phase identification of D-LOFC scenarios (Trends are not shown to scale, Yang *et al.* 2018)

(HPB) can be divided into small, moderate, and large break sizes. While small breaks may occur in the instrumentation or electrical penetration lines in the reactor and steam generator cavities, moderate breaks may occur in the pressure relief line on top of the steam generator vessel (GA Tech. Inc. 1988). A typical example of a large break is an instant rupture of the cross vessel and cross duct, which would fall well beyond the frequency range for design-basis accidents.

The NGNP VLPC can be subdivided into five components along the major vent paths during the

depressurization transient: (1) Reactor cavity with the Reactor Cavity Cooling System (RCCS), (3) Reactor cavity (RC) vent path to the steam generator cavity, (2) Steam generator cavity, (4) equipment well vent compartment, (5) louver vent compartment where pressure relief valve module and fixed/hinged louvers are located. Figure 2.3 shows the identification of VLPC components from a cross sectional view provided by USNC (original source: Saurwein 2011).

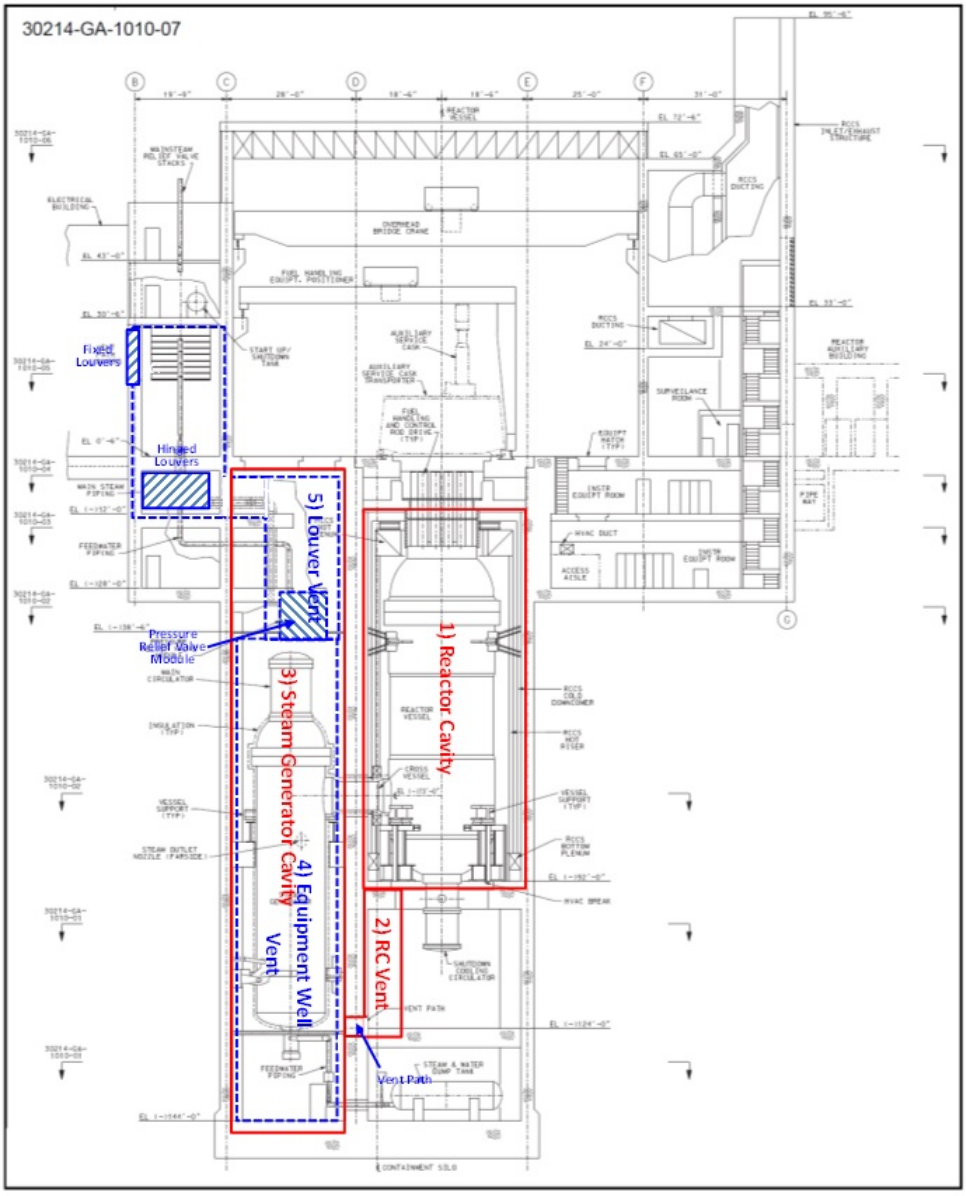

Figure 2.3: Identification of NGNP HTGR RB VLPC components (Saurwein 2011)

The objective of this study is to investigate the RB transient response characteristics in the case of a hypothetical moderate break occurring in the reactor cavity. Under such circumstances, pressure accumulates inside the reactor cavity until reaching the pressure set point of a one-way vent louver (blowdown phase), resulting in the release of a helium and air mixture into the steam generator cavity and other vent paths (depressurization phase). Persistence of this scenario results in the expulsion of all ambient air from the reactor cavity. Because the helium flow exiting from the break site will purge part of the air inside the RB during depressurization, a helium-rich air mixture will remain inside the RB cavities once the RB pressure has reached steady state conditions. While the remaining helium will exit the RB due to the gravity current and natural circulation, the counter-current reversal flow of fresh air from the atmosphere will ingress into the RB through vent and leak paths (air refill phase).

The results of this study provide not only more realistic boundary conditions for air ingress into the RPV, but also an increased understanding of the RB response for the blowdown, depressurization, and air refill phases in the case of a D-LOFC event. Case specific results also can be employed as benchmark database for computer code simulations.

2.2 Experimental Method: TAMU 1/28 Scale NGNP HTGR RB Test Facility

Dimensionless similarity-based scaling was adopted in this study to evaluate the main dimensions and other features of the experimental facility and to represent the main characteristics of the simplified RB design. The scaling approach of this study followed similar procedures and calculations to those performed by previous researchers in the nuclear engineering society (J. Reyes *et al*. 2010, P. Tzanos *et al*., R. Vaghetto *et al*. 2014), and was elaborated to accomplish the desired scope and features of the proposed experimental activity. The scaling is focused on the air refill phase since the most complicated thermal-hydraulic phenomena are occurring in that region.

Figure 2.4 represents a schematic of the full-scale simplified RB model, which was provided by USNC. Descriptions for each component labeled in Fig. 2.4 are provided in Table 2.1. Dimensions are described in terms of height, width, and depth for square columns, and diameter and length for cylinders. All units in the table are United States Customary Units.

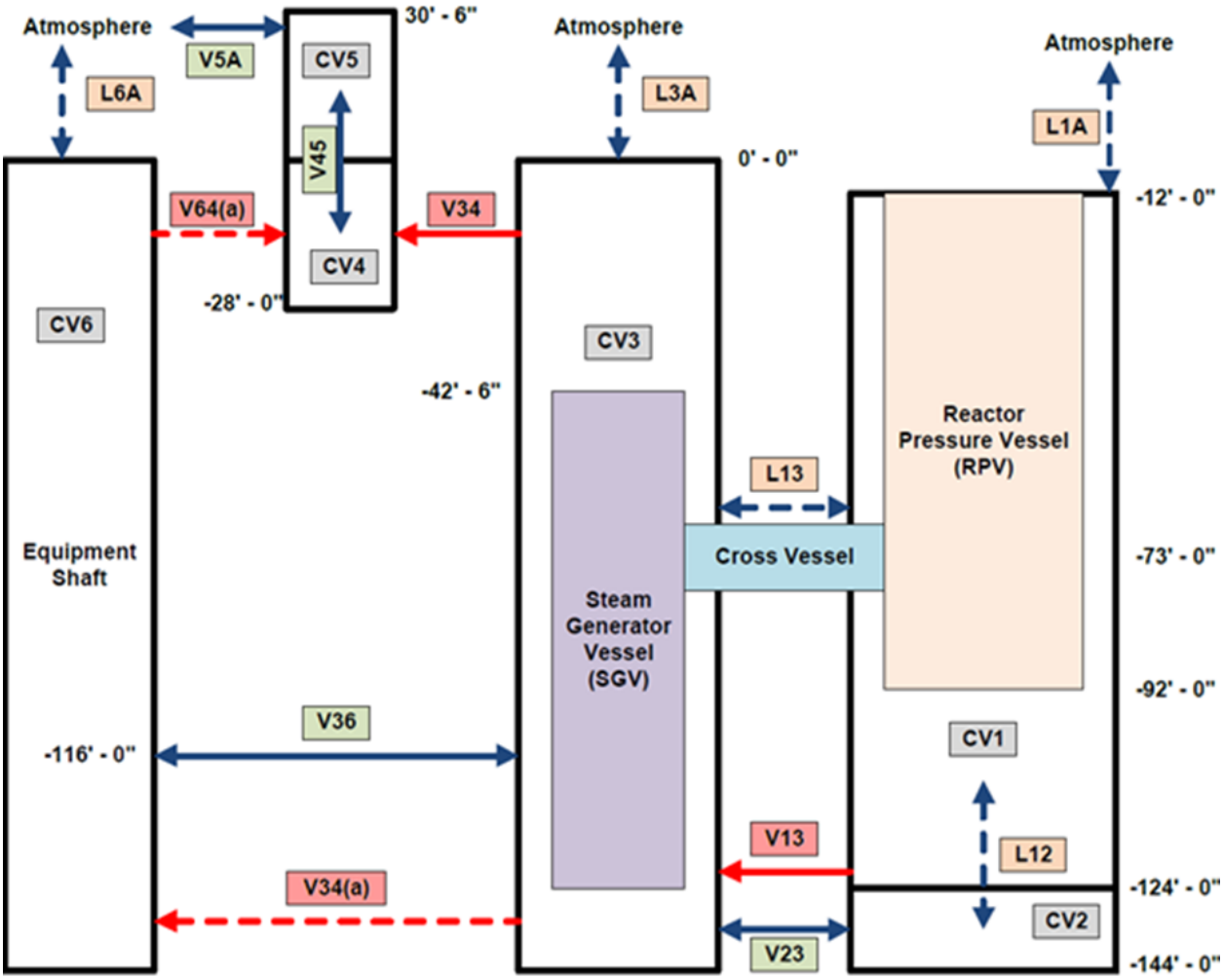

Figure 2.4: Schematic of simplified RB model (Alliance limited, NGNP industry, 2017)

Table 2.1: Component description of simplified RB model

Component ID	**Description**	**Dimensions** (H ×W ×D)(ft.^{3})
CV1	Reactor cavity	$112' \times 28.4' \times 28.4'$
CV2	Steam generator dump tank cavity	$20' \times 28.4' \times 28.4'$
CV3	Steam generator compartment	$144' \times 22.8' \times 22.8'$
CV4	Lower vent space	$28' \times 18.9' \times 18.9'$
CV5	Upper vent space	$30.5' \times 18.9' \times 18.9'$
CV6	Equipment shaft	$144' \times 17.7' \times 17.7'$
RPV	Reactor pressure vessel	$22.4' \times 80'$(diameter × length)
SGV	Steam generator vessel	$14.8' \times 81.5'$(diameter × length)
V13	One-way vent louver	$0.8' \times 7'$(diameter × length)
V23	Manway door	$3' \times 8' \times 7'$
V34	RB pressure relief path	$10' \times 13' \times 3.5'$
V36	Multiple pathways	$14' \times 14' \times 3.5'$
V45	Open connection	$10' \times 13' \times 3.5'$
V5A	RB vent path-fixed louvers	$10' \times 13' \times 3.5'$
L1A	Leak path CV1- atmosphere	-
L3A	Leak path CV3-atmopshere	-
L6A	Leak path CV6-atmopshere	-
L12	Leak path CV1-CV2	Closed
L13	Leak path CV1-CV3	Closed

CV1 represents the reactor cavity which includes the reactor vessel and the vessel supports. CV2 simulates the steam generator dump tank cavity. CV3 represents the steam generator compartment. This volume includes the space occupied by the steam generator and the steam generator's support. CV4 and CV5 are the lower and upper vent cavities respectively (normally connected

together). CV6 represents the containment equipment shaft compartment. Connections between the compartments of the test facility are in place to represent the venting paths and leak paths listed in Table 2.1. In particular:

- The cross-vessel connecting CV1 to CV3 (connection normally closed)
- The 1 psid pressure relief valve (V13), connecting CV1 to CV3
- The flow path V23 (normally closed) connecting CV2 to CV3
- The flow path V34 connecting CV3 to CV4
- The flow path V45, part of the facility chimney, connecting CV4 to CV5 (openly connected)
- The flow path V5A, connecting CV5 with the laboratory atmosphere
- The flow path V36, connecting CV3 to CV6

During the air refill phase of a large break event, all compartments are assumed to be filled mostly with helium, and the initial experimental conditions for the air-helium mixture ratio inside the compartments can be parameterized. Major thermal-hydraulic phenomena expected to occur in the RB during the air refill phase are:

- vertical stratification and mixing,
- horizontal stratification (gravity current),
- gas thermal expansion and contraction, and
- molecular diffusion of the binary gas mixture (air-helium).

Natural circulation driven by temperature differences within the reactor cavity (CV1) may also influence air refill characteristics. To maintain the dynamic similarity between the full-scale simplified RB model and scaled-down experimental facility, five dimensionless numbers were selected to characterize each phenomenon described above. Because the mixture is composed of two fluids

(helium and air), the Froude number should be considered, which represents the ratio of inertial to gravitational forces. The diffusion process between gases is characterized by the Schmidt number. In addition, it is obvious that the flow is affected by buoyancy forces; thus, the Richardson number should be considered. Another referable parameter related to the buoyancy force is the Grashof number. Finally, the experimental boundary and initial conditions are necessarily obtained from available prototype simulations. Under these circumstances, the Reynolds number may be required to account for the imposed flow conditions.

2.2.1 Scaling analysis

To guarantee the similarity of the fluid flow of the model to that of the prototype, the ratio of the dimensionless numbers is imposed as equal to unity:

$$\Psi_R = \frac{\Psi_m}{\Psi_p} = 1 \tag{2.1}$$

where Ψ is an arbitrary dimensionless number. The subscripts *m*, *p*, and *R* denote the model, prototype, and their ratio, respectively. Similarities among the dimensionless parameters are presented below.

• Similarity for the Froude number:

$$\mathrm{Fr}_R = \frac{\mathrm{Fr}_m}{\mathrm{Fr}_p} = \left(\frac{U^2}{gL\Delta\rho/\rho}\right)_m \left(\frac{U^2}{gL\Delta\rho/\rho}\right)_p^{-1} \tag{2.2}$$

• Similarity for the Schmidt number:

$$\mathrm{Sc}_R = \frac{\mathrm{Sc}_m}{\mathrm{Sc}_p} = \left(\frac{\nu}{D_{AB}}\right)_m \left(\frac{\nu}{D_{AB}}\right)_p^{-1} \tag{2.3}$$

• Similarity for the Richardson number:

$$\mathrm{Ri}_R = \frac{\mathrm{Ri}_m}{\mathrm{Ri}_p} = \left(\frac{g\beta\Delta TL}{U^2}\right)_m \left(\frac{g\beta\Delta TL}{U^2}\right)_p^{-1} \tag{2.4}$$

• Similarity for the Grashof number:

$$\begin{aligned} \mathrm{Gr}_R = \frac{\mathrm{Gr}_m}{\mathrm{Gr}_p} &= \left(\frac{g\beta\Delta T L^3}{\nu^2}\right)_m \left(\frac{g\beta\Delta T L^3}{\nu^2}\right)_p^{-1} \\ &= \frac{(\beta\Delta T)_m}{(\beta\Delta T)_p} \frac{(gL^3/\nu^2)_m}{(gL^3/\nu^2)_p} \end{aligned} \tag{2.5}$$

• Similarity for the Reynolds number:

$$\mathrm{Re}_R = \frac{\mathrm{Re}_m}{\mathrm{Re}_p} = \left(\frac{UL}{\nu}\right)_m \left(\frac{UL}{\nu}\right)_p^{-1} \tag{2.6}$$

The Schmidt number similarity is related to the thermal-fluid properties of the gases, while the Froude, Richardson, and Reynolds numbers are concerned with the length, velocity, and temperature scales. From the above similarity equations, the Grashof number similarity between the model and prototype can be divided into two ratios that are treated separately, as shown in Eq. (2.5).

If we assume that each ratio is maintained as unity, the first part of the ratio in the Grashof similarity equation yields

$$\begin{aligned} \frac{(\beta\Delta T)_m}{(\beta\Delta T)_p} &= 1 \\ \therefore \frac{\beta_m}{\beta_p} &= \frac{\Delta T_p}{\Delta T_m} \end{aligned} \tag{2.7}$$

Applying the ideal gas property of $\beta = T^{-1}$ to Eq. (2.7) yields

$$\frac{\Delta T_m}{\Delta T_p} = \frac{T_m}{T_p} \tag{2.8}$$

The second part of the ratio in the Grashof similarity yields

$$\begin{aligned} \frac{(gL^3/\nu^2)_m}{(gL^3/\nu^2)_p} &= 1 \\ \therefore \left(\frac{L_m}{L_p}\right)^{3/2} &= \frac{\nu_m}{\nu_p} = \frac{\mu_m {\rho_m}^{-1}}{\mu_p {\rho_p}^{-1}} \end{aligned} \tag{2.9}$$

The relations for the ideal gas density and dynamic viscosity are as follows:

$$\rho\left(T,P\right)=\rho_0\left(T_0,P_0\right)\frac{P}{P_0}\frac{T_0}{T}, \tag{2.10}$$

$$\mu\left(T\right)=\mu_0\left(T_0\right)\left(\frac{T}{T_0}\right)^{0.5} \tag{2.11}$$

Here, T_0, P_0, and ρ_0 are the reference absolute temperature, pressure, and density, respectively. Selecting $P_{0p}=P_{0m}$ and $T_{0p}=T_{0m}$, and substituting Eqs. (2.10) and (2.11) into Eq. (2.9), the pressure relationship between the model and prototype can be expressed as follows:

$$\frac{P_m}{P_p}=\frac{\nu_{0m}}{\nu_{0p}}\left(\frac{T_m}{T_p}\right)^{3/2}\left(\frac{L_p}{L_m}\right)^{3/2} \tag{2.12}$$

Because the model uses the same gases as the prototype, namely helium and air, the ratio of the reference kinematic viscosity $\nu_{0m}/\nu_{0p}=1$. Furthermore, assuming that the working pressures of the model and prototype during the refilling phase are approximately the same ($P_m=P_p$), Eq. (2.12) combined with Eq. (2.8) yields

$$\frac{L_m}{L_p}=\frac{T_m}{T_p}=\frac{\Delta T_m}{\Delta T_p}=\frac{1}{f_{scale}} \tag{2.13}$$

In the above equation, f_{scale} is defined as the geometric scaling factor between the model and prototype. The Reynolds similarity imposed on unity yields

$$\frac{U_mL_m}{U_pL_p}=\frac{\nu_m}{\nu_p}=\frac{\mu_m{\rho_m}^{-1}}{\mu_p{\rho_p}^{-1}} \tag{2.14}$$

Again, applying the relations for ideal gas viscosity and density provides

$$\frac{U_m}{U_p}=\left(\frac{L_m}{L_p}\right)^{0.5}=\left(\frac{1}{f_{scale}}\right)^{0.5} \tag{2.15}$$

This equation demonstrates the possibility of matching the Reynolds numbers of the model and

prototype by adjusting the velocity scale. The Froude similarity shows that the ratio of the velocity scales is the square root of the length scale and density difference ratios, as follows.

$$\begin{aligned} \mathrm{Fr}_R = \frac{\mathrm{Fr}_m}{\mathrm{Fr}_p} &= \left(\frac{U_m}{U_p}\right)^2 \frac{L_p}{L_m} \frac{(\Delta\rho/\rho)_p}{(\Delta\rho/\rho)_m} \\ &= \frac{(\Delta\rho/\rho)_p}{(\Delta\rho/\rho)_m} \end{aligned} \tag{2.16}$$

If the density difference ratio between the model and prototype can be maintained, the Froude similarity is guaranteed. It should be noted that with the determined geometric scaling factor, f_{scale}, and experimental conditions, distortions can be estimated in the scaled experiments. For example, if one considers matching the Froude and Richardson numbers between the prototype and model, the similarity conditions yield

$$\frac{\beta_m}{\beta_p} \frac{\Delta T_m}{\Delta T_p} \frac{(\Delta\rho/\rho)_p}{(\Delta\rho/\rho)_m} = \mathrm{Fr}_R \mathrm{Ri}_R \tag{2.17}$$

Similarly, maintaining the Schmidt and Reynolds numbers yields

$$\frac{U_m}{U_p} \cdot \frac{L_m}{L_p} = \mathrm{Re}_R \frac{\nu_m}{\nu_p} = \mathrm{Re}_R \mathrm{Sc}_R \frac{(D_{AB})_m}{(D_{AB})_p} \tag{2.18}$$

Matching the Richardson and Reynolds numbers provides,

$$\left(\frac{L_m}{L_p}\right)^3 = \mathrm{Re}_R^2 \, \mathrm{Ri}_R \left(\frac{\nu_m}{\nu_p}\right)^2 \frac{\beta_p}{\beta_m} \frac{\Delta T_p}{\Delta T_m} = \mathrm{Re}_R^2 \, \mathrm{Ri}_R Sc_R^2 \left\{ \frac{(D_{AB})_m}{(D_{AB})_p} \right\}^2 \tag{2.19}$$

while matching the Schmidt, Reynolds, and Froude numbers yields

$$\left(\frac{U_m}{U_p}\right)^3 = \mathrm{Re}_R Sc_R Fr_R \frac{(D_{AB})_m}{(D_{AB})_p} \frac{(\Delta\rho/\rho)_m}{(\Delta\rho/\rho)_p} = \frac{\mathrm{Re}_R \mathrm{Sc}_R}{\mathrm{Ri}_R} \frac{(D_{AB})_m}{(D_{AB})_p} \tag{2.20}$$

In this study, the driving forces of flow are generally integrated from the different dominant phenomena. The driven regimes change spatially and are dependent on local boundary conditions.

For example, the flow phenomena on the path V5A-CV5-V45-CV4 can be characterized by the diffusion and gravity current. However, in CV3, it is likely that the buoyancy force caused by the density difference between the helium and air mixture will constitute the driven flow regime. In CV1, the high temperature difference between the reactor pressure vessel and air entering from CV3 may dominate the flow. Therefore, it is vital that the model is built with the ability to integrate or separate the driven flow regimes using the provided datasets of the initial and boundary conditions for the accident scenarios.

To allow for the use of various visualization techniques during the experimental activity, transparent polycarbonate was selected as the experimental facility material. With the use of such materials and techniques, the optimal facility size must be limited to account for factors such as total weight and deformation. Larger sizes may increase the weight of the cavity panels in the experimental facility, and result in deformation of the side walls. The geometric scaling factor should be determined to consider the desired spatial resolution of measurements (that is, temperature, pressure, and gas concentration) to be performed during the experiments. In general, larger cavities may limit the spatial resolution of the measurements and could require the installation of more instruments (namely thermocouples, pressure transducers, and oxygen probes).

Owing to the small size of certain vents and leak paths included in the simplified RB design, the geometric scaling factor should furthermore be conditioned to avoid very small flow paths in the experimental facility, which may be difficult to construct and may also limit the ability to perform measurements in specific locations. Based on the above considerations, the optimal maximum length of the cavities of the experimental facility was estimated to be approximately 5.25 ft (1.6 m). In the simplified RB design, the largest cavities (steam generator and equipment shaft cavities) are characterized by a total length of 144 ft (43.89 m). The geometric scaling factor, f_{scale}, is determined to be

$$f_{scale} = \frac{L_p}{L_m} = \frac{43.89}{1.6} \approx 28 \tag{2.21}$$

2.2.2 TAMU 1/28 scale NGNP HTGR RB test facility

Table 2.2 describe the scaled dimensions and volumes of the main compartments of the experimental facility with the scaling factor of $f_{scale} = 28$.

Table 2.2: Component description of the main compartments of the scaled facility

Component ID	**Dimensions** (H ×W ×D)(ft.^{3})	**Volume** (ft.^{3})	**Free Volume**[2](ft.^{3})
CV1	$3.92' \times 1.02' \times 1.02'$	4.08	2.45
CV2	$0.62' \times 1.02' \times 1.02'$	0.64	0.64
CV3	$5.058' \times 0.814' \times 0.814'$	3.35	2.84
CV4	$0.958' \times 0.68' \times 0.68'$	0.44	0.44
CV5	$1.1' \times 0.68' \times 0.68'$	0.51	0.51
CV6	$5.058' \times 0.632' \times 0.632'$	2.02	2.02

The experimental facility is a 1/28 geometrically scaled version of the prototype HTGR building and consists of six main volumes numbered CV1 through CV6 and are labeled based on the component ID shown in Table 2.1.

- CV1 represents the reactor cavity and includes the reactor vessel and the vessel supports
- CV2 simulates the steam generator dump tank cavity
- CV3 represents the steam generator compartment. This volume includes the space occupied by the steam generator, and the steam generator's support
- CV4 and CV5 are the lower and upper vent cavities respectively (normally connected together)
- CV6 represents the containment equipment shaft compartment

[2]Free volume is the volume of the compartment not occupied by any structure or other parts

Connections between the compartments of the test facility are in place to represent the venting paths and leak paths listed in Table 2.1. In particular:

- The cross-vessel connecting CV1 to CV3 (connection normally closed)
- The 1psid pressure relief valve (V13), connecting CV1 to CV3
- The flow path V23 (normally closed) connecting CV2 to CV3
- The flow path V34 connecting CV3 to CV4
- The flow path V45, part of the facility chimney, connecting CV4 to CV5 (openly connected)
- The flow path V5A, connecting CV5 with the laboratory atmosphere
- The flow path V36, connecting CV3 to CV6
- The leak path L1A, simulating the leak path from the top of CV1 to the atmosphere (Two needle valves)
- The leak path L3A, simulating the leak path from the top of CV3 to the atmosphere (Two needle valves)
- The leak path L6A, simulating the leak path from the top of CV6 to the atmosphere (Two needle valves)

PT-01, PT-02, and PT-03 are the pressure transducers for gauge pressure measurement during the tests for CV1, CV2, and CV3, respectively, while GP-01, GP-02, and GP-03 are the gas injection ports. Various gas injection combinations are available, depending on the break scenario. V13 is a 1/2″ one-way check valve (CV1

→

CV3). To simulate the leak path generated from the construction tolerance of the RB in the scaled facility, two needle valves were employed per compartment, and are referred to as L1A, L3A, and

L6A at the top of CV1, CV3, and CV6, respectively. Further specifications are described in the following subsections.

2.2.2.1 Reactor cavity compartment (CV1) and internals

The CV1 compartment represents the reactor cavity. Figure 2.5 shows a detailed view of CV1 and its internals. The main constituents of this compartment are the compartment walls, the top and bottom flanges, and the top lid.

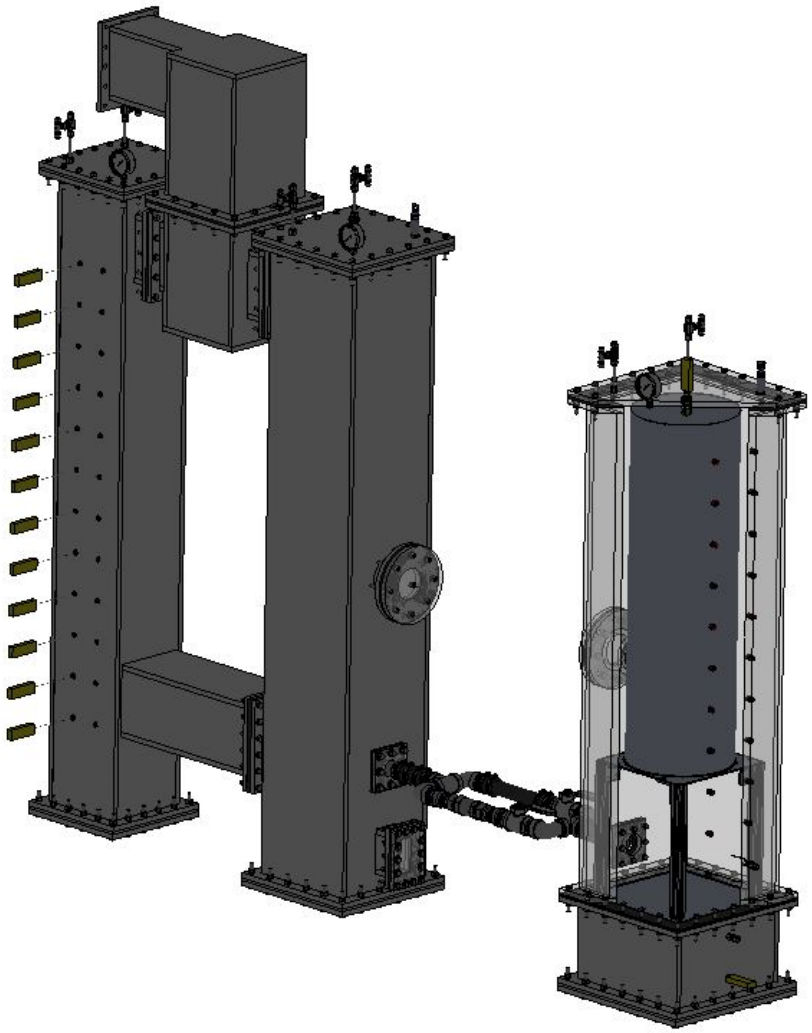

Figure 2.5: CV1 component

The bottom flange is used to connect CV1 with CV2. The compartments are normally isolated by interposing an aluminum plate and gasket between the bottom flange of CV1 and the top flange of CV2. The top flange is connected to the top lid to close the compartment and maintain the pressure during tests. Two needle valves are connected to the top lid to simulate the leak path L1A. The reactor vessel is located inside the compartment CV1 and supported by an aluminum support (plate and structure). Penetrations[3] of the walls of CV1 are installed to:

- Establish flow communication with other compartments
- Impose and control inlet/outlet flows
- Install instrumentation

Flow communications are in place between:

1. CV1 and CV3 via the cross-vessel pipe. This connection is normally closed (Fig. 2.6(1))
2. CV1 and CV3 via the one-way pressure relief valve and the bypass line with ball valve labeled V13 (Fig. 2.6(2))
3. CV1 and the atmosphere
4. CV1 and helium source

[3] All the penetrations described in this document are reflecting the current status of the facility. Additional penetrations can be made if required.

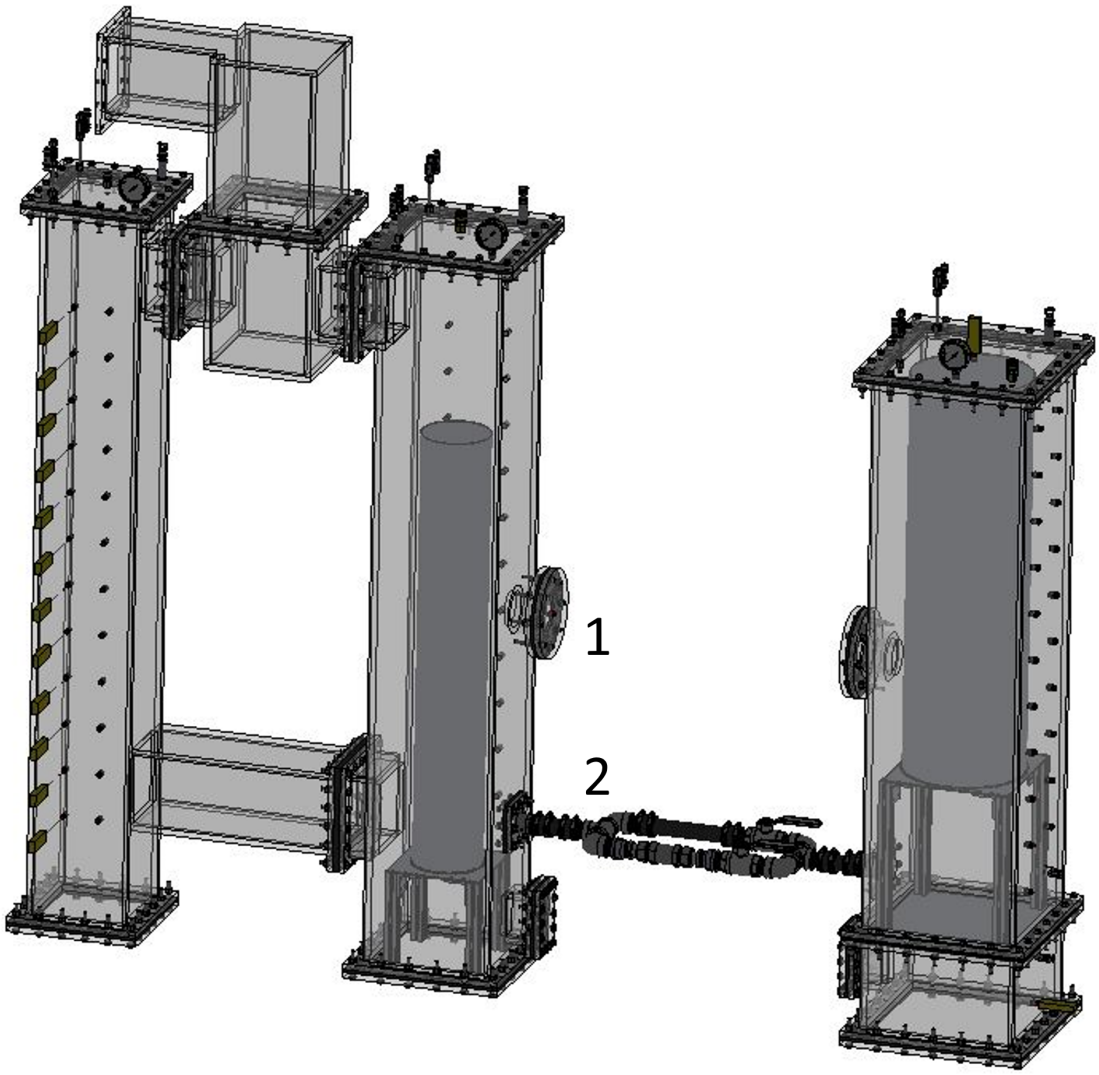

Figure 2.6: CV1 flow connections

Instrumentation is installed in the compartments through a series of 1/4″ NPT threaded holes. These holes are designed to support thermocouple probes, pressure transducers, and/or O_2 sensors, and can be also used for additional inlet/outlet ports. These ports are located at the compartment walls, and at the top lid. Table 2.3 identifies the ports by their ID and location.

Table 2.3: CV1 penetrations locations

Name	**Dimension** (inches)	**Location** (center of hole - inches)	
		X	Y
Fig. 2.7 a			
CV1-T-S1C	ϕ 0.44	7.81	3.03
CV1-T-C	ϕ 0.44	7.81	7.81
CV1-T-S1S2	ϕ 0.44	3.03	3.03
CV1-T-S2S4	ϕ 0.44	3.03	12.63
CV1-T-S1S3	ϕ 0.44	12.63	3.03
CV1-T-S3S4	ϕ 0.44	12.63	12.63
Fig. 2.7 b			
CV1-S1-L1	ϕ 0.44	3.56	3.5
CV1-S1-R1	ϕ 0.44	8.56	3.5
CV1-S1-L2	ϕ 0.44	3.56	7.5
CV1-S1-R2	ϕ 0.44	8.56	7.5
CV1-S1-L3	ϕ 0.44	3.56	11.5
CV1-S1-R3	ϕ 0.44	8.56	11.5
CV1-S1-L4	ϕ 0.44	3.56	15.5
CV1-S1-R4	ϕ 0.44	8.56	15.5
CV1-S1-L5	ϕ 0.44	3.56	19.5
CV1-S1-R5	ϕ 0.44	8.56	19.5
CV1-S1-L6	ϕ 0.44	3.56	23.5
CV1-S1-R6	ϕ 0.44	8.56	23.5
CV1-S1-L7	ϕ 0.44	3.56	27.5
CV1-S1-R7	ϕ 0.44	8.56	27.5
CV1-S1-L8	ϕ 0.44	3.56	31.5
CV1-S1-R8	ϕ 0.44	8.56	31.5
CV1-S1-L9	ϕ 0.44	3.56	35.5
CV1-S1-R9	ϕ 0.44	8.56	35.5
CV1-S1-L10	ϕ 0.44	3.56	39.5
CV1-S1-R10	ϕ 0.44	8.56	39.5
CV1-S1-L11	ϕ 0.44	3.56	43.5
CV1-S1-R11	ϕ 0.44	8.56	43.5

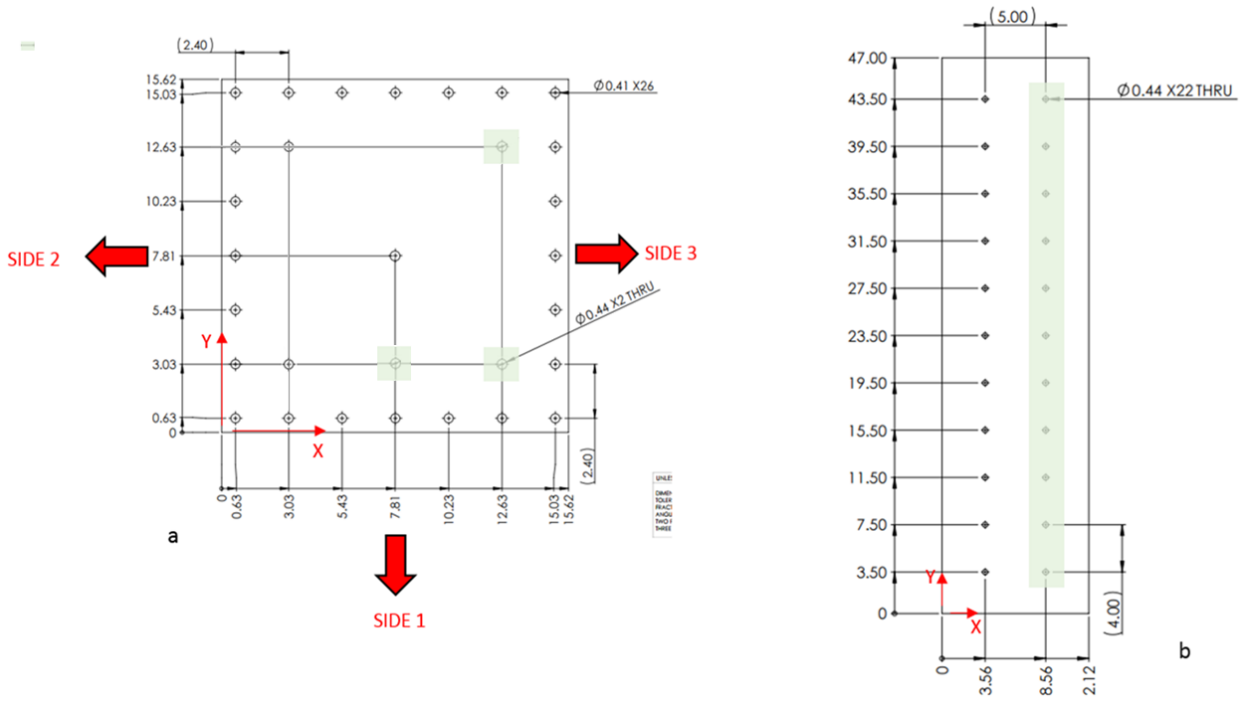

Figure 2.7: CV1 penetrations locations

CV1-T-C port located at the top center of CV1 is used as the RPV heater power connections. Two needle valves are connected to CV1-T-S1S2 and CV1-T-S2S4 to simulate the leak path L1A. Mechanical pressure gauge is connected to CV1-T-S1C. CV1-T-S1S3 port located at the top right-bottom of CV1 is used as gas injection port. The helium source connects to the Coriolis flow meter before traveling to the gas injection port. The mass flow sensor allows for repeatable helium injection rates during testing.

2.2.2.2 *Reactor pressure vessel*

Figure 2.8 represents the Reactor Pressure Vessel (RPV) and the Supports. The RPV of the test facility was made of 18 gauge (0.04 inch thickness) galvanized steel. The dimension of RPV of the prototype plant (full scale) were approximated as a cylinder with height of 80 ft., diameter of 22.4 ft., and volume of 31,530 ft^3. Applying 1/28 scaling resulted in a diameter of 9.6 inches and the height of 34.29 inches, but due to the difficulities of fabrication, 10-inch standard galvanized steel pipe was employed as the RPV (0.4 inches of distortion of the RPV diameter scaling). The RPV inside the CV1 is supportted by a custom fabricated supporting structure made of aluminum materials.

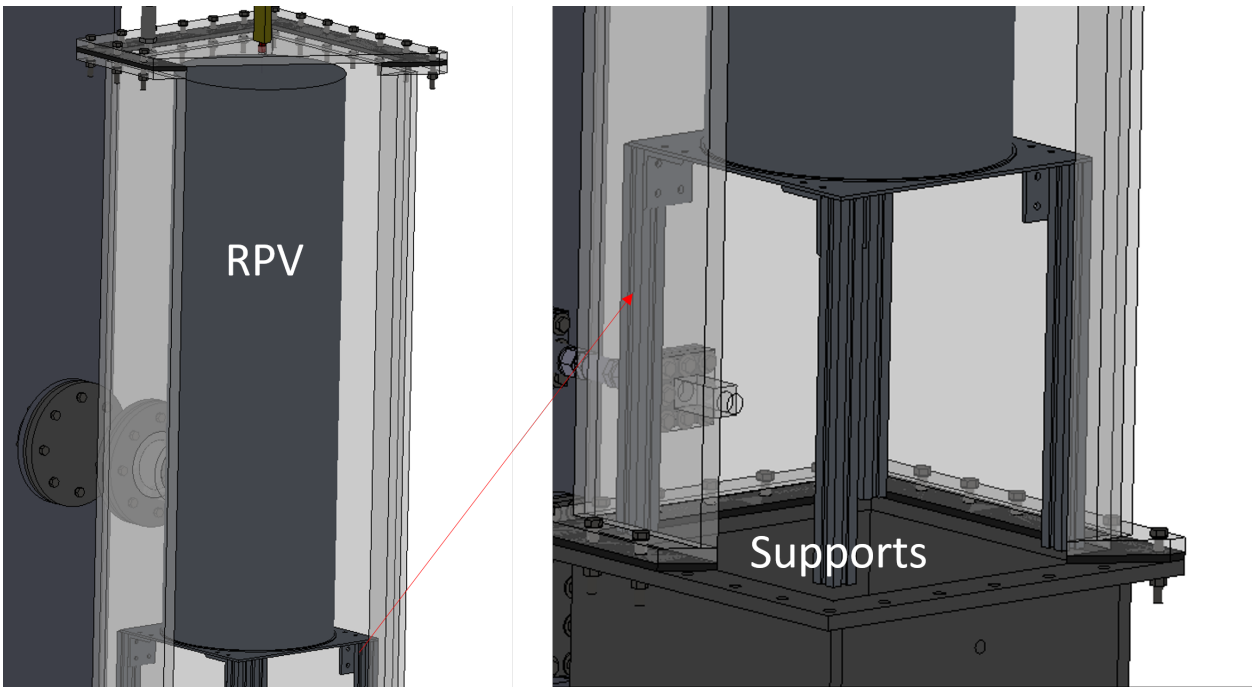

Figure 2.8: Reactor pressure vessel and supports

In order to simulate the decay heat from the RPV, flexible silicone-rubber heat sheets were attached inside the cylinder. Additional details on vessel and heaters are included in Appendix A. Verification of the temperature distribution around the periphery of the RPV was conducted to

determine the temperature limit that not to exceed the softening temperature of the material (120°C for Polycarbonate) of the test facility. Thermal power was applied to the heat sheets through Variacs from the AC power source. Temperature of the RPV cylinder was measured by a thermocouple attached between the inner surface of the cylinder and the heat sheet. Thermal boundary layer of outer surface of the RPV cylinder was measured by a thermocouple rack. 5 Thermocouples were installed in the thermocouple rack and spaced 5 mm apart from the RPV. Figure 2.9 shows the experimental setup for the temperature verification.

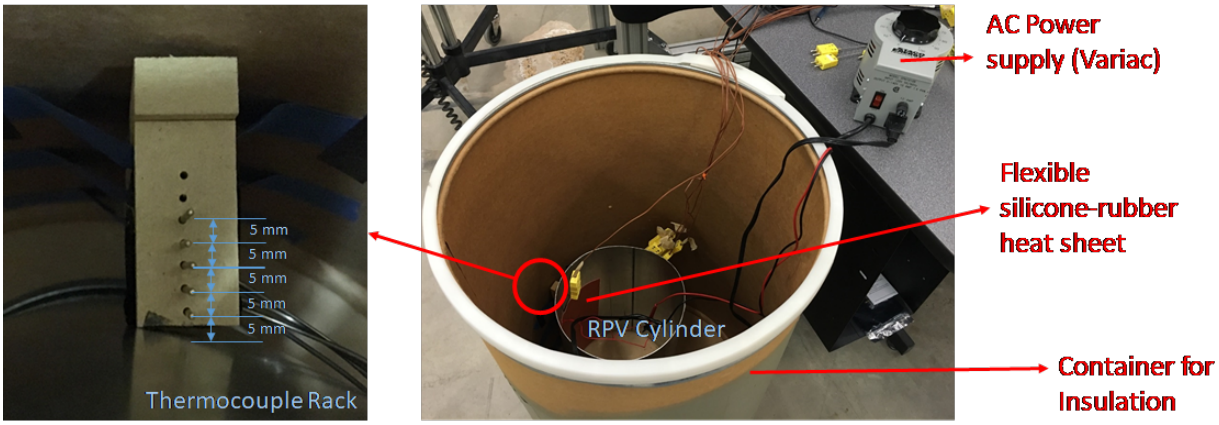

Figure 2.9: Experimental setup for the temperature verification from the RPV

Figure 2.10 shows the experimental results of the temperature of temperature distribution of the thermal boundary layer of outer surface of RPV and applying AC power through single heat sheet. Maximum temperature on the heating pad from the measurement was approximately 80°C where 65 W of AC power was supplied. If we account for the engineering margin for the material temperature limit (120°C for Polycarbonate), 65 W of AC power input can be determined as the input power limit.

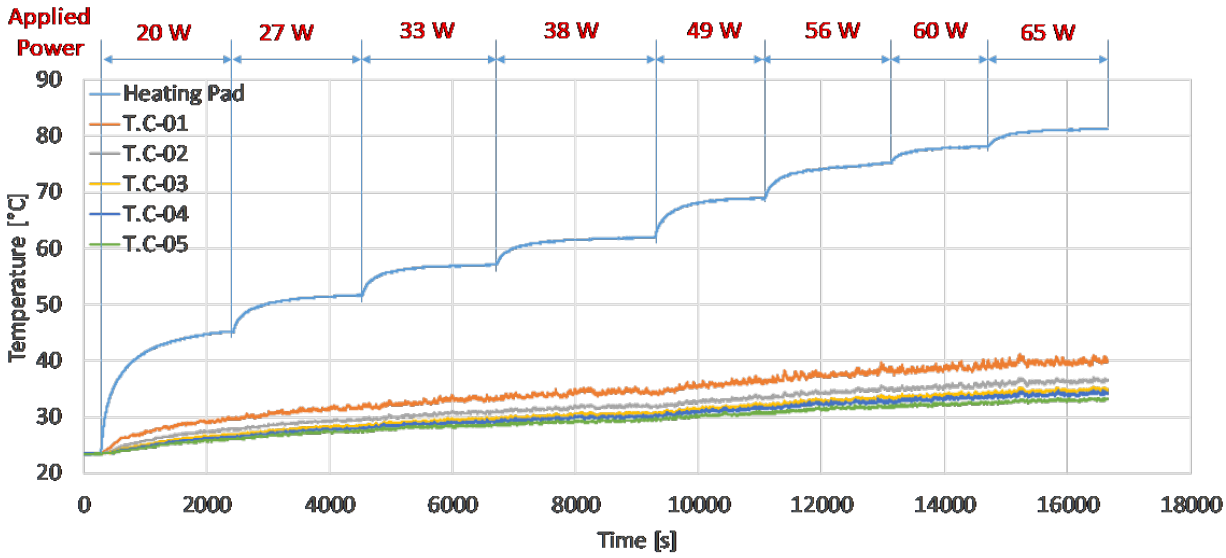

Figure 2.10: Temperature distributions for step increases in applied power

2.2.2.3 Steam generator dump tank cavity (CV2)

The compartment is located at the bottom of CV1 and connected to CV1 by flanges (Fig. 2.11). CV2 and CV1 are normally isolated with the aid of an aluminum panel and gaskets interposed between the flanges mentioned above.

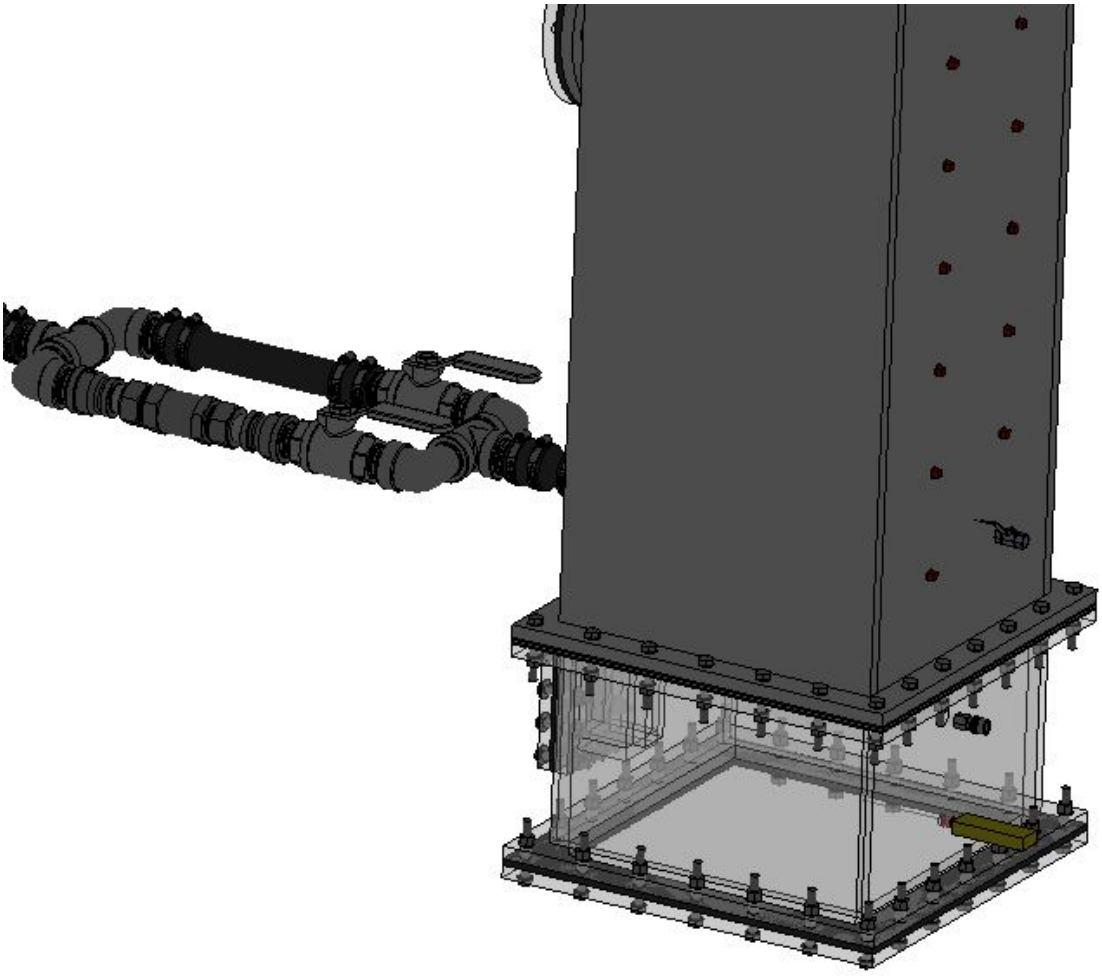

Figure 2.11: View of CV2

Penetrations of the walls are installed in CV2. The penetrations in use in CV2 are listed in Table 2.4.

Table 2.4: CV2 penetrations locations

Name	**Dimension** (inches)	**Location** (center of hole - inches)	
		X	Y
Fig. 2.12			
CV2-S1-High	ϕ 0.44	6.06	1.70
CV2-S1-Low	ϕ 0.44	6.06	5.70

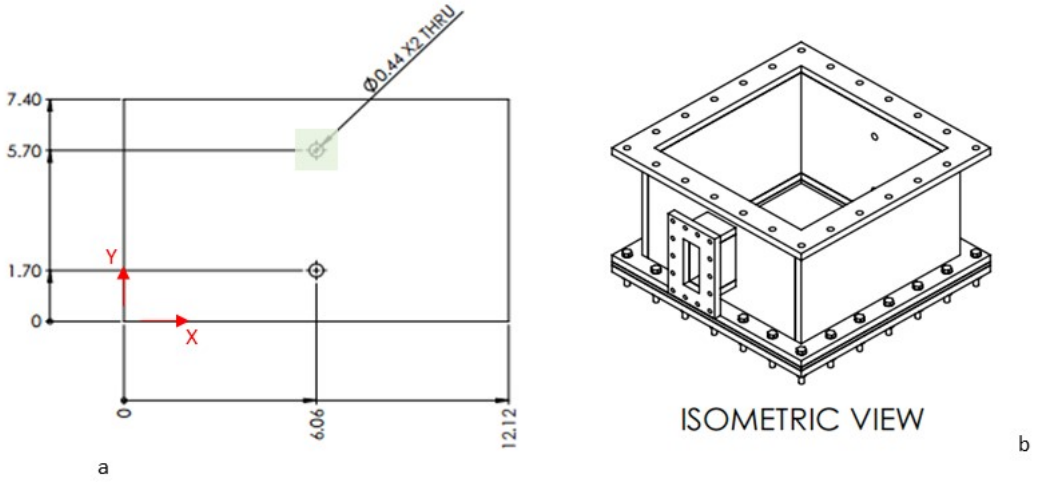

Figure 2.12: CV2 penetration locations

CV2-S1-High port located on the side of CV2 is used as the gas injection port. The helium source connects to the Coriolis flow meter before traveling to the gas injection port. The mass flow sensor allows for repeatable helium injection rates during testing.

2.2.2.4 Steam generator compartment (CV3) and internals

The details of the steam generator compartment are shown in Fig. 2.13. The compartment is connected to CV1, CV2, CV4, and CV6 through flow paths described in this section. The main constituents of CV3 are the compartment walls, and the top and bottom flanges. Both bottom and top flanges are connected to lids to close the compartment and maintain the pressure during tests.

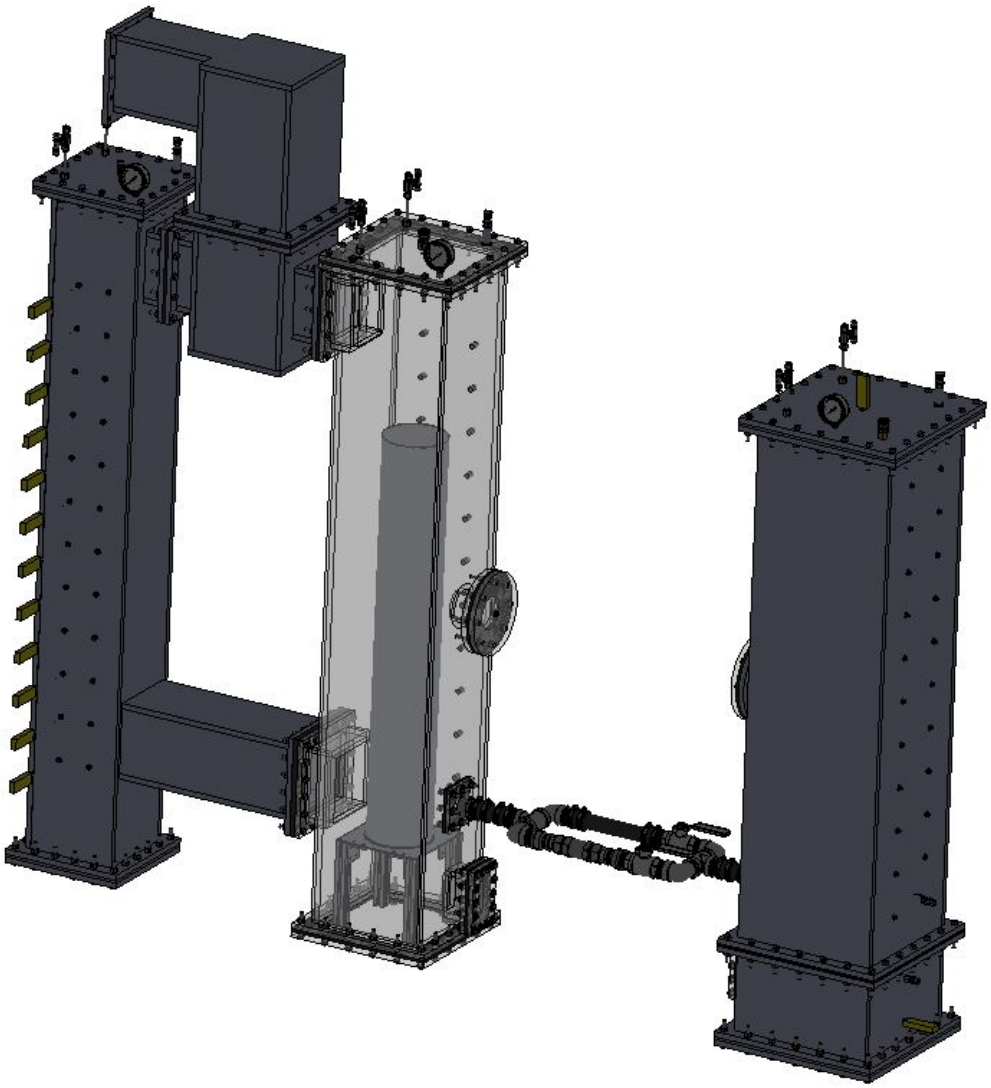

Figure 2.13: CV3 and internals

The steam generator vessel is located inside the compartment CV3 and supported by an aluminum support (plate and structure). Penetrations of the walls of CV3 are installed to:

- Establish flow communication with other compartments
- Impose and control inlet/outlet flows
- Install instrumentation

Flow communications are in place between:

1. CV3 and CV1 via the cross-vessel pipe. This connection is normally closed (Fig. 2.14 (1))
2. CV3 and CV1 via the one-way pressure relief valve V13 (Fig. 2.14 (2))
3. CV3 and CV2 via venting path V23, normally closed (Fig. 2.14 (3))
4. CV3 and CV6 via venting path V36 (Fig. 2.14 (4))
5. CV3 and CV5 via venting path V35 (Fig. 2.14 (5))
6. CV3 and the atmosphere via leaking path L3A (Fig. 2.14 (6))

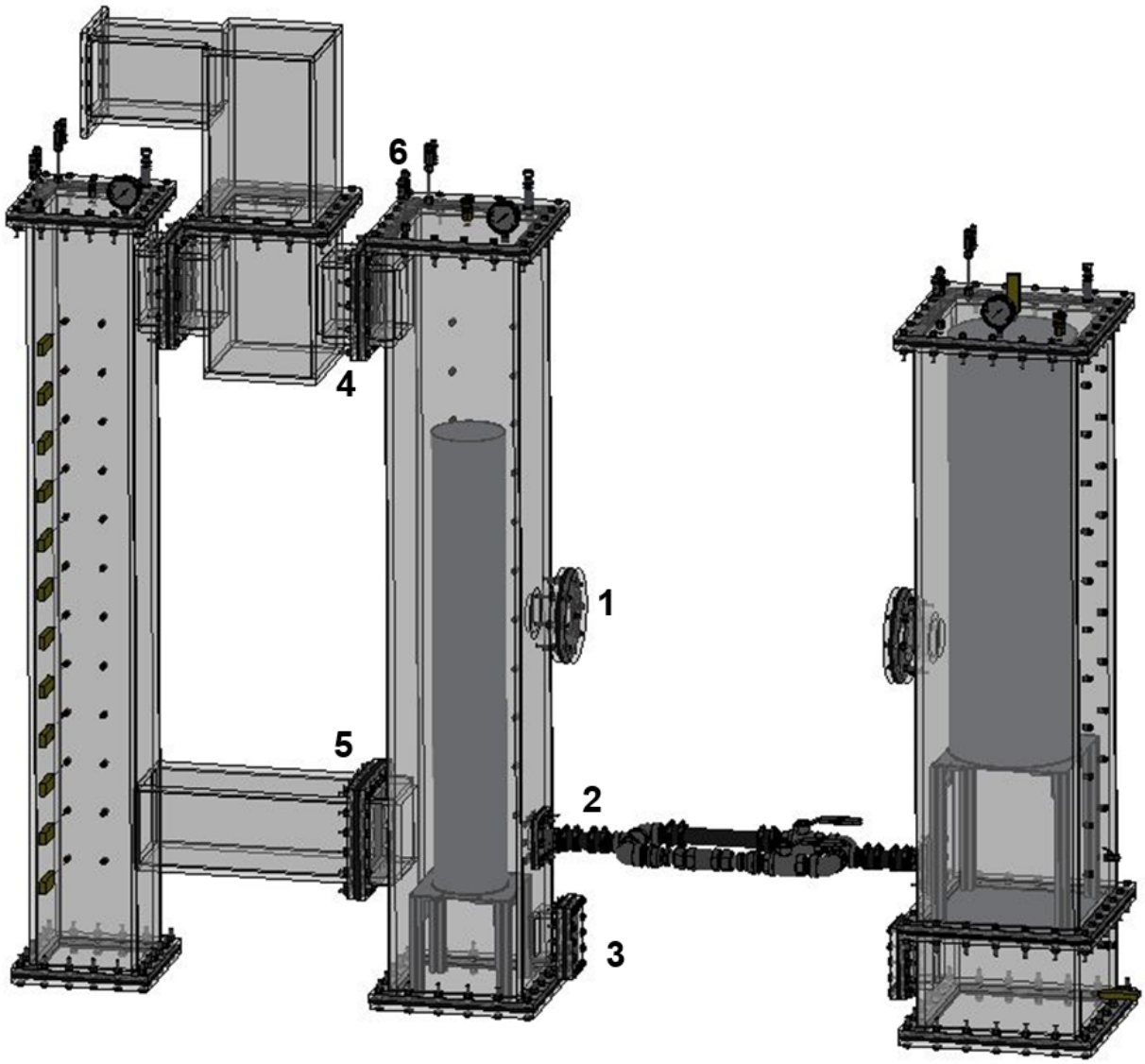

Figure 2.14: CV3 flow paths

Instrumentation is installed in the compartment through a series of 1/4″ NPT threaded holes. These holes are designed to support thermocouple probes, pressure transducers, and/or O_2 sensors, and can be also used for additional inlet/outlet ports. These ports are located at the compartment walls, and at the top lid. Table 2.5 identifies the ports by their ID and location.

Table 2.5: CV3 penetrations locations

Name	**Dimension** (inches)	**Location** (center of hole - inches)	
		X	Y
Fig. 2.15 a			
CV3-T-S1S3	ϕ 0.44	2.62	2.62
CV3-T-C	ϕ 0.44	6.64	6.64
CV3-T-S2S3	ϕ 0.44	10.66	10.66
CV3-T-S1S2	ϕ 0.44	2.62	10.66
CV3-T-S3S4	ϕ 0.44	10.66	2.62
Fig. 2.15 b			
CV3-S1-L1	ϕ 0.44	2.89	11.90
CV3-S1-R1	ϕ 0.44	7.89	11.90
CV3-S1-L2	ϕ 0.44	2.89	15.90
CV3-S1-R2	ϕ 0.44	7.89	15.90
CV3-S1-L3	ϕ 0.44	2.89	19.90
CV3-S1-R3	ϕ 0.44	7.89	19.90
CV3-S1-L4	ϕ 0.44	2.89	23.90
CV3-S1-R4	ϕ 0.44	7.89	23.90
CV3-S1-L5	ϕ 0.44	2.89	27.90
CV3-S1-R5	ϕ 0.44	7.89	27.90
CV3-S1-L6	ϕ 0.44	2.89	31.90
CV3-S1-R6	ϕ 0.44	7.89	31.90
CV3-S1-L7	ϕ 0.44	2.89	35.90
CV3-S1-R7	ϕ 0.44	7.89	35.90
CV3-S1-L8	ϕ 0.44	2.89	39.90
CV3-S1-R8	ϕ 0.44	7.89	39.90
CV3-S1-L9	ϕ 0.44	2.89	43.90
CV3-S1-R9	ϕ 0.44	7.89	43.90
CV3-S1-L10	ϕ 0.44	2.89	47.90
CV3-S1-R10	ϕ 0.44	7.89	47.90
CV3-S1-L11	ϕ 0.44	2.89	51.90
CV3-S1-R11	ϕ 0.44	7.89	51.90

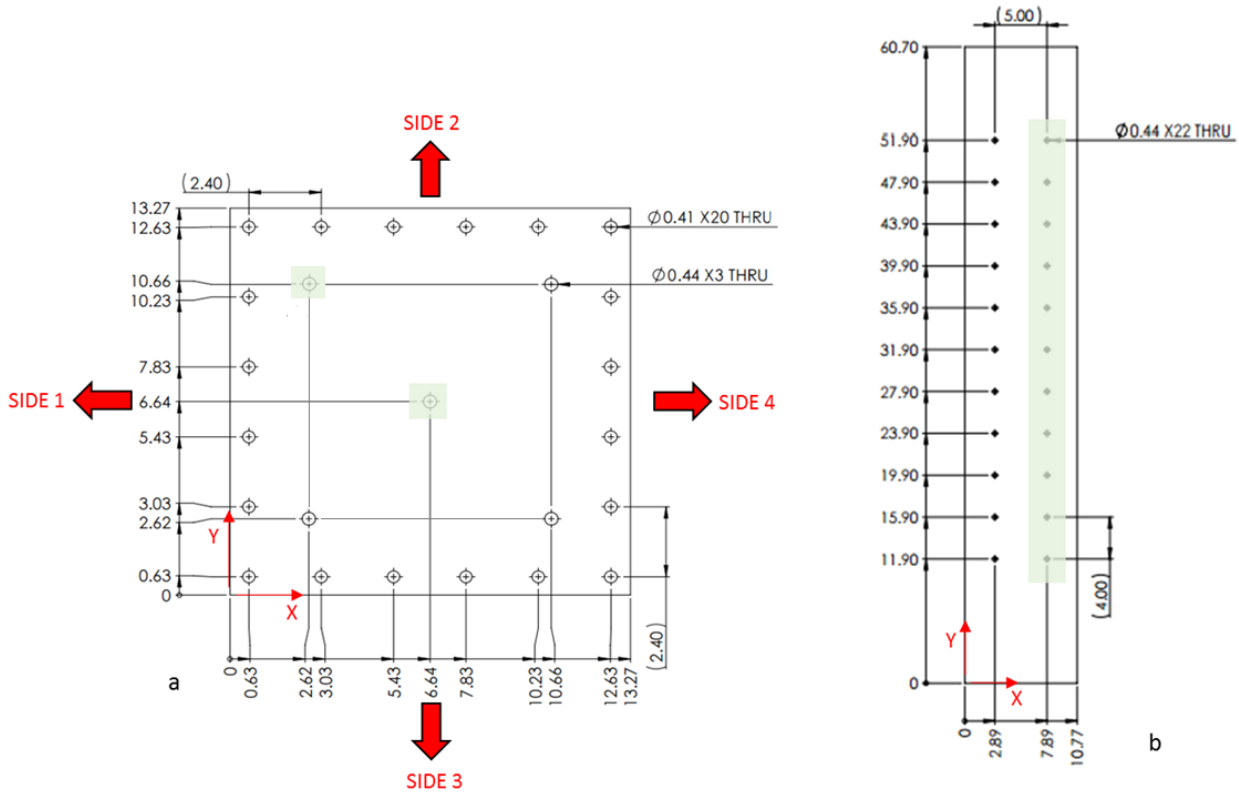

Figure 2.15: CV3 penetration locations

Two needle valves are connected to CV3-T-S1S2 and CV3-T-S2S4 to simulate the leak path L3A. Mechanical pressure gauge is connected to CV3-T-S3S4. Pressure transducer was connected to CV3-T-S2S4 port. CV3-T-C port located at the top center of CV3 is used as the gas injection port. The helium source connects to the Coriolis flow meter before traveling to the gas injection port. The mass flow sensor allows for repeatable helium injection rates during testing.

2.2.2.5 *Steam generator vessel*

Figure 2.16 represents the Steam Generator Vessel (SGV) and the Supports. The SGV of the test facility is made of 18 gauge (0.04 inch thickness) galvanized steel, which is the same material as the RPV. The dimension of SGV of the prototype plant (full scale) were approximated as a cylinder with height of 81.5 ft., diameter of 14.8 ft., and volume of 14,020 ft^3. Applying 1/28 scaling resulted in a diameter of 6 inches and the height of 34.93 inches. There is no scaling distortion for the SGV scaling. The SGV inside the CV3 is supportted by a custom fabricated supporting structure made of aluminum materials.

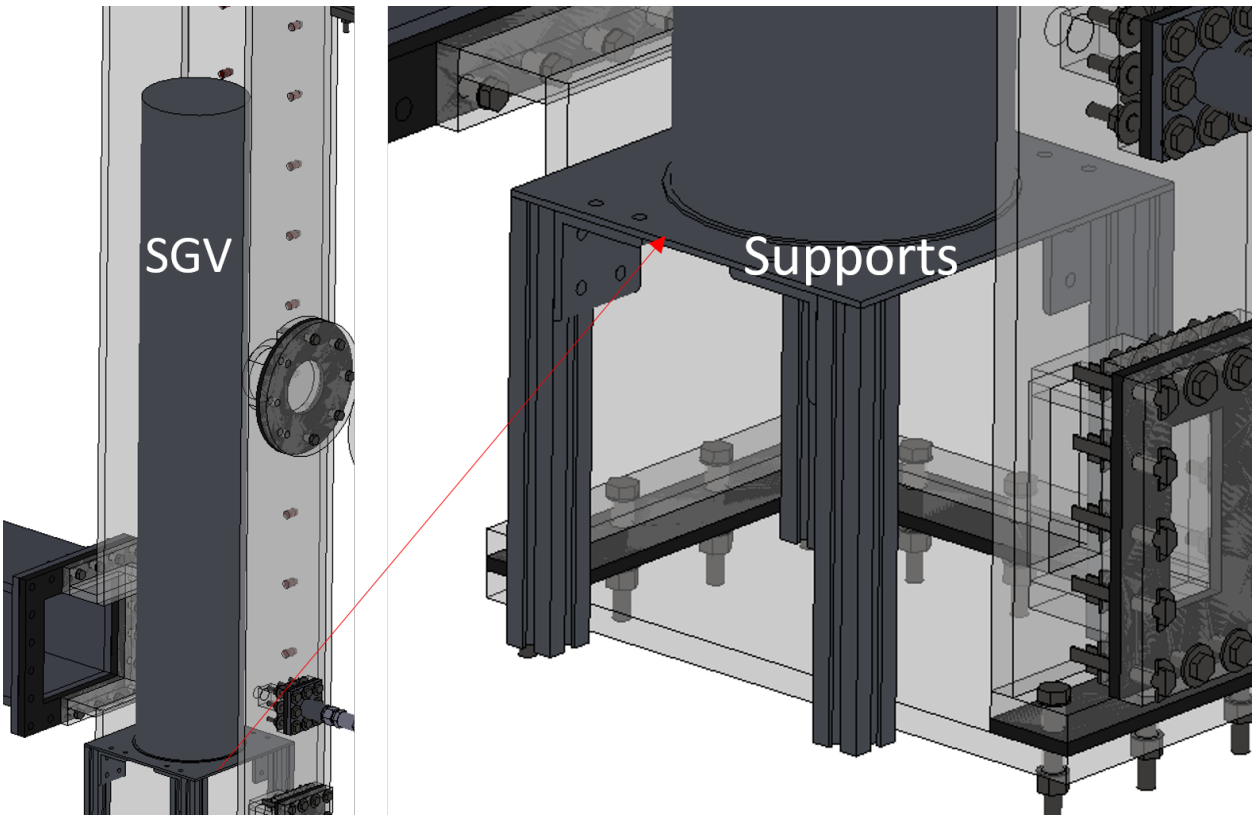

Figure 2.16: Steam generator vessel and supports

2.2.2.6 Lower vent (CV4) and upper vent (CV5) spaces

These compartment are openly connected representing the reactor building chimney. The compartment CV4 is shaped to allow for a connection to CV3 on the right, CV6 on the left, and CV5 at the top. CV5 can be left open to the atmosphere or closed with the use of a proper end plate connected to the flange. Depending on the test requirements, an extra lid on CV5 may have a penetration port for the measurement of temperature, air concentration, and pressure. A view of these compartments is shown in Fig. 2.17.

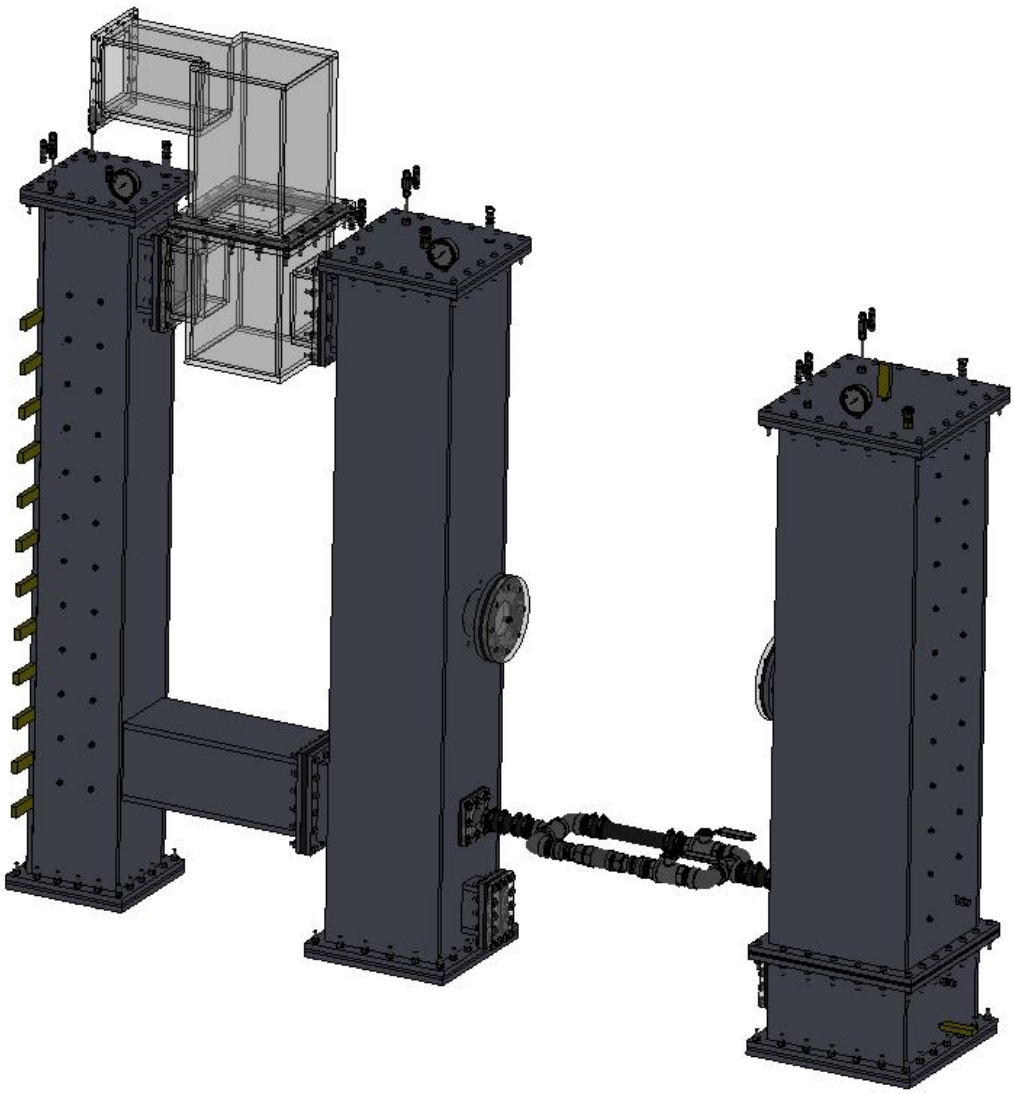

Figure 2.17: View of CV4 and CV5

2.2.2.7 Equipment shaft compartment (CV6)

The equipment shaft compartment is an empty compartment connected to CV3 and CV4. These flow paths are normally open. A view of CV6 is shown in Fig. 2.18.

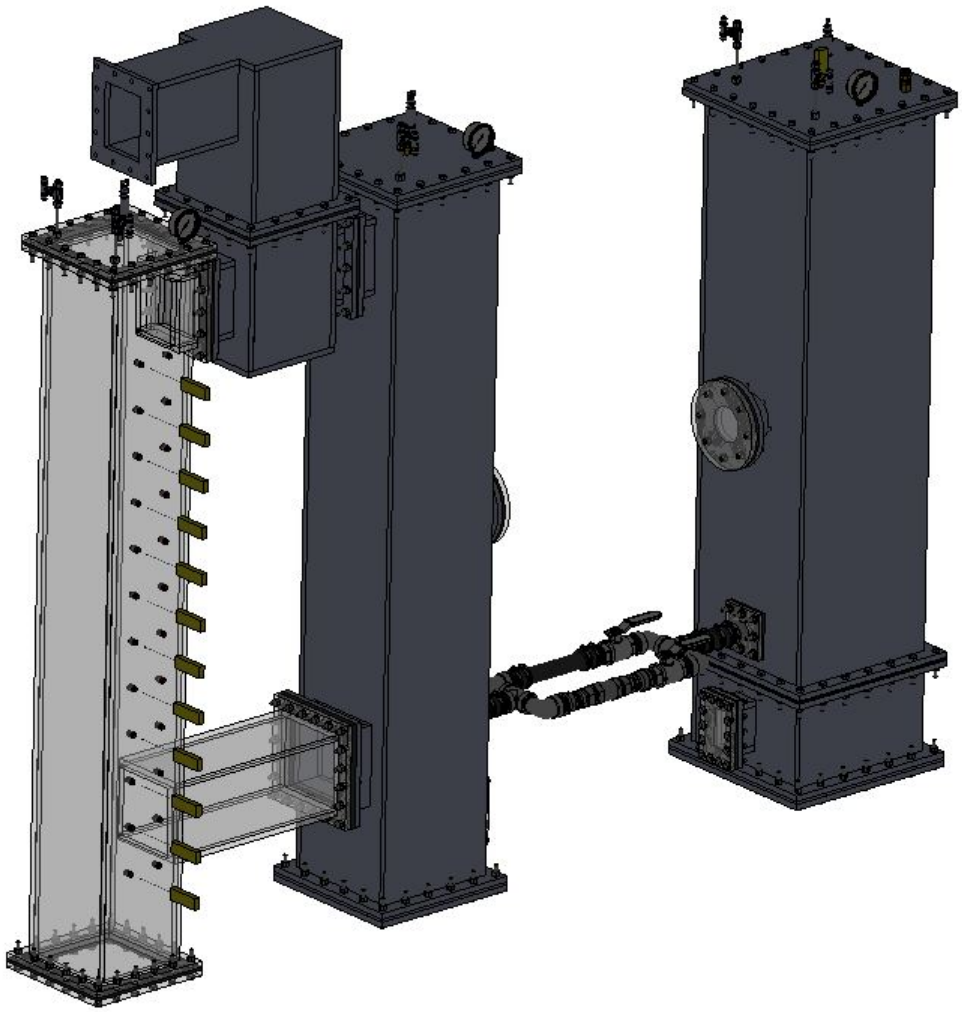

Figure 2.18: View of CV6

The main components of this compartment are:

- The compartment walls
- The compartment top and bottom flanges

- The top and bottom lids.

Lids are normally connected to the flanges with bolts to maintain the pressure inside the compartment during tests. Penetrations of the walls of CV6 are installed to:

- Establish flow communication with other compartments
- Impose and control inlet/outlet flows
- Install instrumentation

Flow communications are in place between:

1. CV6 and CV4 via venting path V64. This connection is normally closed (Fig. 2.19 (1))
2. CV6 and CV3 via venting path V36 (Fig. 2.19 (2))
3. CV6 to ambient via leak path L6A.

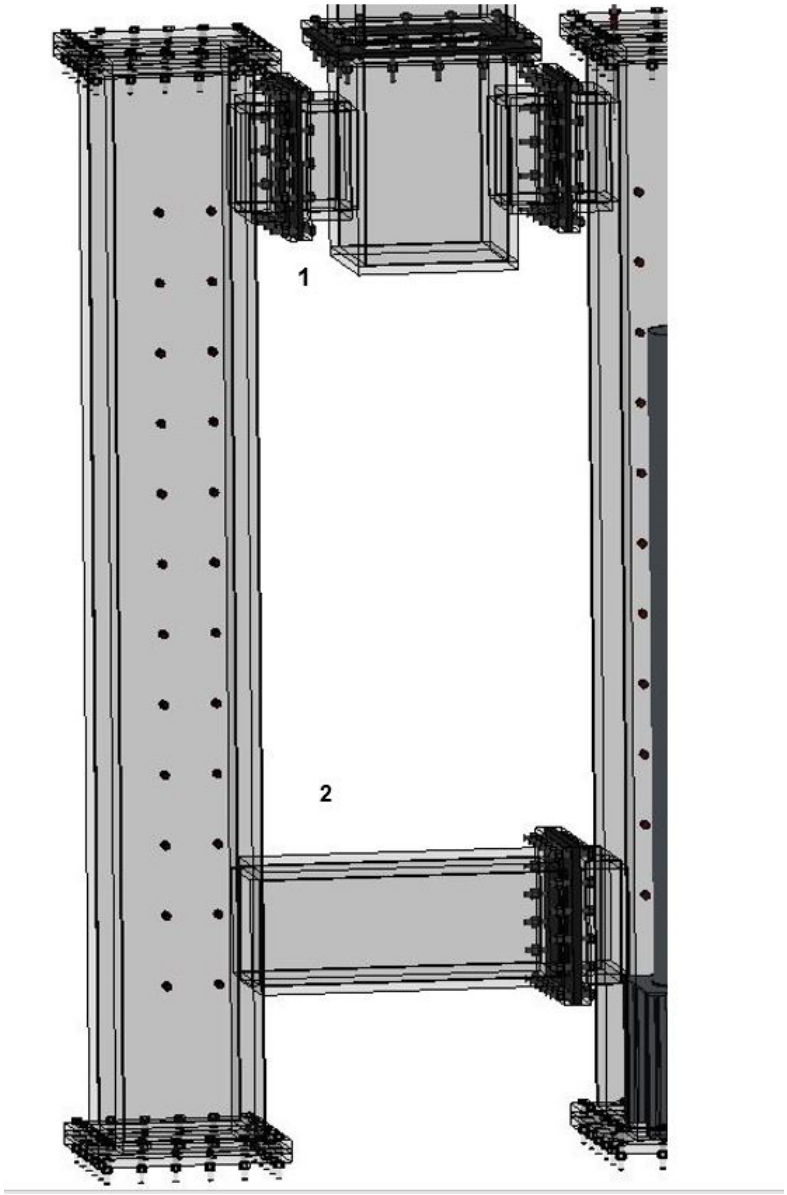

Figure 2.19: CV6 flow paths

Instrumentation is installed in the compartment through a series of 1/4″ NPT threaded holes. These holes are designed to support thermocouple probes, pressure transducers, and/or O_2 sensors, and can also be used for additional inlet/outlet ports. These ports are located at the compartment walls, and at the top lid. Table 2.6 identifies the ports by their ID and location.

Table 2.6: CV6 penetrations locations

Name	**Dimension** (inches)	**Location** (center of hole - inches)	
		X	Y
Fig. 2.20 a			
CV6-T-S1S2	ϕ 0.44	1.99	1.99
CV6-T-C	ϕ 0.44	5.54	5.54
CV6-T-S3S4	ϕ 0.44	9.09	9.09
CV6-T-S1S4	ϕ 0.44	9.09	1.99
CV6-T-S2S3	ϕ 0.44	1.99	9.09
Fig. 2.20 b			
CV6-S1-L1	ϕ 0.44	2.54	8.80
CV6-S1-R1	ϕ 0.44	5.54	8.80
CV6-S1-L2	ϕ 0.44	2.54	12.80
CV6-S1-R2	ϕ 0.44	5.54	12.80
CV6-S1-L3	ϕ 0.44	2.54	16.80
CV6-S1-R3	ϕ 0.44	5.54	16.80
CV6-S1-L4	ϕ 0.44	2.54	20.80
CV6-S1-R4	ϕ 0.44	5.54	20.80
CV6-S1-L5	ϕ 0.44	2.54	24.80
CV6-S1-R5	ϕ 0.44	5.54	24.80
CV6-S1-L6	ϕ 0.44	2.54	28.80
CV6-S1-R6	ϕ 0.44	5.54	28.80
CV6-S1-L7	ϕ 0.44	2.54	32.80
CV6-S1-R7	ϕ 0.44	5.54	32.80
CV6-S1-L8	ϕ 0.44	2.54	36.80
CV6-S1-R8	ϕ 0.44	5.54	36.80
CV6-S1-L9	ϕ 0.44	2.54	40.80
CV6-S1-R9	ϕ 0.44	5.54	40.80
CV6-S1-L10	ϕ 0.44	2.54	44.80
CV6-S1-R10	ϕ 0.44	5.54	44.80
CV6-S1-L11	ϕ 0.44	2.54	48.80
CV6-S1-R11	ϕ 0.44	5.54	48.80
CV6-S1-L12	ϕ 0.44	2.54	52.80
CV6-S1-R12	ϕ 0.44	5.54	52.80

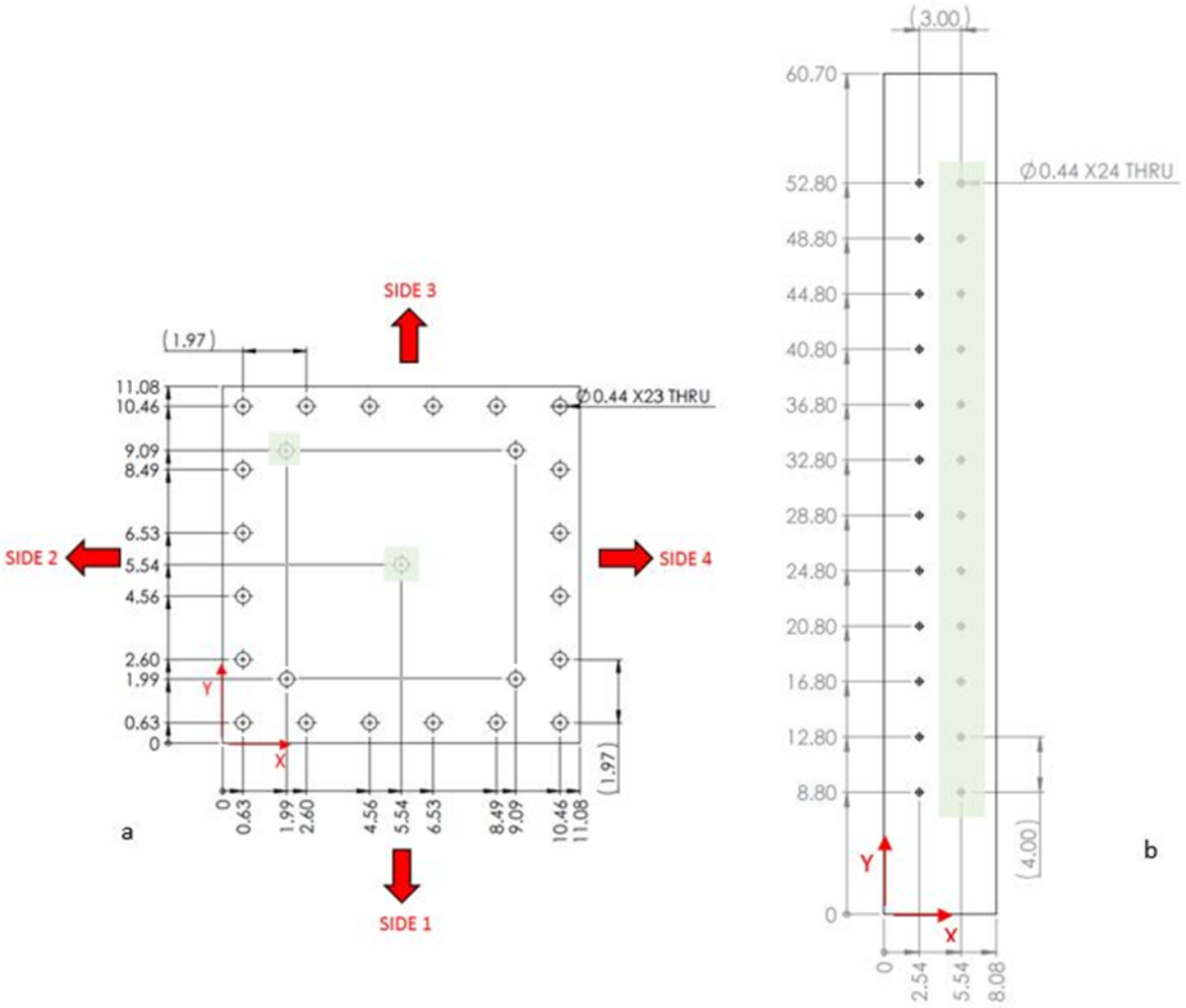

Figure 2.20: CV6 penetration locations

Two needle valves are connected to CV6-T-S1S2 and CV6-T-S2S4 to simulate the leak path L6A. Mechanical pressure gauge is connected to CV6-T-S1S4. Pressure transducer is connected to CV1-T-S3S4 port. CV6-T-C port located at the top center of CV6 is used as the gas injection port. The helium source connects to the Coriolis flow meter before traveling to the gas injection port. The mass flow sensor allows for repeatable helium injection rates during testing.

Table 2.7 summarizes the dimensions and description of the prototype plant (full scale) and the test facility (1/28 scaled down).

Table 2.7: Description of the prototype plant (simplified RB model) and the TAMU test facility compartments

Compartment ID	**Description**	**Full scale simplified model**			**TAMU Test Facility** (1/28 scaled down)		
		H×W×D (ft)	Volume (ft^3)	Free Volume[4] (ft^3)	H×W×D (ft)	Volume (ft^3)	Free Volume (ft^3)
CV1[5]	Reactor Cavity	112×28.4×28.4	90335	48805	1.02×1.02×3.92	4.08	2.45
CV2	Steam Generator Dump Tank Cavity	20×28.4×28.4	16100	16100	1.02×1.02×.62	0.64	0.64
CV3	Steam Generator Cavity	144×22.8×22.8	74860	50840	0.814×0.814×5.058	3.35	2.84
CV4	Lower Vent Space	28×18.9×18.9	10000	10000	0.68×0.68×.958	0.44	0.44
CV5	Upper Vent Space	30.5×18.9×18.9	10895	10895	0.68×0.68×1.1	0.51	0.51
CV6	Equipment Shaft	144×17.7×17.7	4500	45100	0.632×0.632×5.058	2.02	2.02

[4]Free volume is the volume of the compartment not occupied by any structure or other parts

[5]CV1 houses the RPV. The scaled diameter of the RPV of the test facility was distorted 0.4 inches (about 4.2%).

Figure 2.21 illustrates the side view of a 3D CAD drawing of the 1/28 linearly down scaled test facility.

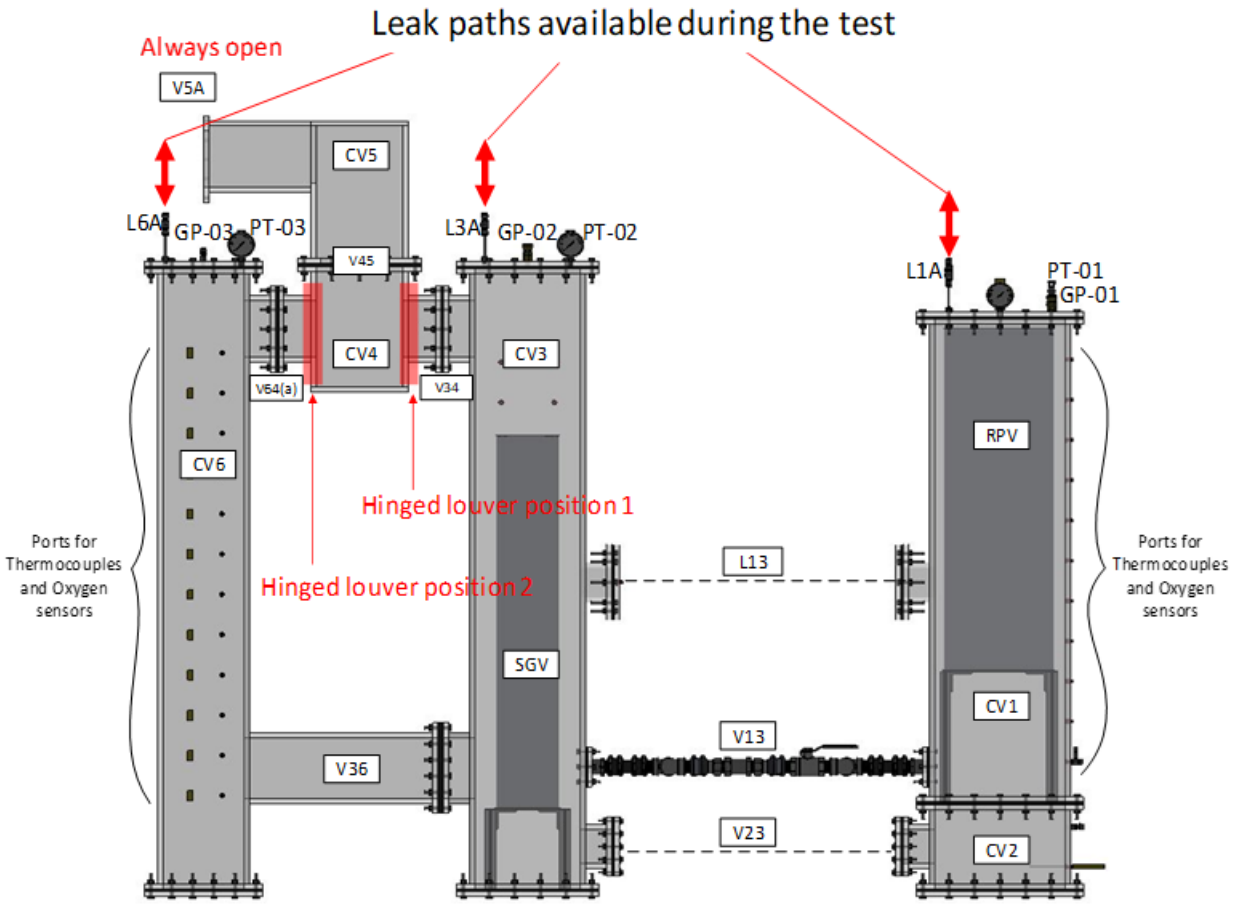

Figure 2.21: 3D CAD drawing of the down-scaled test facility

Figure 2.22 represents the 1/28 scaled experimental facility of the simplified RB model with the heatable RPV. Hinged louver position 1 and 2 will be used discussed in section 2.4. Because the current NGNP HTGR RB conceptual design specifies the RB natural leak rate as the total RB volume per day through the leak path, with a 1 psig constant pressure for the full-scale plant, the target leak rate for the scaled facility was determined using geometric and time scaling. The contributions of the major compartments, namely the reactor cavity (CV1), steam generator cavity

(CV3), and equipment shaft cavity (CV6), to the total natural leak rate were assumed to be 20%, 30%, and 50%, respectively (Alliance limited, NGNP industry, 2017).

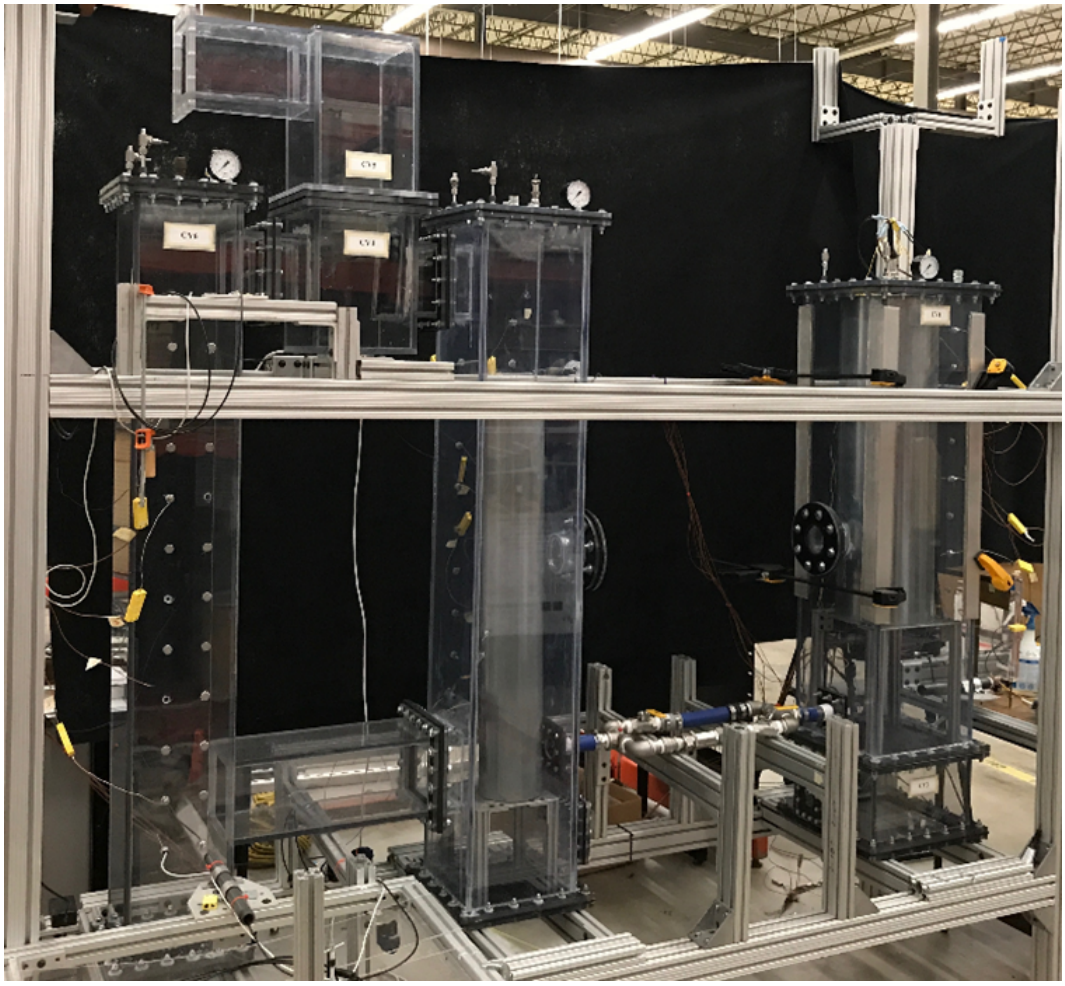

Figure 2.22: Experimental facility of simplified RB model of NGNP

Table 2.8 summarizes the materials used in the test facility and auxiliary components.

Table 2.8: Bill of materials used in the test facility and auxiliary components

Materials	Purpose	Sections
Polycarbonate	The wall frame for the test facility	Used to fabricate test section CV1, CV2, CV3, CV4, CV5 and CV6
Neoprene (ASTM D 2000 M1BC507)	Gasket	Used to fabricate gaskets between: • CV1 top flange and cap • CV1 bottom flange and CV2 top cap • CV1 side flange and smooth aluminum flange (V13) • CV1 and CV3 cross vessel (L13) • CV1 bottom flange and CV2 top cap • CV2 bottom flange and cap • CV2 and CV3 side flange (V23) • CV3 top flange and cap • CV3 bottom flange and cap • CV3 and CV6 side flange (V36) • CV3 and CV1 cross vessel (L13) • CV3 side flange and smooth aluminum flange (V13) • CV3 and CV2 side flange (V23) • CV3 and CV4 side flange (V34) • CV4 and CV3 side flange (V34) • CV4 top flange and CV5 bottom flange (V45) • CV4 and CV6 side flange (V64(a)) • CV5 bottom flange and CV4 top flange (V45) • CV6 top flange and cap • CV6 bottom flange and cap • CV6 and CV3 side flange (V36) • CV6 and CV4 side flange (V64(a))
Polyethylene (1/4″ NPT round plugs)	Sealing	Used to seal off inactive instrument ports
Stainless Steel	Steam generator and reactor pressure vessels	Used to fabricate Reactor Pressure Vessel and Steam Generator Vessel
Aluminum	Supporting structure	•Used to fabricate smooth, 1″ flange for compression fitting between CV1 and CV3 •Aluminum plate for added stability between CV1 and CV2
Helium (Purity - 99.999%)	Working Fluid	Used to provide medium for measuring and analyzing oxygen concentration, pressure and temperature distribution
Fiberglass and Polyurethane Foam	Vessels filling materials	Used to fill the empty volume of the RPV and SG vessel.

The leak rate can be determined experimentally by measuring the pressure response over time for each compartment. After pressurizing each compartment with air to obtain the initial pressure condition with all the appropriate instrumentation in place, the pressure inside the facility is returned to equilibrium with the ambient air outside the test facility by leaking the pressurized air into the atmosphere. The pressure loss in the facility can then be modeled using an exponential function to the leak rate data, as follows:

$$P(t) = P_0 \left(1 - e^{-\lambda t}\right) \tag{2.22}$$

where P_0 is the initial pressure inside the facility, $P(t)$ is the pressure at time t, and λ is the decay constant. For the pressure loss inside the compartment, λ determines how quickly the facility loses pressure because of air leakage. The ideal gas law demonstrates that the pressure can be related to the number of moles of air in the facility if the temperature is known.

$$PV = nRT \tag{2.23}$$

where P is the pressure, V is the total compartment volume, n is the number of moles of air, R is the universal gas constant, and T is the gas temperature. Because the facility's volume is constant, Eq. (2) can be rearranged into the following form with an assumption of a constant temperature inside the compartment:

$$n(t) = \frac{V}{RT} P(t) \tag{2.24}$$

where $n(t)$ is the number of moles of air leaking from the facility, which can be determined by substituting Eq. (22) into Eq. (24) and obtaining its time derivative as follows:

$$\frac{dn(t)}{dt} = \frac{V}{RT} P_0 \lambda e^{-\lambda t} \tag{2.25}$$

By substituting $n = m/M$, where m is the substance's mass and M is the gas's molecular weight, the

air mass in the facility can be determined from Eq. (26):

$$\frac{dm(t)}{dt} = \frac{VM}{RT} P_0 \lambda e^{-\lambda t} \tag{2.26}$$

where *M* can be approximated as 28.9 g/mol for air.

In order to measure the transient response of NGNP HTGR RB test facility during the hypothetical D-LOFC scenario, the following instruments are employed.

- 3 - Omega Rugged Type Stainless Steel High Performance Pressure Transducers (PX329-005GV, $\pm 0.25\%$ full scale accuracy, NIST traceable)

Figure 2.23: Omega PX329-005GV pressure transducer

- 20 - Omega K-Type Thermocouples ($\pm 1°C$ accuracy)

Figure 2.24: Omega K-type thermocouple

- 3 - Ocean Optics Inc. R-Series NeoFox Oxygen Probes and Sensors(5% reading accuracy)

Figure 2.25: Ocean Optics Roxy oxygen sensor

- 1 - Ocean Optics NeoFox oxygen sensor signal handler

Figure 2.26: Ocean Optics Roxy oxygen sensor

- 1 - National Instruments (NI) Data Acquisition System (DAQ)

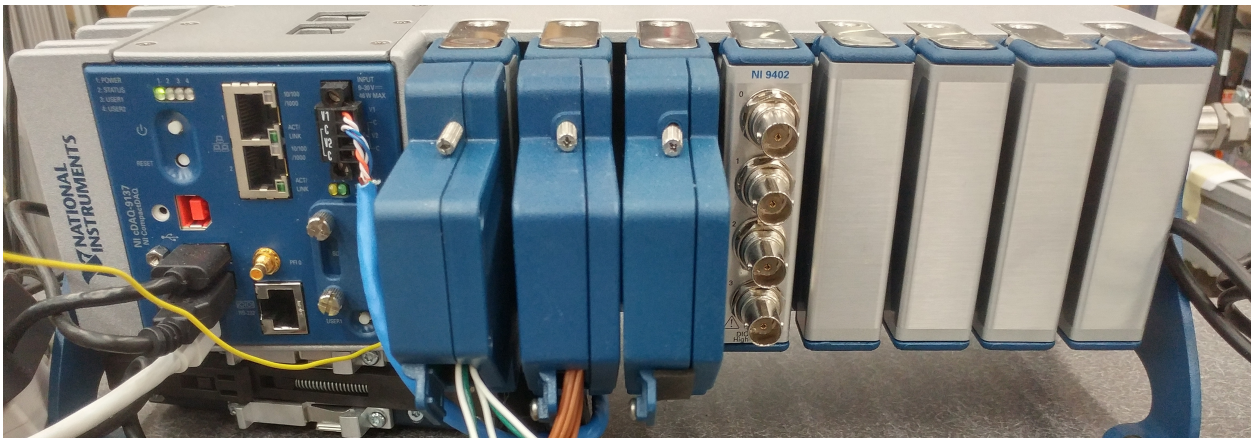

Figure 2.27: National Instruments cRio data acquisition system

- 1 - Micro Motion RFTF9737 Microfluid Transmitter with Coriolis Flow Meter

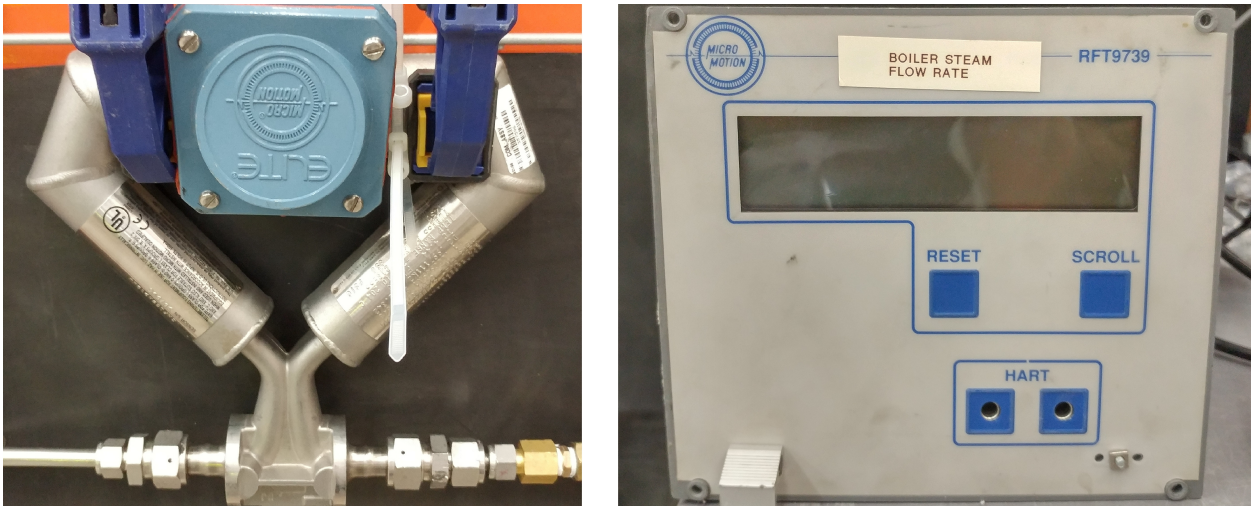

Figure 2.28: Micro Motion Coriolis flowmeter and signal handler

All the sensors are connected to the NI DAQ system and the sensor outputs are recorded in realtime with 1 kHz sampling rate.

2.3 Preliminary Results: Shakedown of TAMU 1/28 scale NGNP HTGR RB Test Facility

A series of shakedown tests to learn about the TAMU 1/28 scale NGNP HTGR RB test facility is conducted. Full research plan will be developed based on the results of shakedown tests.

2.3.1 Leak rate adjustment

The leak rate adjustment tests are performed to match the leak rate design parameter of the major compartments. Figure 2.29 presents the isolation of boundaries drawn on the CAD drawing of the test facility for the leak rate adjustment tests.

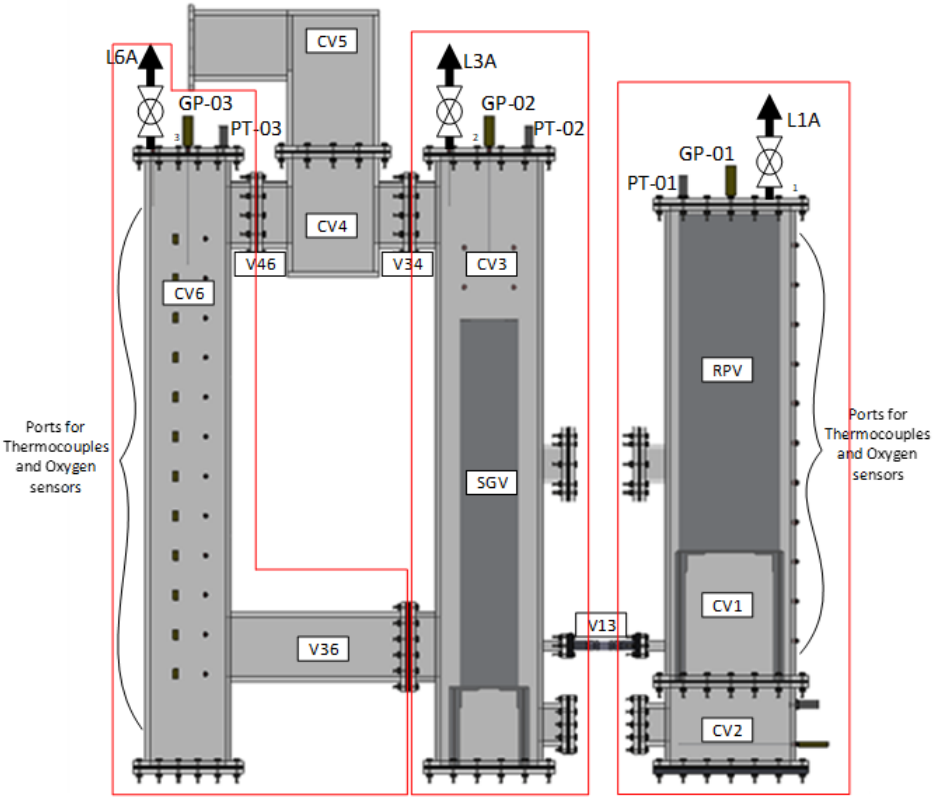

Figure 2.29: Isolation of the experimental facility for leak rate adjustment tests

The experimental facility for the set of leak rate adjustment tests consists of three isolated compartments: CV1, CV3, and CV6 (inside the red boxes) with the remaining test volumes and

connecting sub-volumes shown in Fig. 2.29. In the facility, vent paths V13, V34, V36, and V46 are sealed with polycarbonate flange caps to isolate the compartments from each other. From the HTGR RB design criteria as VLPC, the target leak rate of the simplified RB model was defined as 1 volume/day under the constant 1 psig internal building pressure condition. It means that the initial gas inside all the reactor buildings would be expelled to the ambient environment entirely within a day with the reactor building pressure maintained at 1 psig as mentioned in the previous section. Based on the NGNP conceptual design, USNC indicated the contribution of each compartment to achieve 1 volume/day as 50% of total leakage from CV6, 30% from CV3, and 20% from CV1 (Yang *et al.* 2018).

In each compartment (CV1, CV3, and CV6), the natural leak rate is expected to be less than the target leak rate to allow adjustments of the leak path (L1A, L3A and L6A). The target leak rates are assumed to be achieved when the relative differences of the leak path adjusted measured leak rates are less than 10%. In test P1-A, the CV1 natural leak rate is determined using a characteristic pressure decay curve at 1 psig with air. After the natural leak rate of CV1 is determined, a target leak rate is achieved with the adjustment of leak path L1A in test P1-B. In test P1-C, the natural leak rate of CV3 is determined using a characteristic pressure decay curve at 1 psig with air. After the natural leak rate of CV3 is determined, the target leak rate is achieved with the adjustment of leak path L3A in test P1-D. In test P1-E, the natural leak rate of CV6 is determined using the characteristic pressure decay curve at 1 psig with air. After the natural leak rate of CV6 is determined, the target leak rate is achieved with the adjustment of leak path L1A in test P1-F. Figure 2.30 shows the actual isolated compartments for testing.

Since the TAMU NGNP test facility was geometrically scaled down to a factor of f_{scale} = 28 from the simplified RB model, the time scale should also be scaled down correspondingly. The scaling factor for the time can be determined by maintaining the dynamic similarity of the gas and matching the dimensionless numbers of the full plant and the scaled model. The time scaling then can be determined as follows combining with Eq. 2.15:

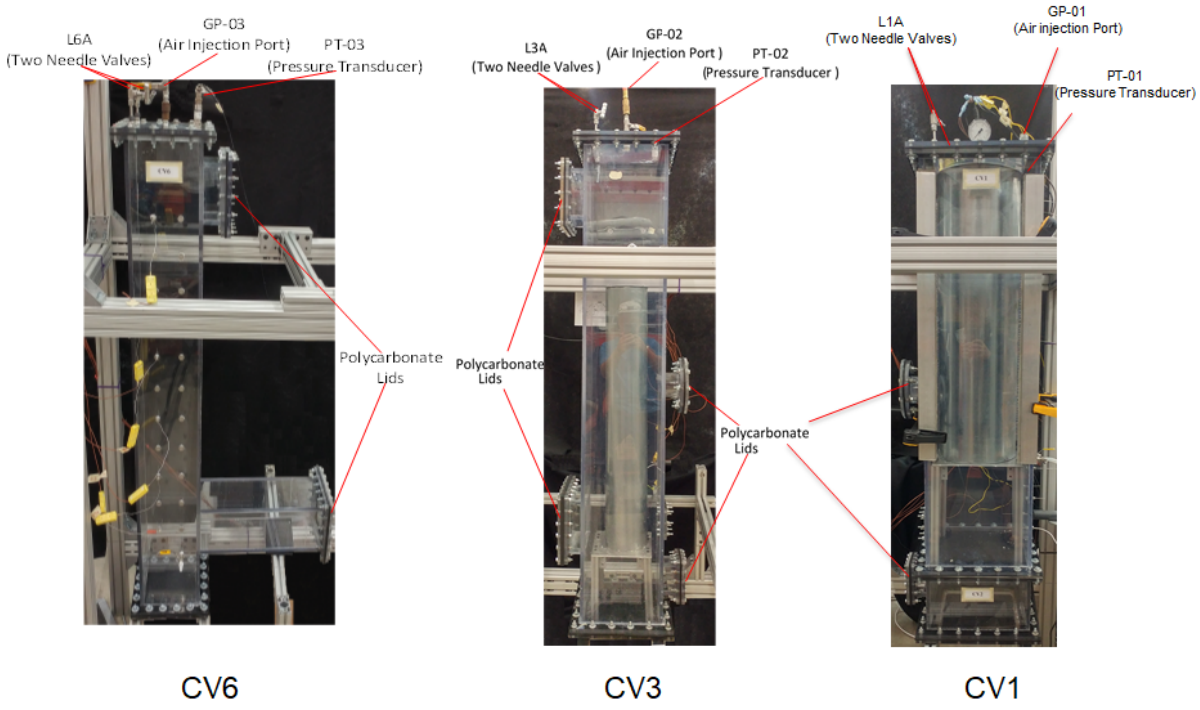

Figure 2.30: Isolated compartments for testing

$$t_R = \frac{t_m}{t_p} = \frac{L_m/U_m}{L_p/U_p} = \left(\frac{L_m}{L_p}\right)\left(\frac{L_m}{L_p}\right)^{-0.5} = L_R^{0.5} \tag{2.27}$$

Applying $f_{scale} = 28$ gives us:

$$t_m = \frac{1}{\sqrt{28}} t_p \tag{2.28}$$

Based on Eq. 2.28, a plant full day was scaled down to our facility and calculated to be approximately 16328 s, or about four and half hours. This scaled time factor from here on will be referred to as the "one day scaled time". With the time scale and length scale identified from the TAMU NGNP test facility, the specific target leak rates for each compartment can be determined. Table 2.9 shows the target leak rate condition for each compartment of the TAMU NGNP test facility.

Table 2.9: Target leak rate condition for each compartment of the TAMU 1/28 scale NGNP HTGR RB test facility

Component ID	**Volume** (m^3)	**Target Leak Rate** (g/s)
CV1	6.938×10^{-2}	3.103×10^{-3}
CV3	8.042×10^{-2}	4.655×10^{-3}
CV6	5.720×10^{-2}	7.759×10^{-3}

Leak rate of each compartment can be calculated using Eq. 2.26 with pressure transducer and thermocouple outputs. Each compartment is pressurized with air to approximately 1.2 psig, and the pressure and temperature responses are measured using NI DAQ system. Figure 2.31 presents the pressure response of each compartment with leak rate adjustment.

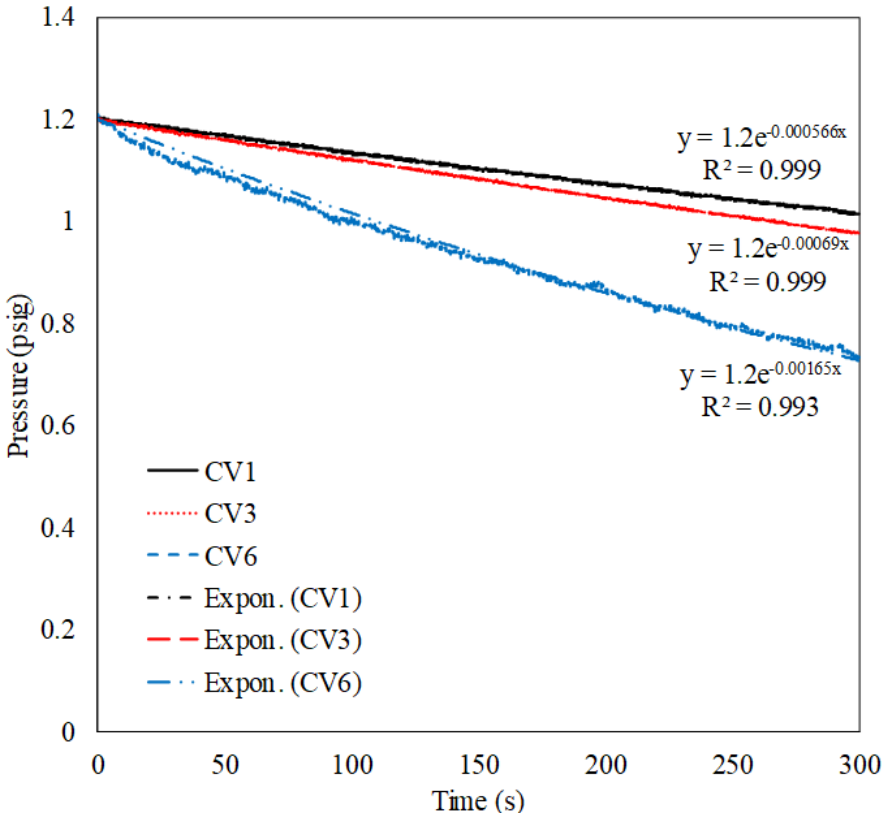

Figure 2.31: Pressure response of compartments

Table 2.10 summarizes the results of the leak rate adjustment tests.

Table 2.10: Summary of the leak rate adjustment tests

TEST ID	**Description**	**Volume** (m^3)	**Average Temperature** (K)	**Target leak rate** (g/s)	**Measured leak rate** (g/s)	**Relative Difference**
P1-A	Intrinsic leak rate with air for CV1	6.938E-02	295	-	1.219E-03	-
P1-B	Target leak rate with air for CV1	6.938E-02	322	3.103E-03	2.908E-03	6.3%
P1-C	Intrinsic leak rate with air for CV3	8.042E-02	295	-	4.600E-04	-
P1-D	Target leak rate with air for CV3	8.042E-02	295	4.655E-03	4.521E-03	2.9%
P1-E	Intrinsic leak rate with air for CV6	5.720E-02	295	-	7.500E-05	-
P1-F	Target leak rate with air for CV6	5.720E-02	295	7.759E-03	7.742E-03	0.2%

As shown in Table 2.10, all the leak rate of three compartments (CV1, CV3, and CV6) are adjusted within 10% of the target leak rate.

2.3.2 Integrity test of the experimental facility

As the purpose of the study is to investigate the transient response of depressurization accidental scenarios in NGNP HTGR RB, flow data of binary gas mixture (air and helium) including inlet flow rate, pressure, and temperature, the fresh oxygen content inside the compartments should be properly acquired. Data surrounding the air ingress rates back into CV6 and CV3 during helium evacuation are vital in determining and verifying scaling factors and distortions, equipment validity functionality as well as proper assembly and design of the experimental test facility.

In this section, two tests including test ID SD0002 and SD0003 were designed to verify the integrity of the test facility and the test operation procedure with repeatable results of oxygen concentration and pressure response of the scaled down simplified RB model regarding the identical initial and boundary conditions within the control volumes (CV1, CV3, and CV6).

A helium source was connected to the gas injection port GP-01 and was used to purge the

chamber (CV1 only) of all air through the purge port installed in the penetration port CV1-S1R1 before starting the test. Intrusive optical oxygen probes (Ocean Optics Neofox Hioxy sensors) were installed in the penetrations ports CV1-S1L1, CV3-S1L1, and CV3-S1L11. CV1-S1L1 is located at the low position of side panel of CV1. CV3-S1L1 is located at the low position of back panel of CV3. CV3-S1L11 is located at the high position of side panel of CV3. The accuracy of the oxygen sensor is $\pm 1\%$ for 20% oxygen concentration. Figure 2.32 shows the location on the penetration ports.

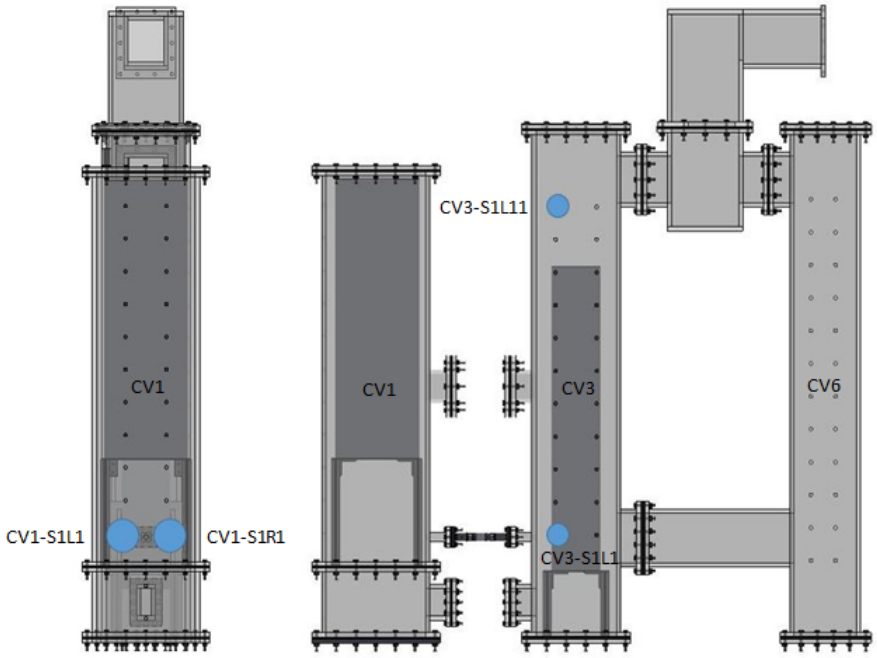

Figure 2.32: Location of oxygen probes (CV1 as the left image and CV3 as the right image) are indicated with blue dots over the port locations.

Three high accuracy silicon sensor type pressure transducers (Omega PX329-005GV) were connected to each chamber through PT-01, PT-02, and PT-03 to monitor any deviations in gauge pressure in the chambers. The accuracy of the pressure transducer is $\pm 0.25\%$ for 5 psig full scale. The test began by allowing helium to flow from the source tank into CV1 at 1.1 kg/h. Helium mass flow rate was measured by Coriolis flowmeter (Micromotion CMF025M/L). Zero stability

for the flowmeter is 0.027 kg/h and the accuracy is ±0.25%. Helium then flowed from CV1 through the check valve (V13) into CV3 once the pressure reached approximately 0.3 psig in CV1 and the check valve cracked. The flow rate was held constant during the experiment. Oxygen concentration and gauge pressure were measured during the tests. Helium was vented from the system throughout the test, either through the chimney (CV4 and CV5) or through CV6 then out the chimney to the atmosphere. The initial and boundary conditions of the two tests (SD0002 and SD0003) are outlined in Table 2.11 below for reference.

Table 2.11: Test Conditions of SD0002 and SD0003

Test Condition	**SD0002**	**SD0003**
Atmospheric O2 Concentration	19.28%	20.93%
CV1 O2 Concentration at test start	0.02%	0.08%
CV3-S1L1 O2 Concentration at test start	20.5%	21.46%
CV3-S1L11 O2 Concentration at test start	20.7%	20.89%
He flow rate into CV1	1.1 kg/h	1.1 kg/h

Figure 2.33 shows the oxygen concentration response for CV1 and CV3 during the tests.

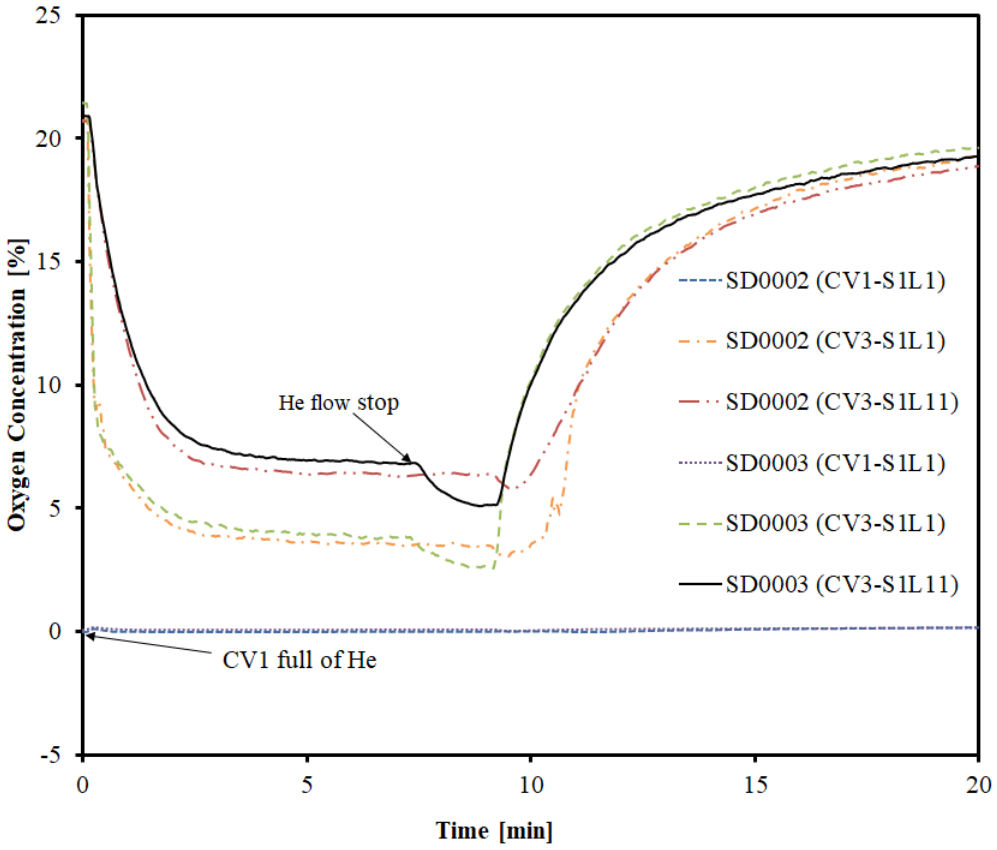

Figure 2.33: Oxygen concentration response of SD0002 and SD0003

As shown in Fig. 2.33, oxygen concentrations of SD0002 and SD0003 show repeatable dynamic response during the tests. Due to the pre purging of CV1 with helium, the oxygen concentration of CV1 was measured below 0.1% from the beginning of the test. Steady state oxygen concentrations measured at the high position (CV3-S1L11) were 6.43±0.05% for SD0002 and 6.94±0.07% for SD0003. Steady state oxygen concentrations measured at the low position (CV3-S1L1) were 3.64±0.06% for SD0002 and 3.93±0.09% for SD0003.

Due to the opening outlet condition, counter current of fresh air is generated into the CV3 through the outlet where helium is going out. Because the helium is less dense than the air, oxygen concentration of the high position (CV3-S1L11) has lower value than that of the low position (CV3-S1L1). Note that with the current experimental setup, there was no louver or one-way valve

installed in the connections between CV3 and CV4 (V34), CV4 and CV5 (V45) that the countercurrent flow probably initiated and happened through the building openings to the atmosphere during the tests. Moreover, stratified flow seemed to established due to the fact that the connection between CV6 and CV4 (V64) was closed, the air in CV6 and fresh air flow penetrated from CV4-CV5 into CV3 would be stratified on the lower part of CV3 and CV6. This could be an explanation what the oxygen concentration at CV3-S1L1 was greater than that at CV3-S1L11. The oxygen concentration of CV3 was stabilized within 4 min, and reached steady state with 1.1 kg/h helium injection through GP-01 into CV1. The steady state can be understood as the balance of the air coming into the CV3 through the outlet and the helium going out through the outlet. Figure 2.34 shows the pressure response of SD0002 and SD0003.

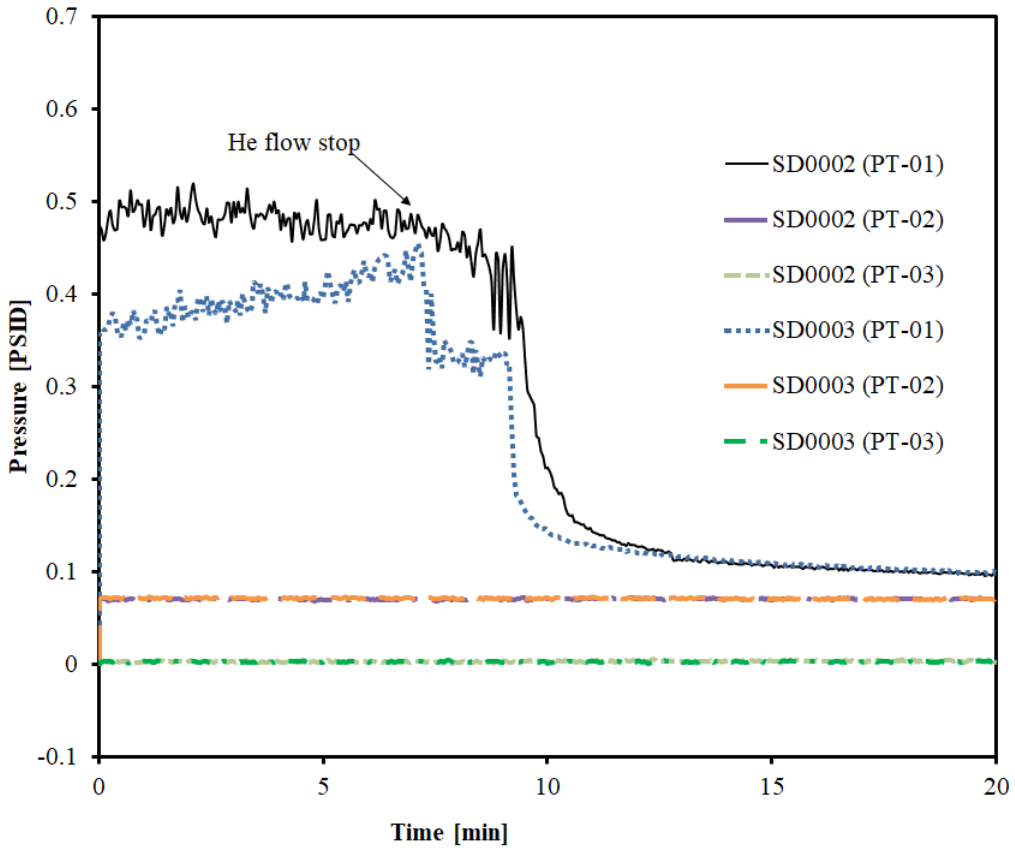

Figure 2.34: Pressure response of SD0002 and SD0003

Pressure of CV1 (PT-01) for SD0002 was 0.48±0.013 psig and 0.39±0.023 psig for SD0003. The pressure of CV1 can be treated as inlet pressure. Higher inlet pressure allows faster helium flow into the other compartments and to the outlet. That faster helium flow resulted in steeper decay of oxygen concentration in CV3 for initial transient response, which is shown in Fig. 2.33. Pressure of CV3 (PT-02) was 0.07±0.0006 psig, and pressure of CV6 (PT-03) was 0.002±0.0006 psig.

2.4 Experiments for Hypothetical D-LOFC Accident

In this section, we describe the experimental setup for studying a hypothetical D-LOFC accident scenario corresponding to moderate-sized breaks in the reactor cavity (CV1) or steam generator cavity (CV3). The depressurization time for a moderate-sized break is estimated to be 5 min. The helium mass flow rate into the compartment through the gas injection port, determined by assuming the equivalent moles of air in four times the test facility free volume, which is equivalent to the total number of moles of helium in the HPB under the 7 MPa initial pressure condition, is 5 min (GA Tech Inc., 2011). The helium injection mass flow rate can be calculated as follows.

$$\dot{m}_{He} = \frac{4 \times \rho_{air} V_{total}}{5} \frac{M_{He}}{M_{air}} \frac{\text{g}}{\text{min}} \frac{60}{1000} \frac{\text{min}}{\text{g}} \frac{\text{kg}}{\text{hr}} \approx 1.68 \text{ kg/hr} \tag{2.29}$$

where $\dot{m}_{He}$ is the helium mass flow rate entering the RB compartment through the injection port, M_{He} is the molecular weight of helium, M_{air} is the molecular weight of air, V_{total} is the total free volume of the RB compartments, and ρ_{air} is the density of air at room temperature. The experiments were performed on the 1/28 scaled NGNP HTGR RB to investigate the response to depressurization accident scenarios, including the flow data of the binary gas mixture (air and helium) and fresh oxygen content inside the RB compartments due to the air ingress from the atmosphere. Data on the air ingress rates back into the equipment shaft (CV6) and steam generator cavity (CV3) during helium evacuation and are vital for determining and verifying scaling factors and distortions, the validity and functionality of measurement devices, as well as the appropriate assembly and design of the experimental test facility.

2.4.1 Hypothetical D-LOFC accident scenarios

In this study, three tests based on hypothetical D-LOFC accident scenarios, namely P3-A(1), P3-A(2), and P3-F, were designed to investigate the oxygen concentration and pressure response of the down-scaled simplified RB model with the designated boundary conditions within the three main control volumes (CV1, CV3, and CV6).

The test P3-A(1) simulates a hypothetical moderate-sized break at the top of the SGV, P3-A(2) simulates a hypothetical moderate-sized break at the top of the SGV with alternative vent path configuration, and P3-F simulates a hypothetical moderate-sized break at the top of the RPV with alternative vent path configuration.

The natural leaking characteristics for each compartment follow the adjusted leak rates provided in Table II. The experimental facility for the set of depressurization tests consists of a combination of the leak rate adjusted for three main volumes, CV1, CV3, and CV6, with the remaining test volumes and connecting sub-volumes illustrated in Fig. 3. A leak-tight magnetic hinged louver was employed to simulate the one-way pressure relief louver in the full-scale plant, which can configure the vent flow path into the atmosphere through CV4, CV5, and V5A. Figure 2.35 presents the implementation of the hinged louver.

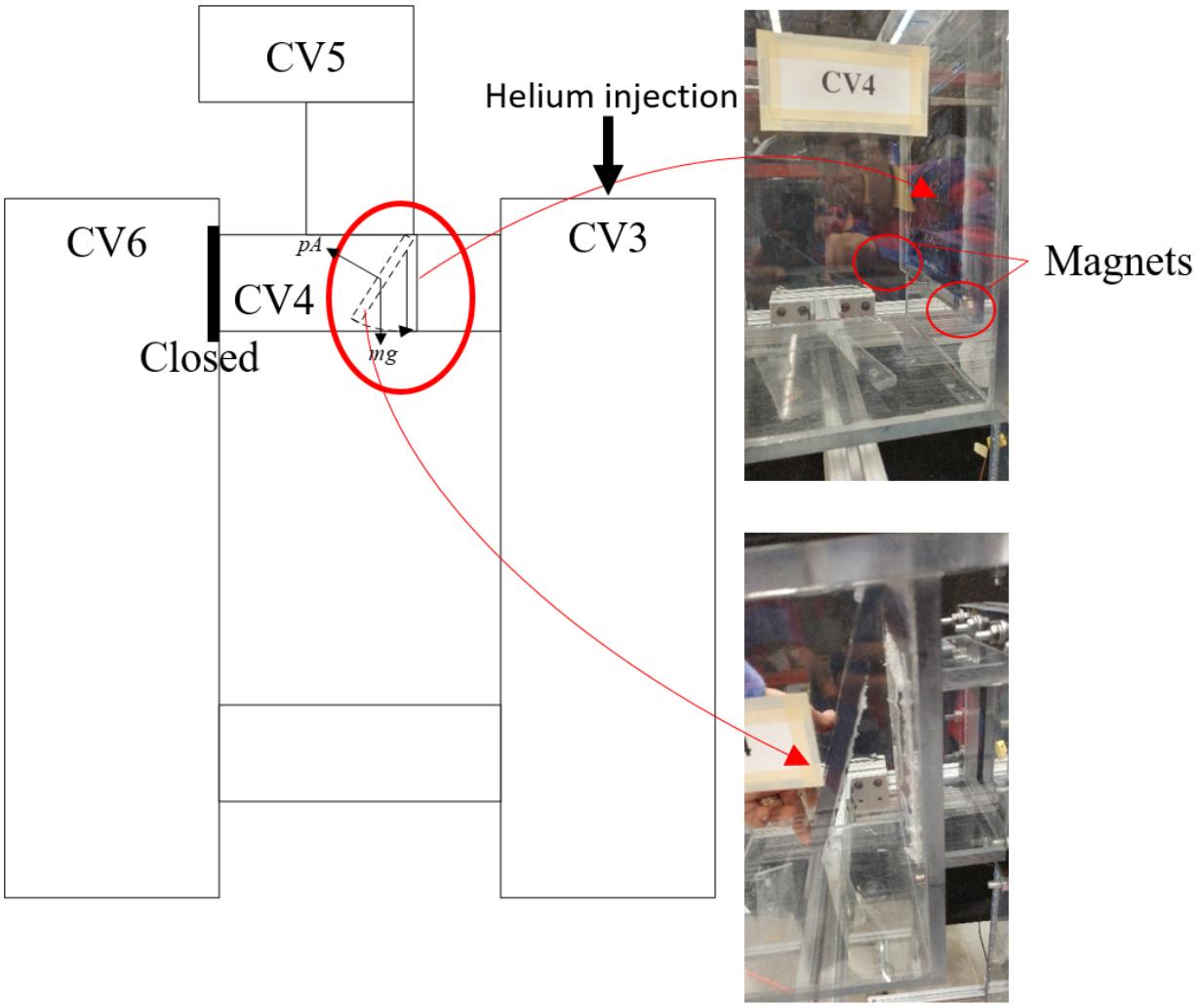

Figure 2.35: Implementation of the hinged louver

As show in Fig. 2.35, the hinged louver employs two magnets at the bottom side corners. The magnetic force holds the louver until the pressure of the inlet side reaches its operational pressure, which is set as 1 psig as desired. Figure 2.36 shows the pressure response of the hinged louver.

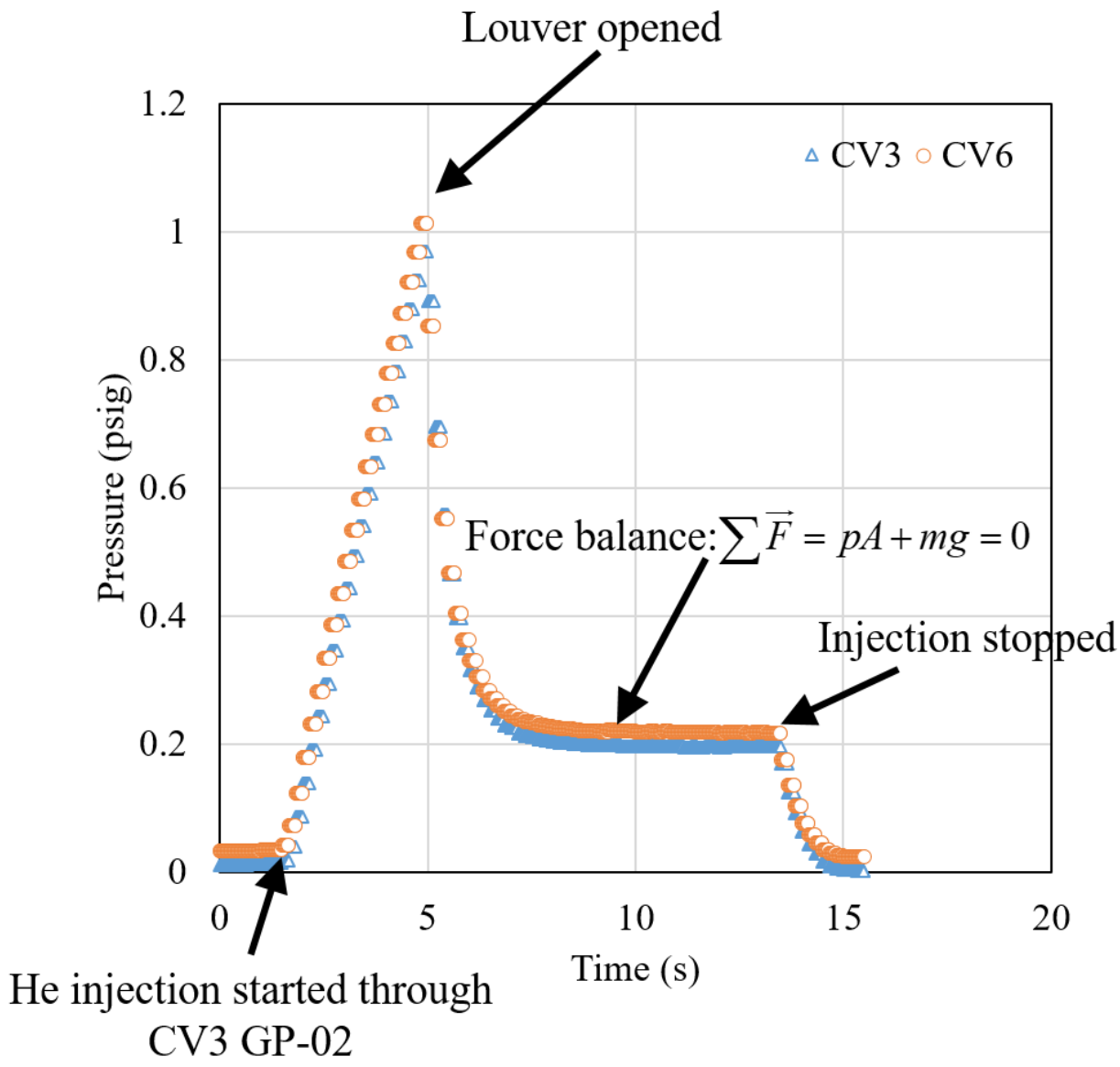

Figure 2.36: Pressure response of the hinged louver

After louver opens, pressure is quickly dropped onto 0.2 psig and settled the force balance between the weight of the louver and the integrated pressure acting on the surface of the louver.

Vent path V13 is a check valve with a 1 psig operating pressure, which only allows for the flow direction from CV1 to CV3. CV3 and CV6 are connected through V36 and CV4. CV4 is connected to CV5, which contains an outlet to the atmosphere (V5A) that always remains open.

In the P3-A(1) test, the hinged louver was placed in position 1, and the hinged louver position 2

was closed using an aluminum plate. In the P3-A(2) test, the hinged louver was placed in position 2 and the hinged louver in position 1 was closed using an aluminum plate. Both the P3A-(1) and P3A-(2) tests used GP-02 as the helium injection port, which means that CV1 was isolated because the check valve prevented backflow into CV1. However, in the P3-F test, helium was injected through GP-01, and the flow path configuration was the same as that of the P3-A(2) test. The initial gas compositions inside CV1, CV3, and CV6 were assumed to be full of air as the normal operation condition. Table 2.12 gives the experimental facility configurations for the three tests.

Table 2.12: Experimental facility configurations

Test ID	**P3-A(1)**	**P3-A(2)**	**P3-F**
Volume used	CV3, CV6	CV3, CV6	CV1, CV3 and CV6
Gas injection	GP-02	GP-02	GP-01
L1A	Closed	Closed	Adjusted
L3A	Adjusted	Adjusted	Adjusted
L6A	Adjusted	Adjusted	Adjusted
V5A	Open	Open	Open
V45	Open	Open	Open
V34	1±0.5 psig hinged louver	Closed	Closed
V64(a)	Closed	1±0.5 psig hinged louver	1±0.5 psig hinged louver
V36	Open	Open	Open
V13	Closed	Closed	1±0.5 psig check valve
V23	Closed	Closed	Closed
L13	Closed	Closed	Closed

Both the P3-A(1) and P3-A(2) tests used GP-02 as the helium injection port, which means that

CV1 was isolated. Because the RPV is assumed as the only heat source, the P3-A(1) and P3-A(2) tests were performed under the isothermal condition at room temperature. However, in the P3-F test, the RPV was heated using the film heater attached to the inner surface of the RPV cylinder, with a constant power of 120 W, to simulate the reactor cavity wall temperature at approximately 50°C, under the assumption that the hypothetical reactor cavity cooling system (RCCS) cools the air properly inside CV1. Figure 2.37 illustrates the expected flow path for tests P3-A(1), P3-A(2), and P3-F with the configurations described in Table 2.12.

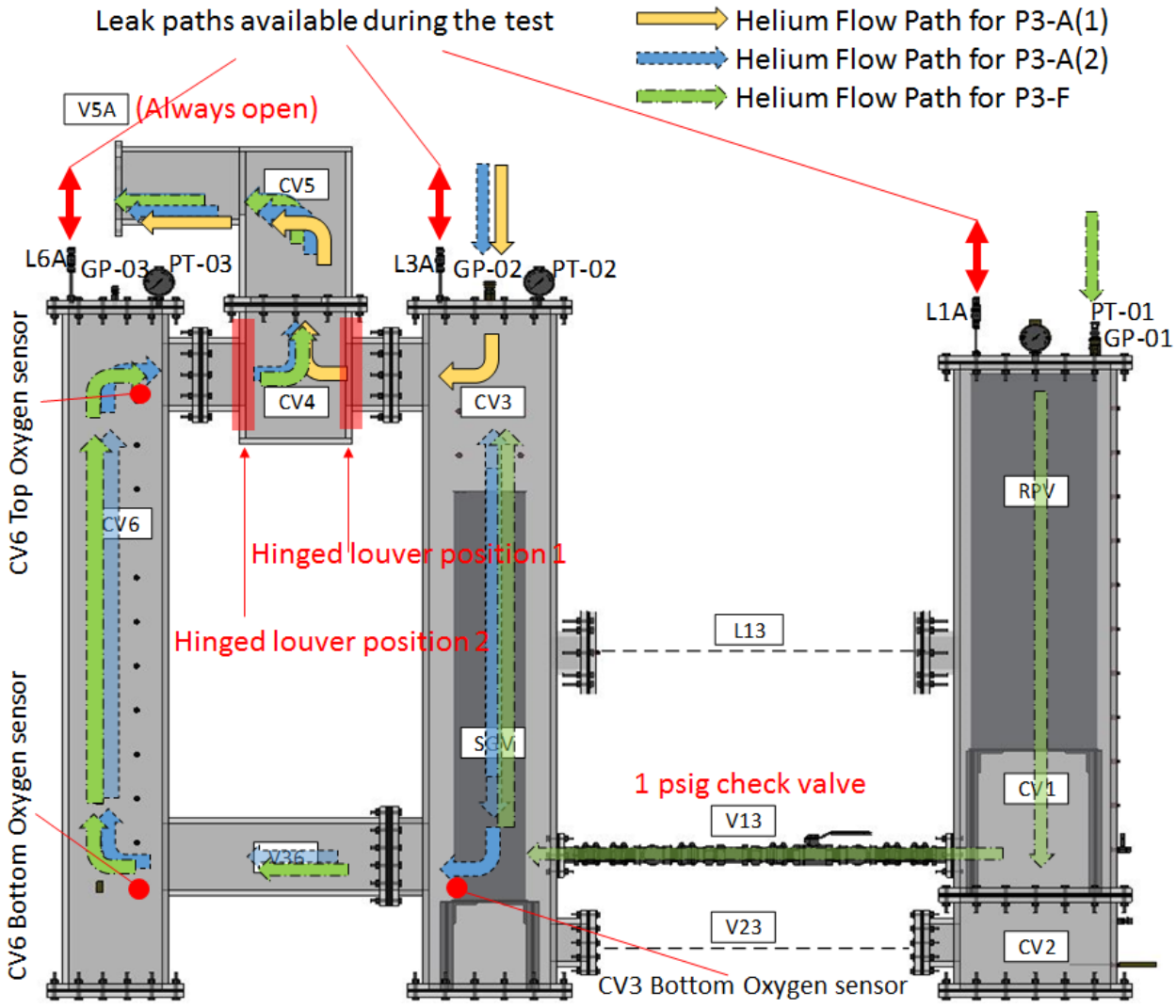

Figure 2.37: Expected flow path for each test

Because the hinged louver was placed in position 1 in the P3-A(1) test, the injected helium could flow as follows: GP-02→CV3→hinged louver→CV4→CV5→atmosphere. In the P3-A(2) case, the injected helium could flow as follows: GP-02→CV3→V36→CV6→hinged louver→CV4→CV5→atmosphere. Finally, for the P3-F test, the injected helium could flow as follows: GP-01→CV1→V13→CV3→V36→CV6→hinged louver→CV4→CV5→atmosphere.

Three intrusive optical oxygen probes (Ocean Optics Neofox Hioxy sensors) were installed in the penetration ports for oxygen concentration measurement. The locations of the oxygen sensors are illustrated in Fig. 2.37 as red points. The accuracy of the oxygen sensors is $\pm 3\%$ for a 20% oxygen concentration at full scale. Three high-accuracy silicon-type pressure transducers (Omega PX329-005GV) were connected to each chamber through PT-01, PT-02, and PT-03 to monitor any deviations in gauge pressure within the chambers. The accuracy of the pressure transducer is $\pm 0.25\%$ for 5 psig at full scale. The helium mass flow rate was measured by a Coriolis flowmeter (Micromotion CMF025M/L), where zero stability for the flowmeter is 0.027 kg/h and the accuracy is $\pm 0.25\%$.

2.4.2 Result and discussion

The helium injection mass flow rate, pressure response, and oxygen concentrations were measured throughout the experiments. The helium mass flow rate was controlled to be constant at 1.68 kg/hr during the tests, as calculated by Eq. 2.28.

2.4.2.1 P3-A(1) test

Figure 2.38 depicts the schematic of P3-A(1) test configuration.

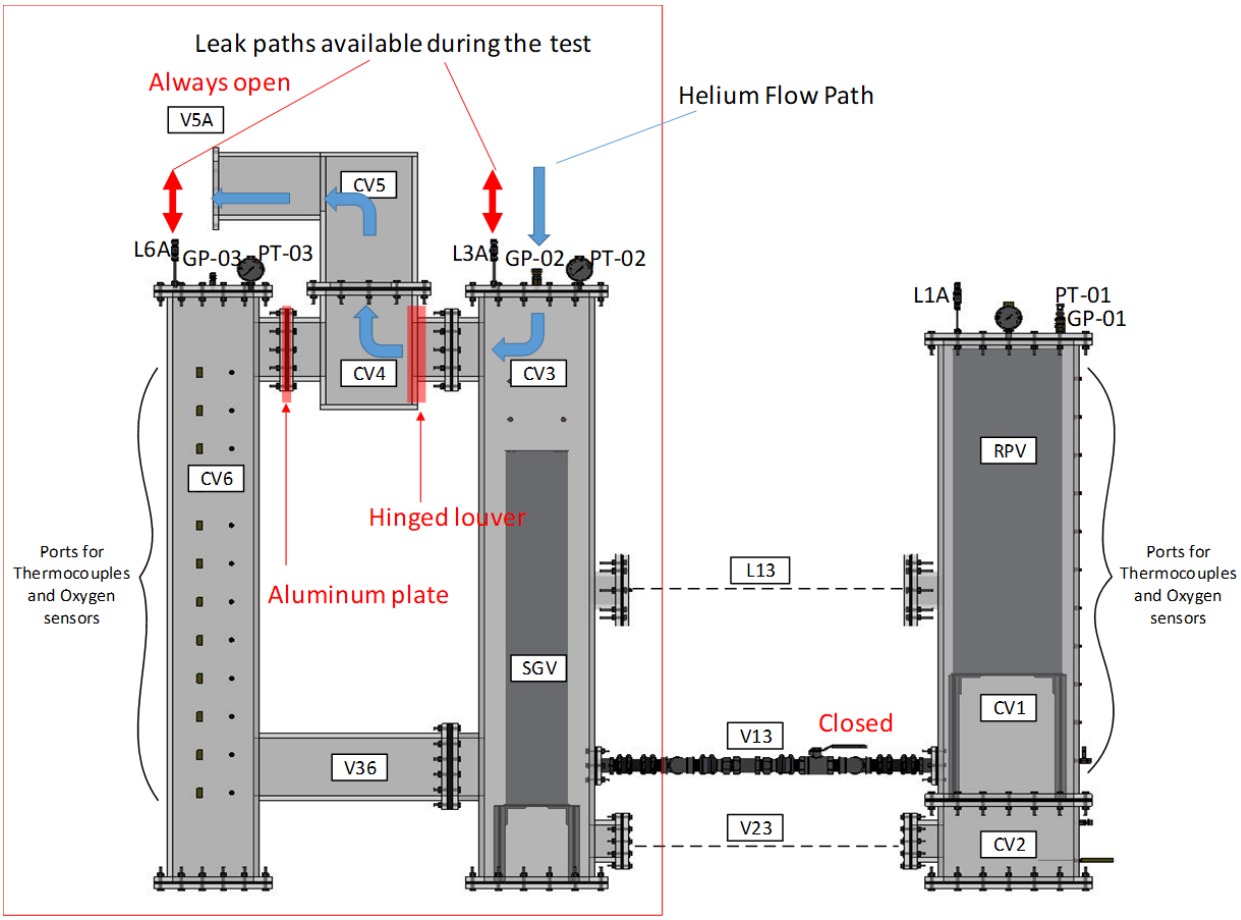

Figure 2.38: Schematic of P3-A(1) test configuration

Figure 2.39 illustrates the pressure responses of CV3 and CV6 for the test P3-A(1).

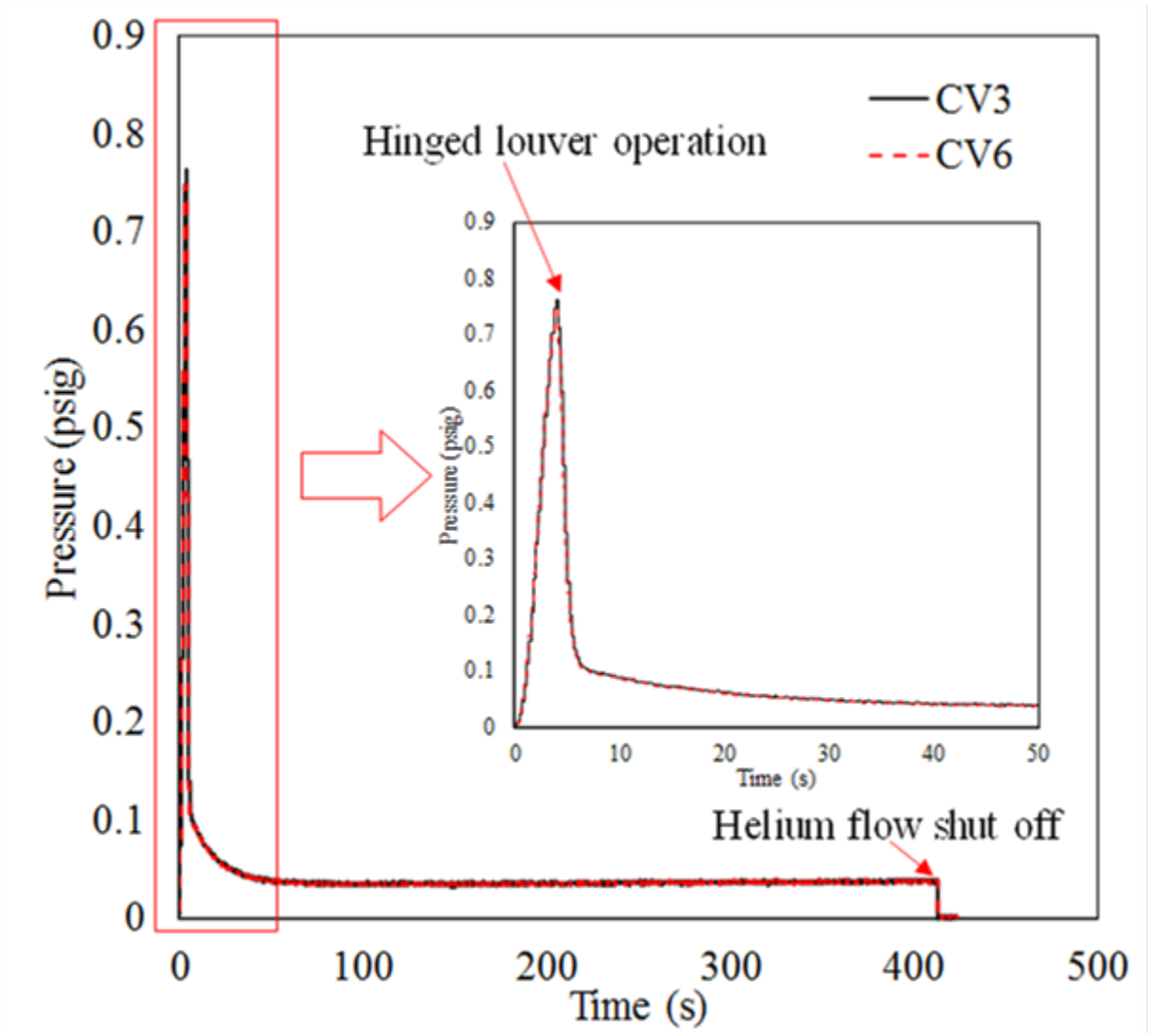

Figure 2.39: Pressure responses of CV3 and CV6 for P3-A(1)

Figure 2.40 shows the oxygen concentration responses of CV3 and CV6 for the test P3-A(1).

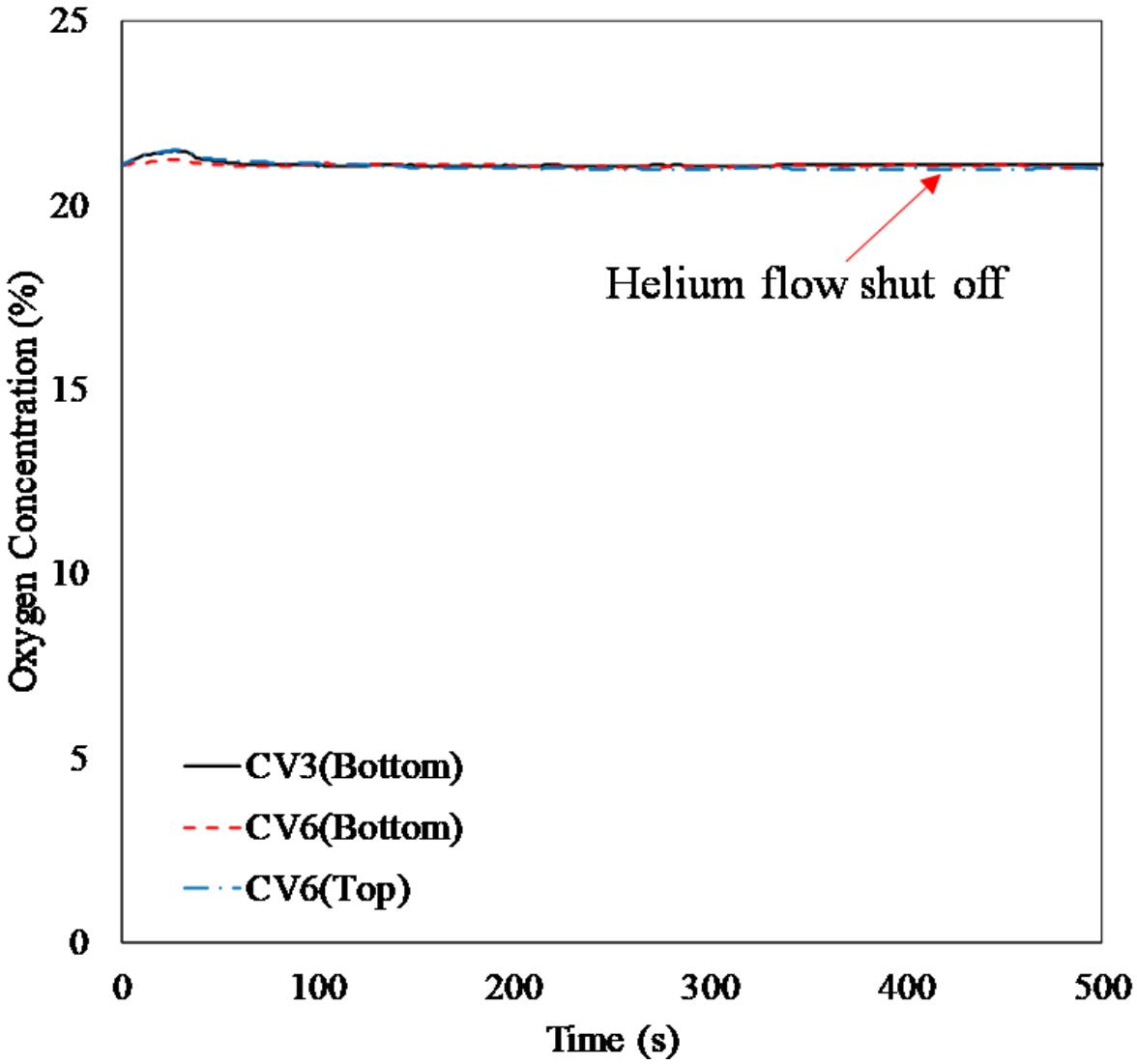

Figure 2.40: Oxygen concentrations of CV3 and CV6 for P3-A(1)

Because the connection between CV3 and CV6 was always open through V36 during the tests, the pressure data for CV3 and CV6 are the same. During the helium injection, the pressure in CV3 and CV6 began to develop until the hinged louver operation, as illustrated in Fig. 2.39. The hinged louver operated at approximately 0.75 psig (5,171 Pa). Following the hinged louver operation, the helium was vented out to the atmosphere and the RB compartment pressure settled at 0.0365 psig (251.66 Pa), balancing the inertia of the flow and flow resistance of the hinged louver. The helium injection was maintained for 7 min. As indicated in Fig. 8, no significant oxygen concentration

change was observed at the bottom of CV3, bottom of CV6, and top of CV6 during the test P3-A(1), as expected from the flow path diagram in Fig. 5. The measured oxygen concentrations were maintained as atmospheric conditions at approximately 21%. The small peak at around 30 s is a result of the pressure gradient-sensitive characteristics of the oxygen probe. As the hinged louver was placed at position 1, which is between CV3 and CV4, the helium injected through GP-02 into CV3 was vented out to the atmosphere directly through CV4 and CV5. This can also be proven by the fact that there was no change in oxygen concentration following helium flow shut off (or after depressurization). Because the oxygen concentration in the RB compartments maintains its atmospheric condition value (21%), the air ingress into the RPV through the break site may occur immediately following the depressurization event, by means of diffusion and natural convection. To secure a certain time frame before the actual air ingress into the RPV, it is important to maintain the oxygen level as low as possible inside the RB compartments. Thus, the results imply that the vent path configuration for P3-A(1) should be modified to defer the air ingress into the RPV.

2.4.2.2 *P3-A(2) test*

Figure 2.41 depicts the schematic of P3-A(2) test configuration.

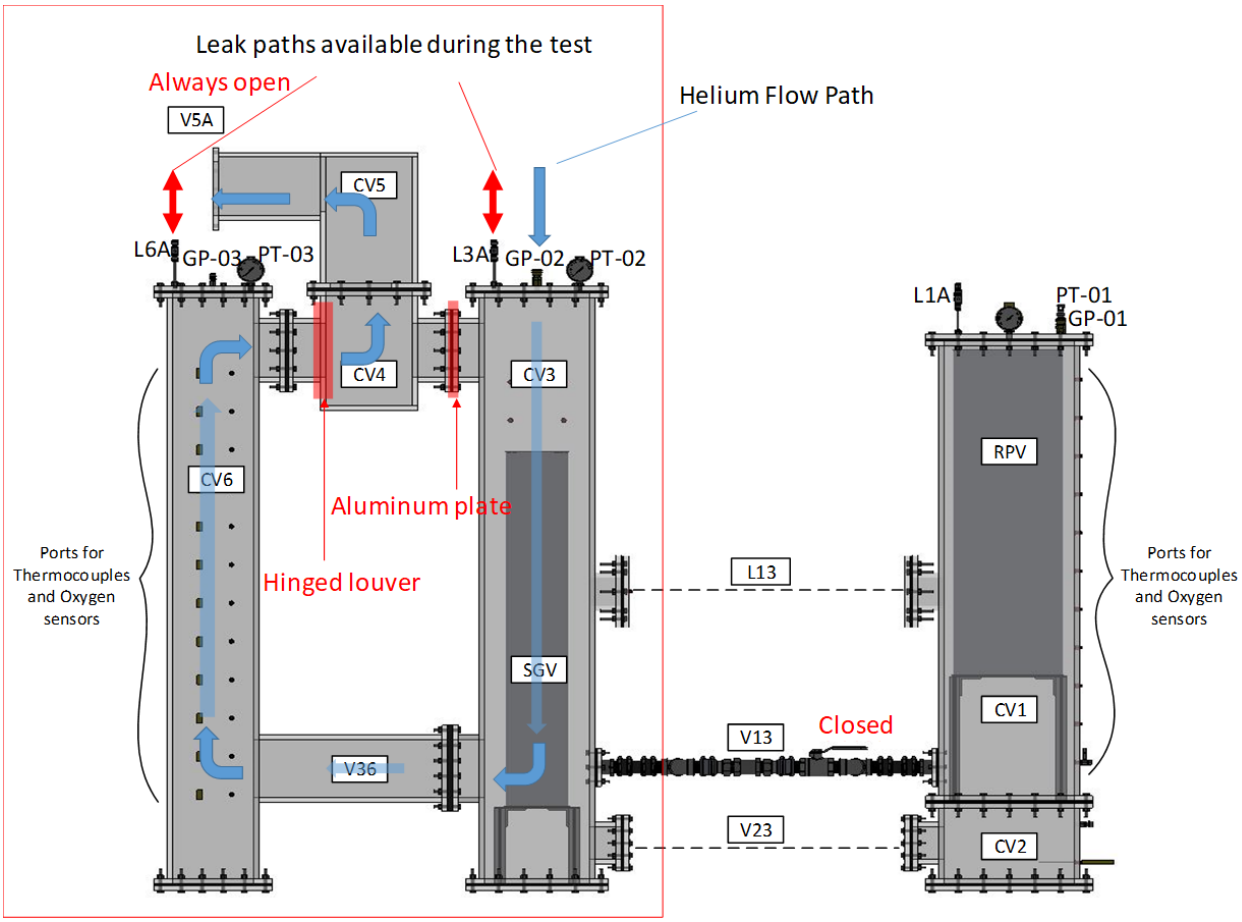

Figure 2.41: Schematic of P3-A(2) test configuration

Figure 2.42 shows the pressure responses of CV3 and CV6 for the test P3-A(2).

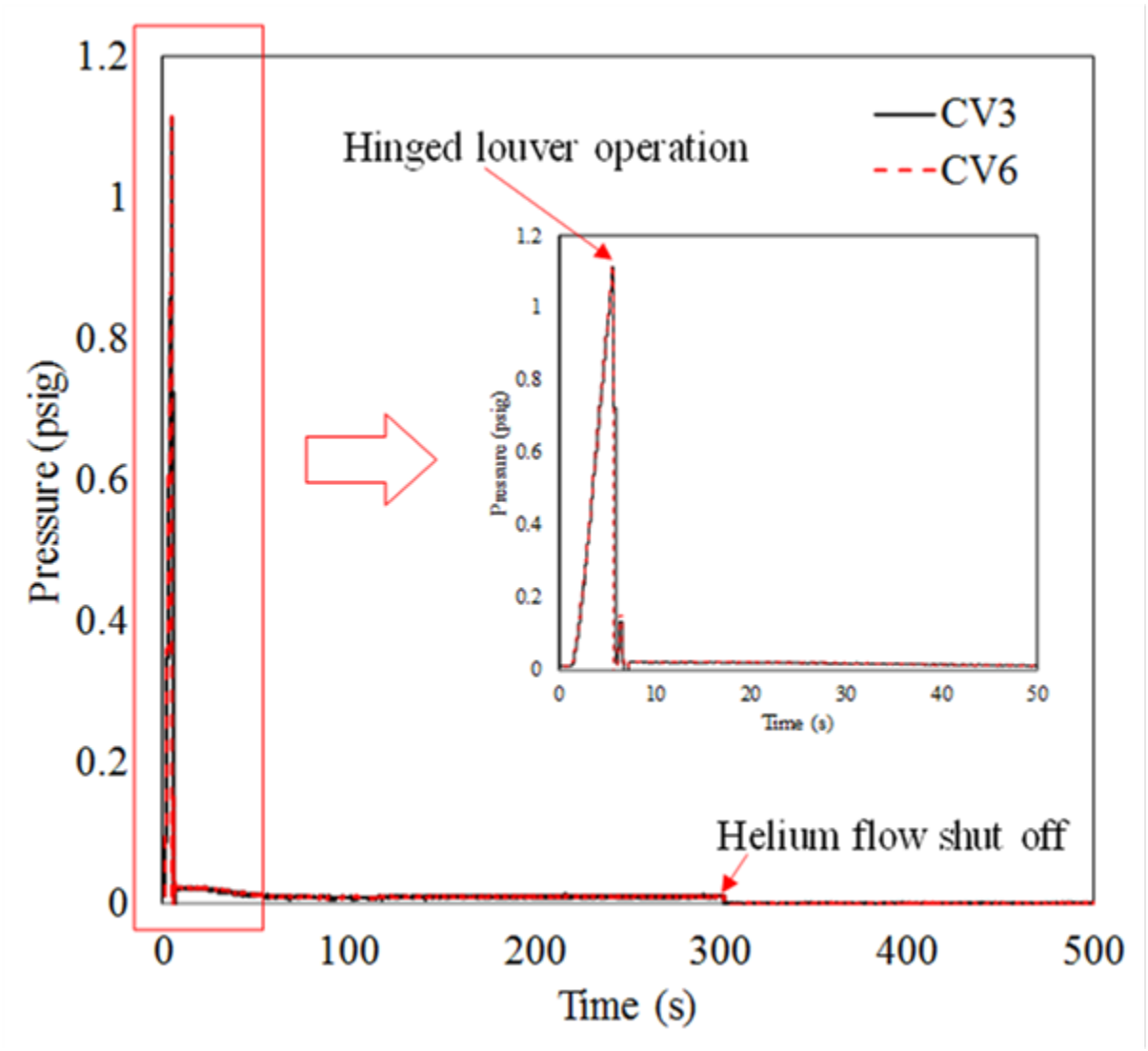

Figure 2.42: Pressure responses of CV3 and CV6 for P3-A(2)

In test P3-A(2), the hinged louver operated at approximately 1.127 psig (7,770 Pa). Following the hinged louver operation, the helium was vented out to the atmosphere and the RB compartment pressure settled at 0.0096 psig (66.19 Pa), balancing the inertia of the flow and flow resistance of the hinged louver. The observed settling pressure for the P3-A(2) test was lower than that of P3-A(1) because of the larger pressure drop of the longer flow path. The helium injection was maintained for 5 min. The test duration was determined to be 15 min to capture the 5 min of helium injection response and air refill characteristics once the helium injection was turned off. Figure 2.43 shows

the oxygen concentration responses of CV3 and CV6 for the test P3-A(2).

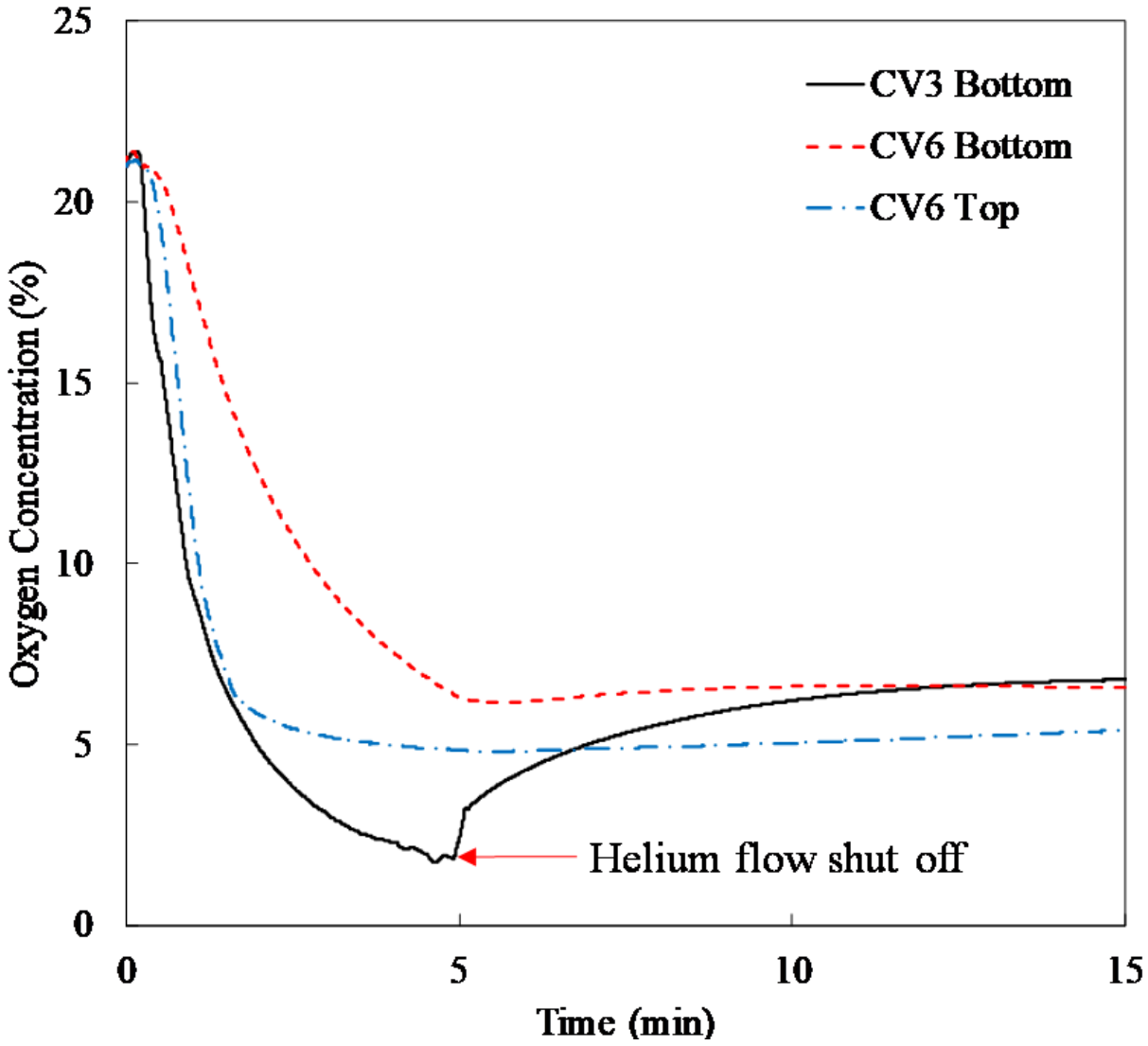

Figure 2.43: Oxygen concentrations of CV3 and CV6 for P3-A(2)

As illustrated in Fig. 2.43, the vent path of the P3-A(2) test can result in a low oxygen concentration in the RB compartments following depressurization, which will allow for a certain time frame before air ingress into the RPV. The results imply that the vent path for depressurized helium should be placed at the bottom of the steam generator compartment as in the P3-A(2) test, and not the top of the compartment as in P3-A(1). In test P3-A(2), the injected helium first filled up CV3

and then flowed into CV6 through V36, which was placed at the bottom of CV3 and CV6. However, the oxygen concentration change rate at the CV6 bottom exhibited a slower gradient than that of the CV3 bottom and CV6 top. This phenomenon can be explained as being the result of the buoyancy force. Since helium is lighter than air, helium accumulates from the top of CV3 until the pressure inside the compartments overcomes the hinged louver operation point. Following the pressure release by the hinged louver operation, a bulk helium bubble passes through V36 and enters CV6, and accumulates from the top of CV6, so the lower part of CV6 will contain trapped air mixed with helium. The diffusion and inertial mixing may contribute the helium concentration increment at the CV6 bottom following this. Figure 2.44 illustrates the conceptual schematic of these phenomena.

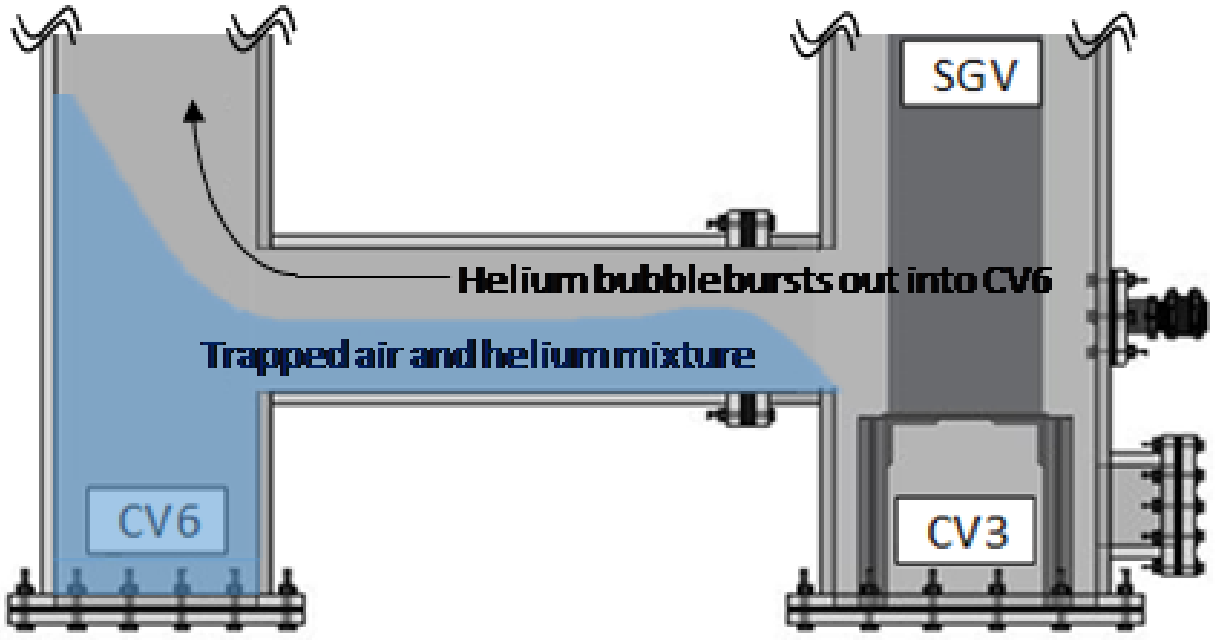

Figure 2.44: Helium flowing mechanism of P3-A(2) test

The CV6 top oxygen concentration was stabilized after 4 min at approximately 5%, where the injected helium entering CV6 and venting out to the atmosphere were balanced. Following the helium flow shut off, a sudden increment in the oxygen concentration of the CV3 bottom was

observed. After this sudden increment, the oxygen concentration of CV3 bottom and CV6 bottom began to increase and the change rates converged. These phenomena can be explained by helium and air stratification due to buoyancy. The slow oxygen concentration change rate resulted from the helium diffusion process.

2.4.2.3 P3-F test

Figure 2.45 depicts the schematic of P3-F test configuration.

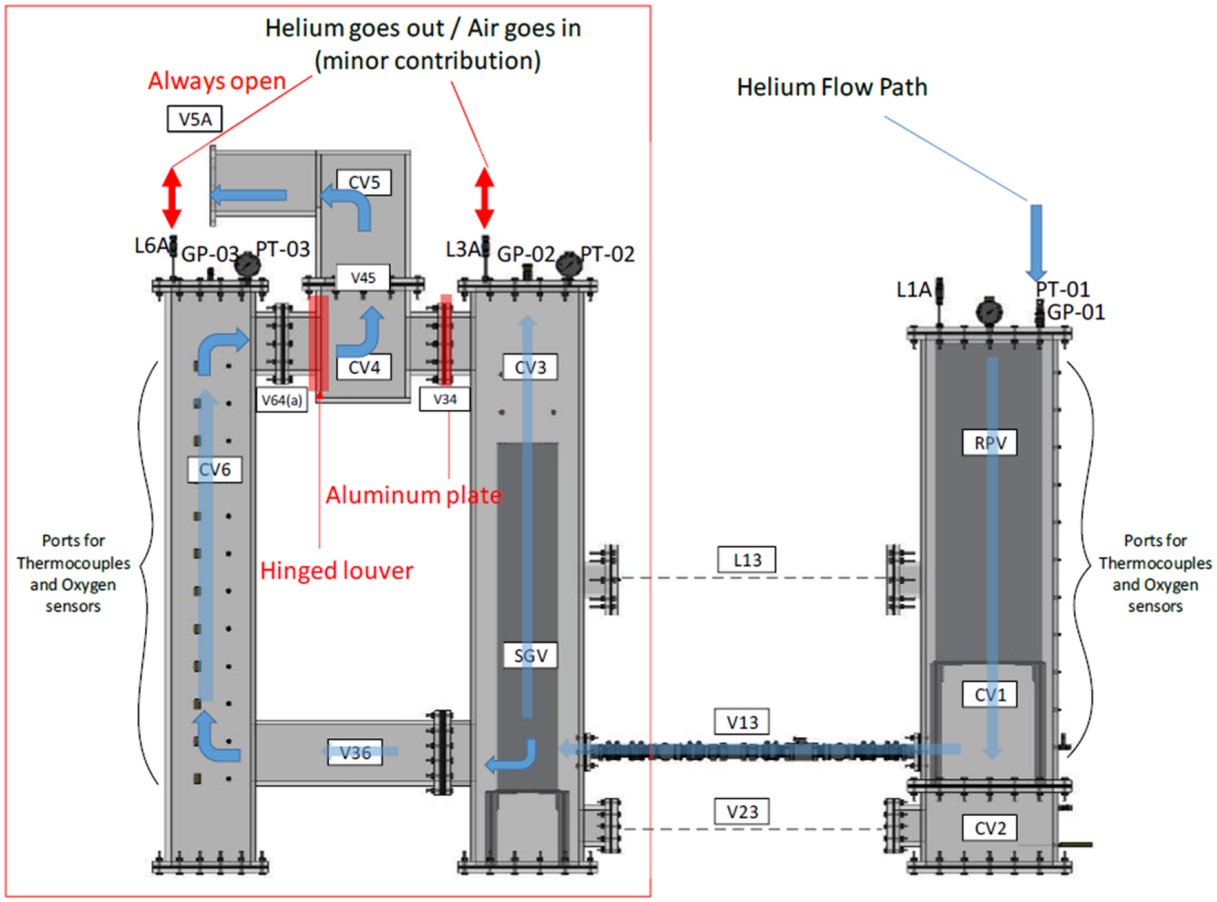

Figure 2.45: Schematic of P3-F test configuration

An issue arose during the P3-F test regarding V13. Instead of using the 1 psig check valve, a 1″ ball valve was employed as V13, which was manually opened at approximately 1.457 psig

(10045.66 Pa) and maintained open, because the 1.68 kg/hr helium injection flow rate exceeded the flow limit of the 1 psig check valve and pressure developed in CV1, which may result in fatal damage to the experimental facility. This may indicate that the current flow area of V13 in the full-scale NGNP HTGR conceptual design should be enlarged. The hinged louver was operated as desired. Apart from this issue, it should be noted that the helium was injected into CV1 where the RPV exists for the P3-F test. As stated previously, the RPV was preheated and the heater power was maintained at a constant to cause the average steady state reactor cavity wall temperature to be approximately 50°C. Figure 2.46 shows the CV1 wall temperature responses for test P3-F.

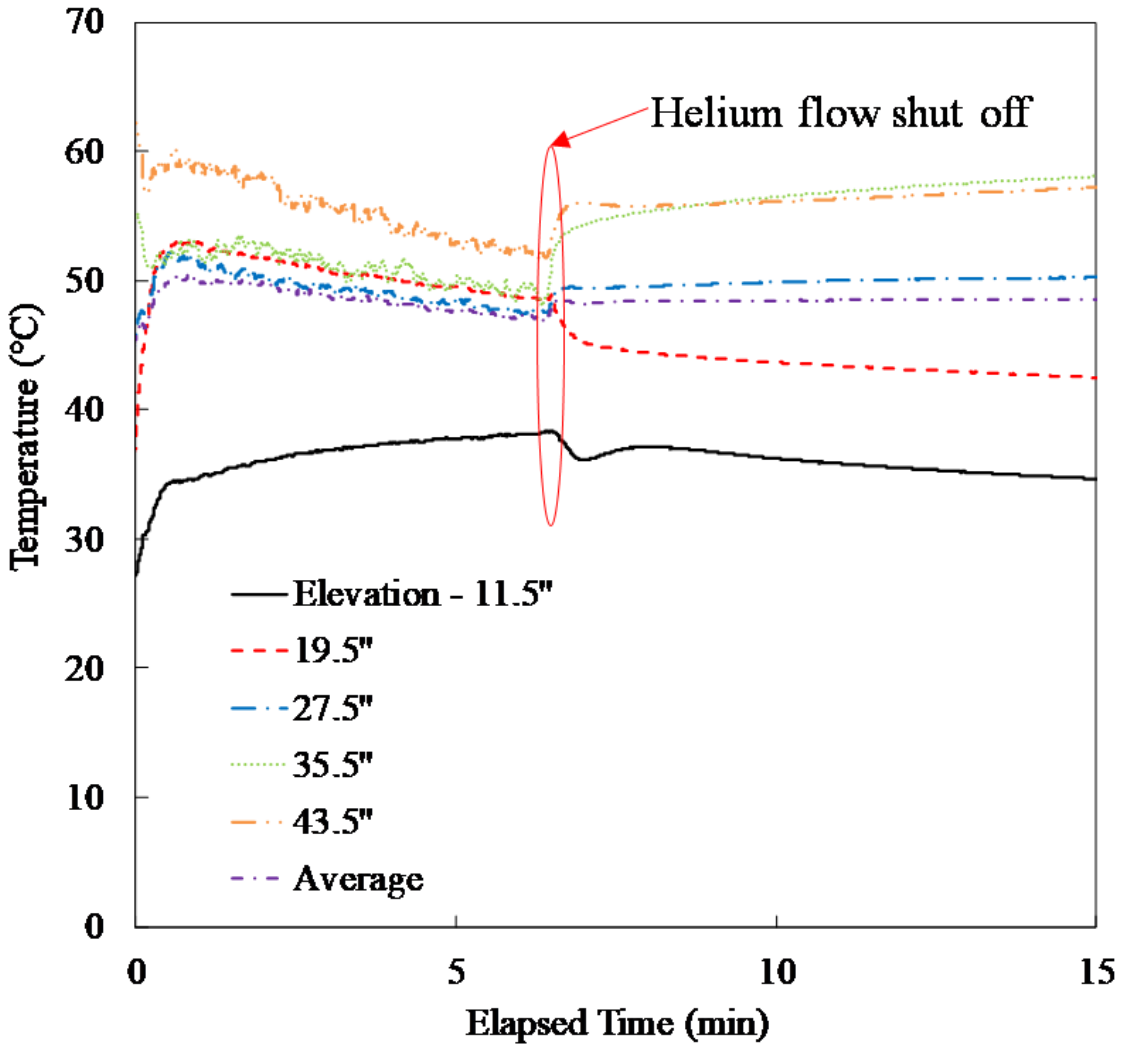

Figure 2.46: CV1 wall temperature responses for P3-F

The test duration was determined to be 15 min, as with the P3-A(2) test, to capture the 6.45 min of helium injection response and air refill characteristics once the helium injection was turned off. Figure 2.47 illustrates the pressure responses of CV1, CV3, and CV6 for test P3-F.

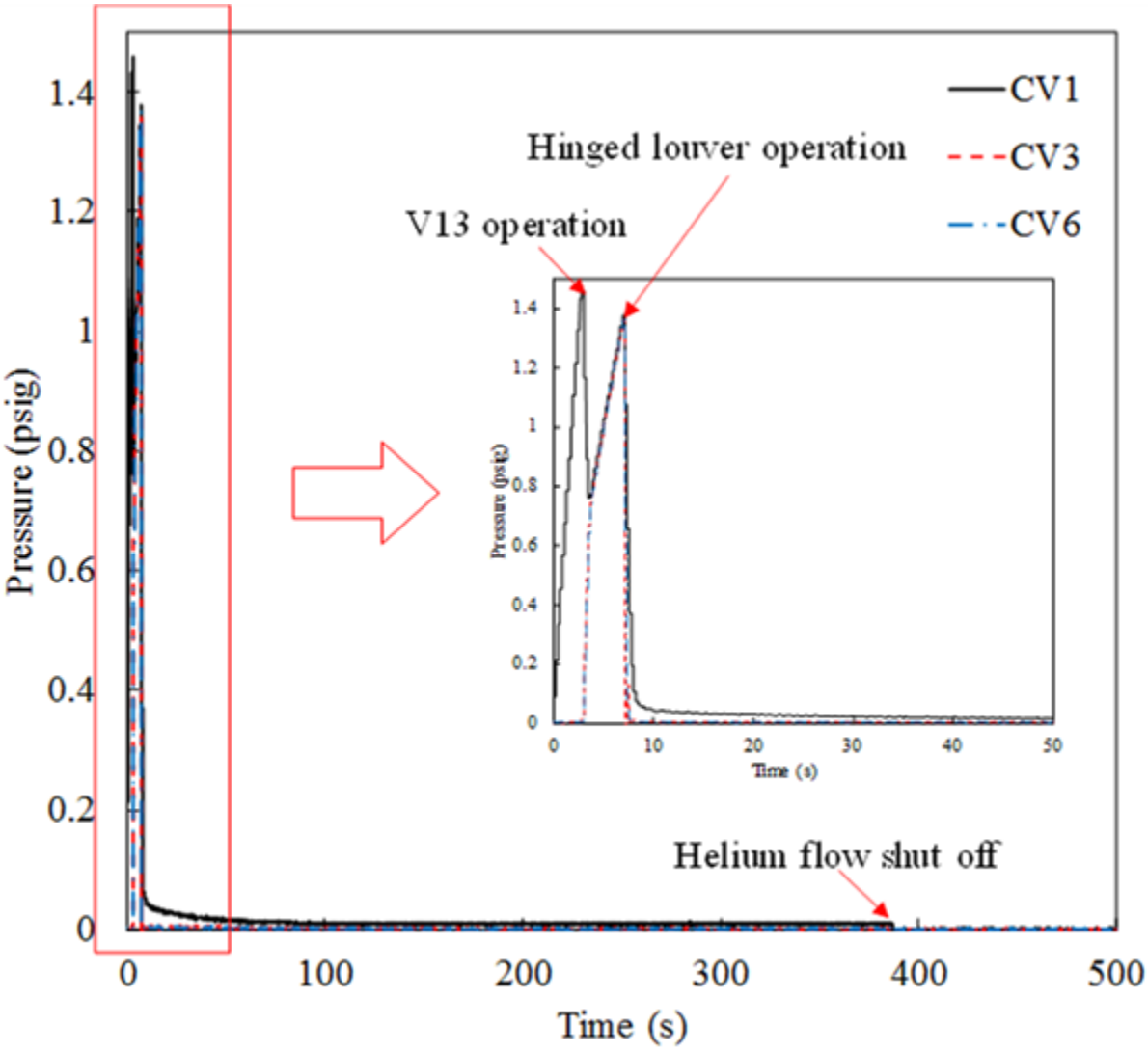

Figure 2.47: Pressure responses of CV1, CV3, and CV6 for P3-F

The hinged louver operated at approximately 1.364 psig (9404.45 Pa), and the helium injection was maintained for 6.45 min. As shown in Fig. 13, following V13 operation, the pressures of CV1, CV3, and CV6 converged until the hinged louver operation. Following the hinged louver operation,

because the helium was vented out to the atmosphere, the CV3 and CV6 pressure settled to 0 psig, due to the large pressure drop in the longest flow path. An interesting phenomenon was observed in that the CV1 pressure exhibited a difference in response from that of CV3 and CV6, even though V13 was maintained open. This is mainly due to the previously stratified air inside CV1 starting to mix because of the injected helium and damping out the pressure equalization between CV1 and CV3 with increased friction in V13. Figure 2.48 illustrates the oxygen concentration responses of CV3 and CV6 for the test P3-F.

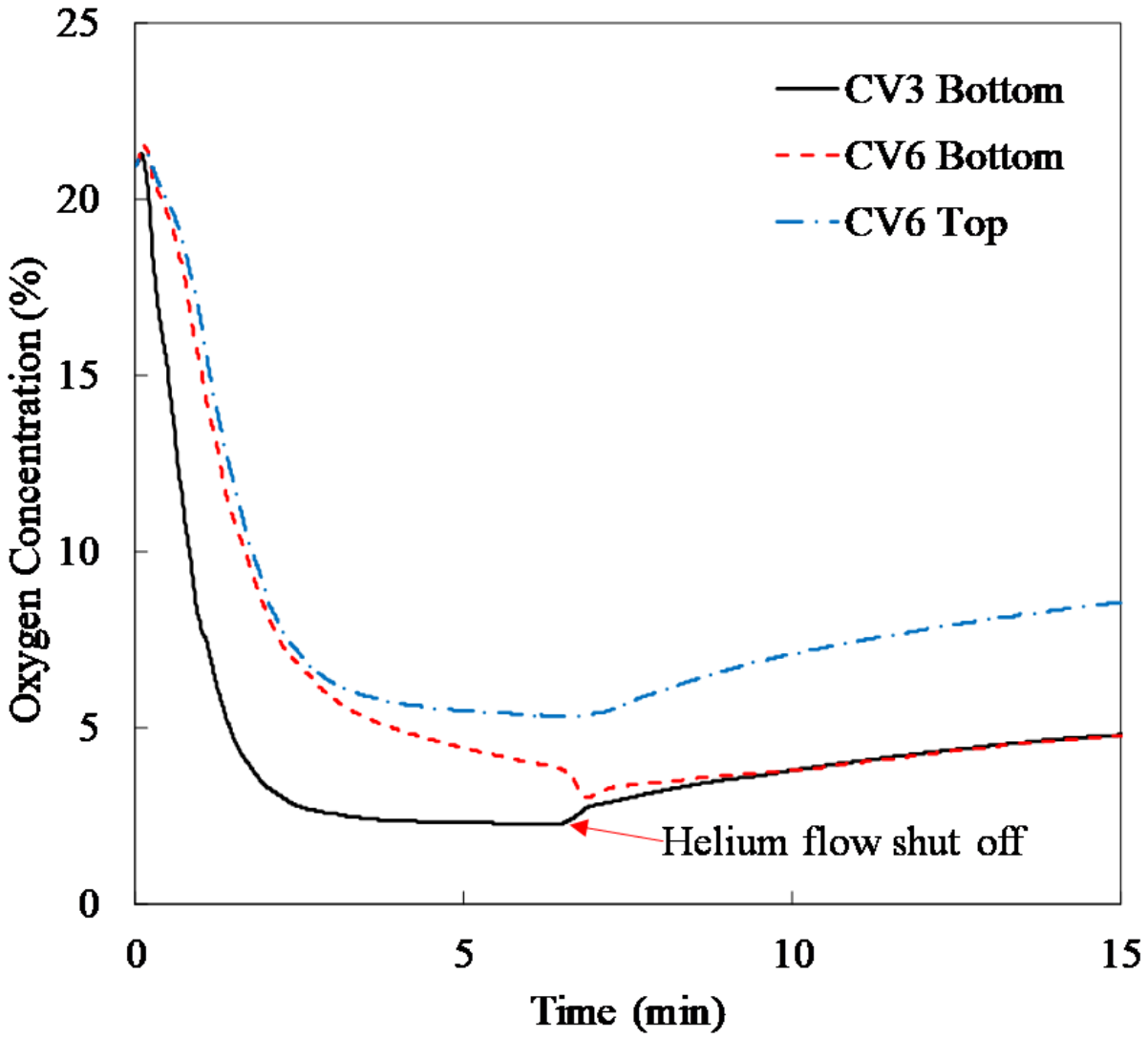

Figure 2.48: Oxygen concentrations in CV3, and CV6 for P3-F

As illustrated in Fig. 2.48, the oxygen concentration change rate of CV3 bottom is approximately the same as the P3-A(2) case. However, there is a difference in that the oxygen concentration change rate of the CV6 bottom follows that of the CV6 top, and not the CV3 bottom as in P3-A(2). Unlike P3-A(2), the trapped air in the CV6 bottom shown in Fig. 11 is generated by the first helium bubble when CV1 releases the pressurized helium and air mixture, and these can be pushed out to the atmosphere by the second pressure release from all compartments. Furthermore, the total injected helium amount is larger than that of the P3-A(2) test as a result of the double time pressurization. In test P3-F, the injected helium first fills up CV1 and then flows into CV3 through V13 once the pressure inside CV1 exceeds the V13 operation pressure. After it enters CV3, pressurization occurs once more with the entire volume of CV1, CV3, and CV6. Thus, the total injected helium amount in CV3 and CV6 at the point of helium venting out to the atmosphere where the hinged louver operates is larger than that of the P3-A(2) test, and more air can be pushed out from the compartments to the atmosphere. The CV6 top oxygen concentration was stabilized after 6 min at approximately 5%, where the injected helium entering CV6 and venting out to the atmosphere were balanced. After the helium flow was shut off, a sudden increment in the oxygen concentration of the CV3 bottom and sudden decrement in oxygen concentration of the CV6 bottom were observed. The oxygen concentrations of the CV3 bottom and CV6 bottom then converged, and began to increase together. These occurrences can also be explained by helium and air stratification due to buoyancy, as in P3-A(2). To investigate these phenomena further, flow and oxygen concentration field measurements combined with computational fluid dynamics (CFD) simulation are required.

3. PART II. STEAM-AIR MIXTURE FLOW IN SUBCOOLED WATER POOL: DIRECT CONTACT CONDENSATION OF STEAM-AIR MIXTURE JET IN A SUBCOOLED WATER *

3.1 Background: Steam Discharge into BWR Suppression Pool

The study of direct contact condensation (DCC) of steam is important owing to its diverse applications, including power plants, heat exchangers, and steam ejectors. The simplicity of design and the high-heat transfer rates are the major advantages of the DCC process. Especially, submerged steam jet condensation process is employed as an important safety feature in nuclear power plant such as pressure suppression system in boiling water reactor (BWR) (Zhao and Hibiki, 2018). The main purpose of the pressure suppression system in BWR is to prevent the containment vessel overpressurization in case of a turbine trips, LOCA, or main steam line break (MSLB) with utilization of DCC process.

In case of a turbine trip, LOCA or MSLB scenario, large amounts of steam would be rapidly discharged into the containment vessel. In order to prevent undesired over-pressurization inside the vessel, safety relief valves (SRVs) mounted on the main steam line are actuated to divert either a portion or all of the steam into the suppression pool (USNRC, 1981). Steam released into the suppression pool then will condense into water so that the pressure transient in the vessel containment can be attenuated. The orientation of the steam discharge line or the nozzle shape may vary by the design, but the key thermal-hydraulic phenomena during the process can be stated as DCC of steam in subcooled water pool. Figure 3.1 represents the different types of BWR vessel system and suppression pool design (Corradini & Klein, 2012).

*Part of this work is reprinted with permission from "Thermal hydraulic characteristics of unstable bubbling of direct contact condensation of steam in subcooled water" by Se Ro Yang, Joseph Seo, Yassin Hassan, 2019, International Journal of Heat and Mass Transfer, Vol. 138, pp. 580–596, Copyrights [2019] by Elsevier Ltd.

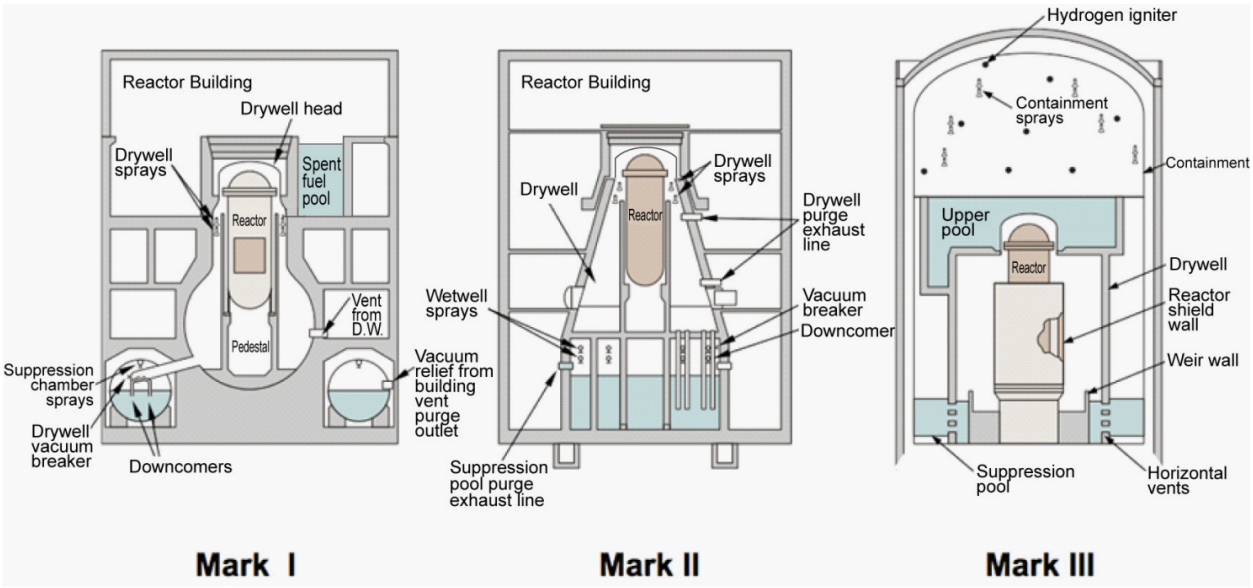

Figure 3.1: Schematic of different types of BWR vessel system design (Corradini & Klein, 2012)

Various studies have been performed on the DCC of steam for specific applications. In a previous study conducted by Chun *et al.* (1996) with steam, the average heat-transfer coefficient of direct contact condensation was reported to be in the range of 1.0-3.5 MW/m^2·K for the steam mass fluxes which exceeded 200 kg/m^2·s. The same authors proposed an empirical correlation shown in Eq. 3.1 to predict the average heat-transfer coefficient (HTC). The experimental data agreed with the empirical correlation within $\pm 30\%$.

$$\overline{h} = 1.3583 c_p G_m B^{0.0405} \left(\frac{G_o}{G_m}\right)^{0.3714} \tag{3.1}$$

Where $\overline{h}$ is the averaged heat transfer coefficient (W/m^2-K), c_p is the liquid specific heat (J/kg-K), G_m is the steam mass flux mean value for steam plume, G_o is the steam mass flux in the injector exit condition, $B = c_p(T_s - T_f)/h_{fg}$ is the driving potential for condensation, T_s is steam temperature, T_f is water temperature, and h_{fg} is latent heat. A different experiment was performed by Gulawani (2006) with the use of a hot film anemometer on a steam condensation jet. The reported heat-transfer coefficient for the vapor liquid interface varied between 0.1-4 MW/m^2·K. The nozzle diameter used during this experiment varied between 1-2 mm, and the velocity ranged between

286-304 m/s. The entire study had remarkable similarities to the study by Kim and Yoon (2008). Aya and Nariai (1991) reported three different heat-transfer coefficients for direct contact condensation. They reported heat-transfer coefficients for a) chugging of 2×106 W/m^2·K, b) condensation oscillation in the range of 0.1-1 MW/m^2·K, and for c) the surface of stratified flow in the range of 3-30 kW/m^2·K. Fukuda (1982) evaluated the average heat-transfer coefficient of the DCC of steam for the vertically downward nozzle into a subcooled pool based on the experimental analysis, as shown in Eq. 3.2. Fukuda modeled the Nusselt number as a function of the Reynolds and Jakob numbers first, and then suggested an expression for the averaged heat-transfer coefficient.

$$\overline{h} = 43.78\frac{k_f}{d}\left(\frac{G_o d}{\mu_f}\right)^{0.9}\frac{c_{p,f}\Delta T}{i_{fg}} \tag{3.2}$$

where $\overline{h}$ is the average heat-transfer coefficient, k_f is thermal conductivity of water at a given temperature and pressure, *d* is the nozzle diameter, G_o is the steam mass flux, ΔT is the temperature difference between the steam and water, and μ_f is the water's dynamic viscosity at given a temperature and pressure. This equation provides the time averaged heat-transfer coefficient of the direct contact condensation of steam. With steam and air mixture, a heat transfer coefficient relating the bubble average area was reported by Qu (2015) as shown in Eq. 3.3. Qu reported that the heat transfer coefficient decreased with the increase of the bubble diameter.

$$h = \frac{H_1 - H_2}{A_{1,2}(t_1 - t_2)\Delta T} \tag{3.3}$$

Where *H* is the enthalpy, *t* is the time, ΔT is the temperature difference between the bubble and water, and *A* is the surface area. This equation is time dependent and can be used to the transient analysis of the heat transfer coefficient. Table 3.1 presents experimental methods and the equations employed to obtain heat transfer coefficients of previous researchers.

In a study by Moon *et al.* (2009), the commercial computational fluid dynamics (CFD) software toolkit CFX was used to simulate the condensation of a steam-air mixture jet. Another numerical study by Qu *et al.* (2016) predicted temperature, velocity, and void fraction profiles of vapor jets

Table 3.1: Experimental methods and the equations employed to obtain heat transfer coefficients of previous researchers

Author	**HTC calculation**	**Experimental method**	**Pool Temperature (°C)**	**HTC (kW/m^2-K)**
Gulawani (2009)	$h = \frac{l^2 R_w}{A_{film}\,(T_R - T_B)}$	Hot Film Anemometer	30 - 50	0.5 - 1.1
Kar (2007)	$h_d = \frac{v_c \Delta H_{lv} \rho_{v,l}}{T_v - T_c}$	-	15 - 65	10 - 75
Ju *et al.* (2000)	$h = \frac{-k_f \left(\frac{dT}{dy}\right)_w}{T_w - T_\infty}$	Holographic Interferometer	25 - 65	2.4 - 3.5
Simpson and Chan (1982)	$h = \frac{m h_{fg} A_0}{\Delta T A_c}$	High Speed Camera	25 - 65	100-800
Brucker and Sparrow(1977)	$h = \frac{\rho_v \left(\frac{dV}{dt}\right) h_{fg}}{A\,(T_{sat} - T_\infty)}$	High Speed Camera	15 - 100	10

for condensation. Chen and Faeth (1982) used a different approach to develop an analytical correlation for the vapor plume length and the temperature profile. The authors used the homogeneous equilibrium model along with the $k - \epsilon$ turbulence model that was normally reserved for combusting flows. However, the correlation obtained proved to be valid only for near-atmospheric pressure flows, and the temperature correlation did not perform as well as the authors had hoped. Liang and Griffith (1994) studied DCC using both analytical and experimental means, and produced results that used the liquid Reynolds, the steam Mach, and the Jakob numbers. Most importantly, this

study developed a jetting criterion as a function of the water Jakob number. In the study by Khan *et al*. (2014), steam condensation was evaluated experimentally. The temperature profile of the steam jet was measured for pool temperatures between 30 and 60°C. Additionally, the same authors presented a discussion about the instabilities associated with steam jets. Kerney *et al*. (1972) obtained the empirical correlation with an error of only 11.7%. The authors proposed that the cavity shape was dependent on the degree of expansion inside the steam injector. The study by de With *et al*. (2007) provided insights into the regime map development, along with newly proposed regime maps for the jet behavior and vapor plume length. In addition to the new plume length regime map, a three-dimensional regime map for the jet behavior was presented as a function of nozzle diameter, steam mass flux, and pool temperature. These dependencies can also be found in other research studies on condensation regime maps (Zhao and Hibiki, 2018). In the study by Song *et al*. (2012), experiments were performed to determine the behavior of the steam jet for a single jet and a multijet sparger. Both apparatuses were submerged in water, and were designed to evaluate the thermal mixing behavior of each system. The authors used the Tollmein model to improve their steam condensation region model predictions. More recently, thermal hydraulic phenomena of DCC related to the suppression chamber of BWR have been intensively studied because it is a subject directly connected to the integrity of the safety system of nuclear power plants. The DCC in BWR safety system is important because it is not only suppressing the exceeding pressure inside the BWR containment, but also transferring the heat from the reactor steam to the subcooled water in the suppression pool during accident scenario (Jo *et al*., 2016). Song *et al*. (2014, 2015) and Jo *et al*., (2016) investigated the effect of thermal stratification in the suppression pool and suggested a steam bubble-induced flow model and reported the relationship between steam flow rate and bubble frequency. Furthermore, the oscillation and periodic characteristics of DCC have been studied as a part of the effort to analyze the fluid structure interaction (FSI) in the pressure suppression pool in BWR which may result in a severe damage to the surrounding equipment (Qiu *et al*., 2014, 2014, 2015). Qiu *et al*. (2014, 2014, 2015) conducted experimental investigations on pressure oscillations and suggested an empirical correlation. Xu and Tian (2016) conducted an

acoustic and visual study of the DCC of a steam jet plume with non-condensable gas by applying Fast Fourier Transform (FFT) to the sound waves of the condensation. There are few experimental researches for steam-air mixture condensation. Table 3.2 summarizes the range of experimental conditions used in literatures including two recently reported steam-air mixture condensation data.

Table 3.2: Experimental conditions from literatures

Year	**Author**	**Steam flux** (kg/m^2-s)	**Air flux** (kg/m^2-s)	**Nozzle diameter** (mm)	**Pool temperature** (°C)
1972	Kerney *et al.*	332-2050	N/A	6	28-79
1996	Chun *et al.*	286-1488	N/A	1.35-10.85	12-87
2009	Gulawani *et al.*	472-501	N/A	1-2	30-45
2012	Song *et al.*	250-1235	N/A	10.15	20-90
2015	Qu *et al.*	0.4-11.2	0.2-2.32	1.5/3	79/87
2016	Cai *et al.*	5.25	0-1.2 (N_2)	6.4	10
2016	Xu and Guo	70-620	N/A	5	20-70
2019	**Present study**	40-350	0.17-356	9.525	75-95

Figure 3.2 shows the DCC regime map proposed by Song *et al.* (2015) and the present regime of interest.

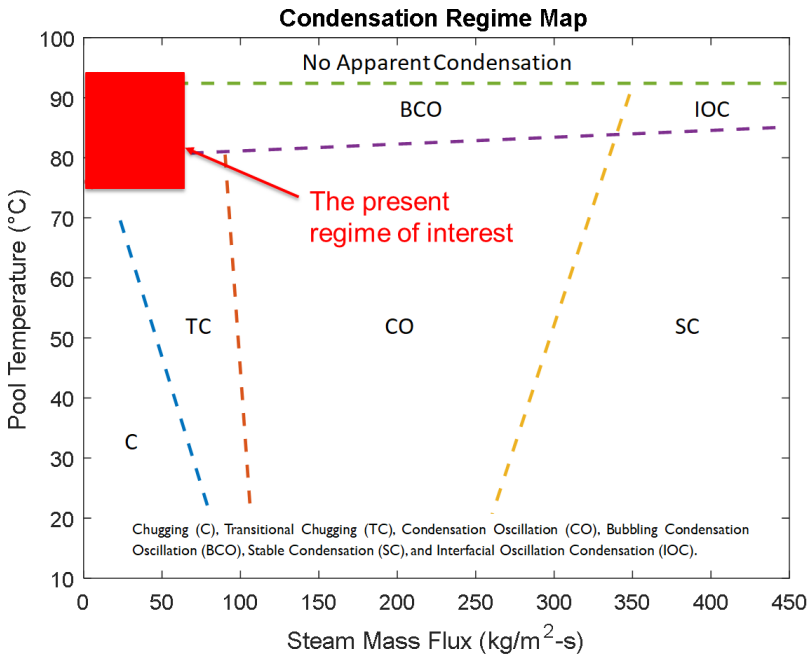

Figure 3.2: Condensation regime map of steam jet from a single-hole nozzle (Song *et al.* 2015)

Most of the previous studies focused on the characteristics of a stable condensation regime where turbulent mixture jets were formed in the water pool. Specifically, thermal hydraulic aspects of transitional chugging and bubbling condensation oscillation regimes such as bubble dynamics were not adequately addressed in previous research studies compared to that of the nucleate boiling. Thus, the present study aims to obtain high-quality experimental data for the C, TC, and BCO regimes and analyze their thermal hydraulic characteristics in comparison with the previous research studies of nucleate boiling. The results of the present study can be employed for the condensation closure model development for computational fluid dynamics (CFD) or nuclear thermal-hydraulic system codes and for the validation of the existing model. Additionally, a new heat-transfer coefficient correlation based on the thermal hydraulic characteristics of the unstable steam condensation in subcooled water will be suggested. The current study considered steam fluxes in the range of 5 and 70 kg/m^2·s for pool temperatures in the range of 71, 78, 83, 86, 90, and 92±2°C.

3.2 Experimental Method: TAMU SAC Test Facility

Since the main purpose of this study is to investigate the fundamental thermal-hydraulic phenomena involved in DCC process, the experimental facility is designed to perform state-of-the-art measurement visualization technique such as particle image velocimetry (PIV) and laser induced fluorescence (LIF) in combinations of conventional temperature, pressure and flow rate measurements using data acquisition (DAQ) system. Figure 3.3 presents the schematic diagram of the TAMU SAC test facility.

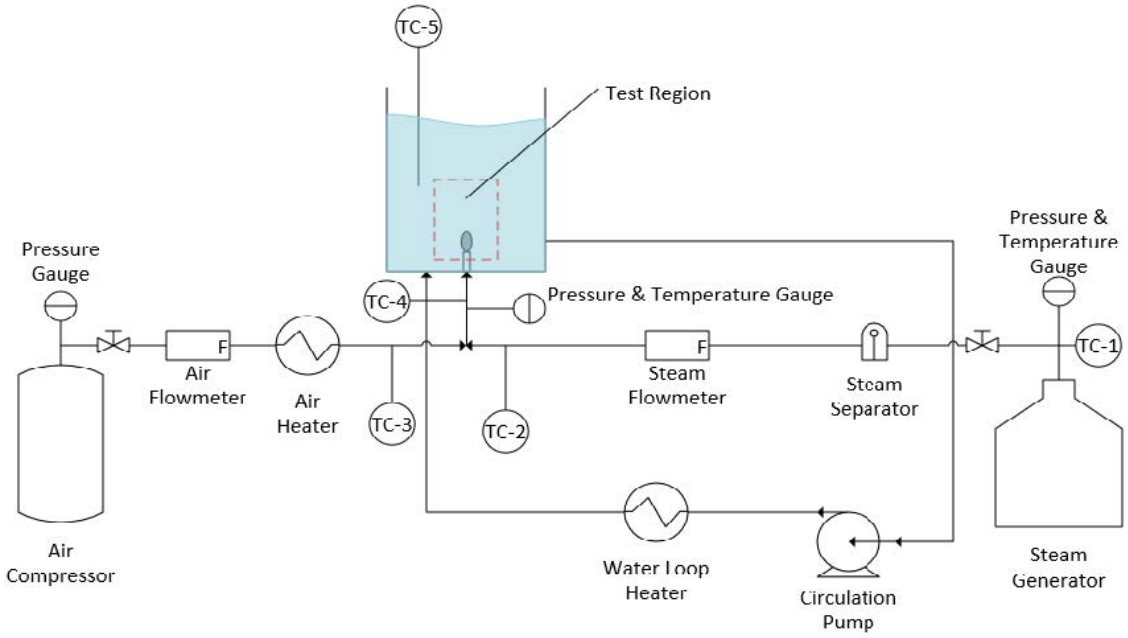

Figure 3.3: Schematic diagram of TAMU SAC test facility

In order to apply the visualization techniques, the test region is made of transparent polycarbonate material. Figure 3.4 and 3.5 show the 3-D CAD drawing of the test facility and the picture of the actual setup of the facility, respectively.

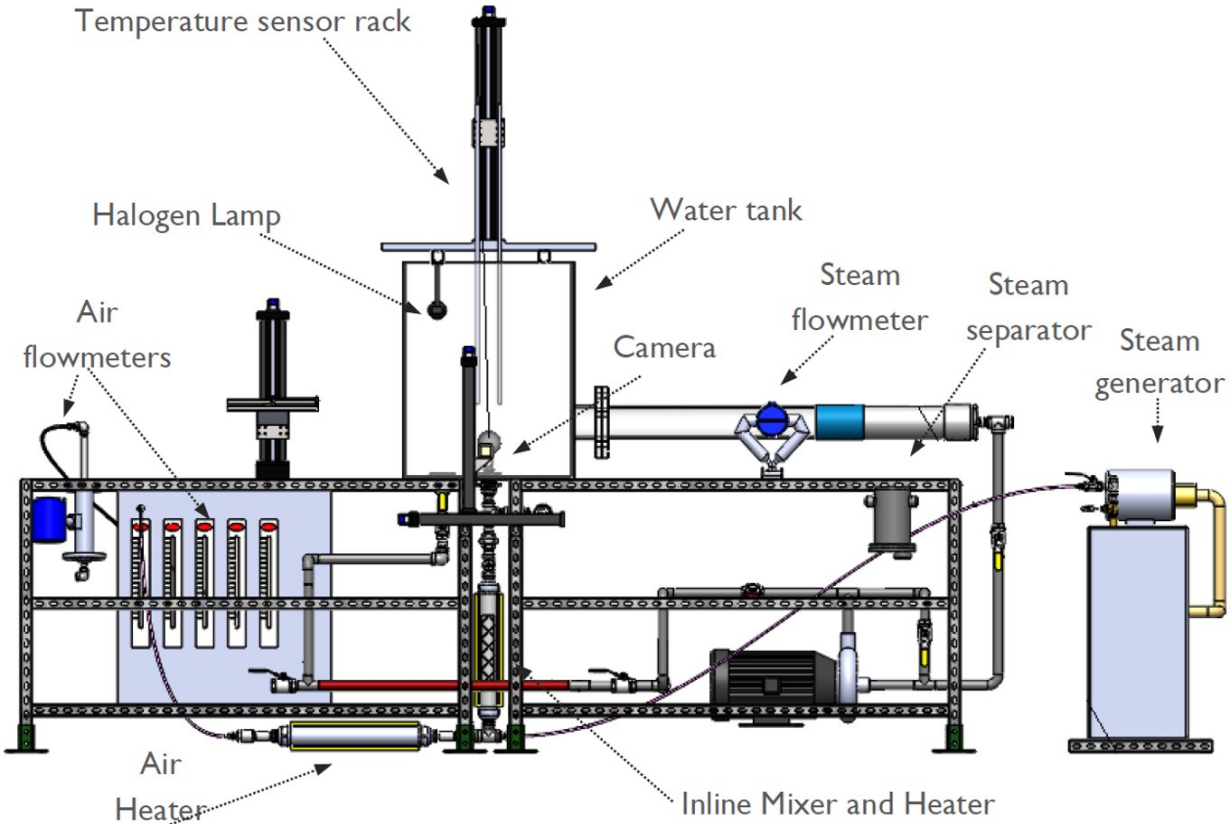

Figure 3.4: 3-D CAD drawing of the TAMU SAC test facility

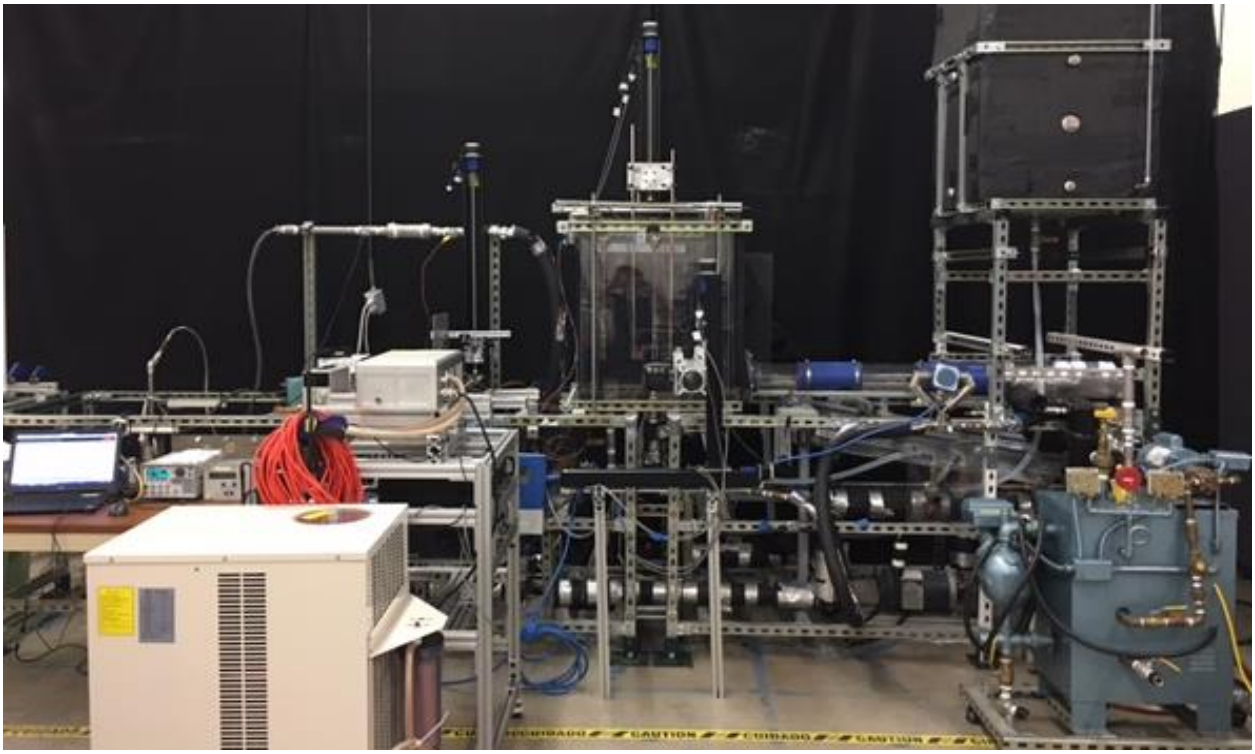

Figure 3.5: Actual setup of the TAMU SAC test facility

This facility consists of five major components, which include the steam supply, steam mixing and reheating, test, and measurement sections. The general configuration of the test section is shown in Figure 3.6.

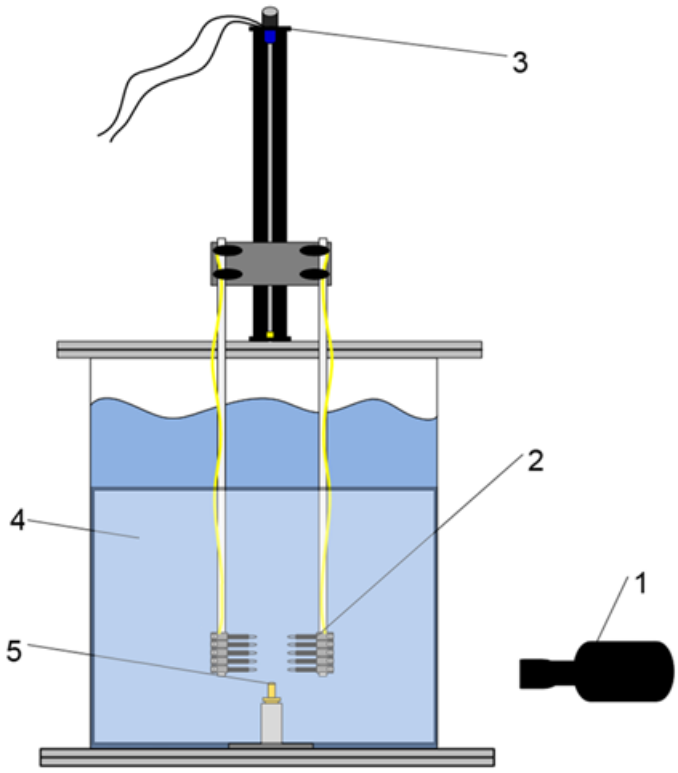

Label	Description	Model/Specification
1	High-speed camera	Phantom V711
2	Thermocouples	K-Type
3	1-D Traverse	VXM step motor
4	LED Backlight	PBD-6060
5	Jet Nozzle	10 mm inner diameter

Figure 3.6: Configuration of the test section

The net nozzle has an inner diameter of 9.525 mm (0.39") and is placed at the center of the bottom of the water tank with a height of 140 mm (5.5"). The free surface of the water is maintained at 584.2±20 mm from the bottom of the tank. Ten thermocouples are located near the nozzle to measure the temperature of the water near the condensation region. The thermocouples are arranged in groups of five at opposite directions of the nozzle, and are held by a traverse system that is capable of adjusting their locations in the z-direction. The whole test facility is in a water tank with dimensions of 578 mm × 578 mm × 762 mm (22.75"×22.75"×30") in width×depth×height. In order to achieve a desired water tank temperature, the water is circulated and heated up before

injecting steam/air. In order to capture the bubble images, the light-emitting diode (LED) backlight and Phantom V711 high-speed camera are installed behind the water tank.

The steam is produced in the Sussman Electric Boiler Model ES-18, which provides a maximum steam rate of 24.58 kg/h and has a design pressure of 0-689.5 kPa. The control valve located on the steam outlet adjusts the steam mass flow rate. The steam supply line is insulated by a fiberglass covering to maintain the generation of high-quality steam throughout the steam line. To remove any liquid, the steam travels through a steam separator model 81SATO designed for a maximum temperature of 232.22°C and a maximum pressure of 1034 kPa. Before steam enters the mixing chamber, the temperature and the flow rate of the steam are measured by a K-type thermocouple and a Micro Motion Coriolis flowmeter model CMF025, which has a gas flow accuracy of $\pm 0.75\%$ of full scale.

The air is supplied from the air compressor model CPF6025VP, which has a pressure limit, 135 psig, and provides 8.3 SCFM at 40 psig continuously. The air mass flow is controlled by adjusting the ball valve placed at the outlet. In order to measure the air flow rate, the air supply line is connected to the flowmeter model Optimass 7300 which has an accuracy of $\pm 0.35\%$ of full scale for T < 100°C. A series of rotameters are connected downstream of the flowmeter as an analog indicator. The air is preheated with a 10 kW band type heater before it enters into the mixing section to prevent any undesired steam condensation in the gas line. The heater power is controlled by a variable alternative current (AC) power supply to control the air temperature. The temperature of the heated air is measured by the K-type thermocouple located after the heating section. The air flowed from the air supply line is injected horizontally and mixes with a vertical flow of steam in the air/steam mixing section. The mixture flows into a 2"$\times$17" inline pipe type mixing chamber with mixing vane to produce homogeneous mixture of steam and air and then reheated with a 10 kW band type heater. In order to measure the temperature of the mixing gas, the K-type thermocouple is installed right before the gas injection nozzle.

To measure the pressure of the gas mixture, a pressure transducer was installed between the jet nozzle and the mixing chamber, which had a pressure operating range of 0-344.7 kPa and

a 0.002% accuracy. All the measurement devices are connected to the DAQ controlled by the National Instruments LabVIEW program.

Table 3.3 summarizes the list of instruments employed for measurements.

Table 3.3: List of instruments for measurements

Instrument	**Model**	**Range**	**Accuracy**
Vortex Flow meter	Krohne VFC070 Optiswirl 4070/C	3-7 g/s, <240°C	Up to 2%
Coriolis Flow Meter	Elite CMF025M	Up to 66.7 g/s, <204°C	0.25%
Coriolis Flow Meter	Krohne Optimass 7000 S06	340 g/s, <100 °C	0.35%
Rotameter	Dwyer RMC-101	5-50 SCFH	2%
Rotameter	Dwyer RMC-103 (x2)	20-200 SCFH	2%
Rotameter	Dwyer RMC-104 (x2)	50-400 SCFH	2%
Rotameter	Dwyer RMA-150-SSV	10-100 cc/min	4%
Rotameter	Dwyer RMB-50	1-10 SCFH	3%
Rotameter	Dwyer VA10422	up to 89.2 ml/min	2%
Rotameter	Dwyer VA10418	up to 25.5 ml/min	2%
Thermocouple	K-type	0-1250°C	1°C

Table 3.4 presents the list of equipment used in the experimental facility.

Table 3.4: List of equipment used in the experimental facility

Equipment	**Model**	**Range**
Steam Generator	Sussman ES-18	∼100 psi ∼52.4 lbs/hr
Air Compressor	CPF6025VP	MAX 135 psi, 25 Gallons 8.3 SCFM @ 40 psi 5.8 SCFM @ 90 psi
Air Compressor	HS7810	MAX 175 psi, 80 Gallons 15.1 SCFM @ 90 psi 13.7 SCFM @ 175 psi
Building Air Supply	N/A	∼80 psi
High-speed Camera	MIRO-M310	10k fps @ 640X480 120k fps @ 128X128
High-speed Camera	FASTCAM-SA5	10k fps @ 1024X744 100k fps @ 320X192
High-speed Camera	PHANTOM V711	7530 fps @ 1280X800 680k fps @ 128X8
Laser	CL-AO-L-532	10W
Laser	CNI-LSR532W	20W

3.3 Preliminary Results: Shakedown of TAMU SAC Test Facility

A series of shakedown tests to learn about the TAMU SAC test facility is conducted.

3.3.1 Visualization and image processing of steam direct contact condensation

Figure 3.7 shows the high resolution and high speed flow visualization of pure steam jet and steam-air mixture jet injection in subcooled water captured by the high speed camera. Frame rate of the recording was 2000 frames per second (fps).

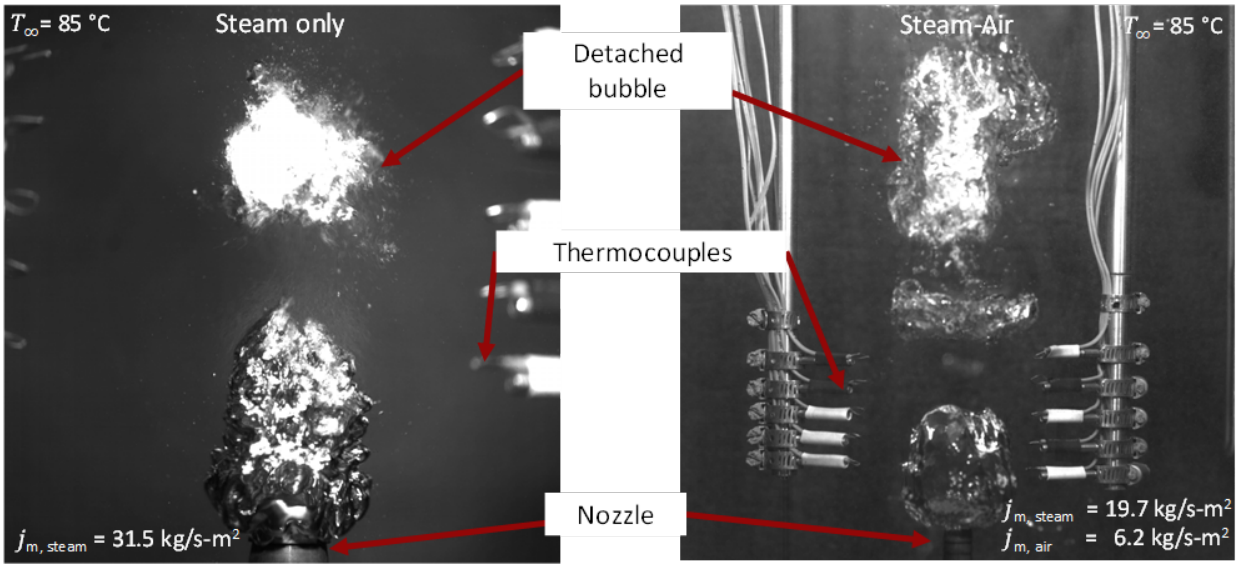

Figure 3.7: High resolution and high speed flow visualization of pure steam jet (left) and steam-air mixture jet (right) injection

Steam/air mass fluxes and pool temperature were recorded using NI DAQ system. After recording of certain period of time of condensation under the steady conditions, each frame was converted into binary image using edge detection algorithm. Examples of the condensing bubble image post processing is shown in Fig. 3.8.

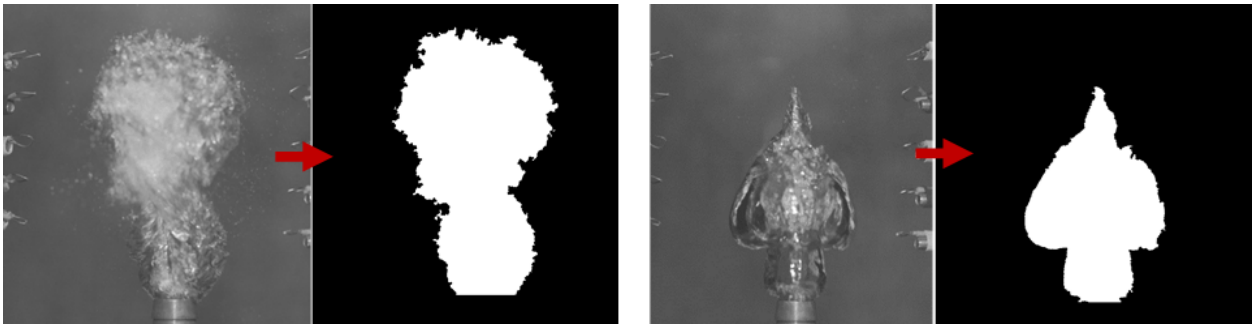

Figure 3.8: Examples of the condensing bubble image post processing

Thermal-hydraulic characteristics for specific test conditions can then be calculated from the image processing results and the DAQ measurements. Further experimental conditions and detailed calculation method will be discussed in section 3.4.

3.3.2 Preliminary temperature measurement of two phase flow using PLIF thermometry

The planar laser induced fluorescence (PLIF) is a non-intrusive measurement technique using high-speed camera flow visualization that can provide concentration or temperature field information with fluorescent dye resolved in the working fluid. The fluorescent dye is usually absorbing specific wave length of light and then emitting different spectrum proportional to the incident light intensity and other variables depending on the dye characteristics. In this study, PLIF is employed to measure the temperature field around the condensing bubble using Rhodamine-B fluorescent dye.

Figure 3.9 shows the schematic of the present LIF setup.

LIF temperature measurement has various advantages compared to the conventional thermocouple temperature measurement because it can produce not only spatially resolved mean temperature field, but also can provide the spatiotemporally resolved instantaneous temperature field information. Furthermore, time response of the measurement is fast (up to 10^{-7} s), which usually depends on the performance of the high speed camera, compared to that of the thermocouple, which is in order of 10 Hz. However, there are not many attempts previously to apply the PLIF technique to two phase flow temperature field measurement.

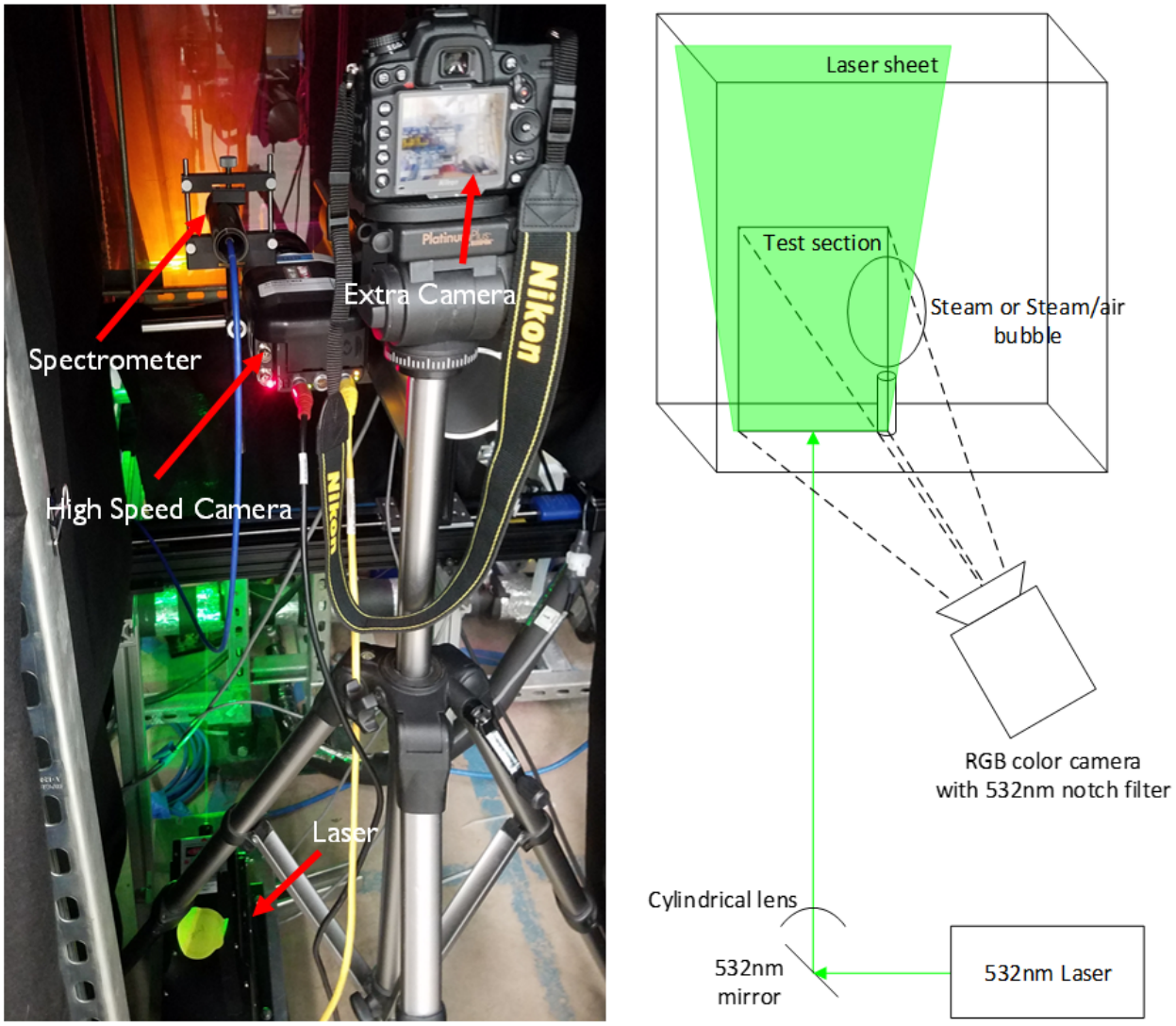

Figure 3.9: LIF setup

Since there are not many references for two-phase flow application of LIF, development of LIF is one of the major goal of this study. LIF is governed by the following equation (Carlos *et al.* 2011):

$$I = I_0 C \phi \epsilon \tag{3.4}$$

where I is emission light intensity, I_0 is incident light intensity, C is the dye concentration, ϕ is quantum efficiency, and ϵ is molar absorption efficiency. Because of the temperature sensitivity of the quantum efficiency for specific fluorescent dyes, it is possible to calculate the temperature

with proper setup. Rhodamine-B is selected as the fluorescent dye for this study because of its linear temperature sensitivity (2.3%/K). Figure 3.10 depicts the present *in situ* calibration for the LIF temperature measurement performed with the Ocean Optics USB400 spectrometer. Since the emission light intensity captured by the high speed camera depends not only on the Eq. 3.4, but also is sensitive to the image sensor characteristics of the spectrometer, it may show a non-linear characteristics.

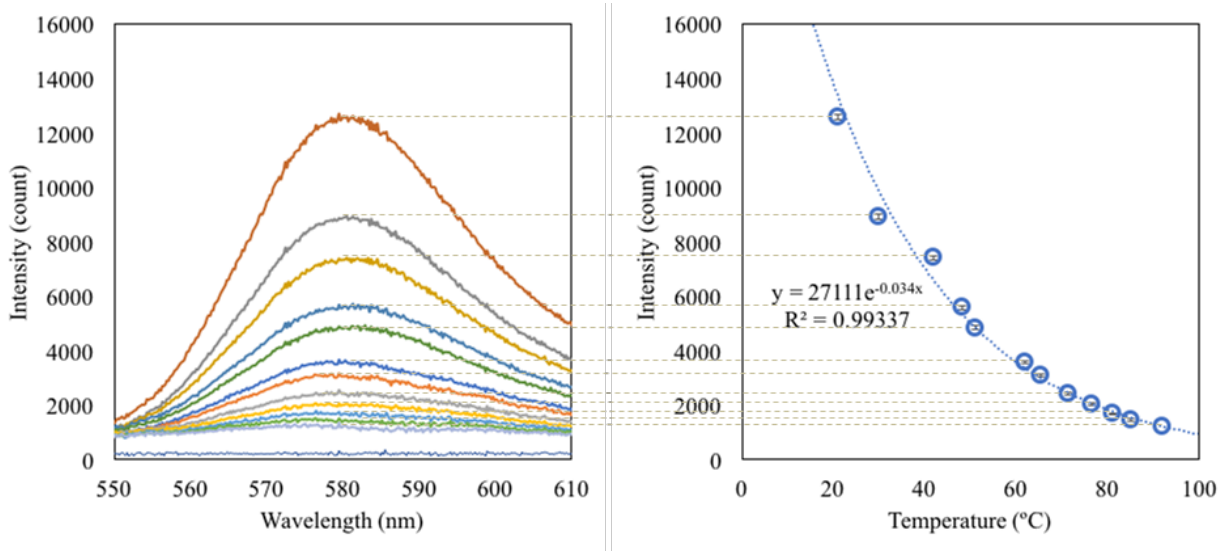

Figure 3.10: *In situ* calibration curve of LIF with the Spectrometer

Rhodamine-B concentration is 20 mL of 1 g/L rhodamine-B aqueous solution with 1 mL of Isopropyl alcohol in 191 $\pm$ 1.72 L of water. The 10 W continuous 532 nm laser is used as the fluorescence excitation source.

Figure 3.11 shows the raw image from high speed camera and LIF processed temperature field of DCC of steam in subcooled water .

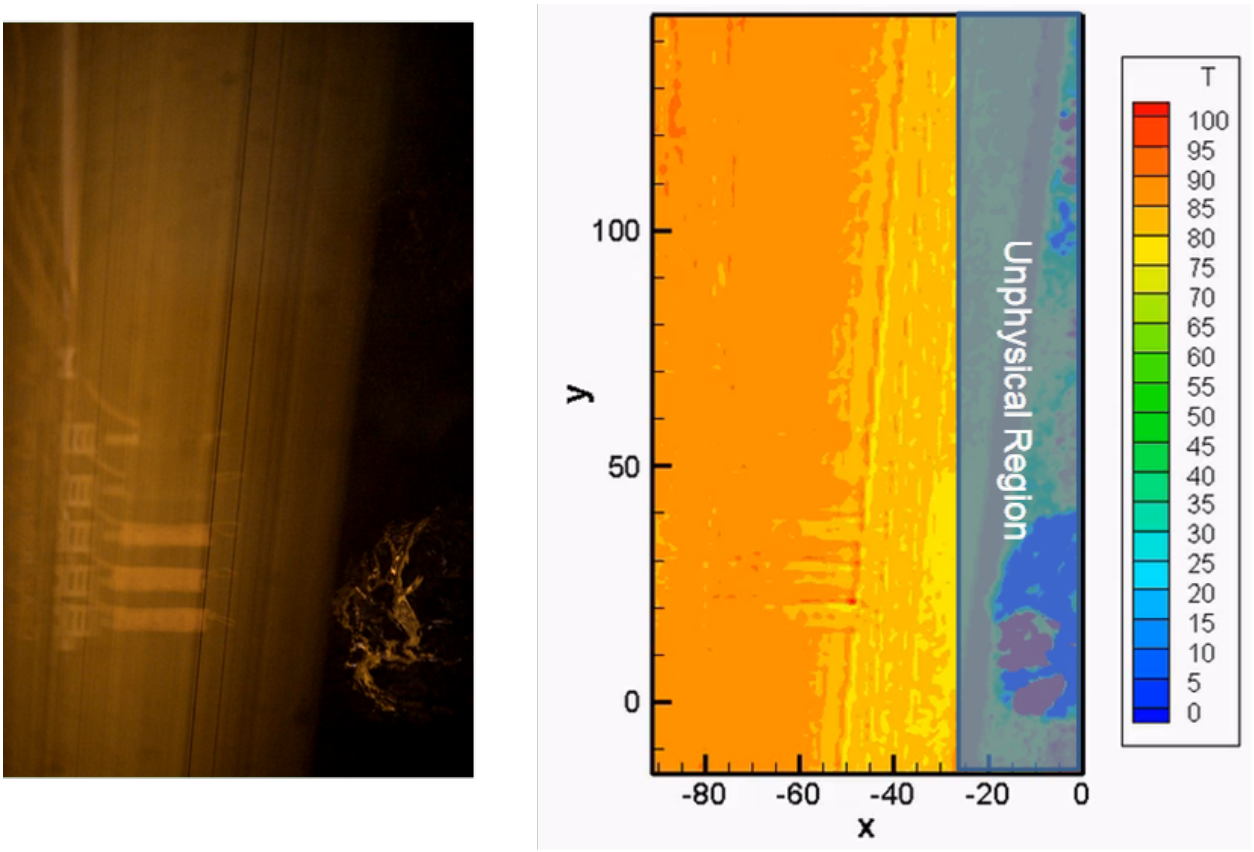

Figure 3.11: Raw image from high speed camera and LIF processed temperature field of DCC of steam in subcooled water

As shown in Fig. 3.11, the quality of the LIF processing is not enough to apply any analysis yet. Further experimental conditions and improvements will be discussed in section 3.5.

3.3.3 Preliminary velocity measurement of two phase flow using PIV

The Particle Image Velocimetry (PIV) technique is employed for the flow field measurement and visualization. Figure 3.12 shows the schematic of the current PIV setup.

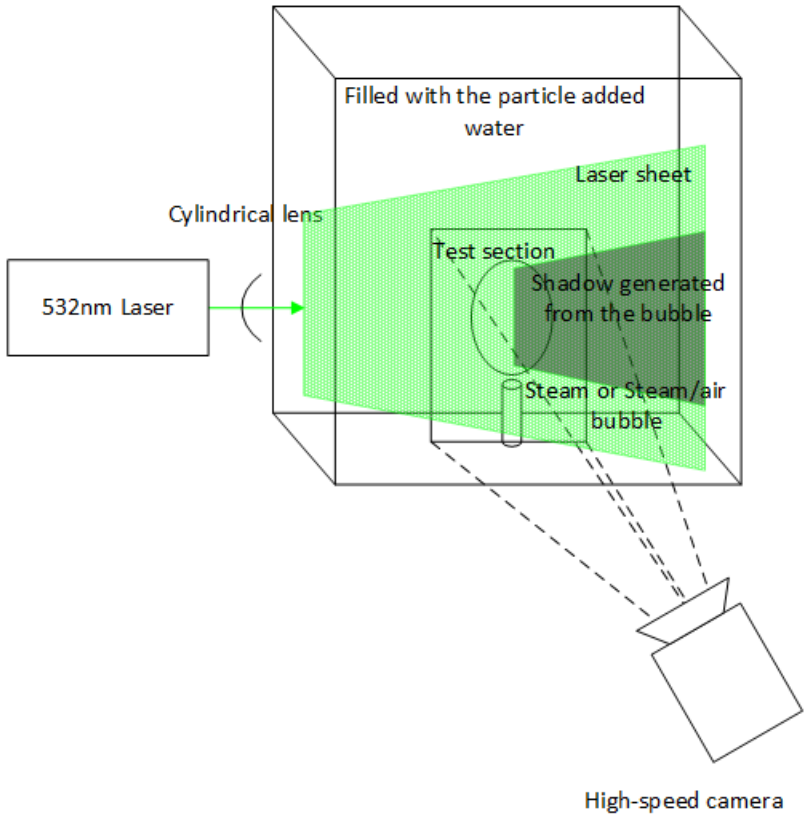

Figure 3.12: Schematic of PIV setup

The PIV is a non-intrusive velocity field measurement technique using high-speed camera flow visualization with the micro sized particles seeded in the working fluid. PIV has various advantages compared to the other velocity measurement techniques because it can produce not only the mean field and turbulent statistics, but also can provide the instantaneous field information. However, the PIV has limitations for the two-phase flow application due to the reflection on the gas-liquid interface and shadow generated from the bubble.

The selection of the particle type is dictated by the fluid physical properties and the flow properties. Since the procedure requires not only the fluid physical properties like viscosity and density, but also requires the flow properties such as Stokes number and Strouhal number and technical specification of the high-speed camera, choosing the right particle is usually a trial and error process to minimize the measurement uncertainty.

Injecting a lot of particles directly into the experimental facility may cause the particle clog in mixing chamber or particles stuck on the submerged heaters, which eventually would result in the damage on the experimental facility. Thus, an independent experimental setup was built to develop the PIV technique for the bubbly flow inside the pool. Because the purpose of the independent setup is sorely to develop the technique itself, but not to obtain the condensation data, PIV technique was developed using air injection into the water with isothermal condition. Figure 3.13 shows the experimental setup for the PIV development for air-water bubbly flow inside a pool.

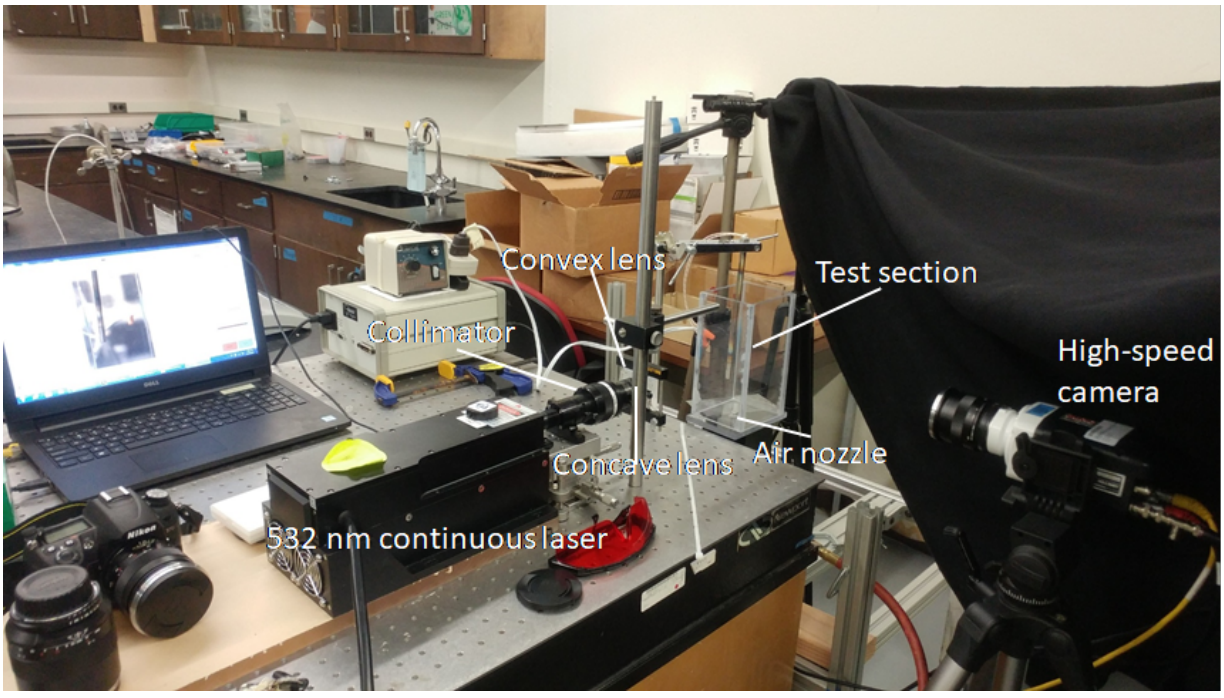

Figure 3.13: Experimental setup of two-phase PIV development

The developed PIV technique will be applied to the actual experimental facility to measure the flow field for the steam condensation. Prana open source PIV toolkit is employed to obtain the PIV results. Figure 3.14 presents the obtained left half plane velocity vector layered on the original high-speed image with seeding particles.

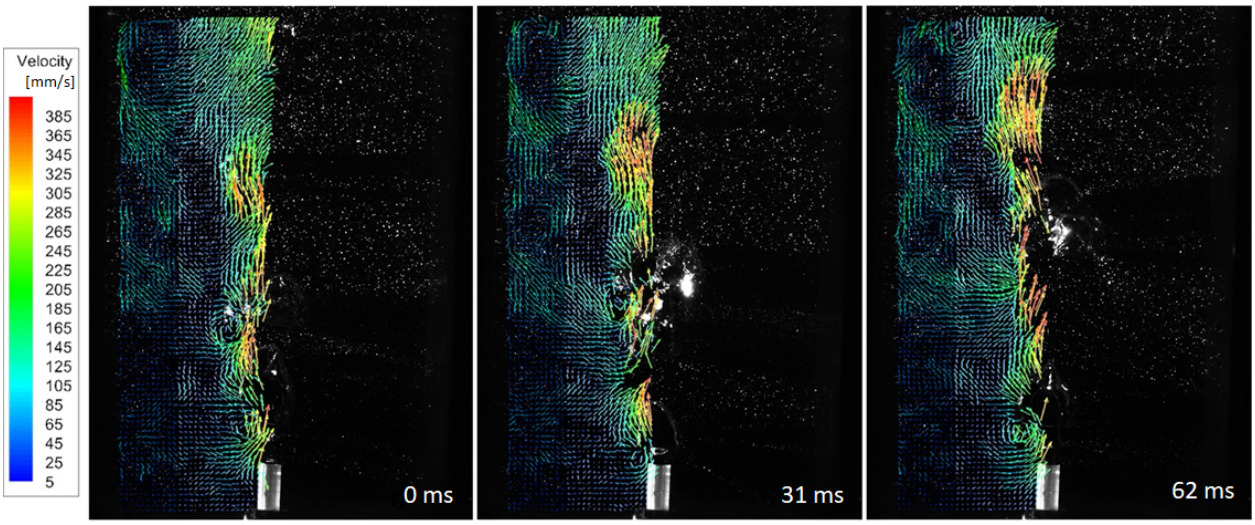

Figure 3.14: Velocity vectors of the left half plane layered on the original image

The right half plane was not calculated because of the shadows generated by the bubble made large uncertainty on the right half plane. Figure 3.15 shows the mean velocity vector for 1.024 s.

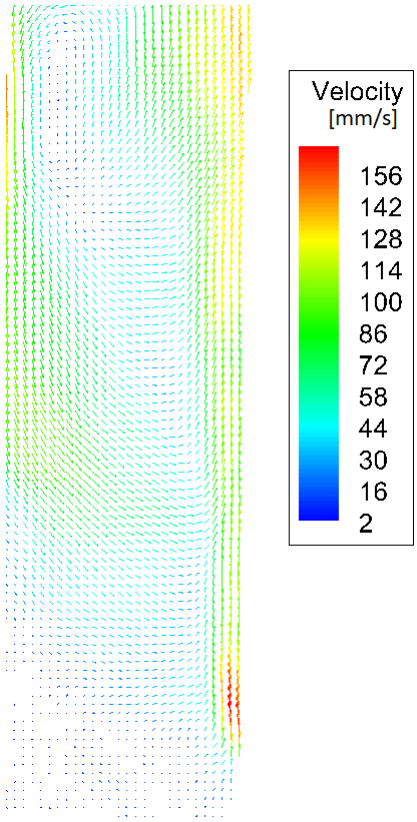

Figure 3.15: Mean velocity vectors of the left half plane

The shadow effect can be resolved either using the image pre-processing and interpolation method or introducing one more laser sheet from the opposite direction of the existing one. In this study, the full plane PIV velocity vector field was obtained using the image pre-processing and linear interpolation method. Figure 3.16 and 3.17 show the full plane velocity vector and mean velocity vector and contour. Further experimental conditions and improvements will be discussed in section 3.6.

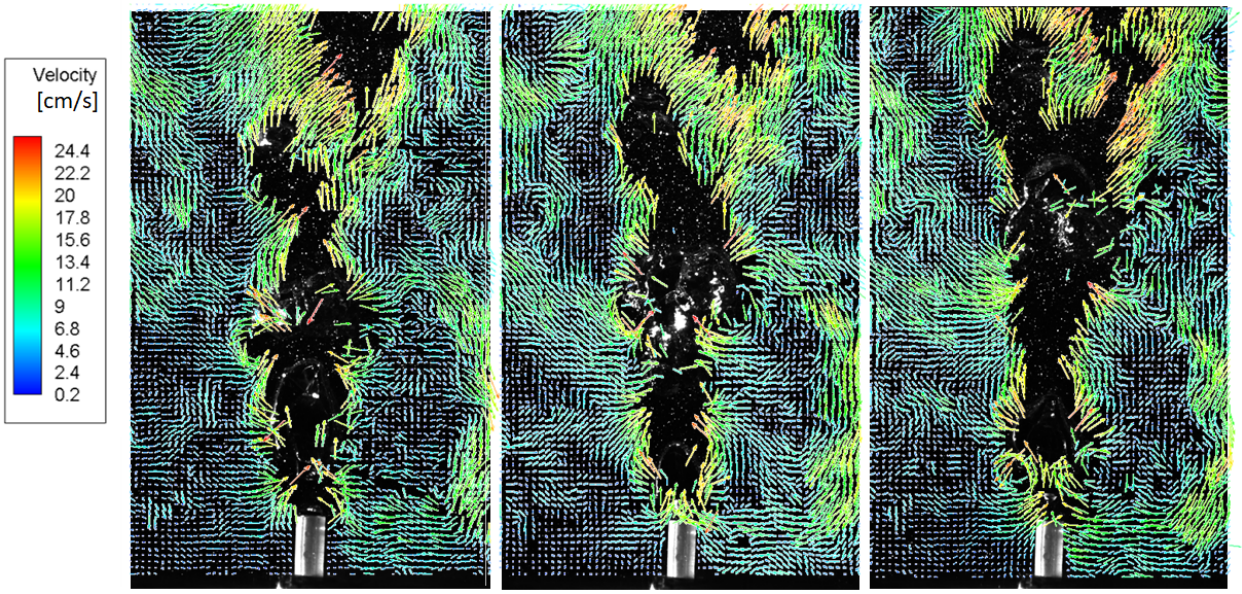

Figure 3.16: Velocity vectors of the full plane layered on the original image

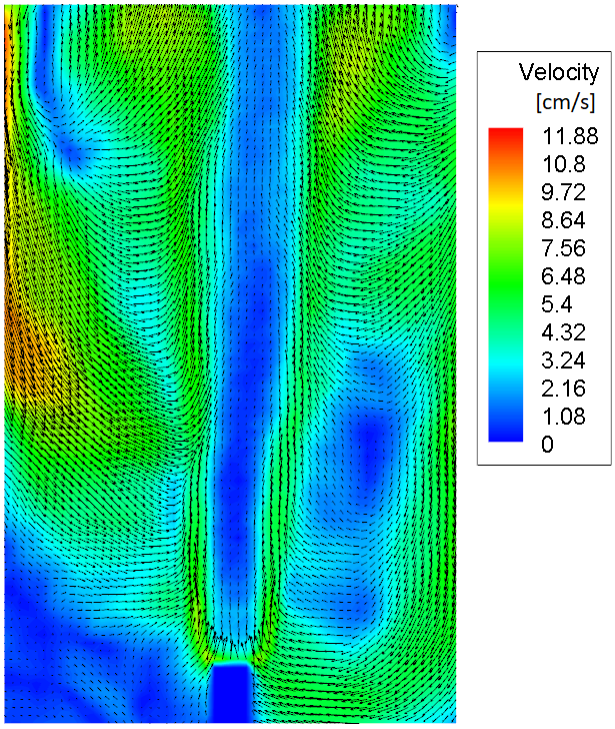

Figure 3.17: Mean velocity vectors and contour of the full plane

3.4 Heat Transfer Characteristics Measurement

3.4.1 Heat transfer coefficient calculation

In the present work, the heat-transfer coefficient was calculated using the following formula, which is similar to that presented by Brucker *et al.* (1977).

$$h = \frac{\rho_g \dot{V}_{\text{cond}} i_{fg}}{A\Delta T} \tag{3.5}$$

where A is the surface area of the bubble in m^2, i_{fg} is the latent heat of steam at the given temperature and pressure in kJ/kg, ρ_g is the density of the steam in kg/m^3, ΔT is the temperature difference between the pool and the steam in Kelvin, and $\dot{V_{cond}}$ is the condensed volume flow rate calculated using the equation listed below.

$$\dot{V}_{\text{cond}} = \dot{V}_{\text{exp}} - \dot{V}_{\text{visual}} \tag{3.6}$$

where $\dot{V}_{exp}$ is the measured volume flow rate of the steam at the upstream of the injection nozzle using the Coriolis flow meter, and $\dot{V}_{visual}$ is the calculated volume flow rate of the steam during the condensation process. The variables ΔT, i_{fg}, ρ_g, and $\dot{V}_{exp}$ were measured and evaluated by the DAQ data, while $\dot{V}_{act}$ and *A* were measured using high-speed camera image processing. The image processing technique is one of the various visualization methods extensively used in two-phase flow research and jet flow investigation (Hassan *et al.*, 1992, Philip *et al.*, 1994, Kim & Park, 2011, Al Issa *et al.*, 2014, Estrada-Pèrez *et al.*, 2018, Nguyen *et al.*, 2018, Lee *et al.*, 2018). In two-phase flow research, the technique was used to obtain the trajectory of gas bubble migration and to acquire high-definition pictures of the steam bubble at high-frame rates for bubble-shape analyses. In the present study, images captured from the high-speed camera are used to obtain the thermal hydraulic characteristics of the bubble, such as the surface area, volume, cross-sectional area, and the characteristic diameter during the condensation process. The image processing programs used for the bubble detection and tracking were developed in MATLAB and ImageJ. Examples of the actual image and the image after post-processing are shown in Fig. 3.18.

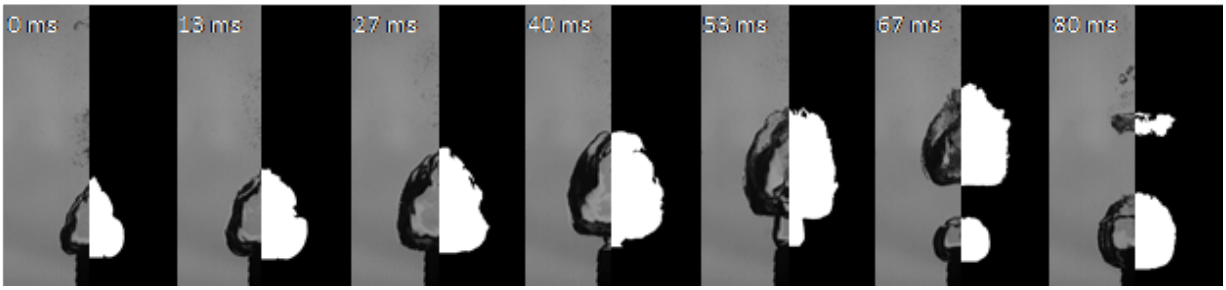

Figure 3.18: Examples of the original (left) and post processed (right) sequentially condensed bubble images

Irrelevant objects other than the traced bubbles, such as the thermocouples and the jet nozzle, are detected and eliminated from the image plane by using software programs to prevent further interference during the extraction of the useful bubble information, and before the generation of binary images. The volume and surface area of the bubbles are calculated by assuming the azimuthal symmetry and by applying numerical integration using cylindrical geometries. The height of the cylinder was set to be one pixel, while the diameter of the cylinder was determined to be equal to the number of pixels found in that lateral-wise axis. Adding all the volumes and surface areas of the cylinders approximates the total volume and surface area of the bubble with a pixel-to-meter conversion. Figure 3.19 represents the example of a raw image and 3-D reconstructed bubble volume and surface area using the image processing algorithm.

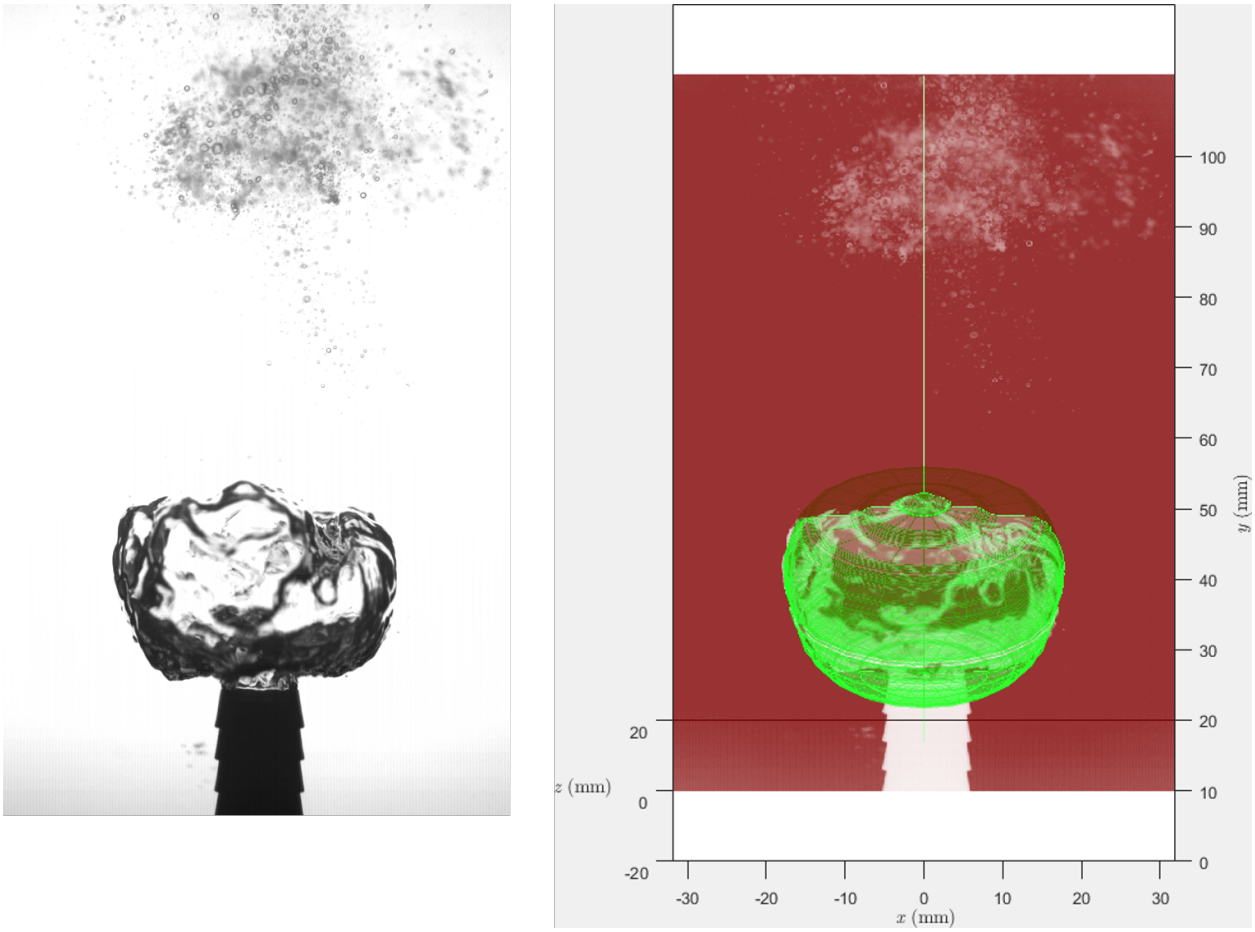

Figure 3.19: Examples of the raw image (left) and 3-D reconstructed (right) bubble volume and surface area

3.4.2 Experimental procedure and conditions

The experimental procedure included steps to prepare the main components, such as the steam generator, the water tank, and the data acquisition (DAQ) system. The steam generator was connected at first to the DI water system to fill the DI water for steam. After the steam generator was turned on, the steam separator was connected to the main steamline to remove any undesired particles or wet content. The water tank was filled with DI water filtered to contain less than 0.05% impurities, and heated up to the desired pool temperature using immersed heaters. Before the onset of the test, a sufficient amount of the steam was ejected into the nozzle in the water tank in order to ensure the discharge of trapped air inside the pipes and to prevent thermal stratification in the water

tank. All the signals from the measurement devices were connected through the DAQ system and controlled by the LabVIEW program. Additionally, the values were recorded on the computer for further analysis. The sampling rate and period for each experiment were 1.0 kHz and 3 s, respectively. The frame rate of the high-speed camera was set to 1000 frames per second (fps) to match the DAQ sampling frequency. During the test, the circulation pump and supplementary heaters for the water and steam were turned off to prevent any mechanical and electrical harmonic noises that could corrupt the raw data. The experimental conditions for the present study are shown in Table 3.5. A total of 48 experiments were performed at various steam mass fluxes at each studied

Table 3.5: Experimental conditions for heat transfer characteristics measurement

Parameter	**Value**	**Accuracy**	**Unit**
Steam temperature	~103	±1	°C
Steam inlet pressure	>110	±0.007	kPa
Nozzle diameter	9.525	±0.01	mm
Steam mass flow rate	0.36-4.55	±0.015	g/s
Steam mass flux	5.05-64.85	±0.22	kg/m^2·s
Pool temperature	71/78/83/86/90/92	±1	°C

temperature, and 48,000 high-speed camera images were analyzed at the specific conditions. The condensation regime of interest of the present work was covered the transitional chugging regime, chugging regime, and the bubbling oscillation regime, according to the condensation regime map shown in Fig. 3.2.

3.4.3 Result and discussion

3.4.3.1 Condensation pattern

Figure 3.20 depicts direction of the buoyancy force corresponding to the orientation of the nozzle. Figures 3.21, 3.22, and 3.23, show the selected sequential bubble images which can represent distinctive patterns observed in the current study for a single period of steam condensation

at the pool temperatures of 78, 86, and 92°C, respectively. As observed in Fig. 6, a bubbling condensation was observed where the steam mass flux was small and in the range of 5.85 to 20.79 kg/m^2·s, while a transitional chugging (TC) was observed for fluxes in the range of 30.89 to 49.77 kg/m^2·s of the steam mass flux. In Figs. 3.22 and 3.23, bubbling condensation oscillation (BCO) was identified for all the various mass flux conditions. From the condensation regime map of the steam jet from a single-hole nozzle shown in Fig. 3.2, the corresponding regimes of the presented experimental data included chugging (C), transitional chugging (TC) (Fig. 3.21), and bubbling condensation oscillation (BCO) (Figs. 3.22 and 3.23). However, in the present study, chugging condensation according to the conventional definition of the presence of the reversal flow of water back into the nozzle was not observed, as shown in Fig. 3.21. This result can be explained by the role of the buoyancy force (F_b in Fig. 3.20) in the force balance analysis during the condensation process, which is conceptually described in Fig. 3.20. If the orientation of the nozzle is vertically downward, then the direction of the steam injection is against the gravity-driven buoyancy force. Because of the opposite direction of the steam flow and the buoyancy force, a larger pressure fluctuation occurs during the condensation process compared to the horizontal and the vertically upward steam injection cases, whereby the sudden change of volume of the steam that condenses into water generates negative pressure towards the core of the bubble. Taking into account the fact that the chugging condensation occurs at the nozzle, the location of the negative pressure is in the nozzle in the vertically downward steam injection case, while the location of the negative pressure is far from the nozzle for the vertically upward steam injection case. In addition to the buoyancy force acting on the bubble, the circulation of the water inside the pool induced by the natural convection contributing to chugging occurs more likely in the vertically downward steam injection case, while chugging occurs less likely in the vertically upward steam injection case. This effect may shift the chugging regime to a lower temperature region for the vertically upward steam injection case. Also, steam mass flux may play a role in chugging since the steam-water interface can move due to the inertia of steam flow. Zhao and Hibiki (2018) sub-divided the chugging regime into internal chugging and external chugging. The internal chugging represents smooth

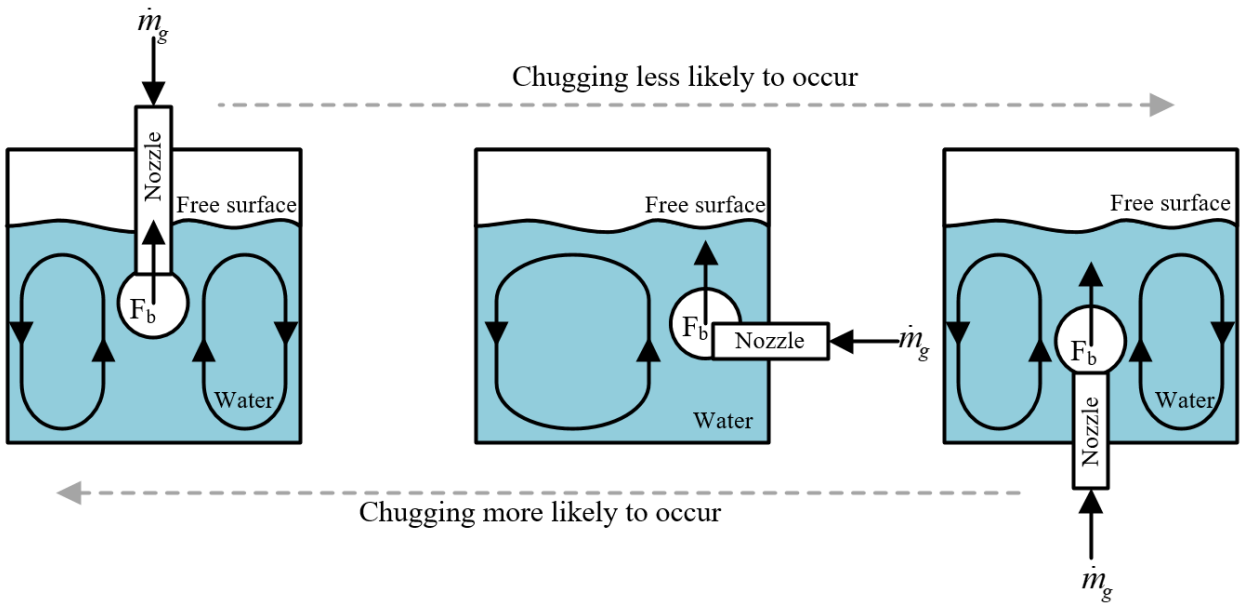

Figure 3.20: Direction of the buoyancy force corresponds to the orientation of the nozzle

steam-water interface oscillating within the nozzle when the steam mass flux is low. The external chugging represents steam-water interface starting to move outside the nozzle when steam mass flux is high. However, internal chugging for the vertically upward steam injection case may have a temperature threshold because it was only observed in the cases at which the pool temperature was lower than 60°C (ΔT_{sub} higher than 40 K) for the present experimental facility. This observation is consistent with the results of Ueno et al. (2011), which presents similar results at ΔT_{sub} of 35-40 K. Bubbling condensation observed with a low mass flux and a pool temperature around 78°C was also reported by previous researchers (Nariai and Aya 1980, 1983, Chun et al. 1996, De With et al. 2007, and Zhao and Hibiki, 2018). Other than transitional chugging, the condensing patterns in this study were observed to exhibit bubbling condensation oscillation (BCO), as shown in Figs. 3.22 and 3.23. Another interesting observation was that spade-shaped bubbling occurred in the lower mass flux regions. Additionally, it was observed that the bubble detachment period changed owing to the pool subcooling temperature and the steam mass flux.

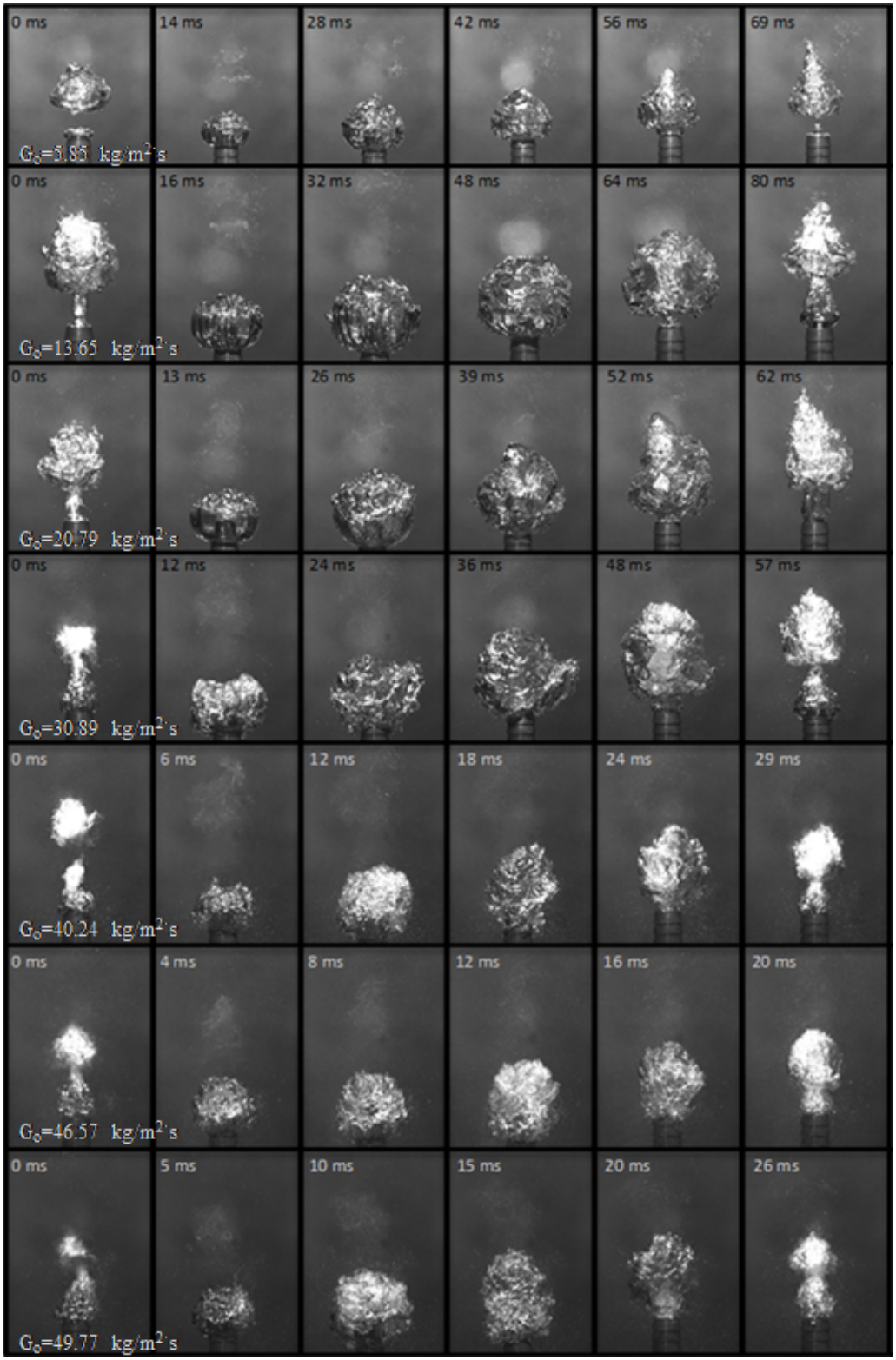

Figure 3.21: Sequential images for a single period of steam condensation at a pool temperature of 78°C

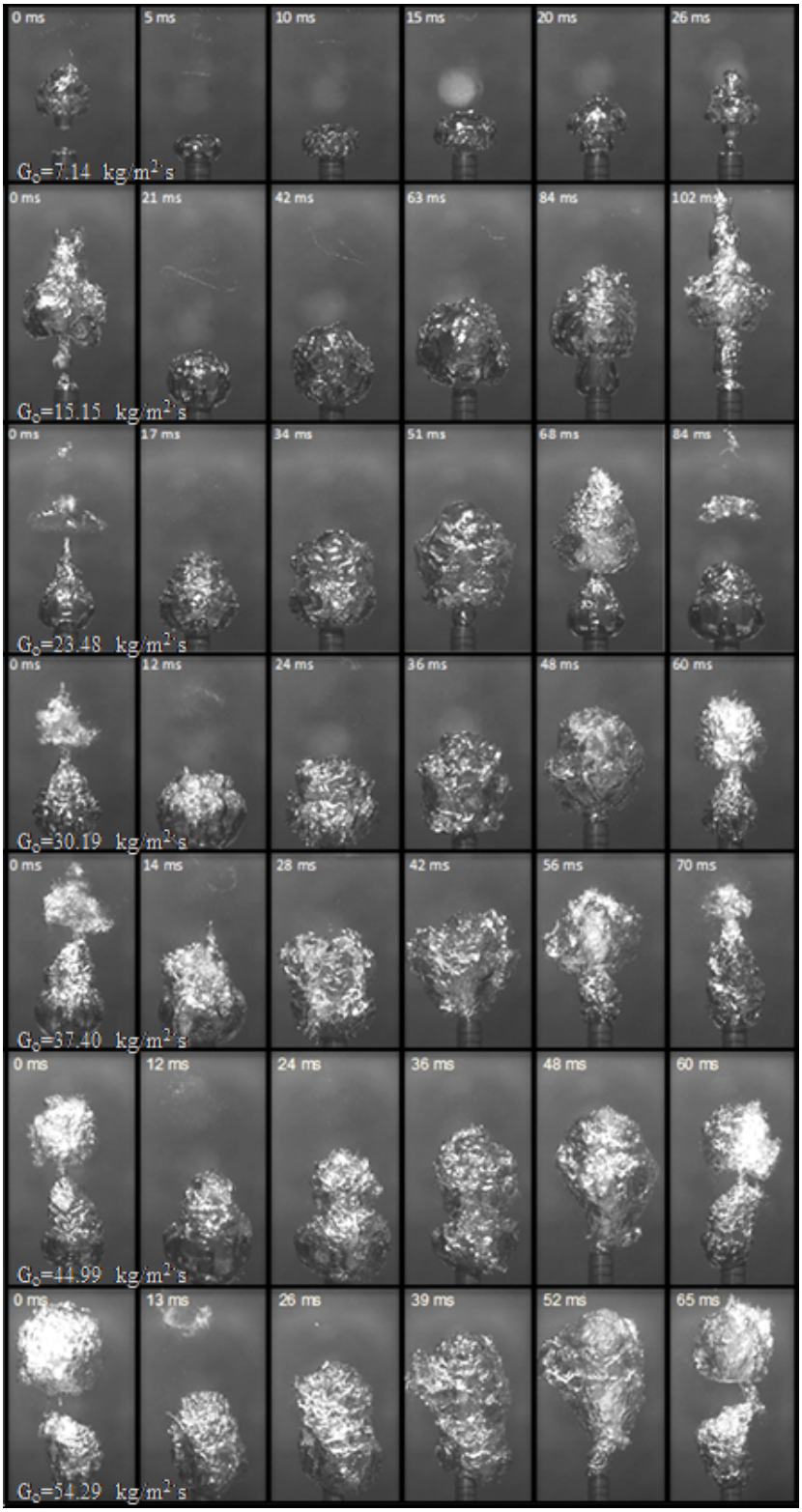

Figure 3.22: Sequential images for a single period of steam condensation at a pool temperature of 86°C

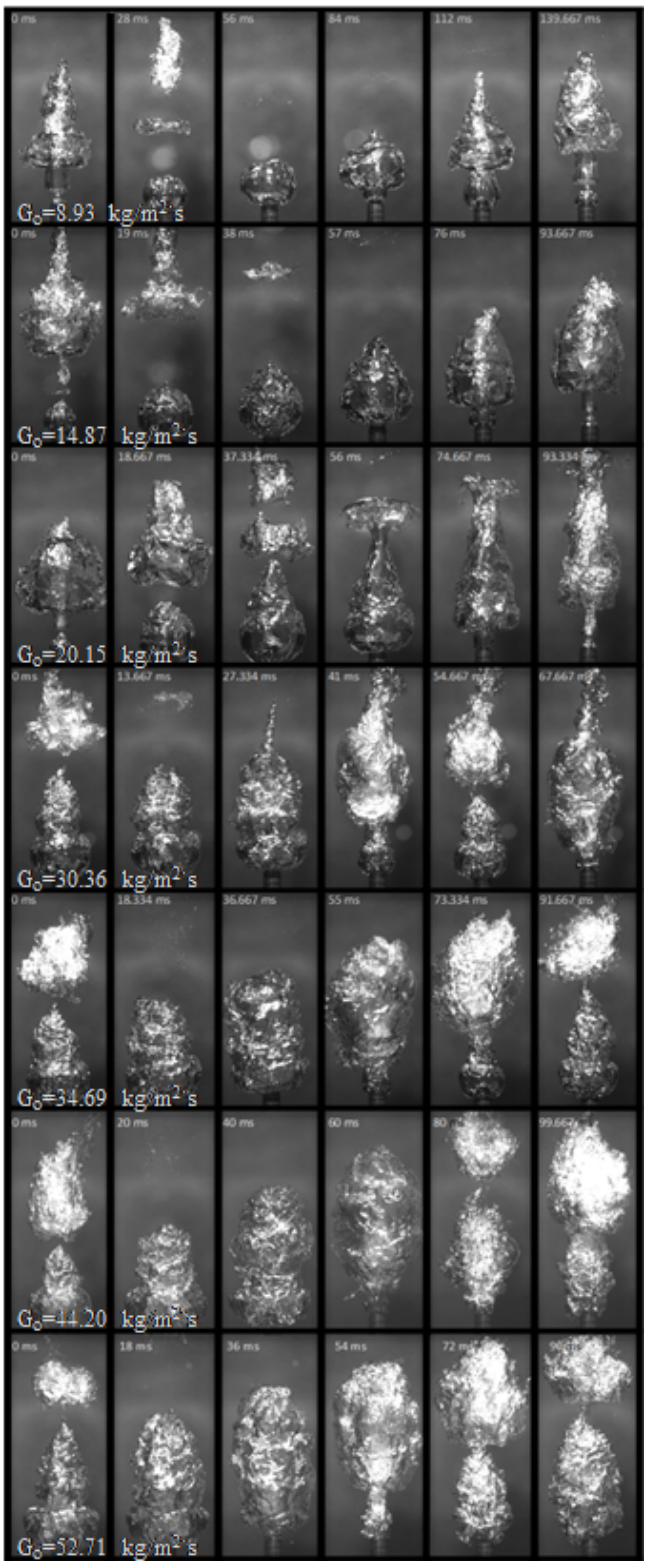

Figure 3.23: Sequential images for a single period of steam condensation at a pool temperature of 92°C

3.4.3.2 *Heat-transfer coefficient*

Since the boundary conditions of the current study includes the steam mass flux and the pool temperature, sensitivity analysis on these parameters are essential to investigate the heat-transfer characteristics. Bubble rising velocity, bubble surface area, and the bubble detachment frequency, are determined by these boundary conditions, and directly affect the heat transfer characteristics during the condensation process. Thus, it is expected that identifying a corresponding variable which can correlate the boundary conditions and the determined variables, is the key to the modeling of the heat transfer of unstable, direct contact condensation. Figure 3.24 presents the experimental results of the heat-transfer coefficient and the correlations suggested by Fukuda (1982) and Chun et al. (1996).

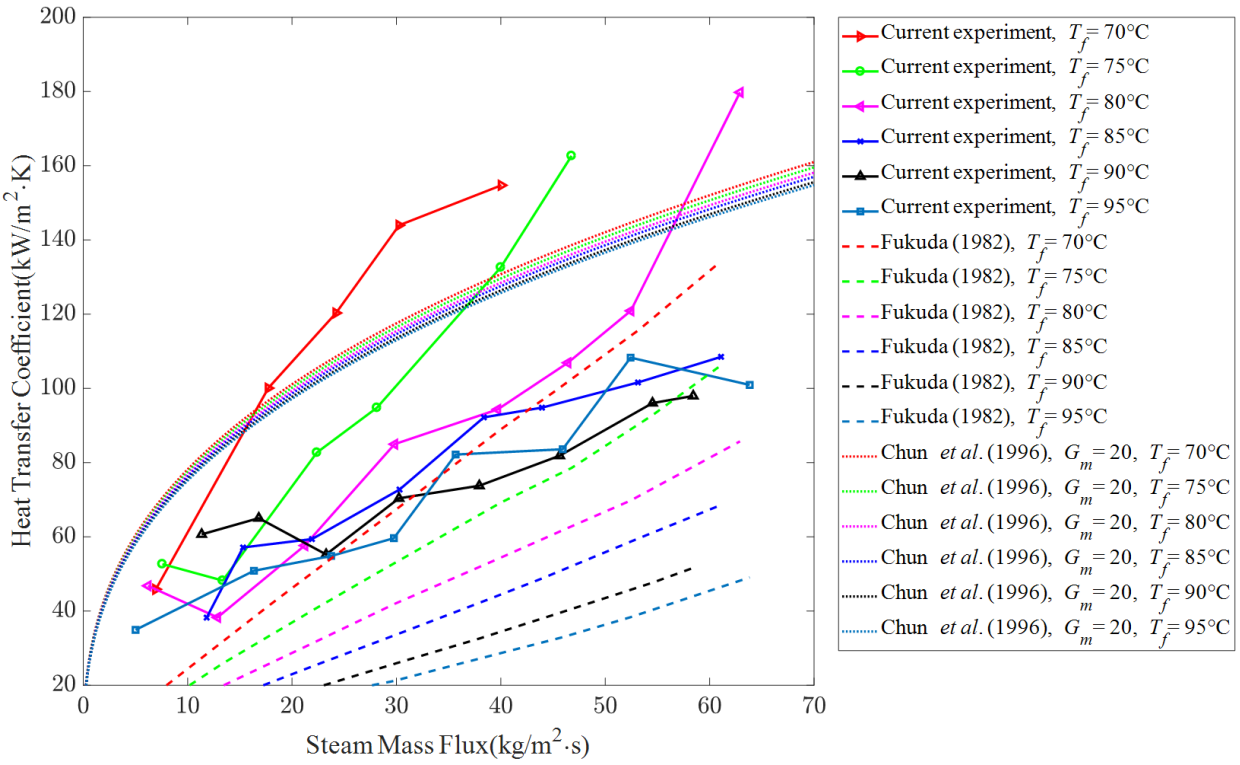

Figure 3.24: Variations of heat-transfer coefficients as a function of steam mass flux

As shown in the plot, the rate of change of the heat-transfer coefficients to the steam mass

flux decreases when the pool temperature increases (water subcooling temperature is also decreasing). The correlations of the present experimental data lie between the correlations obtained from Fukuda (1982) and Chun et al. (1996). The correlation of Chun et al. (1996) was originally suggested to have a higher value equal to G_m, 275 kg/m^2·s. As the prediction of the original correlation was excessively high, the value of Gm was modified to 20 kg/m^2·s for comparisons with the experimental results. However, even with the modified G_m, the effect of the pool temperature is not reflected adequately compared to the experimental results. This is mainly because of the power of the driving potential *B* in Chun's correlation-which is the only term which includes temperature information in the equation-is small (0.0405). It was reported that his correlation is more suitable for higher mass flux regions, such as in condensation oscillations and stable condensation regions. Conversely, the correlation of Fukuda (1982) represents the temperature effect suitably, and can also predict rate of change of the heat-transfer coefficient to the steam mass flux. The deviation of the absolute value of the heat-transfer coefficient from Fukuda's correlation from the experimental results can be explained by the difference of the orientation of the nozzle in Fukuda's experiment (vertically downward) and the present study (vertically upward). The same experimental results showing the variations of the heat-transfer coefficient to the pool temperature at various mass flux conditions are shown in Fig. 3.25.

The effect of the pool temperature on the decreased rate of change of the heat-transfer coefficient for different steam mass flow rates is also observed here. The heat-transfer coefficient tends to decrease when the pool temperature is increased. Higher steam mass flow rate resulted in higher heat-transfer coefficients. As the pool temperature approaches the saturation temperature of water, the heat-transfer coefficients are expected to decrease given the decreased condensation.

3.4.3.3 Bubbling frequency concept

Before steam enters into the water, it can be treated as a steady, single-phase, and fully developed channel flow. After it reaches the tip of the nozzle, the flow turns immediately into an unsteady, two-phase flow, owing to the formation of the gas-liquid interface. In other words, the tip of the nozzle can be considered as the optimal location to analyze the behavior of the transient

response of the transition from the steady flow into the unsteady flow. In order to investigate the transient at the nozzle, a fixed interrogation window was set for the sequential bubble images, and the extracted images were synthesized in a timely manner. Figs. 3.26 and 3.27 show examples of the image synthesizing process.

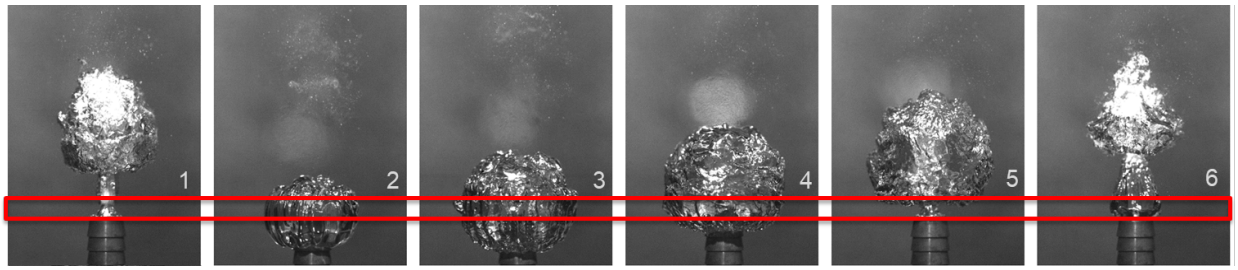

Figure 3.26: Interrogation window for sequential image extractions (red boxed area) at the tip of the nozzle

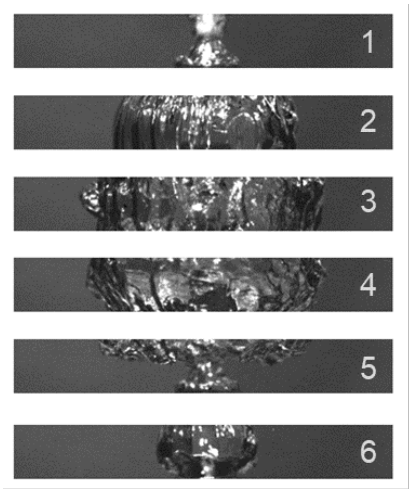

Figure 3.27: An example of image synthesis from the extracted images of Fig. 11

As shown in Fig. 3.27, each extracted image segment represents a time step in the synthesized image. In order to guarantee the continuity of the gas-liquid interface on the synthesized image,

the height of the fixed interrogation window was decided to be as small as three pixels. The extraction for the actual analysis was performed for all photos at every time step obtained by the high-speed camera to generate a single synthesized image. As mentioned in the experimental methods section, the frame rate of the high-speed camera was set to 1000 fps, which means that 1000 extracted images were synthesized into a single photo to obtain the transient response of the gas-liquid interface at the tip of the nozzle during a period of 1 s. Figure 3.28 shows the sample of the synthesized image and its description for G_o = 7.14 kg/m^2·s ($\dot{m}_g = 0.51$g/s) for the case at which the pool temperature was 86°C.

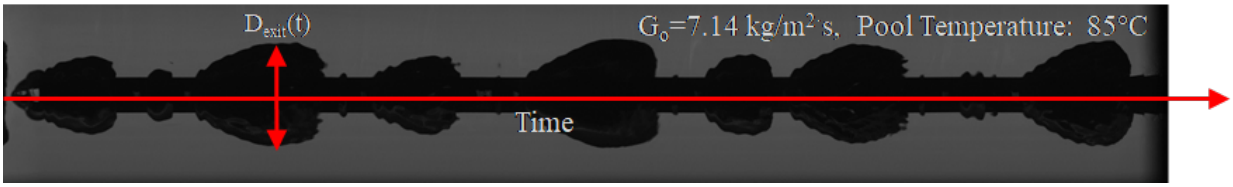

Figure 3.28: Sample of the synthesized image and its description

As shown in Fig. 3.28, the exit diameter of the steam flow is represented as a function of time and presents a certain periodic behavior. Figures 3.29, 3.30, and 3.31, display the synthesized images corresponding to Figs. 3.21, 3.22, and 3.23.

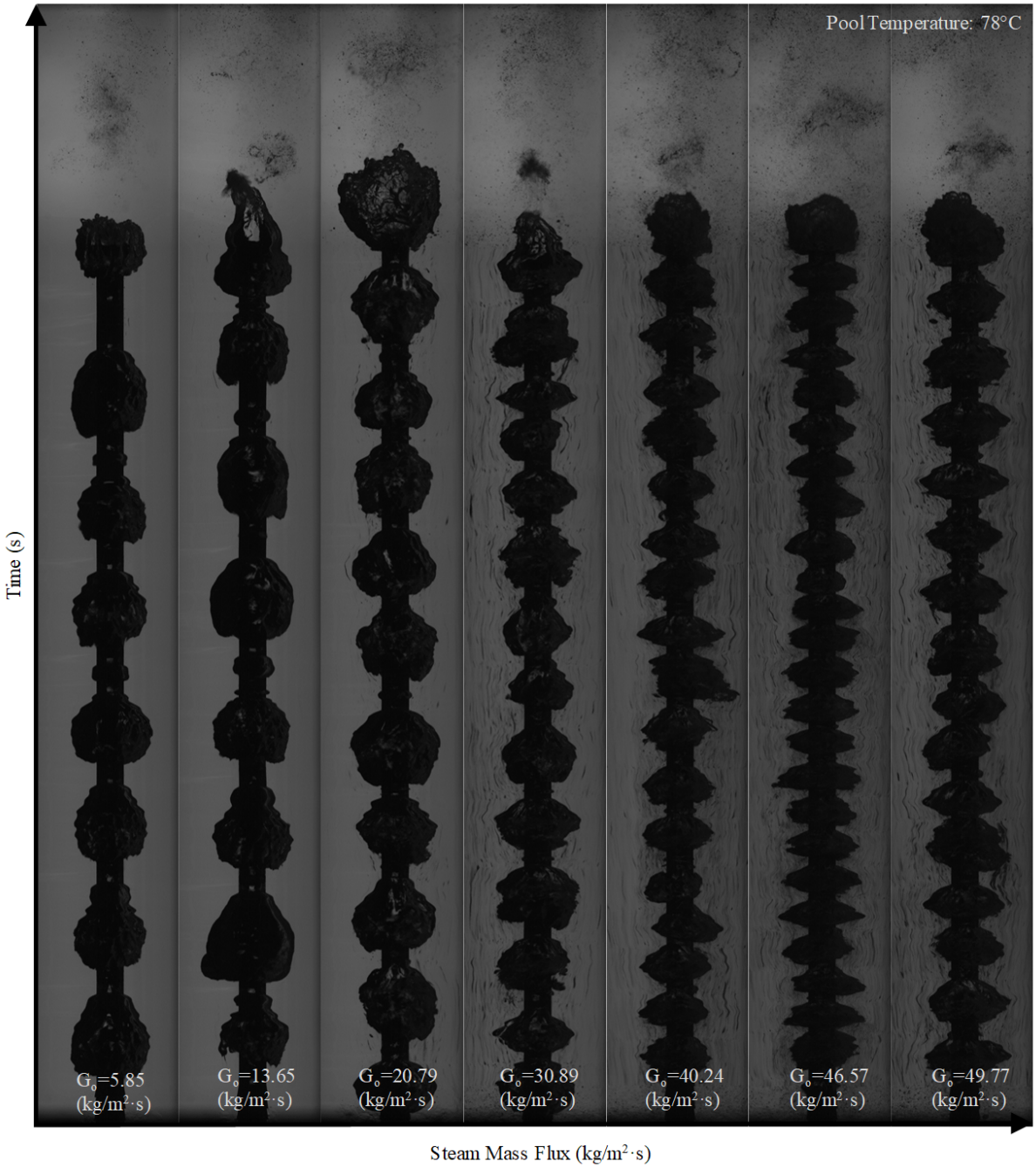

Figure 3.29: Synthesized images for the bubbling frequency at a pool temperature of 78°C

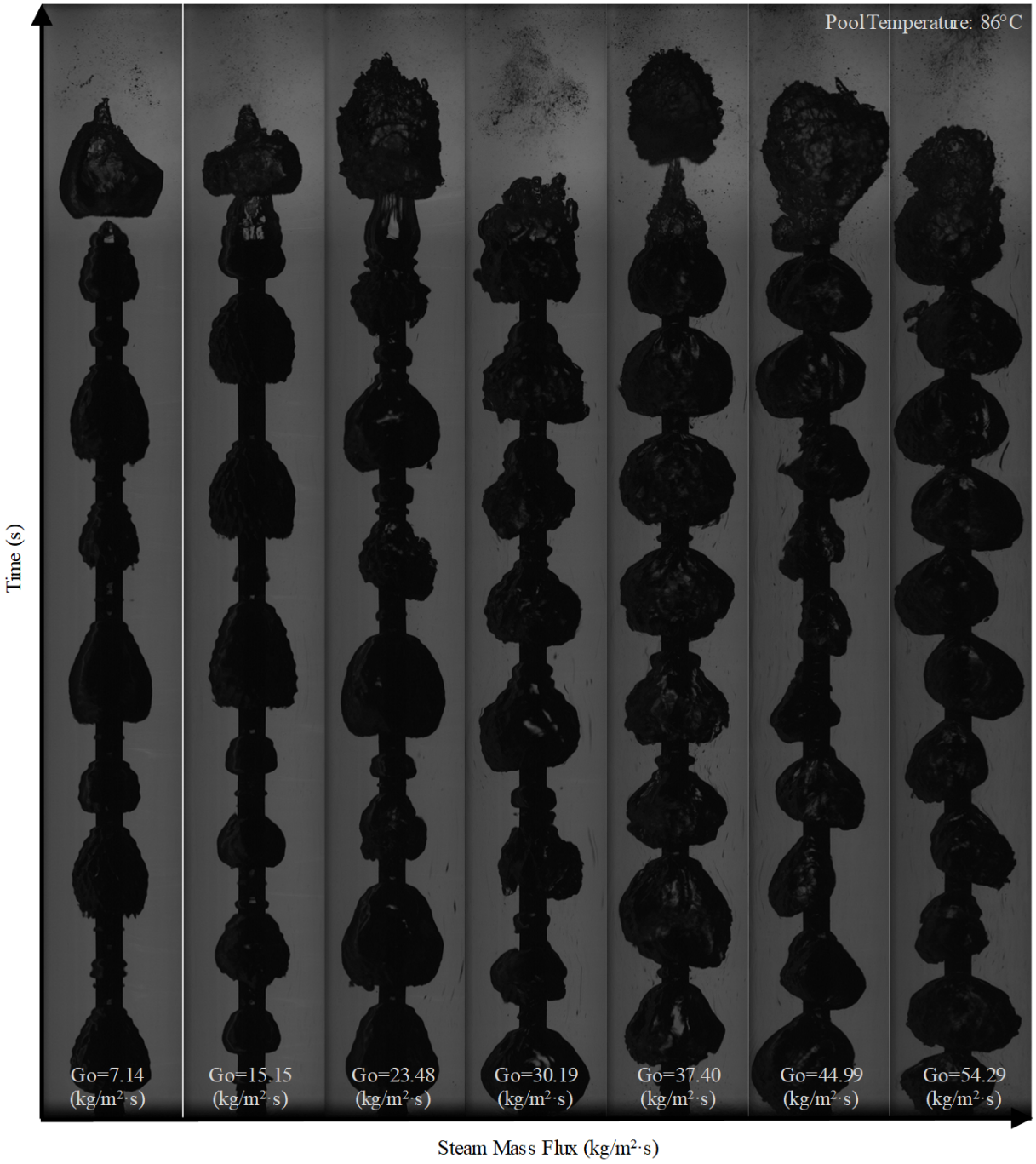

Figure 3.30: Synthesized images for the bubbling frequency at a pool temperature of 86°C

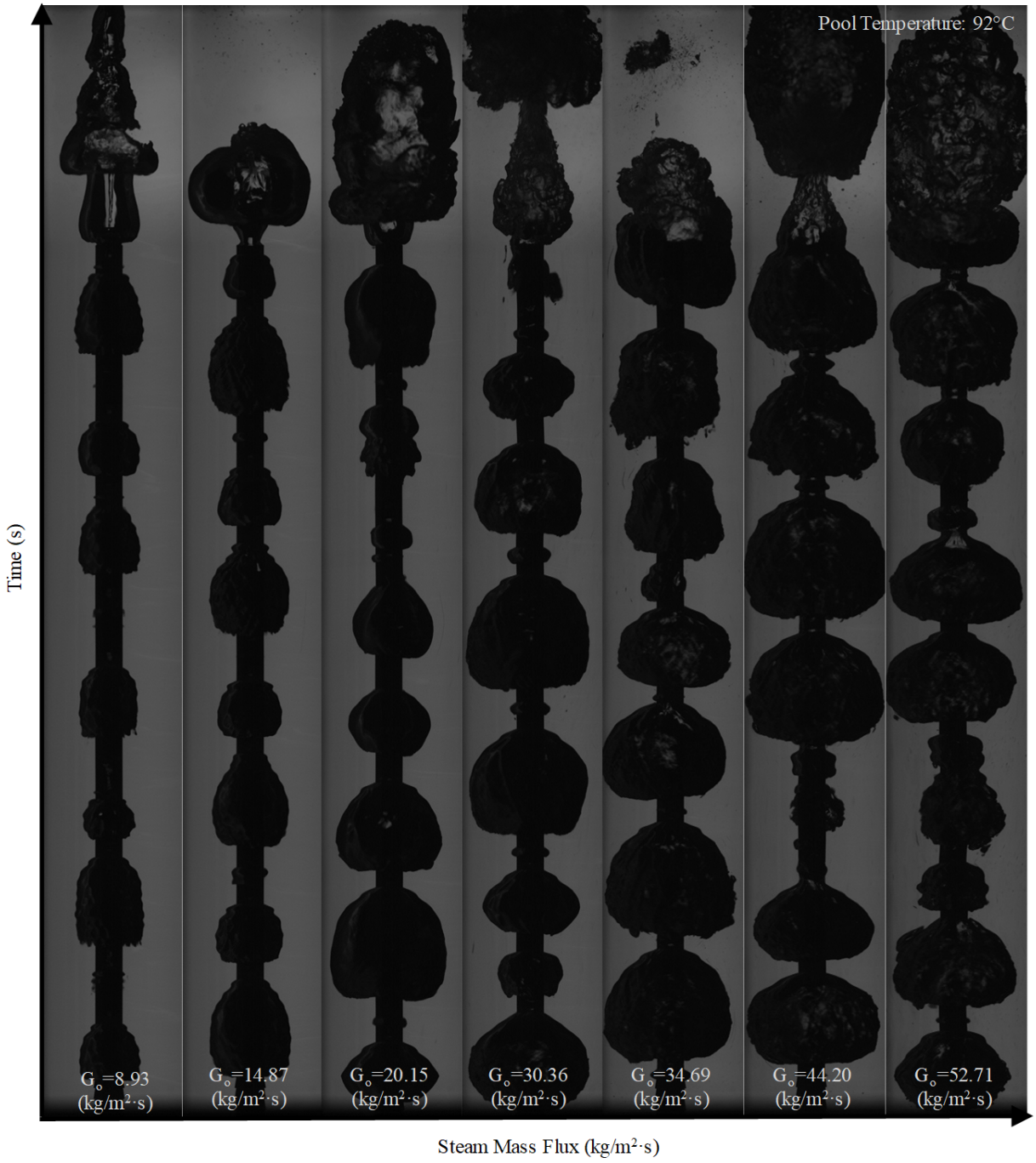

Figure 3.31: Synthesized images for the bubbling frequency at a pool temperature of 92°C

The edge detection algorithm was applied to the images to obtain the steam exit diameter as a function of time. Moreover, frequency analysis was applied to the function $D_{exit}(t)$ shown in Fig.

3.28 to obtain the characteristic dominant frequency of the exit diameter in the synthesized images, which was defined as the bubbling frequency in this study. As it is also possible to calculate another bubble characteristic frequency from the inverse of the average period determined from the bubble sequential images shown in Figs. 3.22, 3.23, and 3.24, the frequency was defined as the condensing frequency ($f_{cond} = 1/\langle\tau_{cond}\rangle$). Figure 3.32 depicts the relationship of the condensing frequency and the bubbling frequency.

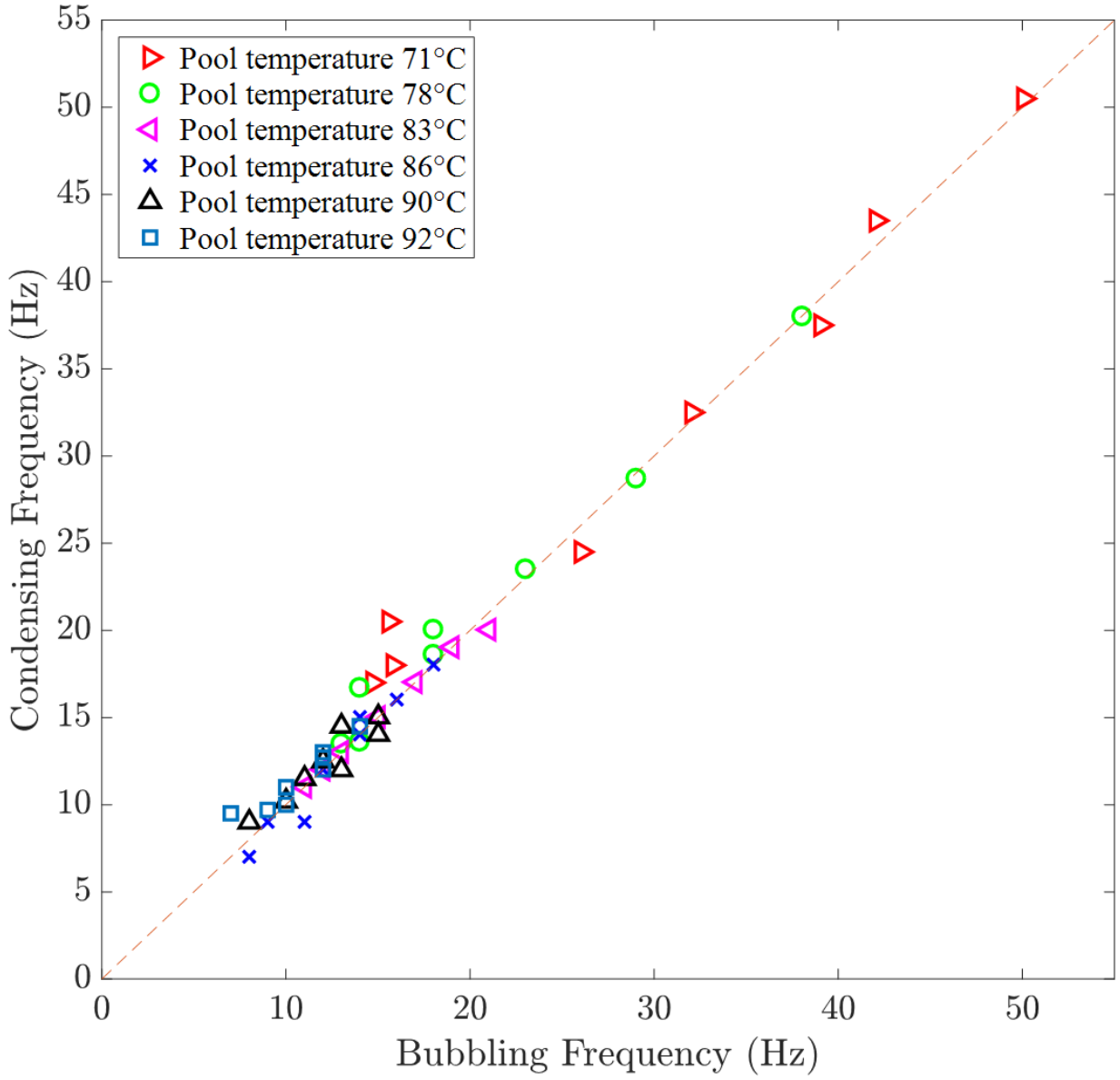

Figure 3.32: Relationship of the condensing frequency and the bubbling frequency

As presented in Fig. 3.32, the condensing frequency and the bubbling frequency were in good agreement with each other. Figure 3.33 depicts the relationships of the bubbling frequency regarding the steam mass flux and pool temperature.

As observed in Fig. 3.33, the bubbling frequency can be determined from the boundary condition of the experiments as a function of pool temperature and steam mass flux. Additionally, it is obvious that the bubbling frequency is a function of the specific and latent heats of water. The bubbling frequency increases as the higher steam mass flux is injected through the nozzle. The higher bubbling frequency was observed in the case of low-pool temperatures, and a decreasing tendency was noted as the pool temperature increased. This tendency was more evident in higher mass flux regions than lower mass flux regions. From the observations, we have modeled the bubbling frequency as a function of boundary conditions, including the fluid properties as,

$$f_b\left(G_o, \Delta T\right) = 142.9\left[\mathrm{Bo}\cdot \mathrm{Ja}^2 \frac{G_o}{\rho_f d}\right] + 7.642 \tag{3.7}$$

where Bo is Bond's number that represents the ratio between the gravitational and the surface tension forces defined as,

$$\mathrm{Bo} = \frac{\Delta \rho g d^2}{\sigma} \tag{3.8}$$

and Ja is Jakob's number that represents the ratio of sensible heat to latent heat released during the condensation process defined as,

$$\mathrm{Ja} = \frac{c_{p,f}\Delta T}{i_{fg}} \tag{3.9}$$

Figure 3.34 shows the experimental results and the correlation described by Eq. 3.7.

Figure 3.35 represents the comparison of the bubbling frequency with the experimental results and the prediction from the suggested correlation.

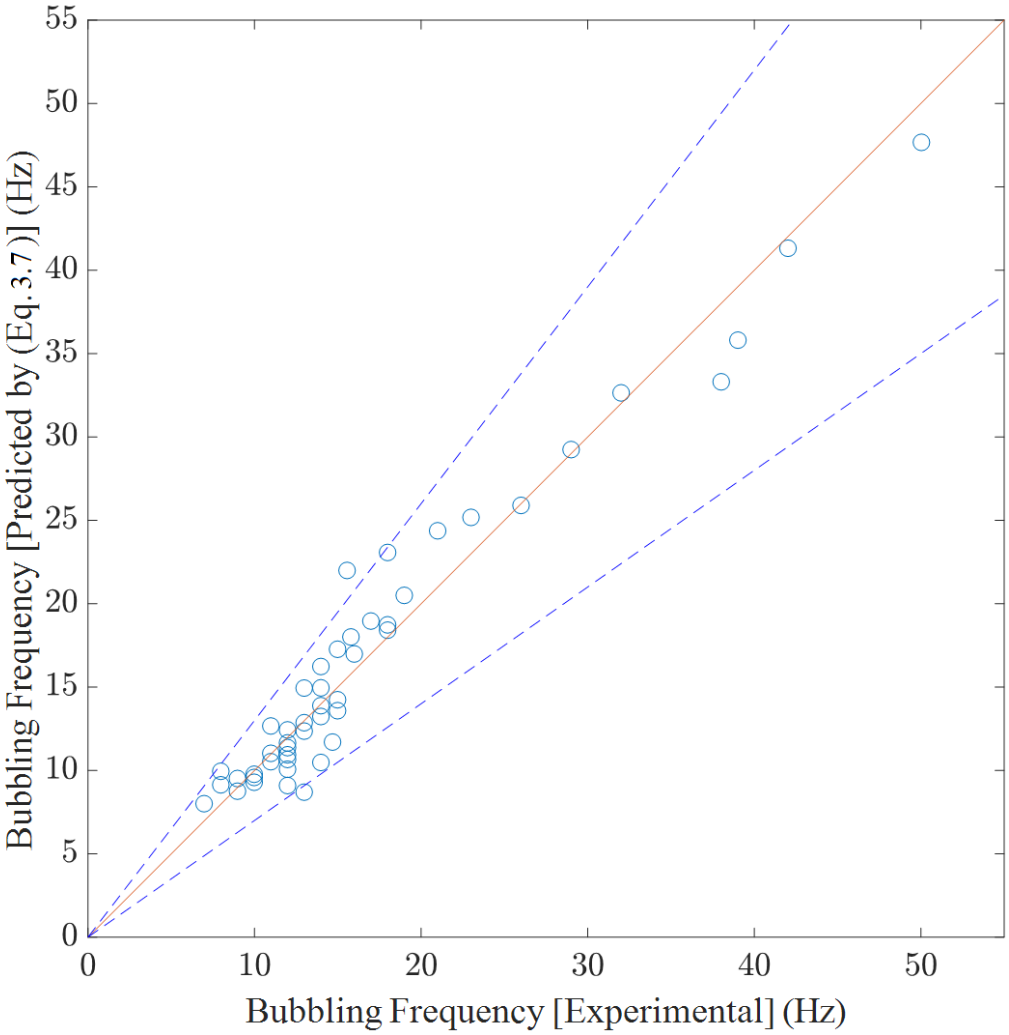

Figure 3.35: Comparison of the bubbling frequency between the experimental and the predicted results (dashed line shows $\pm 30\%$ bounds)

As shown in Fig. 3.35, the predictions suggested from the present correlation formulated by Eq. 3.7 is within the $\pm 30\%$ bounds. From the attained condensing frequency and the bubbling frequency, a hydrodynamics approach was applied based on this study to investigate the relationships between hydraulic and thermal characteristics of the unstable direct contact condensation. Such strategies have been extensively adapted in the field of nucleate pool boiling that was initiated by prominent researchers, including Zuber (1959), Cole (1960), and Ivey (1967). From the bubble dynamics point-of-view, the nucleate boiling regime of the pool boiling and the unstable bubbling

regime of the direct contact condensation of steam in subcooled water can be treated as similar phenomena after the bubble departure from the heating surface or the injection nozzle. An interesting similarity of these two cases is the fact that continuous sources resulted in discontinuous bubble departures. In nucleate boiling, the continuous heat flux on the heating surface is controlling the bubble dynamics, such as the bubble growth rate and the detachment frequency from the heating surface. In the condensation case, the continuous steam mass flux upstream of the injection nozzle resulted in the bubble dynamics of the unstable condensation regime. Thus, the validity of the correlations for the bubble dynamics of nucleate boiling suggested by Zuber (1959), Cole (1960), and Ivey (1967), was evaluated with the present experimental results for the case of unstable, direct contact condensation. In 1959, Zuber suggested a correlation that can explain the bubble dynamics of the nucleate boiling as follows

$$fD_b = 0.59\left(\frac{\sigma g \Delta\rho}{\rho_f^2}\right)^{0.25} \approx 0.5U_b \tag{3.10}$$

where f is the nucleate bubble departure frequency, D_b is the bubble's departure diameter, σ is the surface tension, g is the gravitational acceleration, $\Delta\rho$ is the density difference of the gas and the liquid, U_b is the bubble growth velocity, and ρ_f is the liquid density. Cole (1960) suggested a similar relationship according to,

$$fD_b^{0.5} = 0.59\left(\frac{4}{3}\frac{g\Delta\rho}{\rho_f}\right)^{0.5} \approx \frac{U_b}{D_b^{0.5}} \tag{3.11}$$

Finally, Ivey (1967) proposed three correlations for different regions formulated as,

$$fD_b = \begin{cases} 0.90(gD_b)^{0.5}, \text{ Hydrodynamic region} \\ 0.44g^{0.5}D_b^{0.5} \times (\text{cm}^{0.25}), \text{ Transition region} \\ \text{constant}(\text{cm}^2/\text{s}) \times D_b^{-1}, \text{ Thermodynamic region} \end{cases} \tag{3.12}$$

In this study, the correlation of the hydrodynamic region was employed. Figure 3.36 shows the plots of the bubbling frequency as a function of the averaged detached-bubble equivalent diameter,

which were obtained from the image processing of the raw data of Fig. 3.21,3.22 and 3.23.

In Figure 3.36, the experimental results for condensation and the predictions of the former studies that were suggested for the pool boiling condition are plotted for different temperature and mass flow rates, respectively. The predictions of the models of Ivey (1967) and Cole (1960) provided reasonable agreements with the experimental data for the lower mass flux region. Even though the hydrodynamic models of the bubble's departure frequency and diameter were developed for the boiling phenomena, the results imply that they can be extended to condensation phenomena since they follow similar thermal hydraulic processes. Additionally, it is possible to propose a different condensation regime map concept for unstable condensation because certain segregation trends were observed for the experimental data with the use of the pool temperature and the mass flow rate as the boundary conditions. The main differences between these phenomena are the limiting criteria of the sources of the growing bubbles. In practical applications of nucleate boiling, critical heat flux governs the nominal operating conditions for the stable heat transfer with a controllable heater surface temperature. However, in the condensation case, higher steam mass flux elicits higher heat transfer rates with stable heat transfer characteristics (stable condensation regime) with predictable turbulent jet interfaces and void fractions. The deviation of the experimental results in higher mass flux regions from the previous correlations may be owing to the difference of the driving force of bubble departure. Unlike nucleate coiling, the momentum generated by the inertia of the steam mass flux should account for bubble dynamics other than the surface tension and the buoyancy force in the condensation case. In other words, the hydrodynamic characteristics of unstable, direct contact condensation can be modeled by the balance of inertia, surface tension, and the buoyancy forces. As shown in Fig. 3.36, an increment of the steam mass flux at different pool temperatures can be interpreted from two different perspectives. In the lower pool temperature region, it seems that the increment of the steam mass flux resulted in higher bubble departure frequencies, while the increment in higher pool temperature yielded a larger bubble departure diameter. These trends were also reported by Zuber (1964) in nucleate boiling research as the laminar bubble departure (isolated bubble) and turbulent bubble departure (interfering bubbles)

regimes of single nucleation sites. In the laminar bubble departure regime, the vapor flow rate was low and bubble tended to rise at constant speed. The two entities did not interfere with each other. The bubble's departure frequency increased with the vapor flow rate. In the turbulent bubble departure regime where the vapor flow rate was intermediate, the bubble's departure diameter tended to increase at higher vapor flow rates, while the bubble's departure frequency remained constant. Detached bubbles interacted with each other and created irregularities in the bubble shapes.

3.4.3.4 Heat transfer coefficient modeling

In reference to the experimental results, the average heat-transfer coefficient for the unstable direct contact condensation is modeled by the united factor of the bubbling frequency, as follows:

$$\overline{h} = 7.092 \left[\frac{\text{kW·s}}{\text{m}^2\text{·K}}\right] f_b - 13.9 \left[\frac{\text{kW}}{\text{m}^2\text{·K}}\right] \tag{3.13}$$

The relationship described in Eq. 3.13 is very intuitive, which presents the faster bubbling would result in transferring more heat. In the right hand side of Eq. 3.13, specific units are multiplied to match the dimensions to those of the heat-transfer coefficient. Since $U_{b,avg}/D_{eq,avg} \propto f$, it is also possible to model the heat-transfer coefficient as,

$$\overline{h} = 4 \left[\frac{\text{kW·s}}{\text{m}^2\text{·K}}\right] \frac{U_{b,avg}}{D_{eq,avg}} + 20 \left[\frac{\text{kW}}{\text{m}^2\text{·K}}\right] \tag{3.14}$$

where $U_{b,avg}$ is the average of detached bubble centroid velocity, and $D_{eq,avg}$ is the averaged detached-bubble equivalent diameter which were obtained from the image processing of the raw data of Fig. 3.21, 3.22 and 3.23. Equating Eqs. 3.13 and 3.14 yields,

$$f_b = 0.5638 \frac{U_{b,avg}}{D_{eq,avg}} + 4.78 \left[\frac{1}{\text{s}}\right] \tag{3.15}$$

Equation 3.15 may provide useful information for condensation closure model development for CFD in combination with Eq. 3.7. Figure 3.37 represents the heat-transfer coefficient as a function of the bubbling frequency and the bubble rising speed divided by equivalent bubble departure

diameter.

As shown in Fig. 3.37, the suggested correlation (Eq. 3.13 for the bubbling frequency and Eq. 3.14 for $U_{b,avg}/D_{eq,avg}$) showed good agreement with the experimental data of the heat-transfer coefficient throughout the experiments. Figure 3.38 represents the comparison of the heat-transfer coefficient with the experimental results and the prediction from the suggested correlations.

As shown in Fig. 3.38, the predictions suggested from the present correlations formulated by Eqs. 3.13 and 3.14 are generally within the $\pm 30\%$ bounds. Further research is required to investigate the overprediction of the heat-transfer coefficient in the range of 30 and 60 kW/m^2·K, and to explain the physical meaning of the coefficients of the suggested correlations formulated in Eqs. 3.13 and 3.14.

3.5 Tempearture Field Measurement: Development of Backlight Aided Planar Laser Induced Fluorescence (PLIF) Thermometry for Two Phase Flow

After the discovery of laser-induced fluorescence (LIF) by Tango *et al*. (1968), it has been widely used in various research fields including chemical sciences, medical applications, and studies of fluid flow. Planar laser-induced fluorescence (PLIF) has especially been applied for various studies about thermofluids, such as quantitative concentration field measurements, investigations of eddy/turbulent structures, and temperature field measurements using temperature-sensitive fluorescent dyes. Temperature field measurement using PLIF, which is also known as PLIF thermometry, has an advantage compared to conventional temperature measurements because of its great spatiotemporal resolution and nonintrusiveness.

Conventional temperature measurements such as a thermometer and thermocouples, have temporal resolution limitations on the order of 10 Hz due to the slow conduction characteristics at the contact points. Additionally, it is hard to obtain temperature fields of fluid flows using conventional measurement techniques without distorting the flow since the methods are intrusive to the flow, and the spatial resolution is limited by the number of probes and the contact area. On the other hand, the spatial and temporal resolutions of PLIF thermometry using a high-speed camera could be as high as the camera sensor resolution, along with the optical configuration of the region of interest, and as fast as the fluorescence process, which is on the order of 10^{-7} s.

Due to the abovementioned advantages, many previous studies of temperature field measurements using PLIF thermometry with high-speed cameras can be found for single phase flows. Seritzman *et al*. (1985) conducted a measurement of temperature fields in combustion flows using PLIF. Using nitric oxide as a seed molecule, a two dimensional temporally and spatially resolved temperature field was measured. Sakakibara and Adrian (1997, 1999) introduced a two-color LIF technique which uses the ratio of intensities from two fluorescent dyes, Rhodamine B (RhB) and Rhodamine 110 (Rh 110), as a temperature indicator. A stable, thermally stratified layer of water was successfully measured with the system. Instead of widely used combinations of RhB and Rh 110, Estrada-Pèrez *et al*. (2011) investigated the temperature sensitivity of RhB and

2′,7′-Dichlorofluoresceinfluorescence (2′,7′DCF) combination for two-color, two-dye LIF. They reported that the temperature sensitivity of the combination under a 532 nm laser was found to be better than other studied configurations.

Even though numerous studies on the technique and the applications have been conducted, few studies have applied this technique to measure the temperature field in a gas-liquid two-phase flow, because sudden change of the refractive index at the interface create unpredictable optical distortions which degrade the credibility of the raw data. Estrada-Pèrez *et al*. (2011) conducted simultaneous PLIF and particle tracking velocimetry (PTV) measurements on a flow boiling experiment using the new mixture of two dyes that they suggested. Two-dimensional temperature and velocity fields were measured at the same time and its application to a cavity flow was suggested. More recently, experimental research on the applications of PLIF for temperature measurements of evaporating water droplets have been conducted (Volkov & Strizhak 2018, 2019, Piskunov & Strizhak 2018). By introducing a correction factor to compensate for the change in the dye concentration, the unsteady temperature fields of water droplet were measured. Table **??** summarizes the experimental methods and the temperature ranges of previous LIF thermometry studies.

In this section, a novel method for a PLIF thermometry configuration is suggested to minimize the effects of dark noise and the random reflection effect. This novel technique is to put a backlight behind the test section that serves as a constant photon bias to the camera sensor. Since the sensitivity of the conventional sensor of a high-speed camera is governed by the quantum efficiency, which is a function of the number of photons reaching the sensor, a constant photon bias reduces the noise-to-signal ratio specifically for the dark noise. Furthermore, the random reflection effect at the gas-liquid interface is notably improved with the backlight.

3.5.1 Rhodamine B aqueous solution

An aqueous solution of Rhodamine B was prepared for the PLIF thermometry. One gram of Sigma-Aldrich R6626 Rhodamine-B powder was measured and dissolved into 1 L of deionized (DI) water obtained from a reverse osmosis system with a DI filter. To increase the solubility of the dye 1 mL of isopropyl alcohol was added to the solution. The total dissolved solids (TDS) of

the DI water was less than 6 ppm, and the pH level of the DI water was approximately 7.5. The electric conductivity of the DI water was less than 40 μS/cm. The prepared Rhodamine B aqueous solution was mixed into 191$\pm$1.72 L of water in the test facility. A continuous 532 nm laser was used to excite the fluorescence. Table 3.6 summarizes the measurement devices employed during the Rhodamine B solution preparation.

Table 3.6: Measurement devices employed for Rhodamine B solution preparation

Equipment	**Model number**	**Accuracy**	**Quantities measured**
Scale	Adam AAA250L	$\pm$0.3 mg	Mass of Rhodamine-B
Measuring cylinder	VWR 89000-258 (500 mL)	$\pm$2.6 mL@20°C	1 L of DI water
Electric pipet	Eppendorf Repeater® Xtream (1 mL)	$\pm$0.8%	1 mL of isopropyl alcohol
TDS meter	HM Digital PS-100	$\pm$2%	TDS of DI water
pH meter	Mettler-Toledo SevenCompact S210	$\pm$0.0002	pH of DI water
Conductivity meter	Eutech PCSTestr 35	$\pm$1.99μS	Conductivity of DI water

3.5.2 Backlight aided PLIF thermometry

A detailed experimental configuration of the backlight-aided PLIF thermometry in comparison with the preliminary configuration is shown in Figure 3.39. This configuration includes significant improvement from the preliminary test described in section 3.3.2.

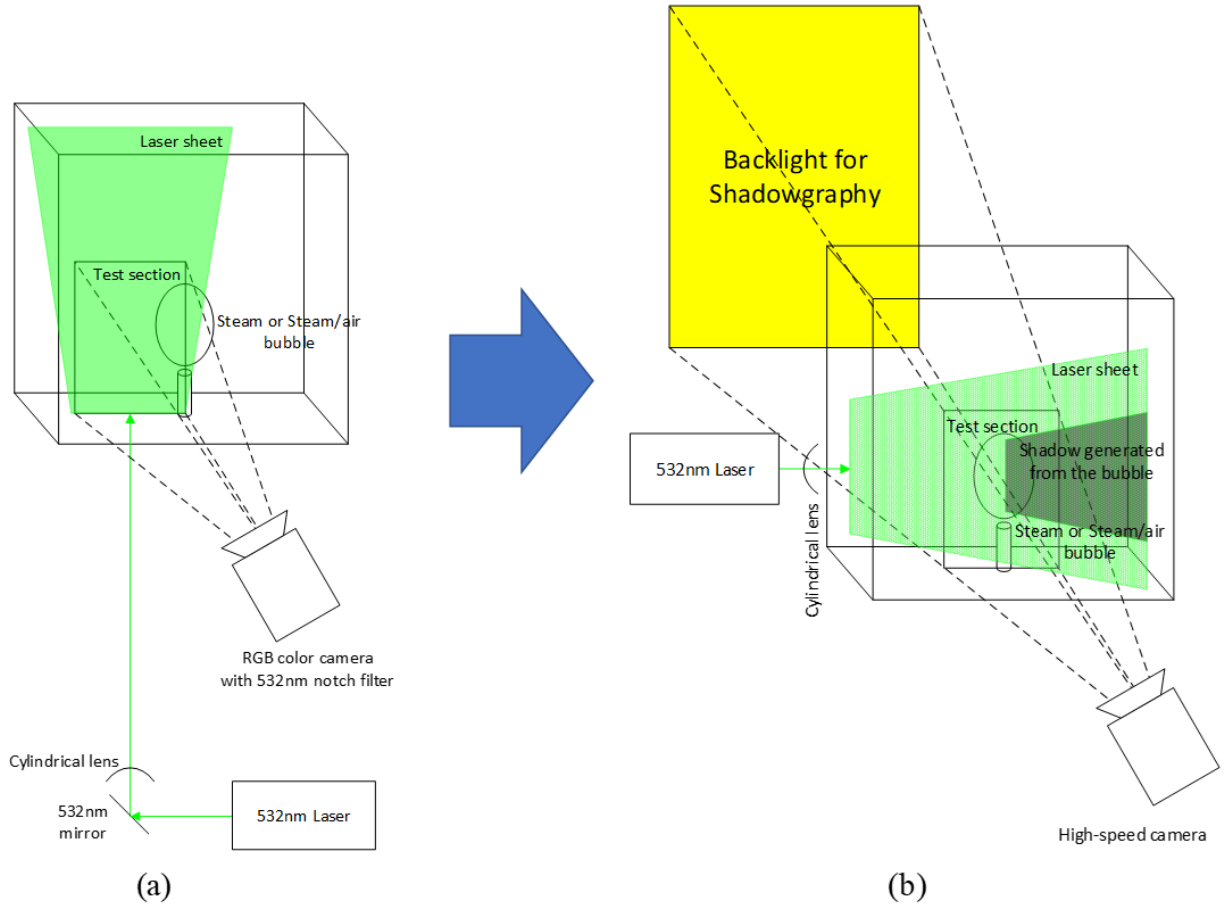

Figure 3.39: LIF Setup: (a) the preliminary setup with the laser shooting from the bottom, (b) the present PLIF thermometry configuration with the laser shooting from the left side and backlight added behind the test section

As shown in Fig. 3.39, the orientation of the laser was configured to be from the left side of the test section, and an LED backlight was added behind the test section. The effect of the backlight will be discussed further.

Figure 3.40 presents the snapshots of the experimental setup.

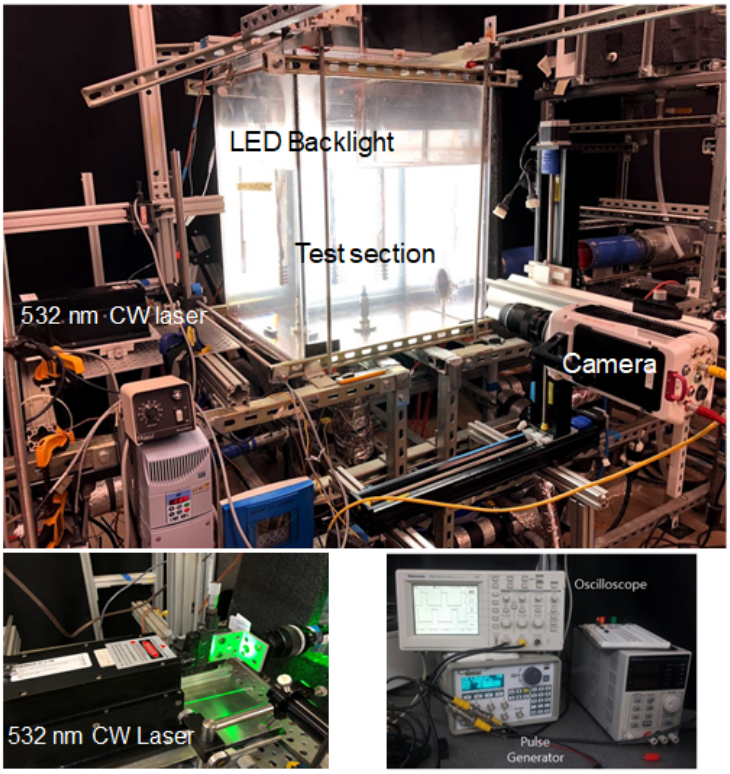

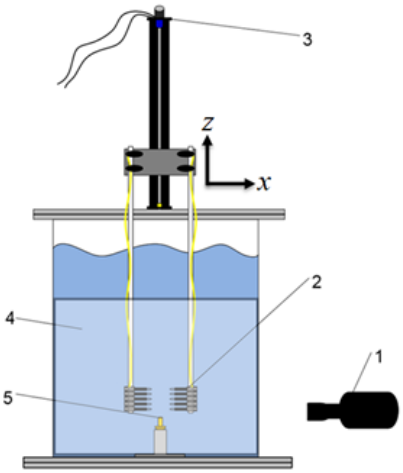

Label	Description	Model/specification
1	High-speed camera	Phantom V711
2	Thermocouples	K-type
3	1-D traverse	VXM step motor
4	LED backlight	PBD-6060
5	Jet nozzle	9.525 mm inner diameter

Figure 3.40: Experimental setup for backlight aided PLIF thermometry

In Figure 3.41, a set of sample images with different visualization configurations (LIF only and backlight-aided LIF, which was named as LIF+Backlight in the figure) are shown and compared.

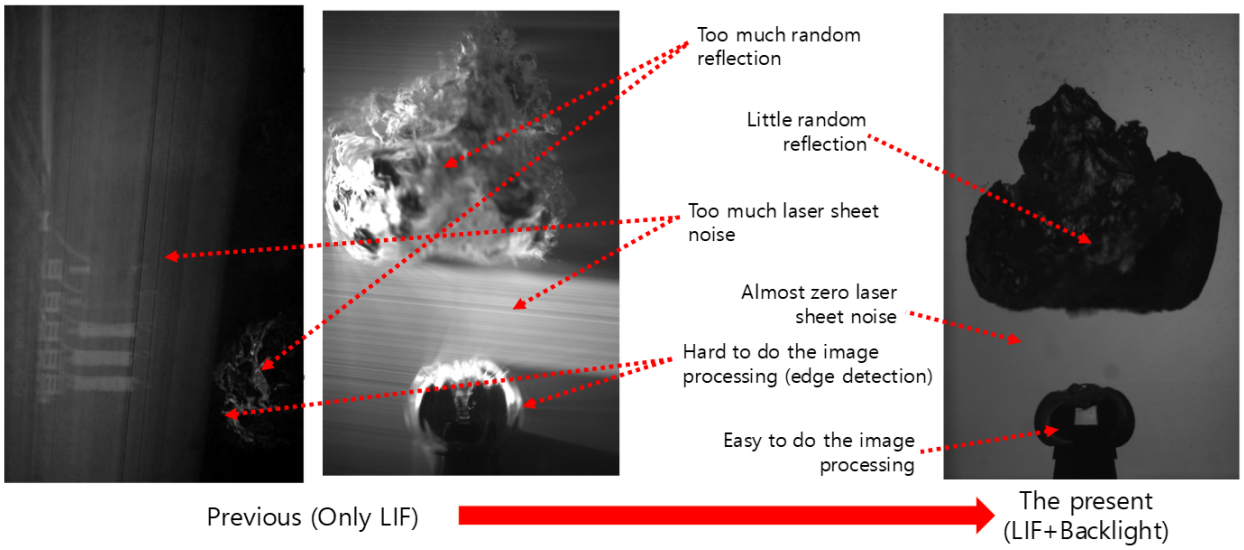

Figure 3.41: Comparison between simple LIF and backlight aided LIF (LIF+Backlight)

In the image of the LIF only case, the difficulty of using LIF with a two-phase flow is well shown. Reflections at the interface of the two phases, noise in the laser sheet and blurred edges of the steam bubbles can all be factors of poor measurement. An LED backlight was applied to overcome this problem as shown in the right side of Fig. 3.39. From the raw image of the rising steam bubble, it is obvious that the problems mentioned above have been noticeably improved.

To verify the effects of the backlight, two independent experiments were designed and conducted. The first experiment was designed to visualize the characteristics of the CMOS type high-speed camera sensor. Figure 3.42 shows the light intensity distribution of the 1000 averaged images captured by the high-speed camera with 1280×960 resolution and 1/2000 s shutter speed for four different configurations.

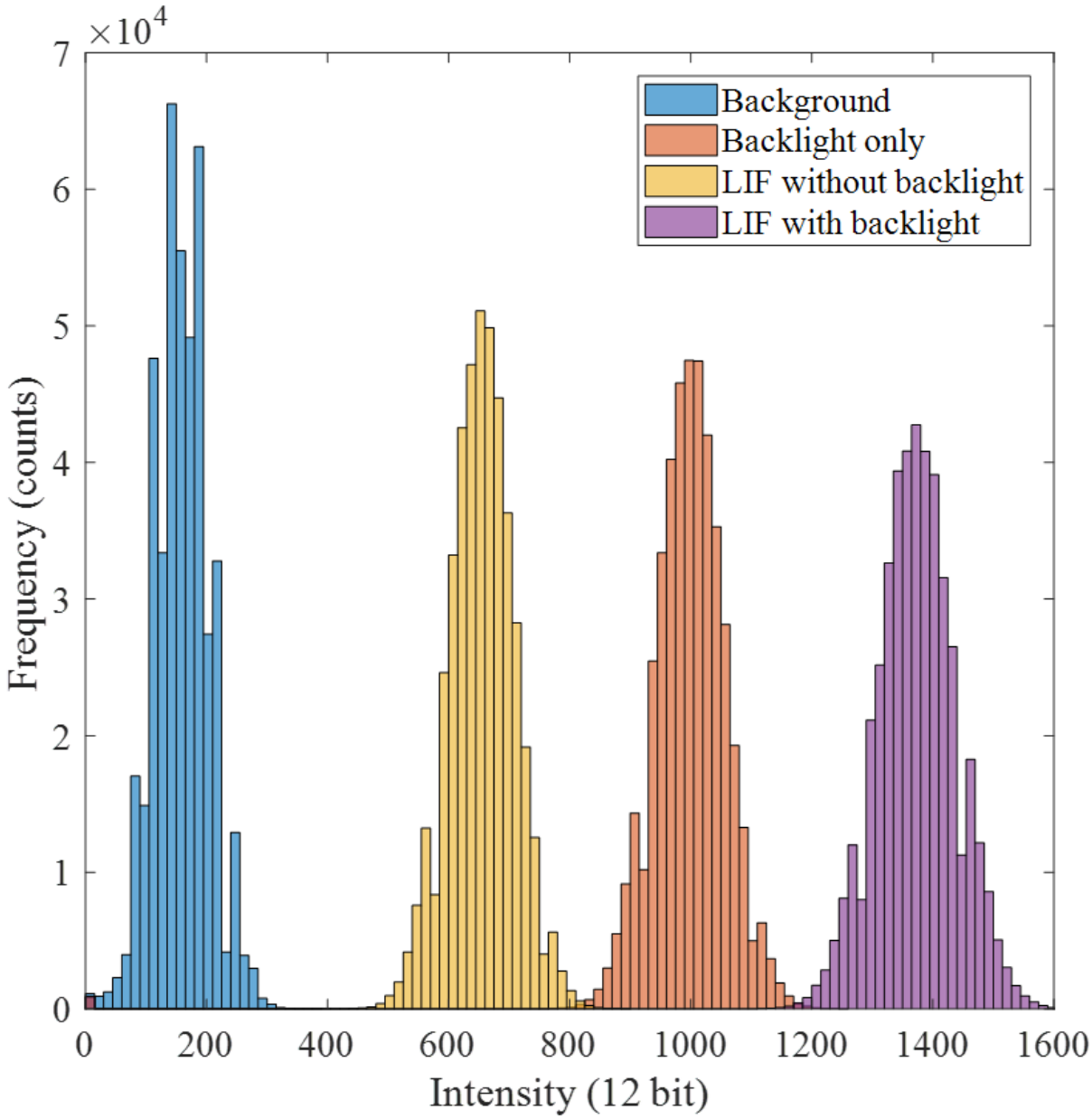

Figure 3.42: Light intensity distributions at the camera sensor for different configurations

In Fig. 3.42, the intensity (x-axis) represents how bright the incoming light is, and the frequency (y-axis) shows how many pixels have that intensity value. As seen in Fig. 3.42, the sensor captures the background noise, even though the image was captured in the laboratory dark room without any artificial light. As expected, the case of LIF with a backlight showed the highest in-

tensity distribution. The backlight only case was found to be brighter than the case of LIF without a backlight, but was dimmer than the case of LIF with a backlight. Since the dark noise effect of the CMOS sensor is reciprocally proportional to the mean intensity captured by the sensor, it is obvious that the configuration of LIF with the backlight would provide the clearest raw image with a low noise-to-signal ratio. It can also be said that as the mean intensity increases, the background noise effect decreases (as in the multi-spectrum scintillation detectors).

The improvements to the dark noise are not the only reason for the enhanced raw image. As shown in Fig. 3.41, random reflection effects around the bubble interfaces were also significantly reduced, which would result in a more accurate temperature calculation in PLIF thermometry. The reason this improvement is obtained by adding a backlight can be recognized by a simple calculation of light intensity under the assumption of light intensity superposition. Figure 3.43 depicts a schematic of the light source configuration during the backlight aided PLIF thermometry.

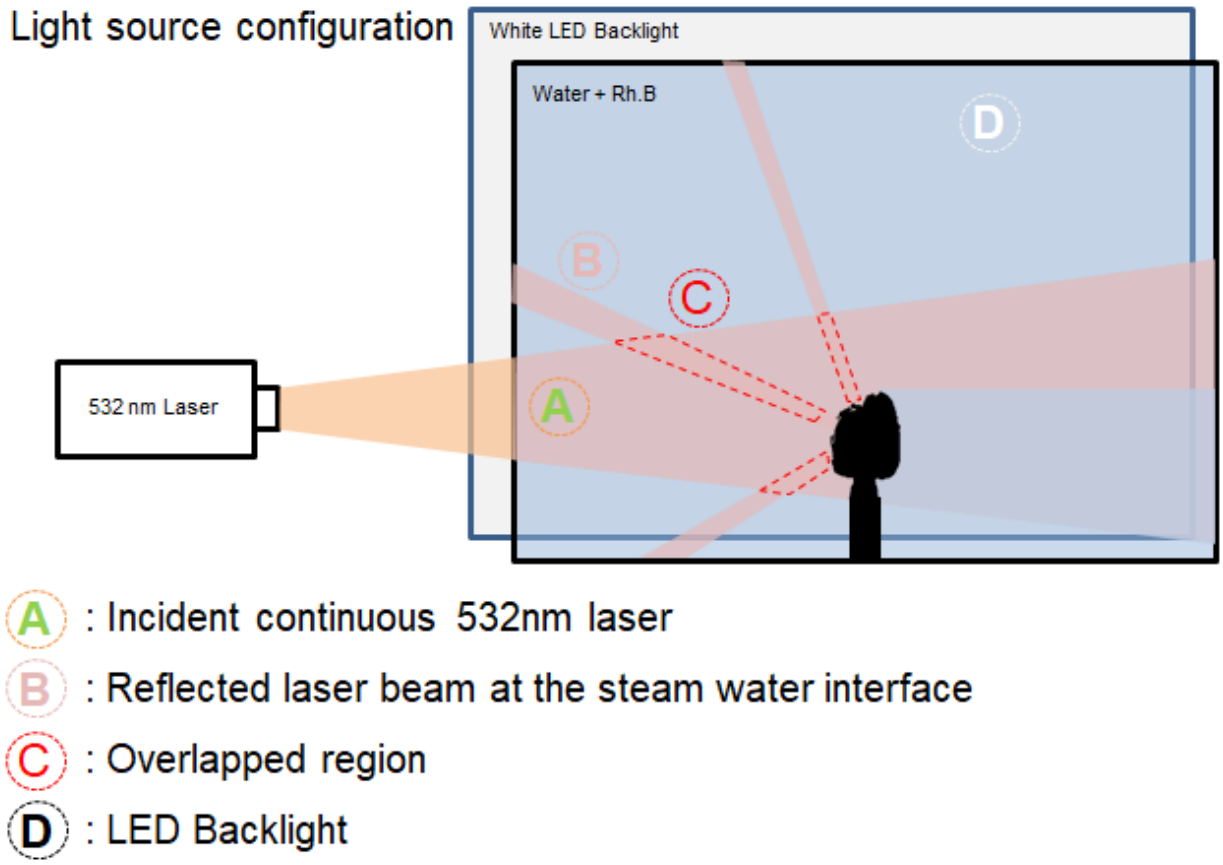

Figure 3.43: Light source configuration during backlight aided PLIF thermometry

As shown in Fig. 3.43, the light captured by the camera can be distinguished in 4 regions by the source of the light and the intensity level. The light source marked as (A) is from the incident laser sheet, (B) is from the reflected laser sheet at the interface of two phases. The overlapped region marked as (C) can be considered as a different light source from (A) and (B) since it has a different intensity level (overlapping of multiple lights results in a higher intensity). Lastly, the light from the LED backlight is marked as (D).

If there is no backlight, the light intensity of the overlapping region (C) can be calculated by adding the intensities of region (A) and (B) under an assumption of linear superposition of light without any photon attenuation. For the simplicity, let us have (A) as the light intensity of region

(A) and so on. Then the equation can be expressed as follows.

$$(C) = (A) + (B) \tag{3.16}$$

If we define the intensity (A') and (B') as the cases with the backlight, then it can be expressed as follows.

$$\begin{aligned} (A') &= (A) + (D) \\ (B') &= (B) + (D) \end{aligned} \tag{3.17}$$

As seen in Eq. 3.17, the intensity in region (A) and (B) increases by the amount of the intensity of the backlight ((D)). However, in the overlapping region, the intensity is not equal to a summation of (A') and (B') as in Eq. 3.16, but is less than the summed value because the direction of the backlight is perpendicular to the reflection surface (the steam-water interface) on the plane. Equation 3.18 describes the light intensity in the overlapping region for the cases with the backlight. (The LED backlight was assumed to be a mono-directional planar beam, and the shadowgraph effect was neglected.)

$$\begin{aligned} (C') &= (A) + (B) + (D) \\ &\neq (A') + (B') = (A) + (B) + (D) + (D) \end{aligned} \tag{3.18}$$

From Eq. 3.18, it can be said that the reflection is suppressed by adding the backlight because the fluorescence light emission is proportional to the incident light. Here, one can notice that if the value of the light intensity (D) increases, the relative reduction of light intensity in the overlapped region can increase.

Since the calculations were made with ideal assumptions, a simplified experiment was designed that can simulate the reflection at the steam-water interface to verify the backlight effect. Figure 3.44 illustrates the experimental setup to simulate the incident light, its reflection, and the overlapping regions.

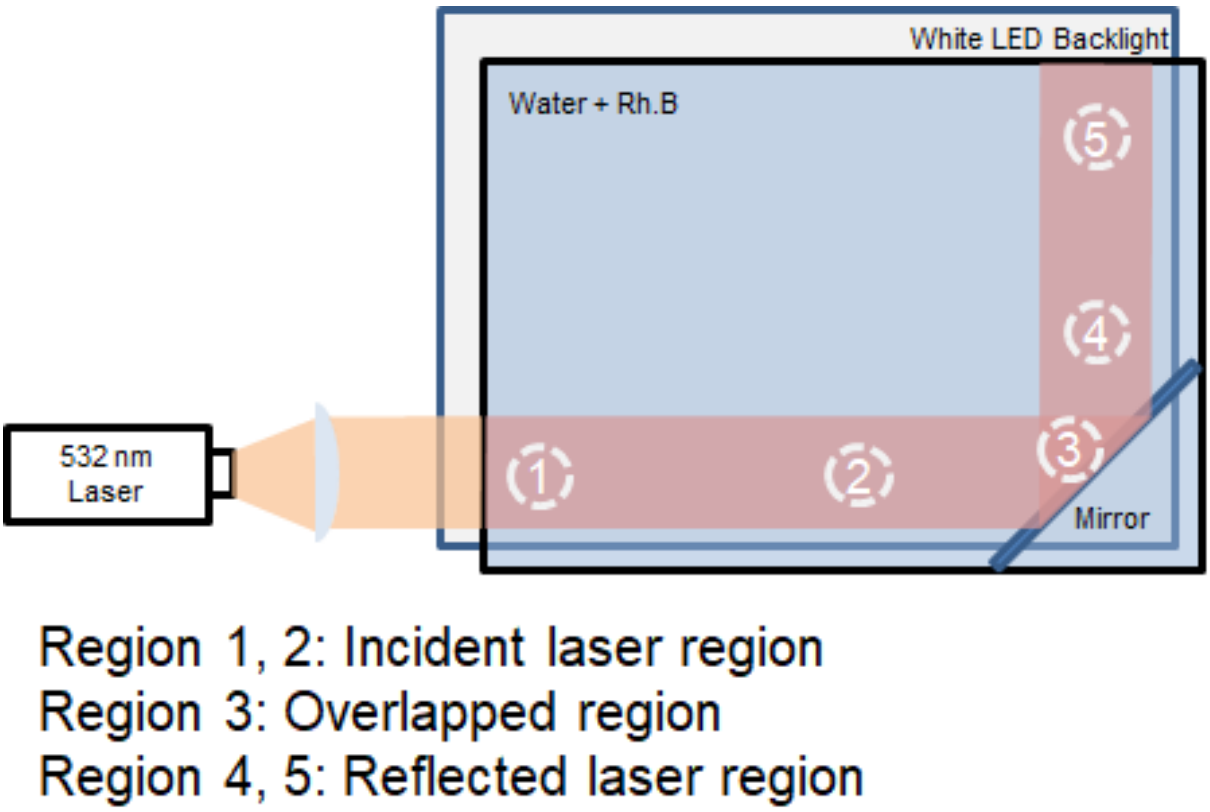

Figure 3.44: Experimental configuration to simulate the effects of reflection at the steam-water interface

This simplified setup allows a realistic analysis of the light spectrum and the intensity of actual LIF using the spectrometer and the high-speed camera. The spectrometer was used to measure the light spectrum and intensity in five regions. Regions 1 and 2 represent the fluorescence from the incident laser, while 4 and 5 represent the fluorescence from the reflected light. Region 3 is the fluorescence from the overlapping region. Figure 3.45 presents a snapshot of the experimental setup and examples of each case.

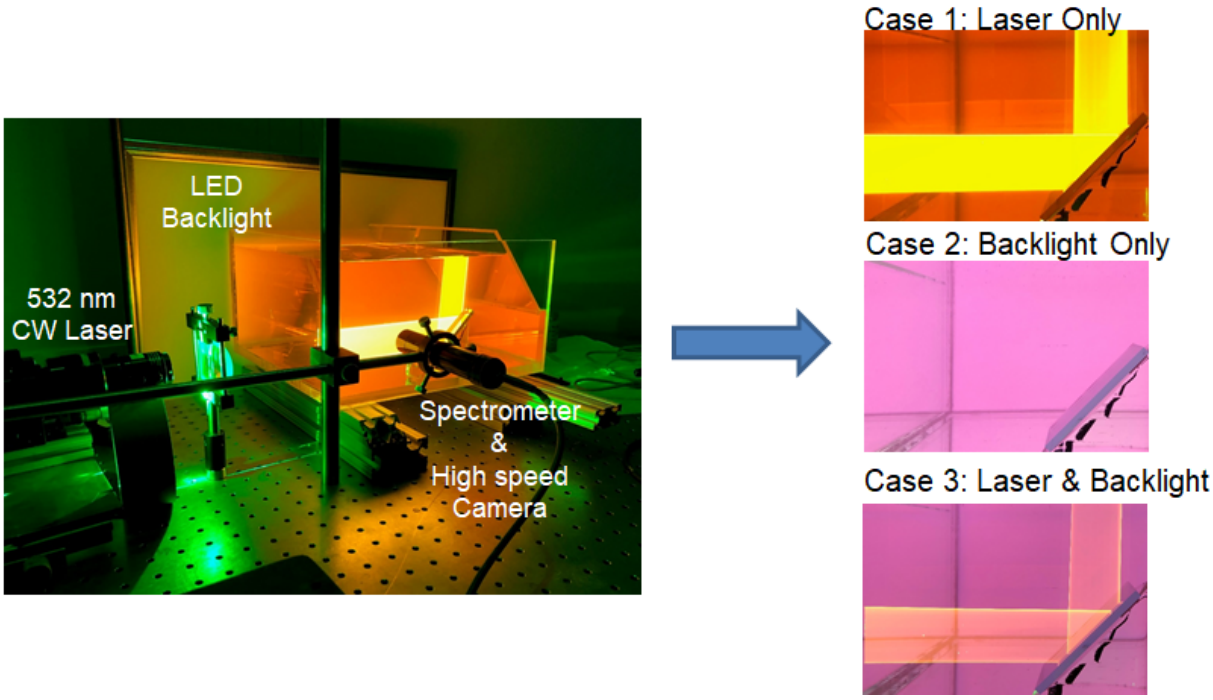

Figure 3.45: Snapshot of the experimental setup and examples of each case

Measurements of the light spectrum in the five regions were conducted for three cases: laser only, backlight only, and laser & backlight. To investigate the suppression of reflections by the backlight, the spectrum of the laser only and backlight only cases were summed up and compared with the laser & backlight case. The results of the measurements are shown in Fig. 3.46.

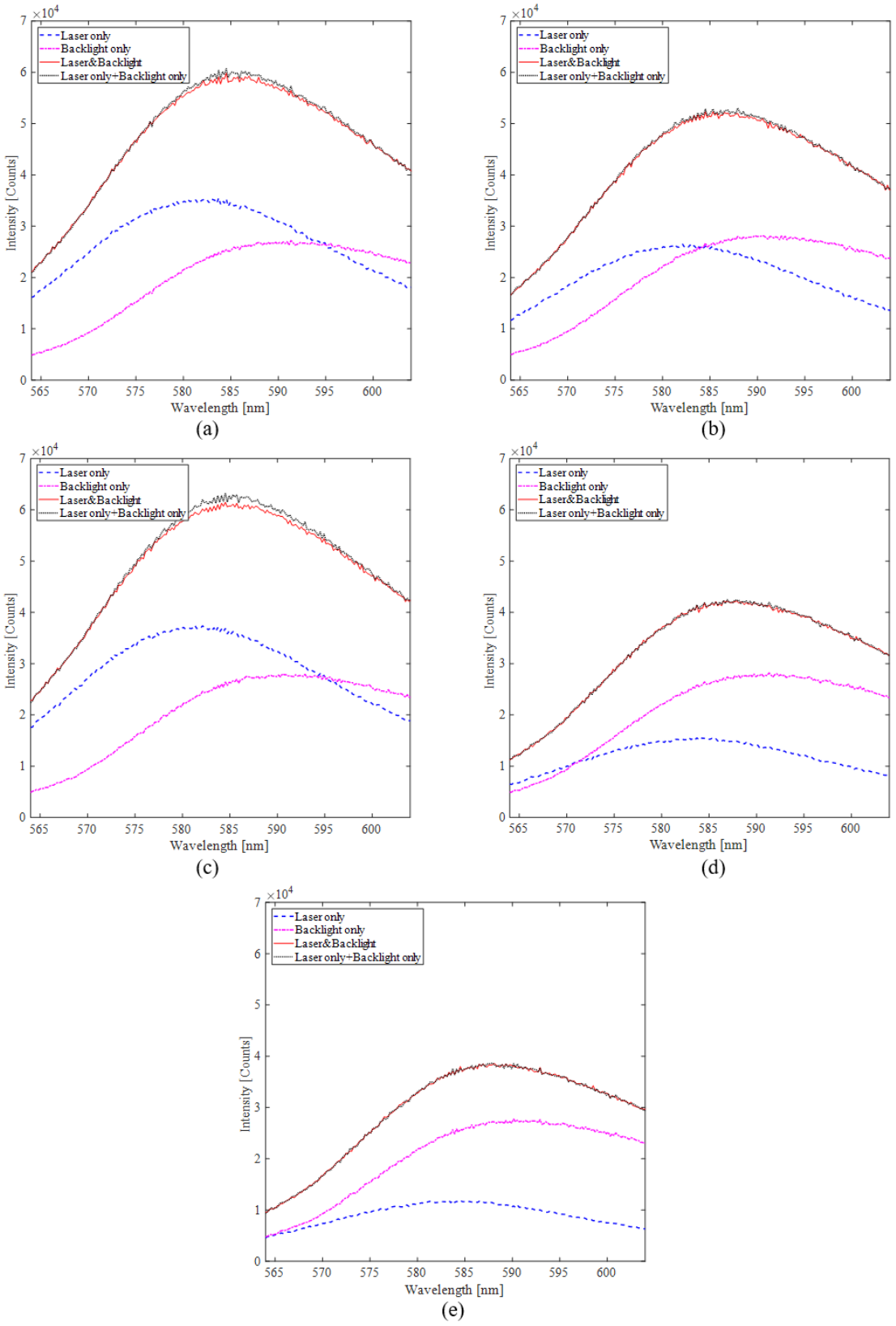

Figure 3.46: Spectrometer data at regions 1, 2, 3, 4, and 5 (a, b, c, d, and e, respectively)

As shown in Fig. 3.46, gaps between the spectra of the simultaneous laser and backlight case (laser&backlight) and the sum of the laser only and backlight only cases were observed especially in Fig. 3.46 (a) and Fig. 3.46 (c). To quantify and compare the gaps from each region an integration of spectrometer measurement counts was calculated, as shown in Fig. 3.47, from a wavelength of 564 nm to 604 nm, which is the same wavelength-interval that the bandpass filter used in the actual PLIF thermometry experiment.

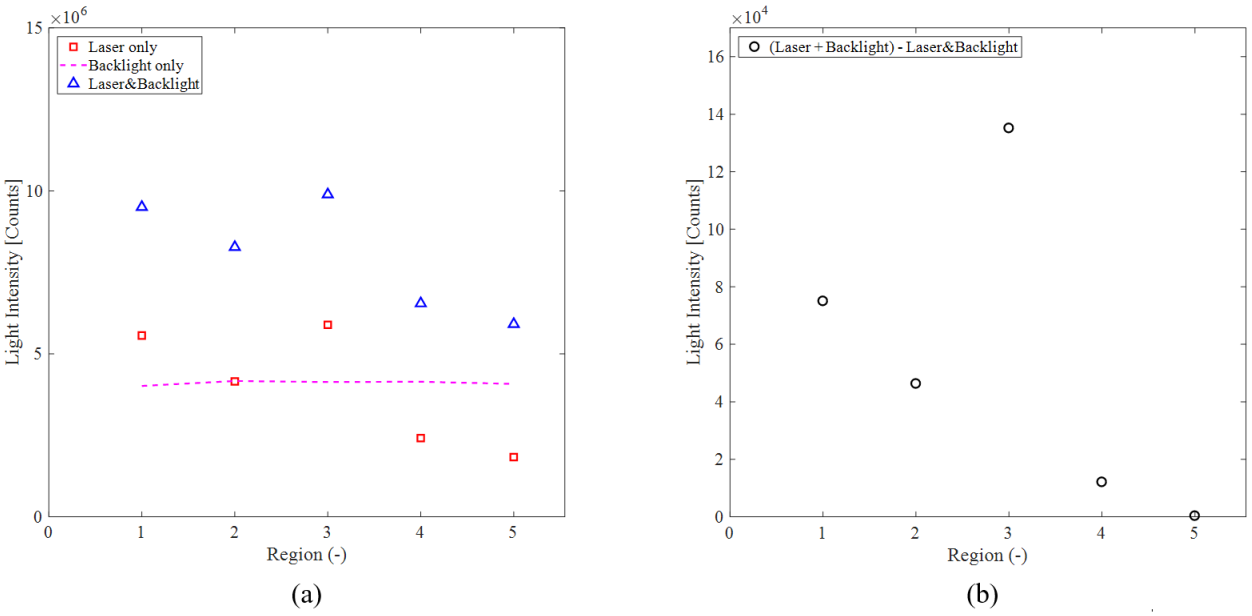

Figure 3.47: Spectrometer data comparison: (a) raw spectrometer data and (b) processed spectrometer data compared by region

As seen in Fig. 3.47 (a), the light intensity decreases when the light goes from region 1 to 5 for the laser only case, except in the overlapping region (region 3). However, the backlight only case maintains almost a constant intensity throughout the region. The decreasing of intensity in the laser only case can be explained by the incident light attenuation due to the fluorescence reaction, because the incident light of the laser only case was coming from region 1 to 5. On the other hand, the direction of the backlight is perpendicular to the direction of the incident light from the laser only case and coincident to the direction of the sensor, thus no decreases can be detected.

Meanwhile, the peak found in region 3 shown in Fig. 3.47 (b) proves the reflection suppression effect is due to the backlight, because the value represents a calculation of the superposition of the laser only and backlight only cases, minus the simultaneous laser and backlight intensities.

By combining the background noise reductions on the high-speed camera sensor and the reflection suppression effects by adding LED backlight, it was proven that backlight aided PLIF thermometry can provide better quality raw images using a high-speed camera with CMOS sensor, which results in a better resolution in temperature measurements.

3.5.3 High-speed camera sensor specific calibration

A high-speed, camera sensor specific, in situ calibration was conducted for an intensity–temperature correlation. The region of interest was segmented with the intensity averaging area of 4×4 pixels, and linear calibration curves were calculated for each area (a total of 68,800 calibration curves within the region of interest). The 4×4 averaged calibration curves were then applied to each pixel in the area for the temperature calculation. Thus, the temperature calculation result has the full resolution of the high-speed camera. Figure 3.48 shows the high-speed, camera sensor specific, in situ calibration curve for the present LIF experiments. The pixel to length conversion factor was 0.98 mm/pixel (100 pixels = 98 mm).

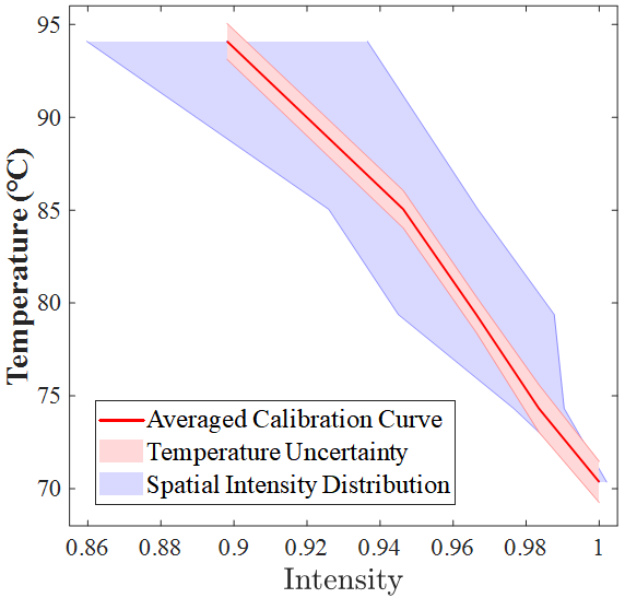

Figure 3.48: Specific in situ calibration curve for the high-speed camera sensor in the present PLIF thermometry

In Fig. 3.48 the red shaded area represents the temperature distribution measured by the ten K-type thermocouples. This area indicates the uncertainty of the reference temperature measurement. The blue shaded area stands for the spatial intensity distribution. The spatial intensity distribution represents the sensitivity of each segmented area caused by the optical intensity decay and the pixelwise high-speed camera sensor's characteristics. This distribution of normalized intensities can be minimized when the amplitude of the intensity is high. For the same reason, the calibration result for the lower temperature cases shows a lower distribution due to the high intensity, which is a characteristic of the Rhodamine B dye. Thus, using an LED backlight can be beneficial because it can reduce the distribution of the intensity field and increase the reliability of measurements. By considering that the blue shaded area shows the uncertainty of the intensity measurement by the camera, it can be noticed that there is a smaller uncertainty for the lower temperature cases, while the uncertainty increases as the temperature increases.

3.5.4 Experimental procedure and conditions

The experimental procedure includes steps to prepare the main components, such as the steam generator, the water tank, and the data acquisition (DAQ) system. The steam generator, at first, is connected to DI water system to fill the DI water for steam. After turning on the steam generator, the steam separator was connected to the main steam line to remove any undesired particles or wet content. The water tank is filled with DI water filtered to a concentration of less than 0.05% impurities and is heated up to a desired pool temperature using immersed heaters. Before starting the test a sufficient amount of steam was ejected into the nozzle in the water tank in order to ensure trapped air was discharged from the piping and to prevent thermal stratification in the water tank. The prepared Rhodamine B aqueous solution was then mixed into the water inside the test facility. All the signals from the measurement devices were connected through the DAQ system and controlled by a LabVIEW program, and the values were recorded on a computer for further analysis. The sampling rate and period for each experiment are 1.0 kHz and 3 s, respectively. The frame rate of the high-speed camera was set to 2000 fps, which was two times faster than the DAQ sampling frequency. During the test the circulation pump and the supplementary heaters for the water and steam were turned off to prevent any mechanical and electrical harmonic noises that could corrupt the raw data. The experimental conditions for the present study are shown in Table 3.7.

Table 3.7: Experimental conditions for PLIF thermometry

Parameter	**Value**	**Accuracy**	**Unit**
Steam temperature	$\sim$103	$\pm$1	°C
Steam inlet pressure	>110	$\pm$0.007	kPa
Nozzle diameter	9.525	$\pm$0.01	mm
Steam mass flow rate	0.6	$\pm$0.09	g/s
Steam mass flux	7.017	$\pm$0.22	kg/m^2·s
Pool temperature	75.44	$\pm$0.06	°C

3.5.5 Results and discussion

A spatially and temporally resolved temperature field was obtained for the unstable, bubbling steam condensation in direct contact with subcooled water using PLIF thermometry. As expected, periodic bubble condensation was observed throughout the experiments. Instantaneous temperature fields for the convective heat transfer during a single bubble's life time (62 ms) in an unstable, bubbling, direct contact steam condensation process are well presented in the series of temperature contour plots shown in Figs. 3.49-3.50.

Distinctive patterns were observed during the condensation process. As shown in Fig. 3.49, detached bubbles from the nozzle collapsed quickly, within 5.5 ms. Again, conventional temperature measurement technique cannot capture this sudden temperature change due to their slow response time. After the condensation of a detached bubble, growing the next bubble takes a relatively longer period of time, approximately 56 ms, as seen in Fig. 3.50, which is almost ten times slower than the condensing period. Some portion of condensed water was not fully mixed with the surrounding cold water and maintained the saturation temperature. This saturated water portion formed a vortex ring started from approximately 30 ms and continued rising downstream due to the buoyancy and forced convection generated by the upstream vapor jet.

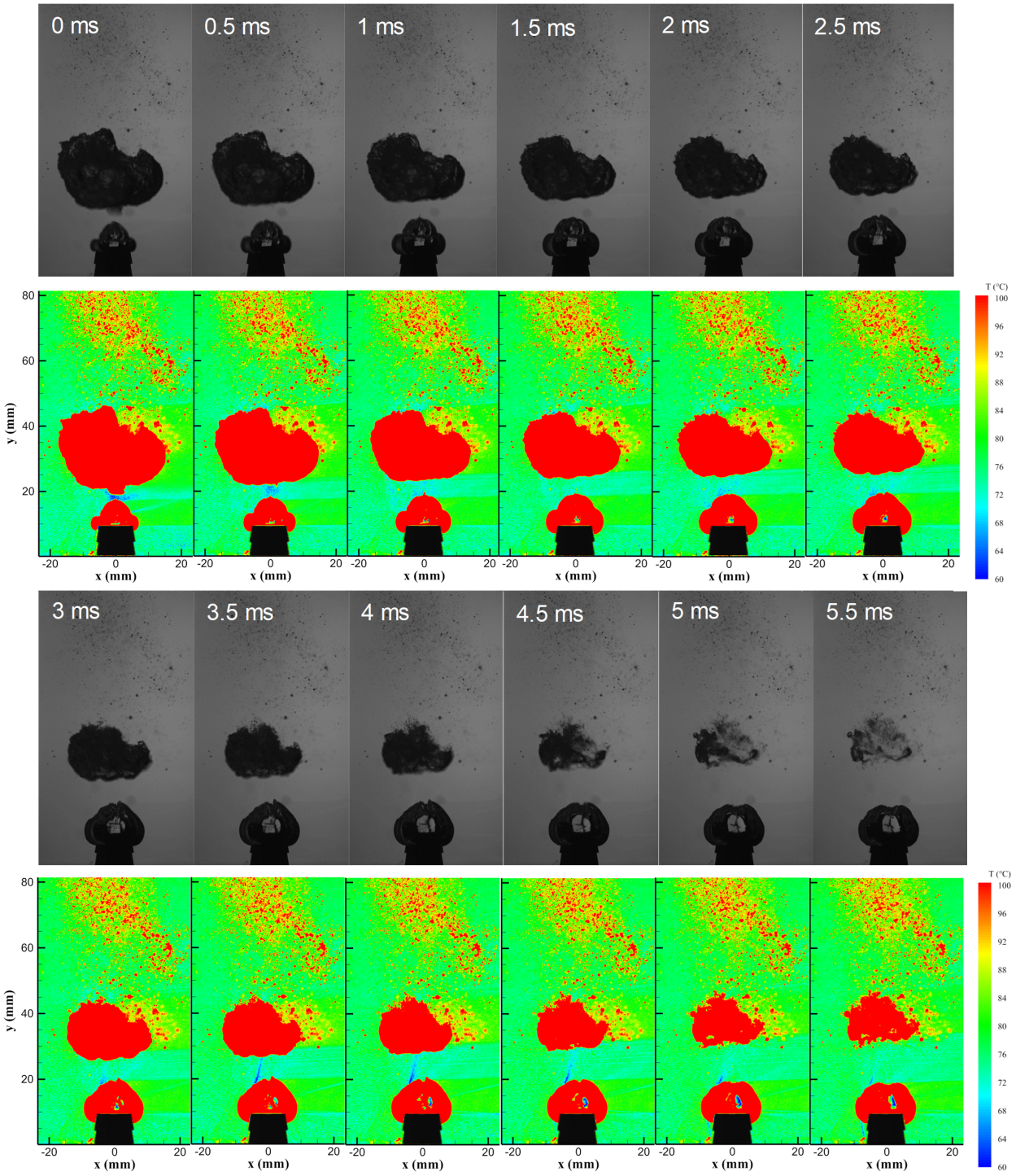

Figure 3.49: Consecutive images of unstable direct contact steam condensation in subcooled water, and spatiotemporally resolved temperature fields measured with backlight aided PLIF thermometry for a condensing period of 0-5.5 ms

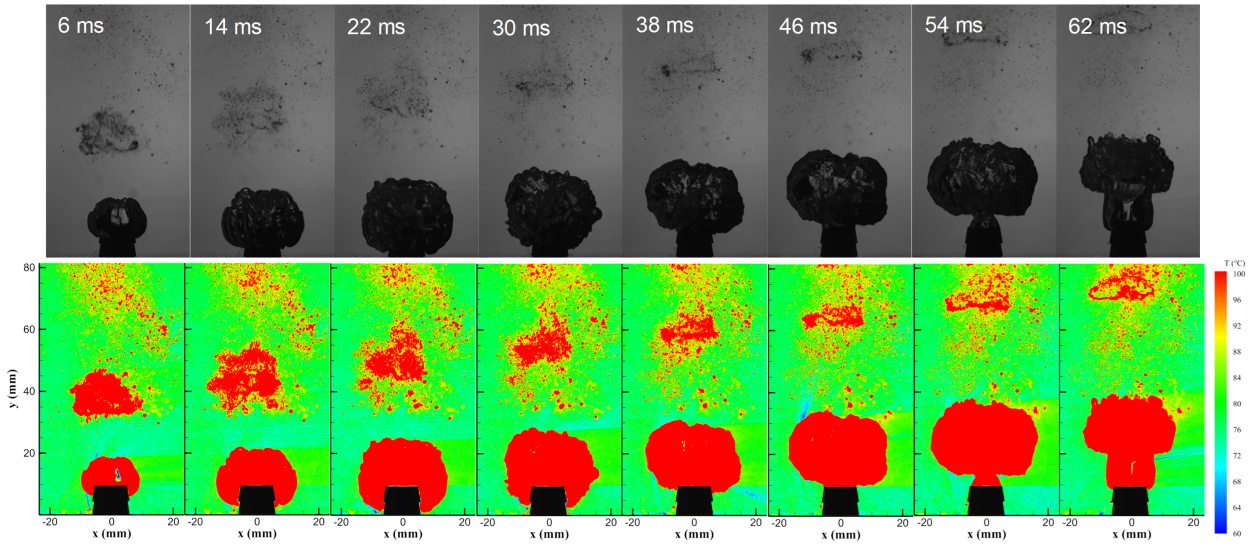

Figure 3.50: Consecutive images of unstable direct contact steam condensation in subcooled water, and spatiotemporally resolved temperature fields measured with backlight aided PLIF thermometry for a growing period of 6-62 ms

Figure 3.51 presents the average temperature fields during 0.5 s with 1000 consecutive frames (approximately 8 bubble life cycles).

As illustrated in Fig. 3.51, the maximum temperature region was observed near the nozzle outlet (the black bulk body shown in the figure) where continuous steam existed throughout the bubble life cycles (see Figs. 3.49 and 3.50). At y = 14 mm, the steepest temperature gradient was observed. As the elevation increases the temperature gradients gradually change to a gentler curve. At y = 70 mm, the temperature gradient was found to be similar to that found in single phase buoyant jets.

The average temperature measured by the 10 K-type thermocouples located at the right and left edges of the image (at y = 15–55 mm, x = $\pm$30 mm) was 75.44$\pm$0.98 °C in this experiment, while PLIF thermometry showed 75.89$\pm$0.84 °C at y = 15–55 mm, x = -20 mm.

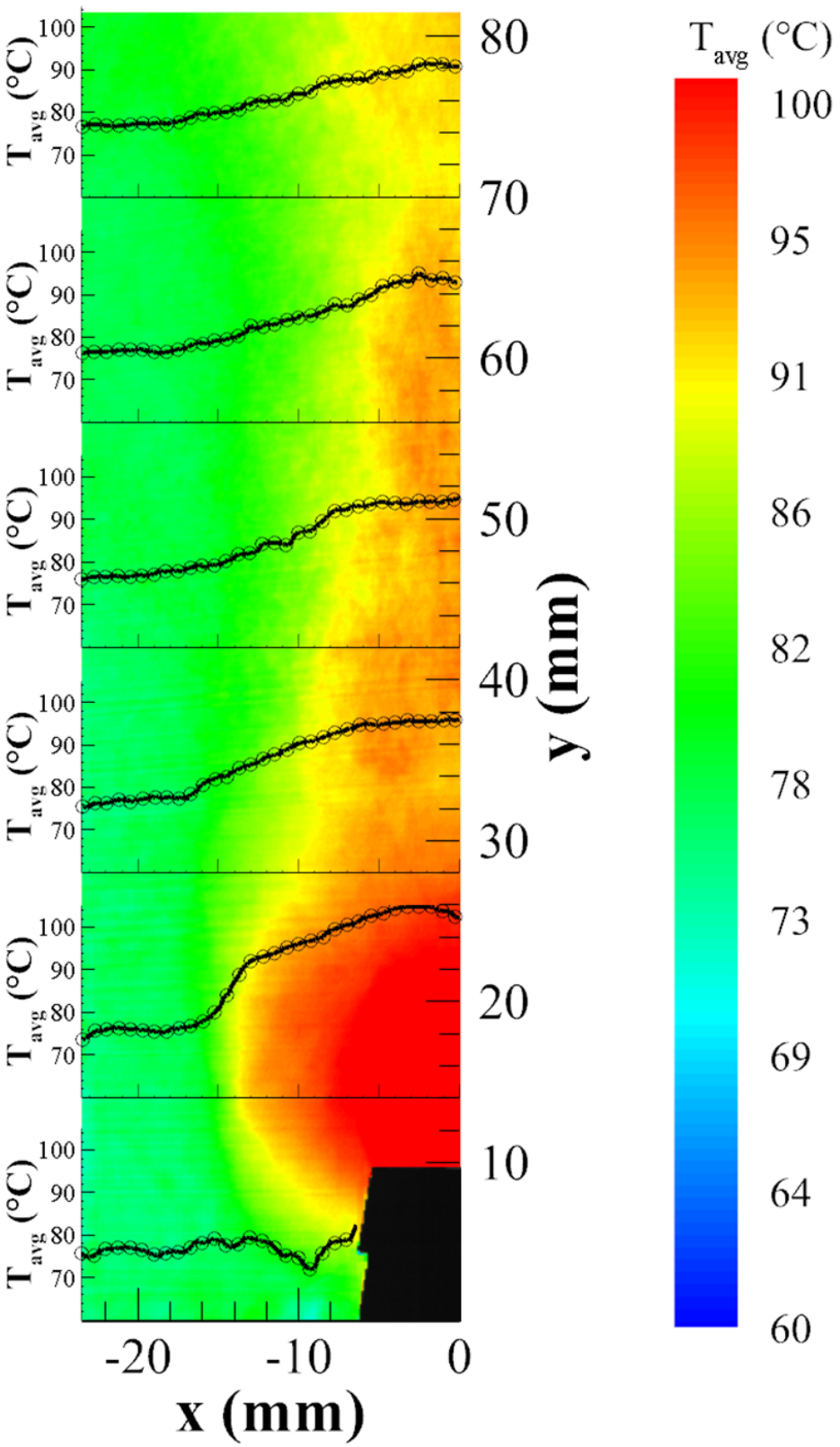

Figure 3.51: Time-averaged temperature contours of unstable direct contact steam condensation in subcooled water

Figure 3.52 shows a comparison between the average temperature data from the PLIF thermometry and the thermocouple measurement.

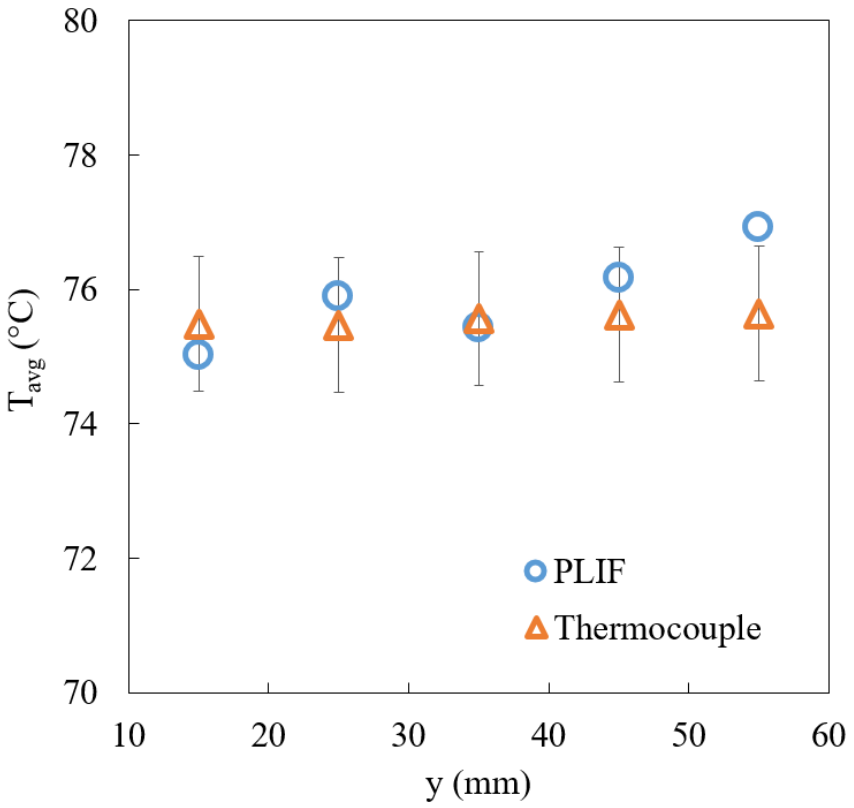

Figure 3.52: Comparison of averaged temperature data between PLIF thermometry and thermocouple measurements

Even though the location of the averaging points was not identical, the result implies that the current development of PLIF thermometry was successful. Figure 3.53 shows the average temperature profiles of the extracted points for different y locations from the contour plot. The verification of the PLIF thermometry could only be conducted at the single phase region far enough from the actual condensation that occurs to prevent flow distortions from thermocouple intrusions. Moreover, it is impossible to obtain reliable temperature measurements in the condensation region using a thermocouple due to its slow response time. Cross-validation of PLIF thermometry and CFD

simulations may give an insight for future verification, validation and uncertainty quantifications of each technique.

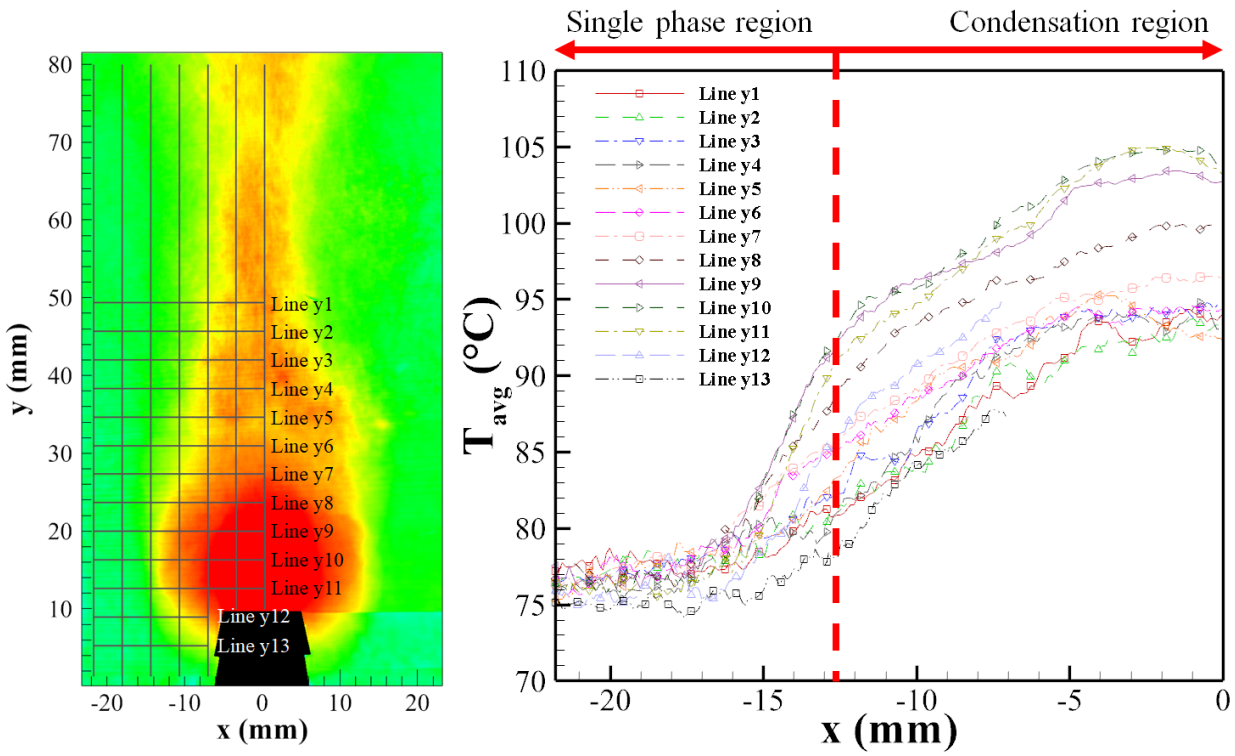

Figure 3.53: Averaged temperature profiles of the extracted points for different y locations

In Fig. 3.53 more details on the gradual change of the slope of temperature profiles for different elevations can be observed. Additionally, the single-phase region and the condensation region can be distinguished where a sudden slope change is observed in the profile from Line y10. Figure 3.54 represents the average temperature profiles of the extracted points for different x locations from the contour plot.

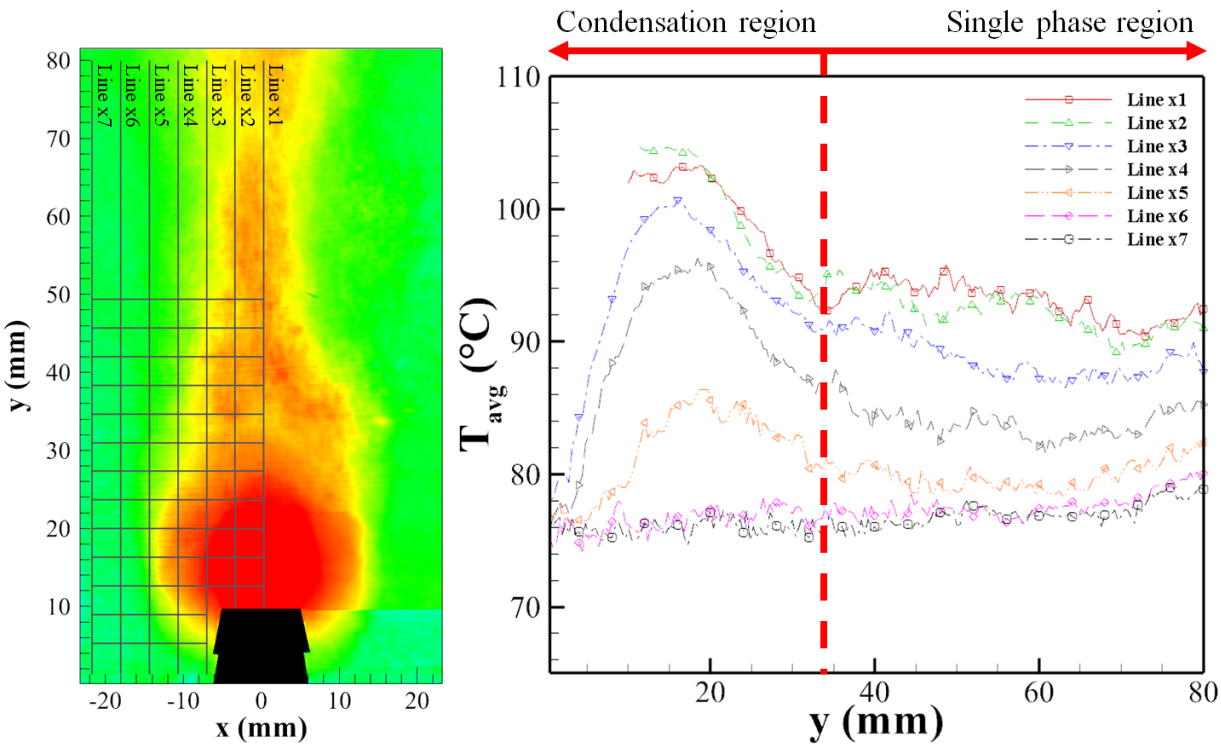

Figure 3.54: Averaged temperature profiles of the extracted points for different x locations

As shown in Fig. 3.54, a gradual change of the slope of temperature profiles for different x locations can be observed. The single-phase region and the condensation region can be distinguished by the local minimum in Line x1. From this point of view, the temperature contour plot can be interpreted as an approximate, average, void fraction.

It should be noted that the right half of the measured temperature has higher uncertainty due to the shade of the bubble, as shown in Fig. 3.43. Additionally, the effects of random reflection still exist, even though the PLIF thermometry was improved significantly by adding the LED backlight because it was suppressed, but not perfectly removed. Further improvements using two-color, two-dye PLIF thermometry with a backlight and two cameras may perfectly remove the random reflection effect.

3.6 Simultaneous Velocity and Temperature Field Measurements using Two Camera PIV and PLIF

Simultaneous velocity and temperature field measurements using two camera PIV and PLIF is developed. This technique includes the improvement of the PIV algorithm with the dynamic masking of the bubble movement. Figure 3.55 depicts the schematic of the experimental configuration of the simultaneous PIV & PLIF.

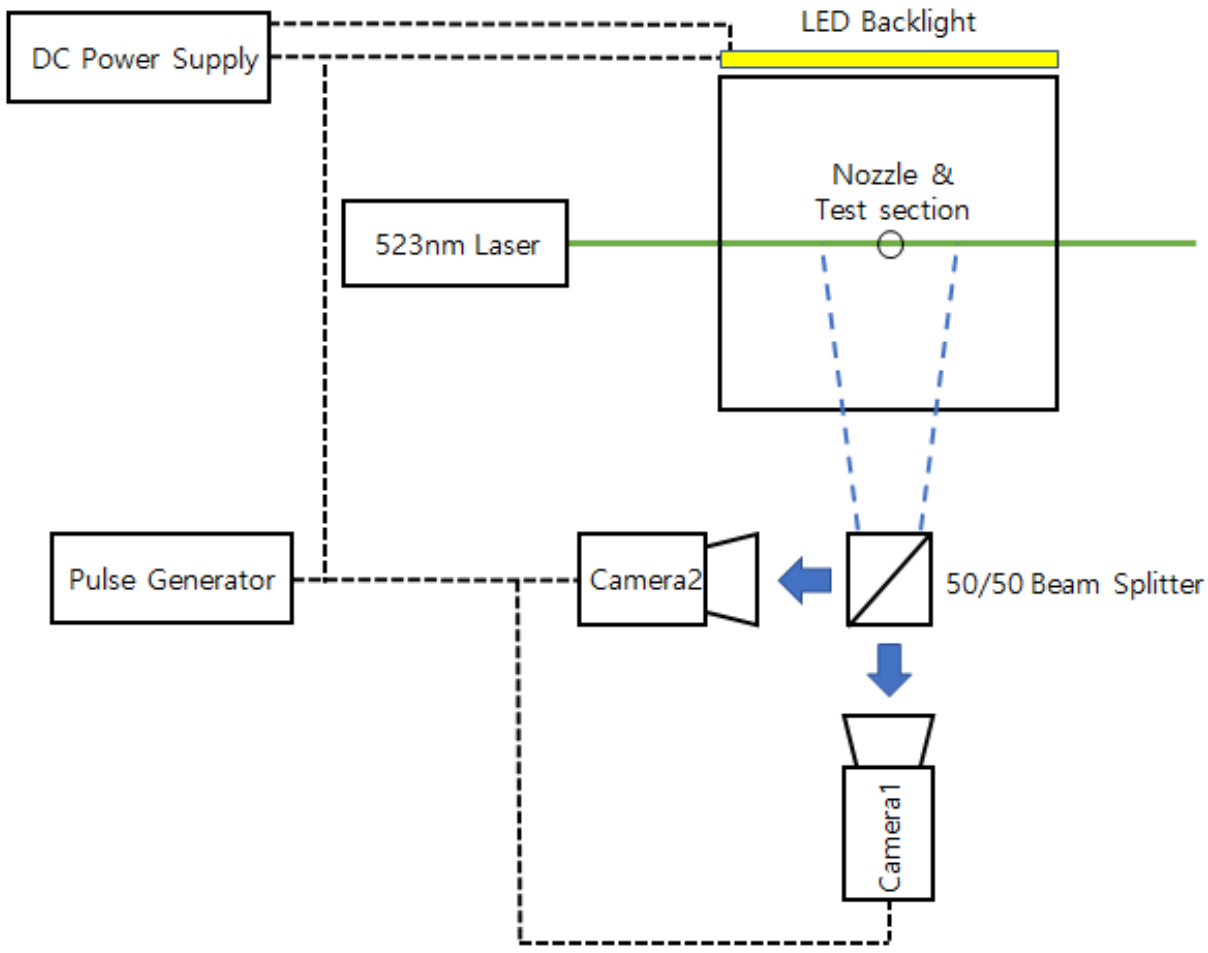

Figure 3.55: Schematic of the experimental configuration of the simultaneous PIV & PLIF

Figure 3.56 presents the snapshot of the experimental setup.

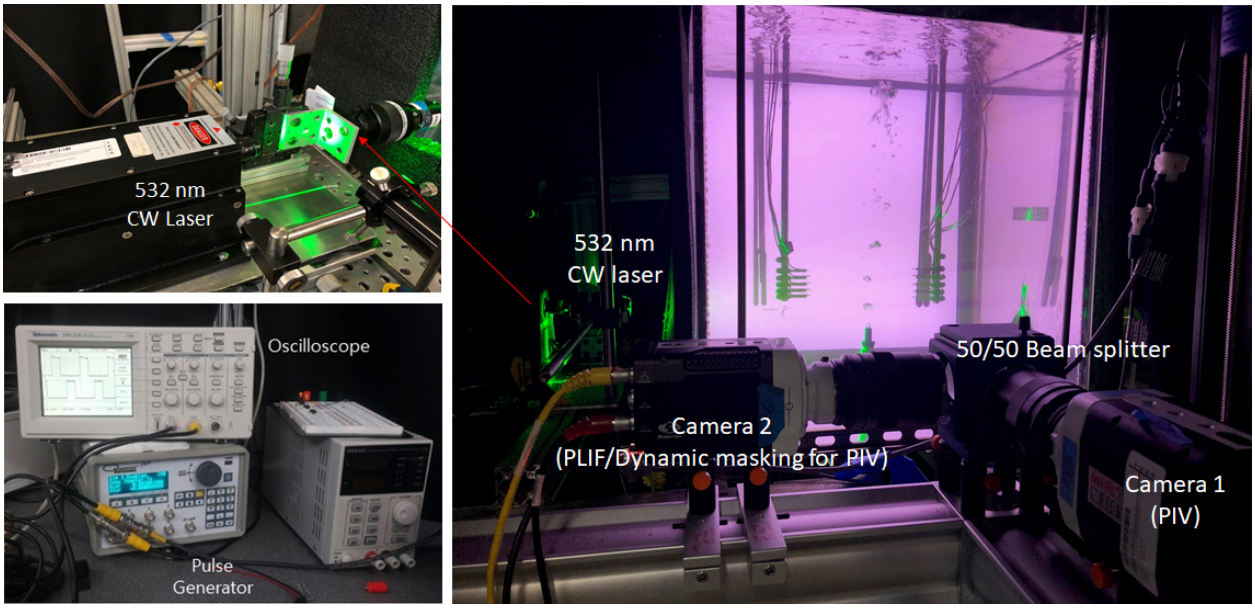

Figure 3.56: Experimental setup of the simultaneous PIV & PLIF

As presented in Figs. 3.55 and 3.56, this technique uses two identical high-speed cameras with 50/50 beam splitter and the LED backlight is added behind the test section for PLIF improvement. A pulse generater was connected to both cameras and the LED backlight to trigger the recording and bursting of the backlight at the same time.

3.6.1 Experimental procedure and conditions

The experimental procedure of the simultaneous velocity and temperature field measurement using two camera PLIF and PIV is similar to that of the PLIF thermometry described in section 3.5.4. Additional steps will be described accordingly. The experimental procedure includes steps to prepare the main components such as the steam generator, the water tank, and the data acquisition (DAQ) system. The steam generator, at first, is connected to DI water system to fill the DI water for steam. After turning on the steam generator, the steam separator was connected to the main steam line to remove any undesired particles or wet content. The water tank is filled with DI water filtered to less than 0.05% impurities, and heated up to desired pool temperature using immersed heaters. Before starting the test, a sufficient amount of the steam was ejected into the nozzle in

the water tank in order to ensure discharging trapped air inside the piping and preventing thermal stratification in the water tank. The prepared Rhodamine-B aqueous solution then resolved into water inside the test facility.

The Conduct-O-Fil® SH400S20 silver coated particles was employed as the PIV seeding particle. The particle has a 13 μm of mean diameter and a 1.6 g/cc of density then added to the water and mixed well using the circulation pump to make sure the particle can be observed evenly within the test section. The maximum Stokes number of the present study is 0.0003, which is was smaller than the perfect advection condition (0.1). All the signals from the measurement devices are connected through the DAQ system and controlled by LabVIEW program, and the values were recorded on the computer for further analysis. The sampling rate and period for each experiment are 1.0 kHz and 3 s, respectively. The frame rate of both high speed cameras of PLIF and PIV were set as 2000 fps, which was 2 times faster than the DAQ sampling frequency. Before starting the test, the image frames on both cameras were adjusted to have coincident plane. Figure 3.57 presents the image planes captured by the camera 1 and the camera 2.

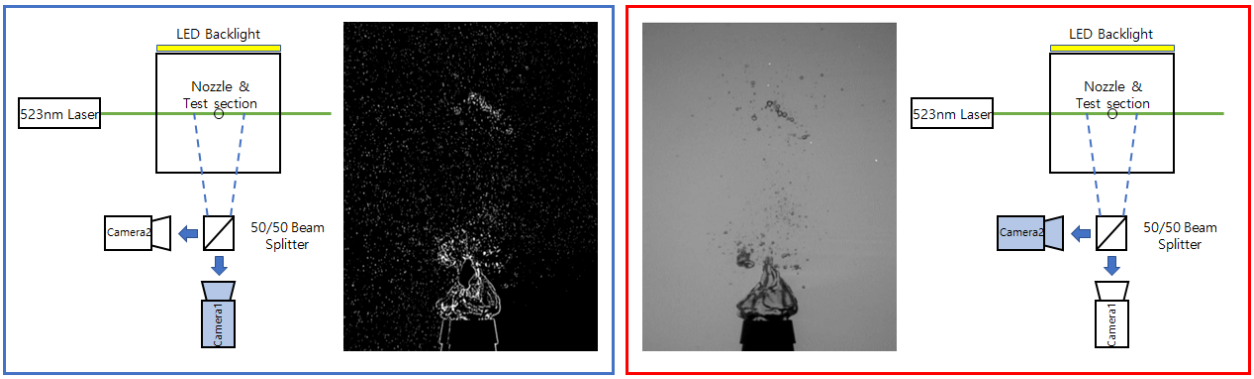

Figure 3.57: Image planes captured by the camera 1 and the camera 2

Obtained PIV images were processed using PRANA (Eckstein and Blachos 2009a, b) Matlab toolkit with the robust phase correlation (RPC) cross correlation algorithm to reduce bias errors and peak locking effects in the presence of high shear and rotational motion (Nguyen *et al.* 2018).

In order to prevent undesired cross correlation and interpolation, dynamic masking for the bubble region was applied. A minor modification to the PRANA program was made to enable the dynamic masking and parallel processing.

During the test, the circulation pump and supplementary heaters for water and steam were turned off to prevent any mechanical and electrical harmonic noises that can corrupt the raw data. The experimental conditions for the present study are shown in Table 3.8.

Table 3.8: Experimental conditions for simultaneous velocity and temperature measurement

Parameter	**Value**	**Accuracy**	**Unit**
Steam temperature	$\sim$103	$\pm$1	°C
Steam inlet pressure	>110	$\pm$0.007	kPa
Nozzle diameter	9.525	$\pm$0.01	mm
Steam mass flow rate	0.5	$\pm$0.09	g/s
Steam mass flux	7.017	$\pm$0.22	kg/m^2·s
Pool temperature	76.45	$\pm$0.06	°C

3.6.2 Results and discussion

Spatially, temporally-resolved simultaneous velocity and temperature field measurement was conducted for the unstable bubbling direct contact condensation of steam in subcooled water using two camera PIV and PLIF. As described in the previous sections, periodic bubble condensation was observed throughout the experiments. Since the experimental condition of the simultaneous PIV & PLIF is similar to that of the PLIF thermometry reported in section 3.5, experimental results of this section will be presented in the same manner. Time resolved instantaneous velocity and temperature field during the unstable direct contact condensation process for the single bubble life time (68.5 ms) is presented in the series of the plots shown in Figs. 3.58-3.60.

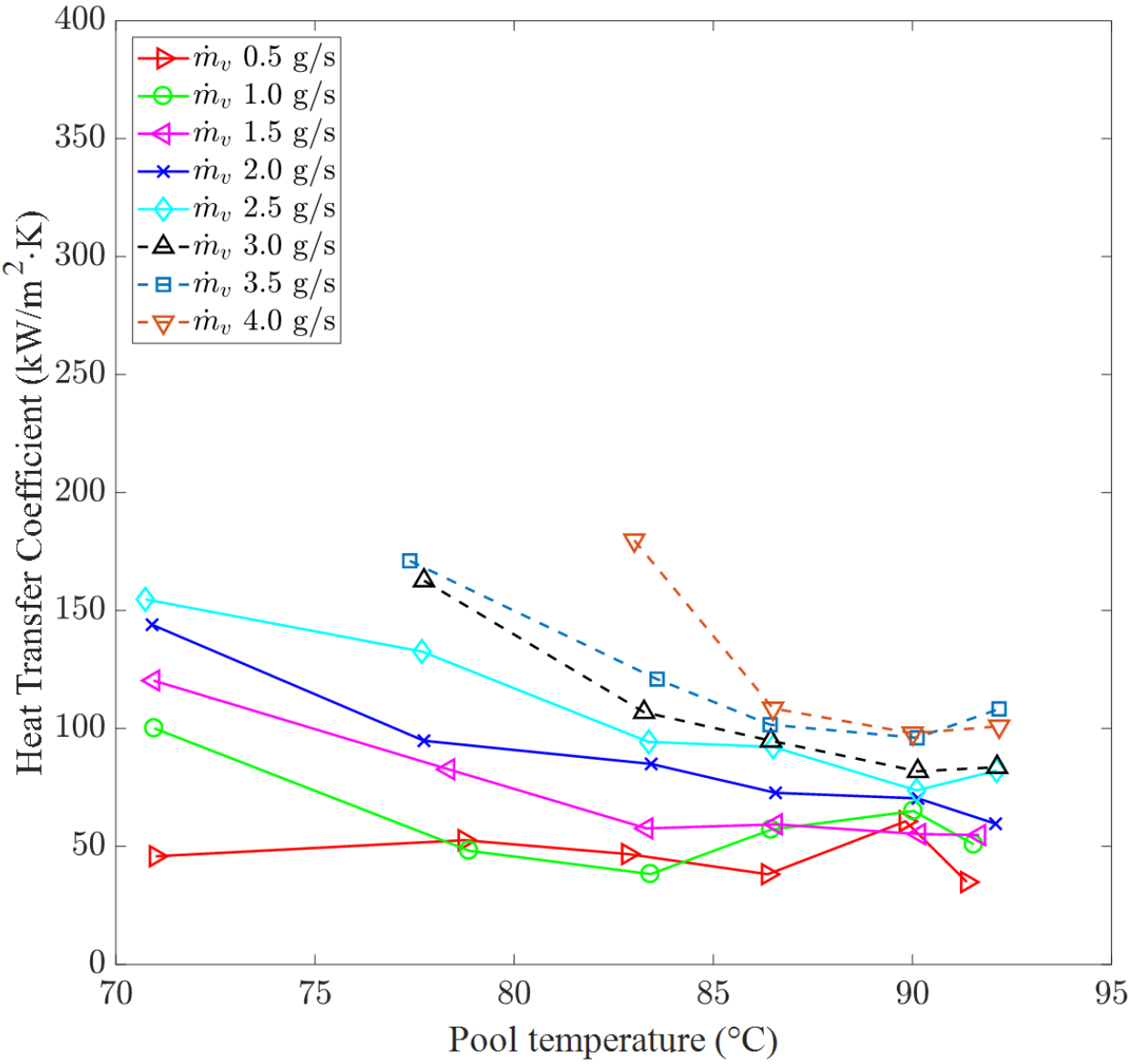

Figure 3.25: Plots of heat-transfer coefficient as a function of pool temperature

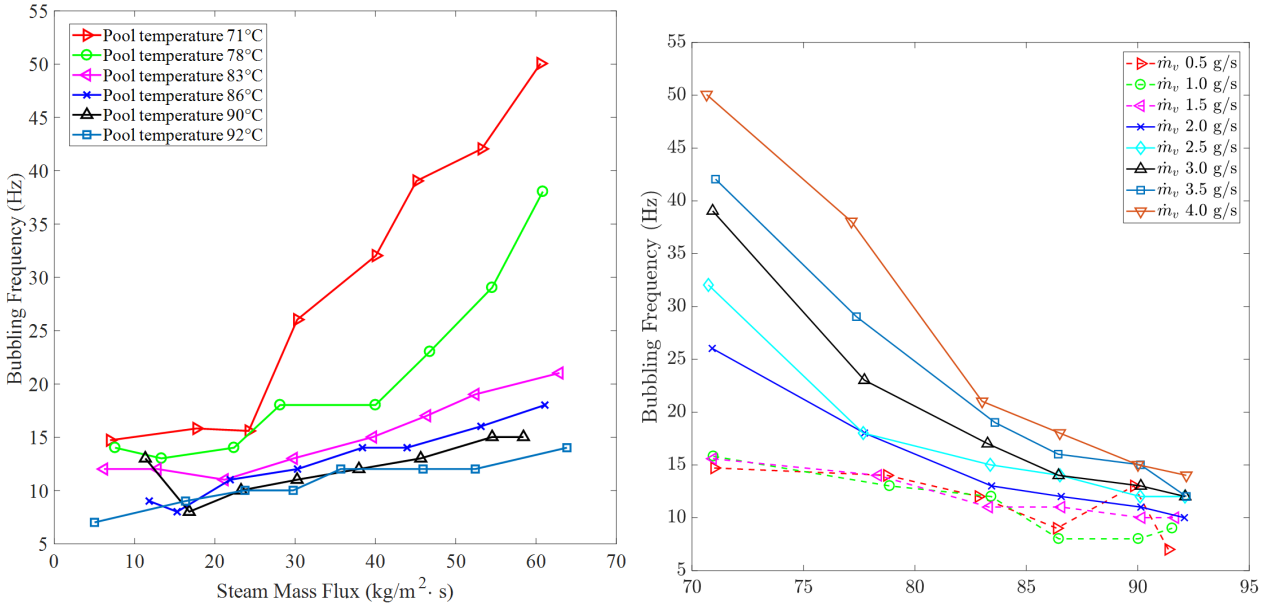

Figure 3.33: Variations of bubbling frequencies as a function of the steam mass flux at different pool temperatures, and as a function of the pool temperature at different steam mass fluxes

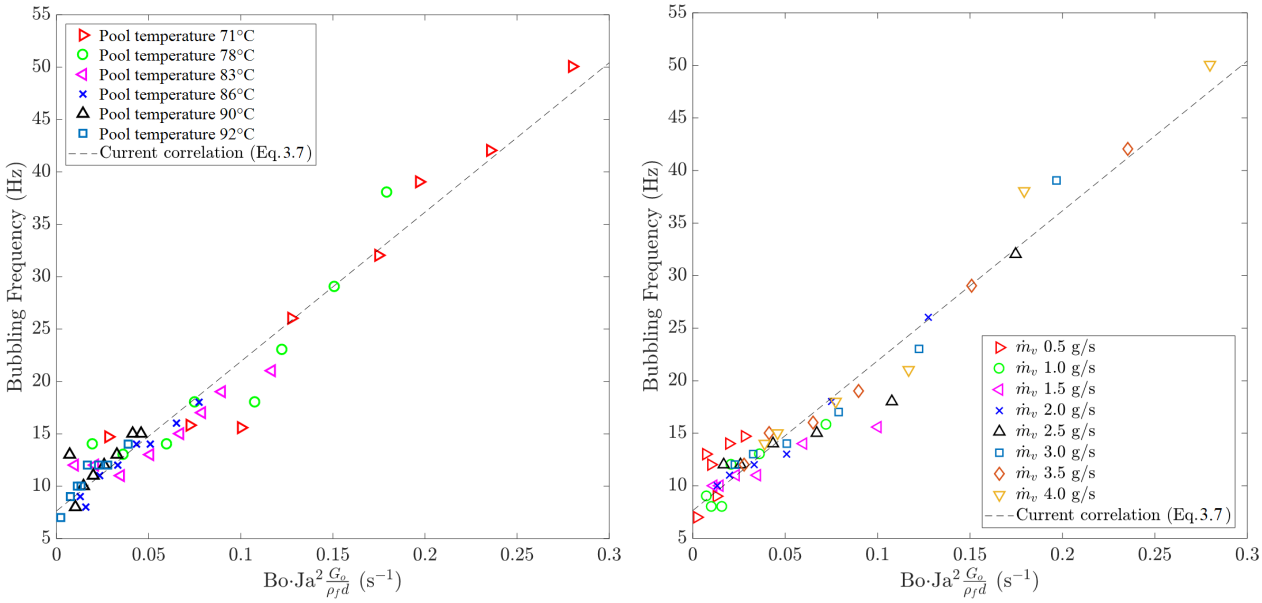

Figure 3.34: Correlation of bubbling frequency with the quantitative estimates of the boundary condition expressed by Eq. 3.7

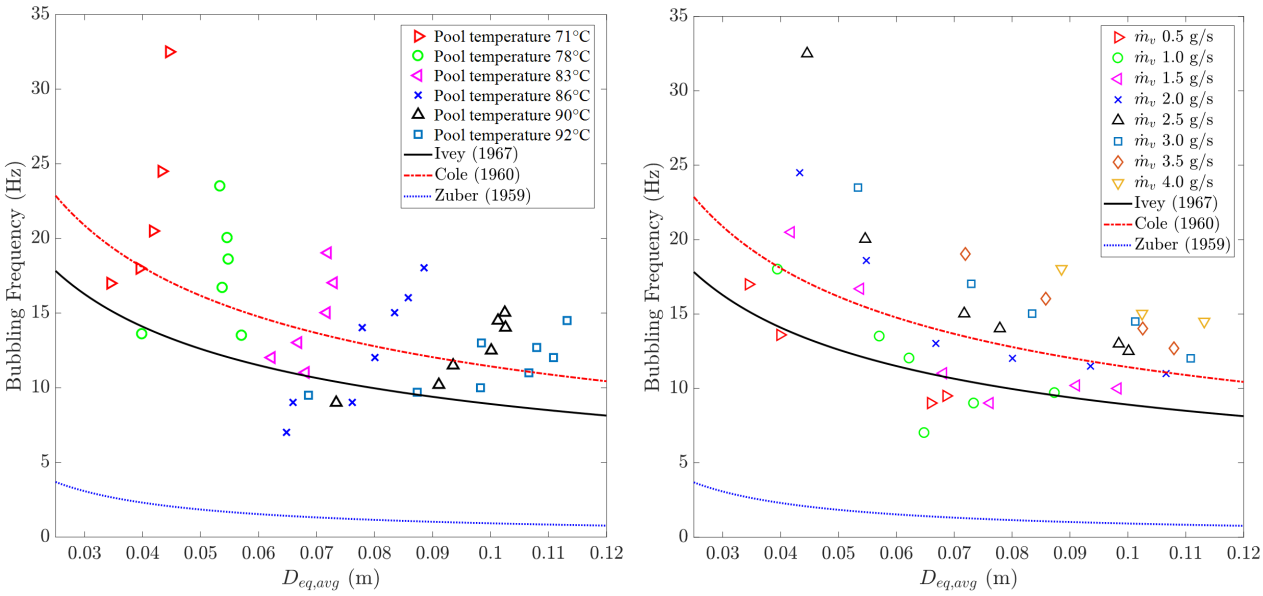

Figure 3.36: Bubbling frequency as a function of the averaged detached-bubble equivalent diameter

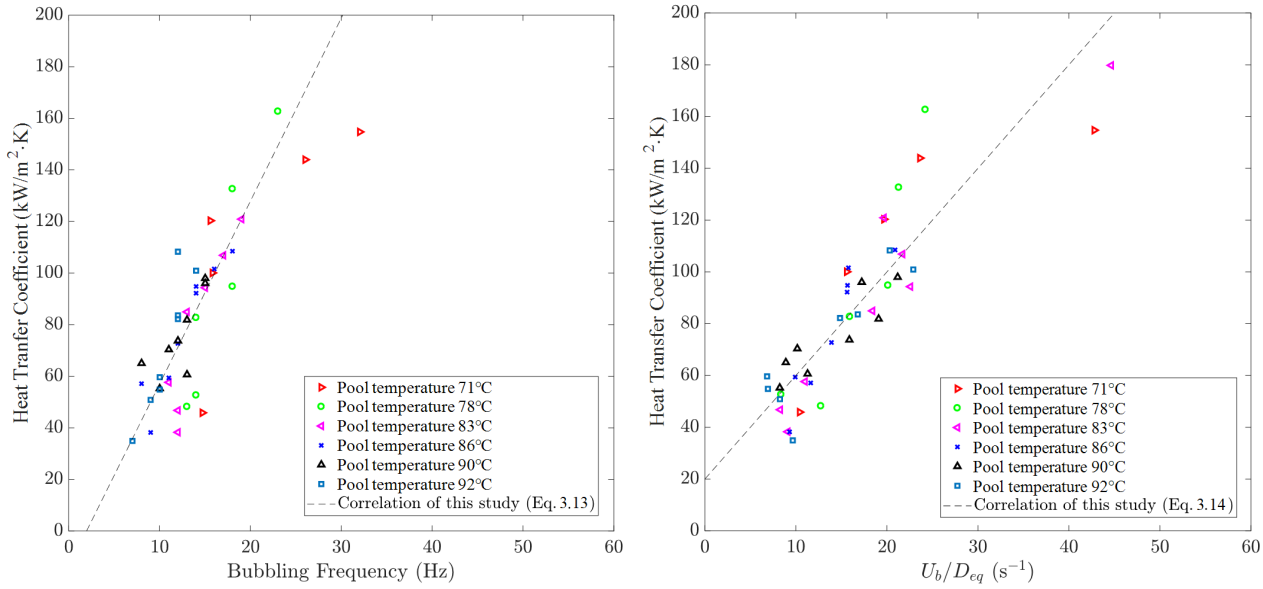

Figure 3.37: Variations of the heat transfer coefficients as a function of frequency, and averaged bubble rising speed divided by the equivalent bubble departure diameter

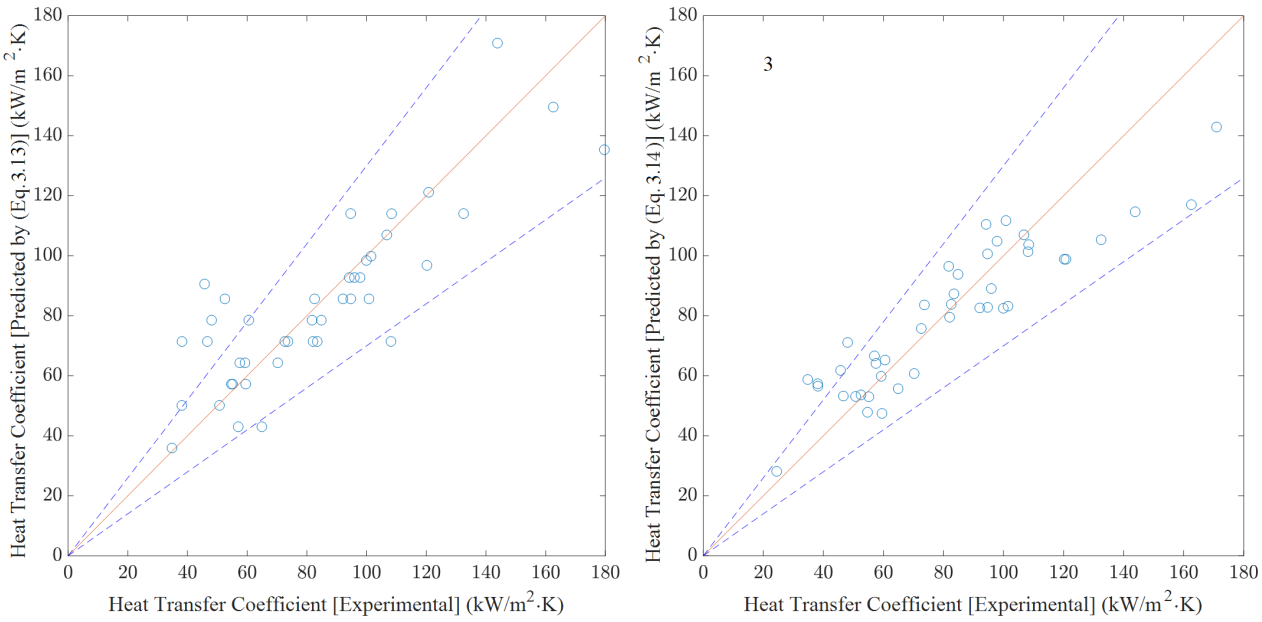

Figure 3.38: Comparison of the heat-transfer coefficient between the experimental and the predicted results(dashed line shows $\pm 30\%$ bounds)

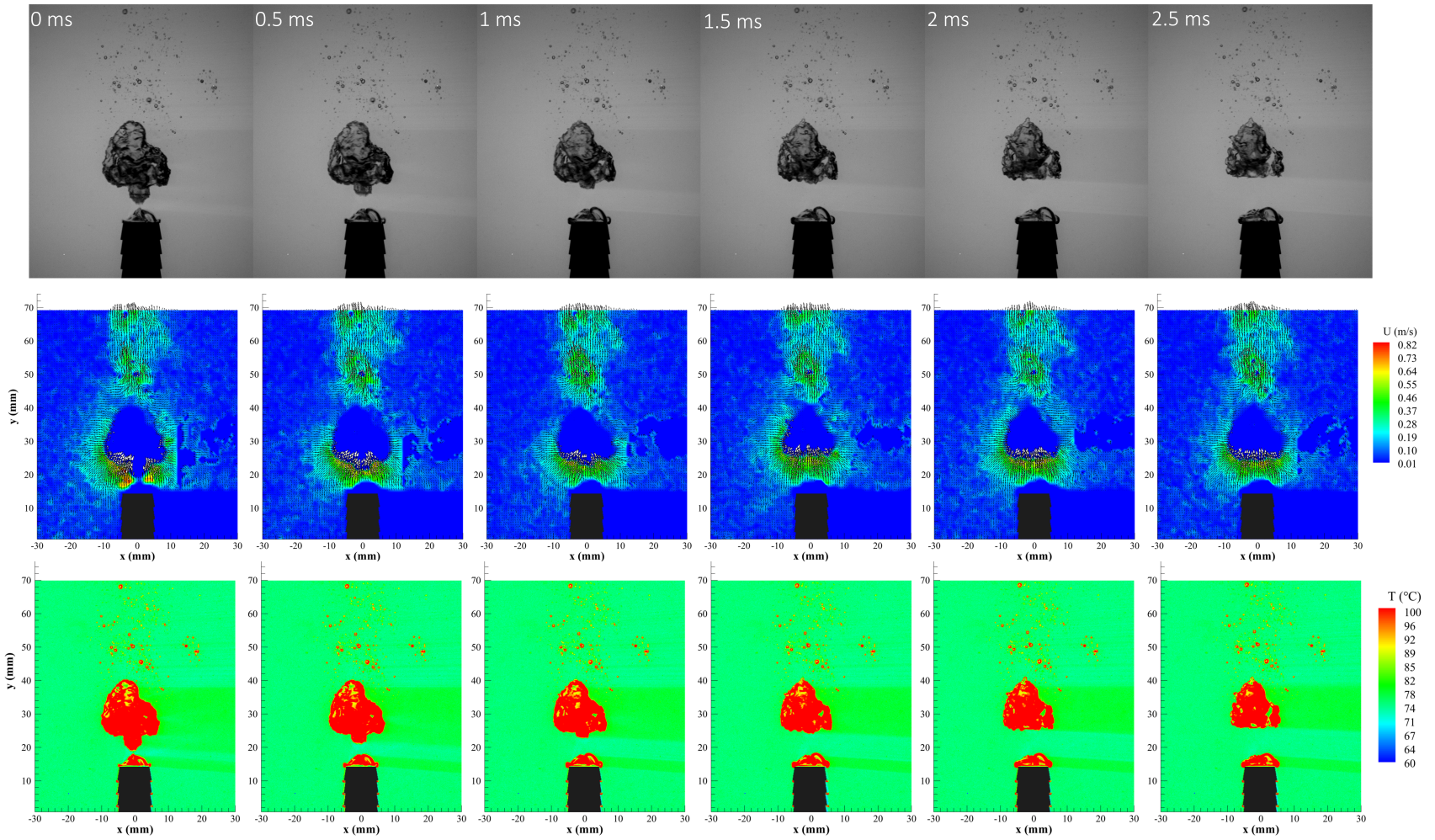

Figure 3.58: Consecutive images of unstable direct contact condensation of steam in subcooled water (top), and spatiotemporally resolved velocity field (middle) and temperature field (bottom) measured by the simultaneous PIV & PLIF for condensing period (0-2.5 ms)

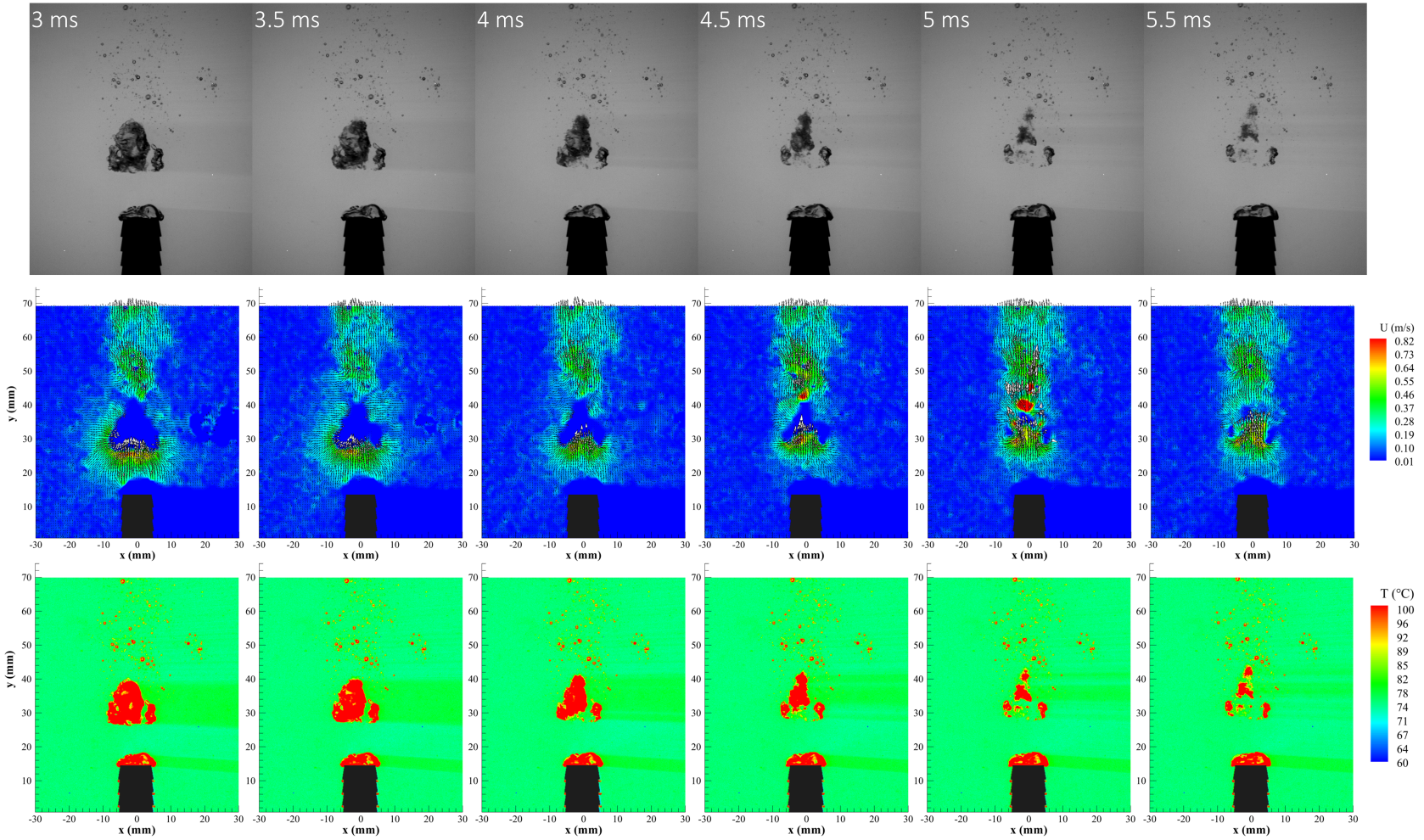

Figure 3.59: Consecutive images of unstable direct contact condensation of steam in subcooled water (top), and spatiotemporally resolved velocity field (middle) and temperature field (bottom) measured by the simultaneous PIV & PLIF for condensing period (3-5.5 ms)

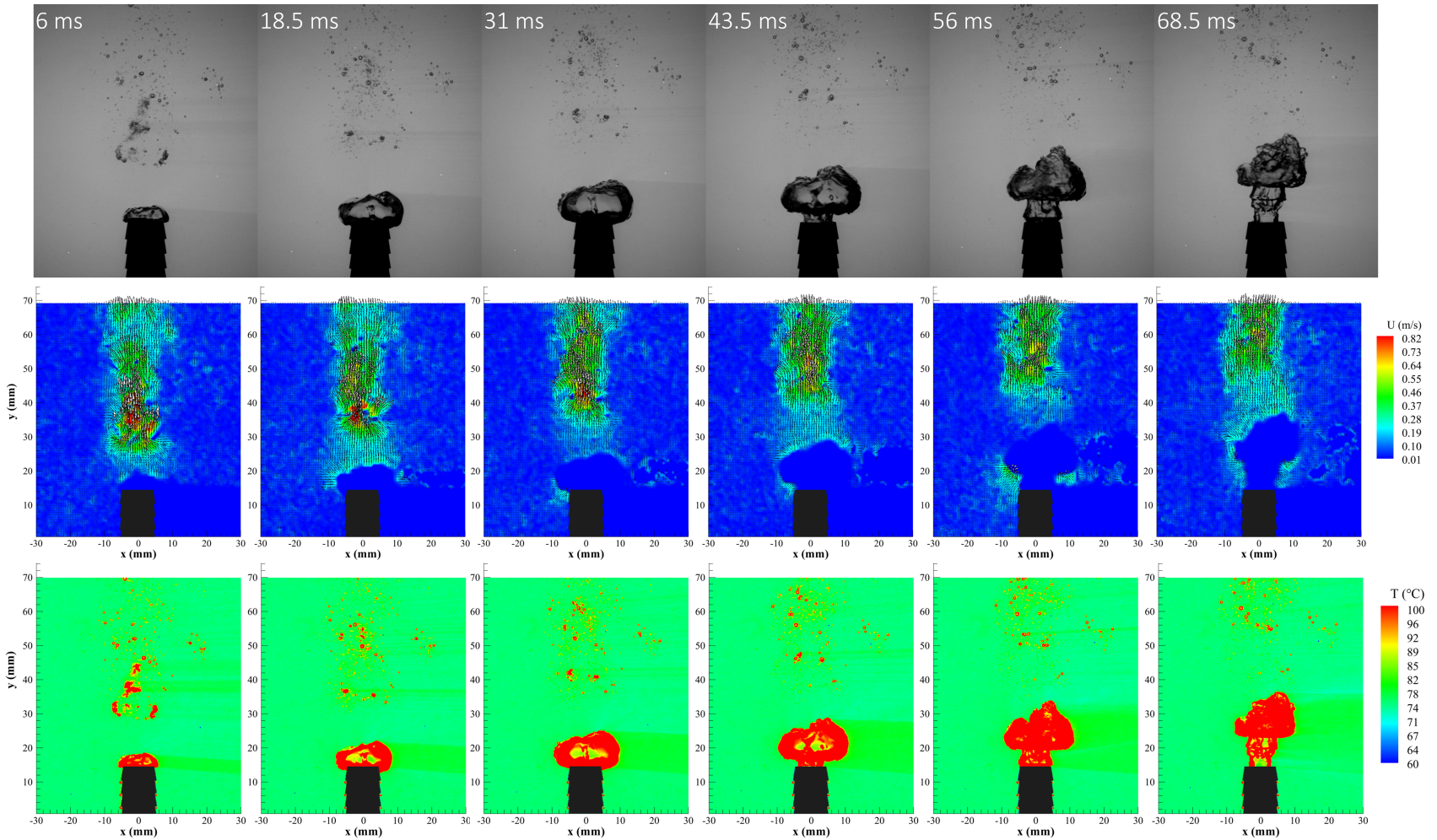

Figure 3.60: Consecutive images of unstable direct contact condensation of steam in subcooled water (top), and spatiotemporally resolved velocity field (middle) and temperature field (bottom) measured by the simultaneous PIV & PLIF for growing period (6-68.5 ms)

Similar patterns as the PLIF experiment were observed during the condensation process. As shown in Figs. 3.58 and 3.59, detached bubble from the nozzle was collapsed quickly within 5.5 ms. Velocity vectors well captured the inward acceleration due to the condensation and the circular motion at the end of the condensing period at 5-5.5 ms. Also, general upward motion like in the buoyant jet can be observed downstream.

After the condensation of the detached bubble, growing of the next bubble takes relatively longer period of time about 63 ms in this case as seen in Fig. 3.51, which is about 10 % slower than the condensing period observed in the PLIF experiment. Since controlling the initial and boundary conditions during the phase change process is extremely difficult, extensive case study is required for a future study. After bubble condenses, velocity vector tends to flow towards free surface due to the buoyancy and the following bubble. However, a certain inward vectors perpendicular to the bubble surface was captured at the bottom side of the bubble after 18.5 ms, which is an evidence of condensation even during the growing period. Some portion of condensed water was not fully mixed with surrounding cold water and was maintained as saturation temperature as observed from the PLIF experiment.

Figures 3.61 and 3.62 present the averaged velocity field combined with velocity vectors and the averaged temperature contour during 0.5 s with 1000 consecutive frames (about 7 bubble life cycle), respectively.

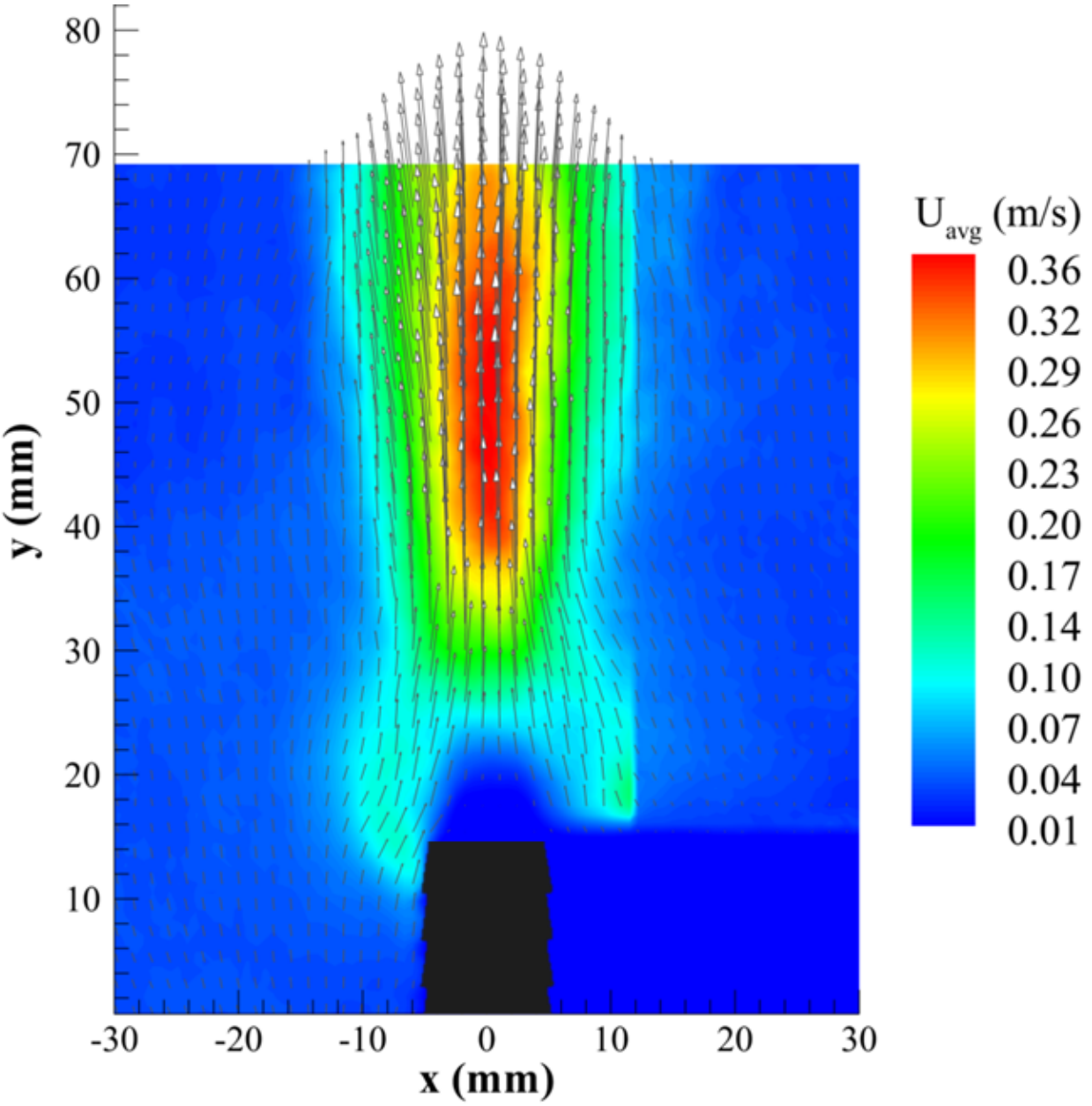

Figure 3.61: Time averaged velocity contour and vectors of unstable direct contact condensation of steam in subcooled water

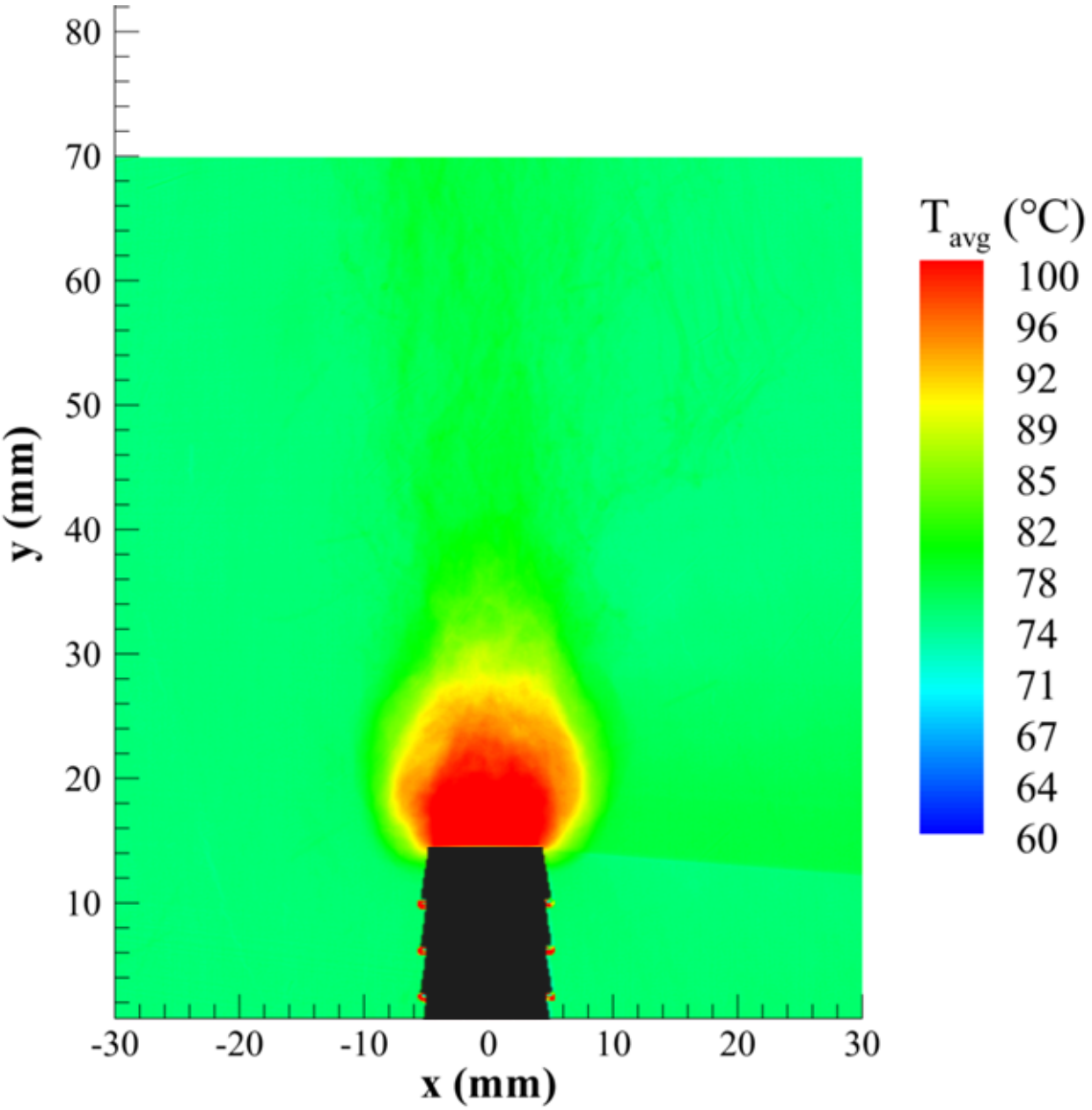

Figure 3.62: Time averaged temperature contour of unstable direct contact condensation of steam in subcooled water

As seen in the figures, the maximum velocity region was observed far from the nozzle (black bulk body shown in the figure) while the maximum temperature region was observed near the nozzle outlet where continuous steam existed throughout the bubble life cycle (see Figs. 3.58-3.51). Figure 3.63 shows the centerline averaged velocity profile at x = 0 mm.

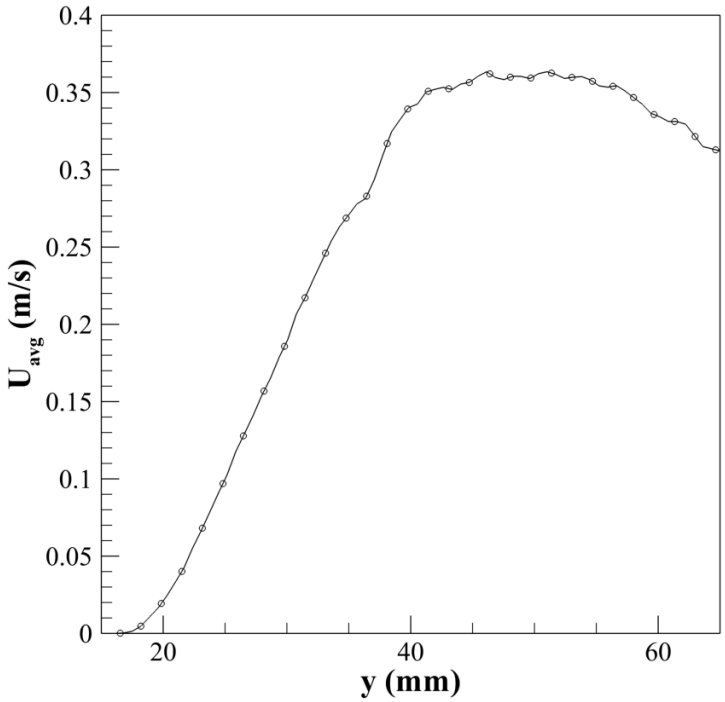

Figure 3.63: The centerline averaged velocity profile at x = 0 mm

As shown in Fig. 3.63, maximum velocity of 0.3634 m/s was found at y = 46.14.

Figure 3.64 depicts the combined velocity and temperature contours with extract lines at different elevations. Note that the image was synthesized to represent the same x-axis range, but the temperature contour part was mirrored.

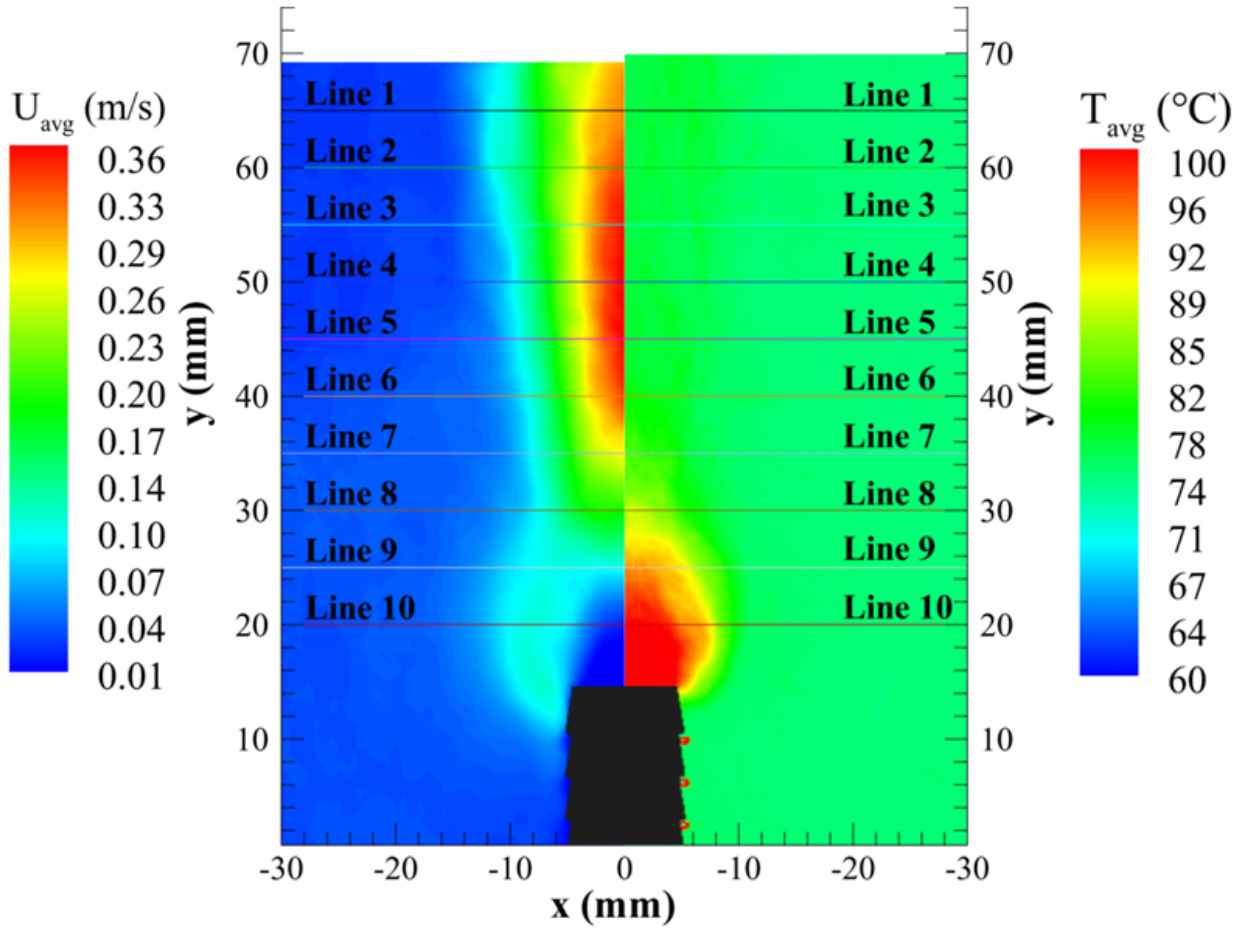

Figure 3.64: Combined velocity and temperature contours with extract lines at different elevations

Figure 3.65 presents the combined velocity and temperature profiles from the extract lines. Again, note that the x-axis of the right-half plane is mirrored.

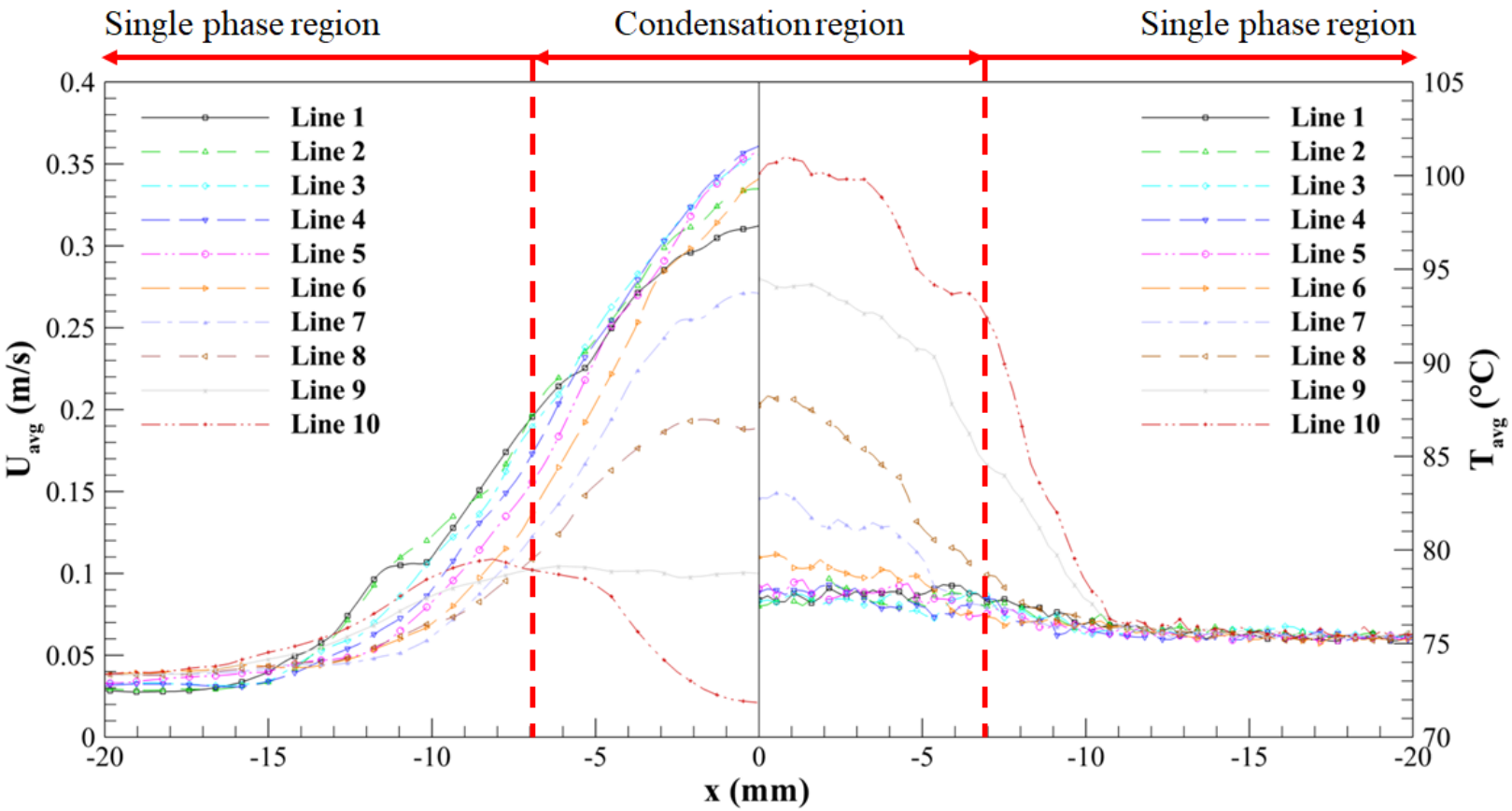

Figure 3.65: Combined velocity and temperature profiles from the extract lines

As presented in Fig. 3.65, the maximum velocity gradient was found in Line 4 while the temperature gradient in Line 4 showed the minimum profile. Correspondingly, the maximum temperature gradient was found in Line 10 while the velocity gradient in Line 10 showed negative slope within the condensation region. Figure 3.66 illustrates the Reynolds stress defined by $-\overline{u'v'} = \bar{U}\bar{V} - \overline{UV}$ where U & V are x & y directional instantaneous velocities, respectively, u' & v' are x & y directional fluctuation velocities, and overbar denotes the time average.

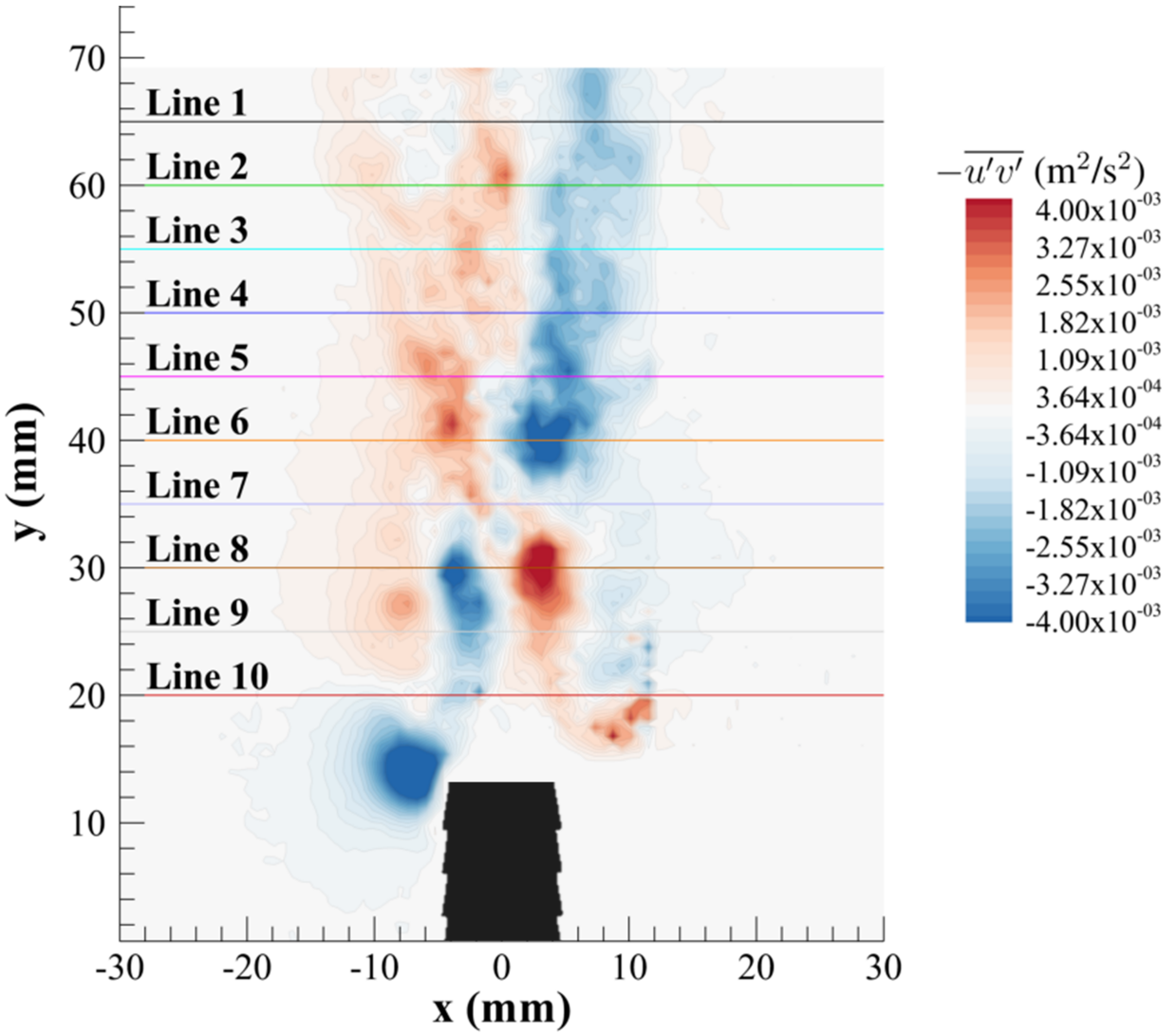

Figure 3.66: Contour of the Reynolds stress with extract lines at different elevations

Figure 3.67 represents the profiles of the Reynolds stress from the extract lines.

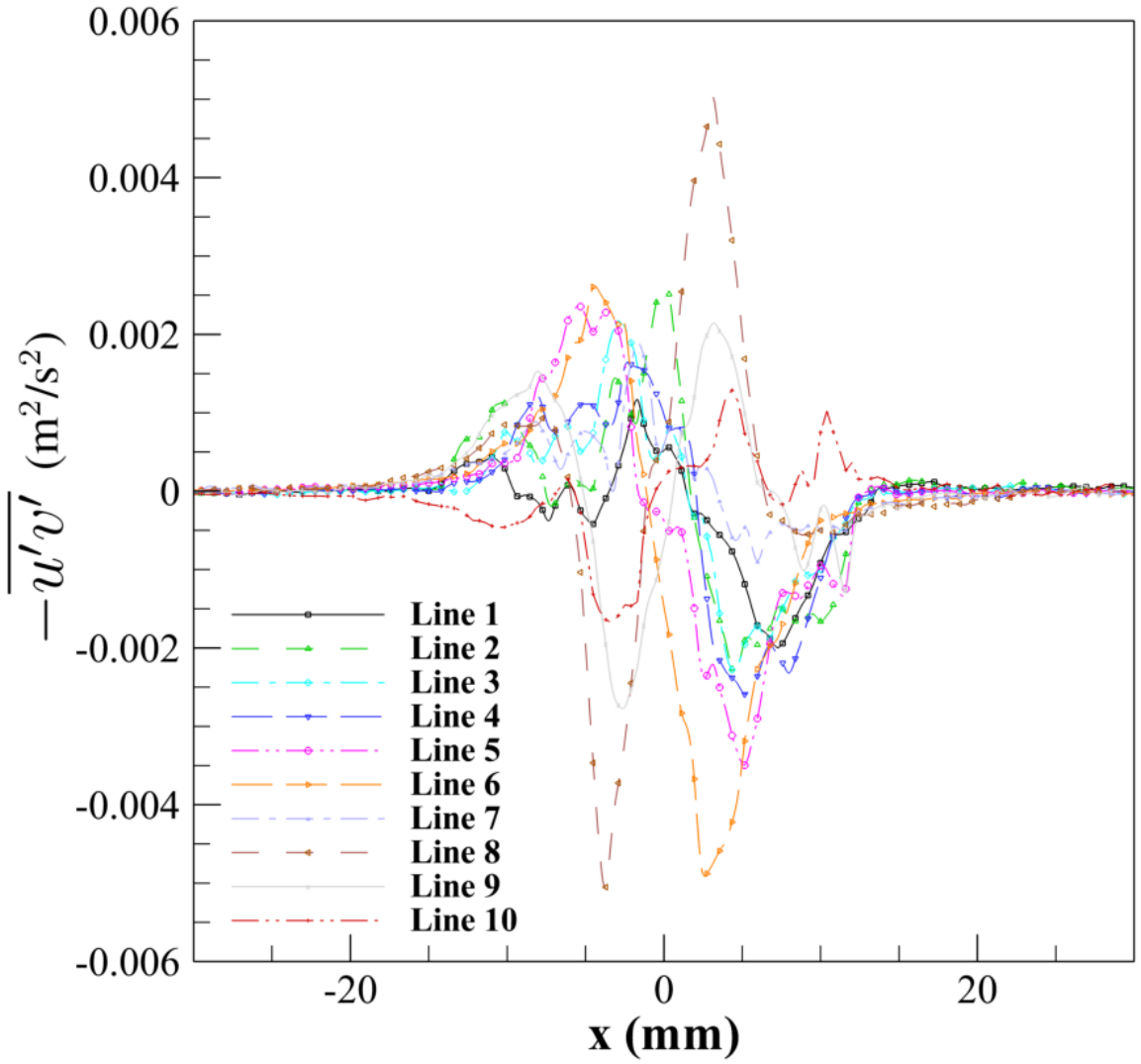

Figure 3.67: Profiles of the Reynolds stress from the extract lines

From the above contour and profiles of the Reynolds stress, it should be noted that there is a direction change in the product of fluctuation velocities at around Line 7 and x = 0 mm. This area can be interpreted as the most probable region of condensation. The Reynolds stress in this region has high values due to the complex steam/water mixture flow caused by the mass transfer. As noticed from the instantaneous velocity vectors shown in Fig. 3.60, bottom side of the bubble

surface produced fluctuations due to the expansion from the bubble growing and contraction due to the condensation, high Reynolds stress can be seen at around the nozzle tip. Also, downstream behavior after Line 7 is similar to that of ordinary buoyant jet.

Here again, it should be noted that the right half of the measured temperature has higher uncertainty due to the shade of the bubble as shown in Fig. 3.43. Also, the effect of random reflection still exists even though the PLIF thermometry was improved significantly by adding the LED backlight because it was suppressed, but not perfectly removed. Additionally, nonphysical temperature inside the bubble region should be corrected in future study. Similar dynamic masking as in PIV might be the candidate to fix this problem. Furthermore, enhancement through two-color two-dye PLIF thermometry with backlight using two camera may perfectly remove the random reflection effect.

The detailed spatio-temporally resolved velocity and temperature field data obtained from this study can be extended to further experimental or CFD investigations on the thermal-hydraulic bubble dynamics models for the specific condensation process. To be specific, a new closure model for CFD simulation of unstable bubbling direct contact condensation process is expected to be developed utilizing the field data in combination with the heat transfer coefficient modeling based on the frequency analysis discussed in section 3.4. Furthermore, the data themselves can be used as a reference for CFD simulation validation.

4. SUGGESTION FOR FURTHER WORK

4.1 Part I. Helium-air Binary Gas Mixture Flow: NGNP HTGR Reactor Building Response to Depressurization Event

Since the current study only performed limited number of point-wise measurement of oxygen concentration, pressure and temperature, further experiments for high-fidelity, high-resolution helium/air mixture flow reference data may provide useful information in addition to the present work. State-of-the-art measurement techniques such as background oriented schlieren, molecular tagging velocimetry and laser induced fluorescence with a dye laser may be a candidate for oxygen/helium concentration and velocity field measurements for a specific accident scenario. Furthermore, utilizing the CFD simulation with realistic initial and boundary conditions provided from this work will give an insight to the complex helium/air mixture flow during a certain accident scenario.

4.2 Part II. Steam-air Mixture Flow in Subcooled Water Pool: Direct Contact Condensation of Steam-air Mixture Jet in a Subcooled Water

Further investigations are required to extend the present study to intensive experimental conditions, including a wider range of steam mass fluxes and pool temperatures, and different nozzle orientations and sizes in the unstable bubbling condensation regime since this process is extremely sensitive to the initial and boundary conditions. The uncertainty quantification of the laser induced fluorescence is not well studied compared to that of the particle image velocimetry; thus a cross validation of the experimental data sets provided from this work with CFD simulation may give an insight for the future verification, validation and uncertainty quantification of each method. Establishing a standard procedure for the laser induced fluorescence for single-phase flow and two-phase flow may be a good starting point. Further improvement of temperature measurement of two-phase flow using two-color two-dye PLIF thermometry with backlight with two camera may perfectly remove the random reflection effect at the steam/water interface.

4.2.1 Continuous wavelet transform on high-speed video

Figure 4.1 illustrates a preliminary result of a continuous wavelet transform on high-speed video of unstable bubble direct contact condensation of steam in subcooled water.

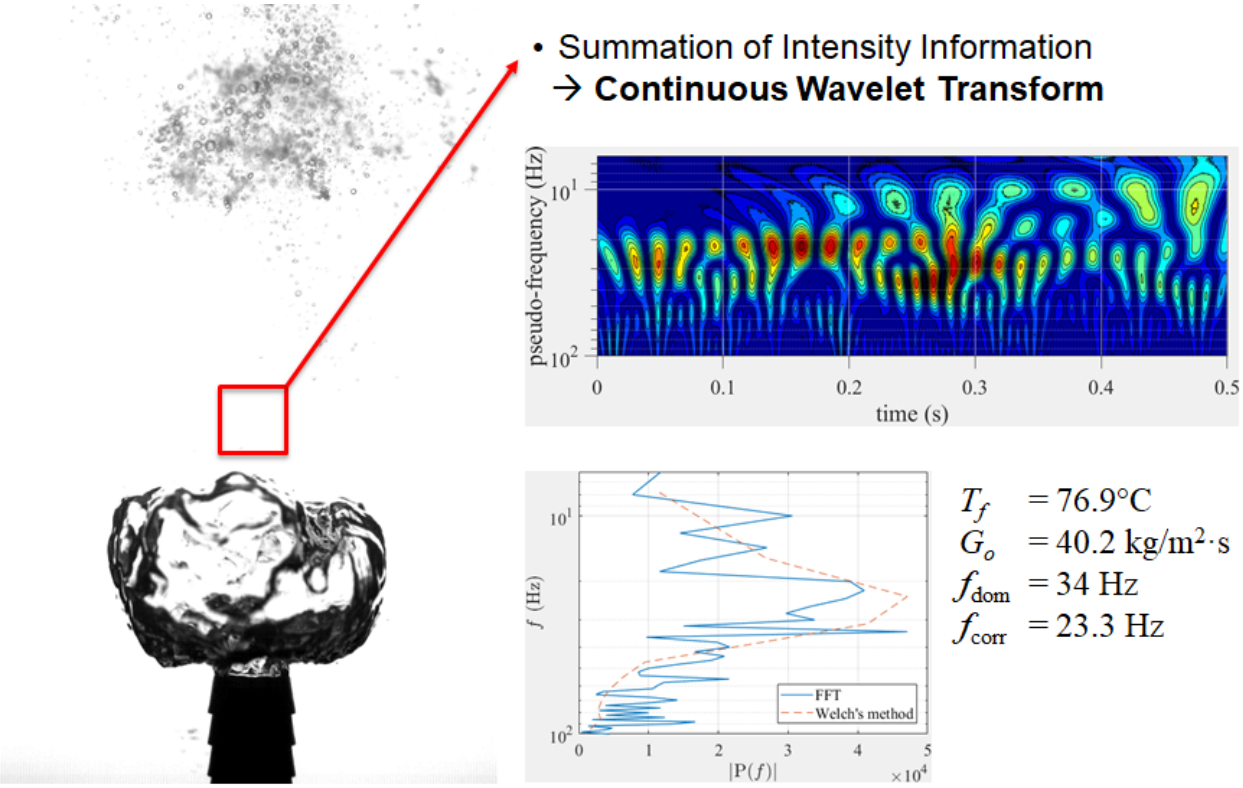

Figure 4.1: Continuous wavelet transform on high-speed video

T_f, G_o, f_{dom} and f_{corr} are the averaged pool temperature, steam mass flux, the dominant frequency detected from the Fast Fourier Transform and the dominant frequency calculated by Eq. 3.13. In Fig. 4.1, intensity value inside the red boxed area was summed sequentially for the high-speed images, and the continuous wavelet transform was applied to the summed value. As seen in the continuous wavelet transform result (contour plot in the figure), the maximum peak frequency region was fluctuating temporally while the Fast Fourier Transform result showed characteristic frequency peaks as the time invariant form. More in-depth frequency analysis on the data sets pro-

vided from this work using the continuous wavelet transform in combination with the conventional Fourier analysis may give a further understanding of the phase change phenomena.

4.2.2 Non-condensable gas effect on unstable bubbling direct contact condensation

Figure 4.2 depicts a preliminary result of unstable bubble direct contact condensation of steam/air mixture in subcooled water with different air ratio.

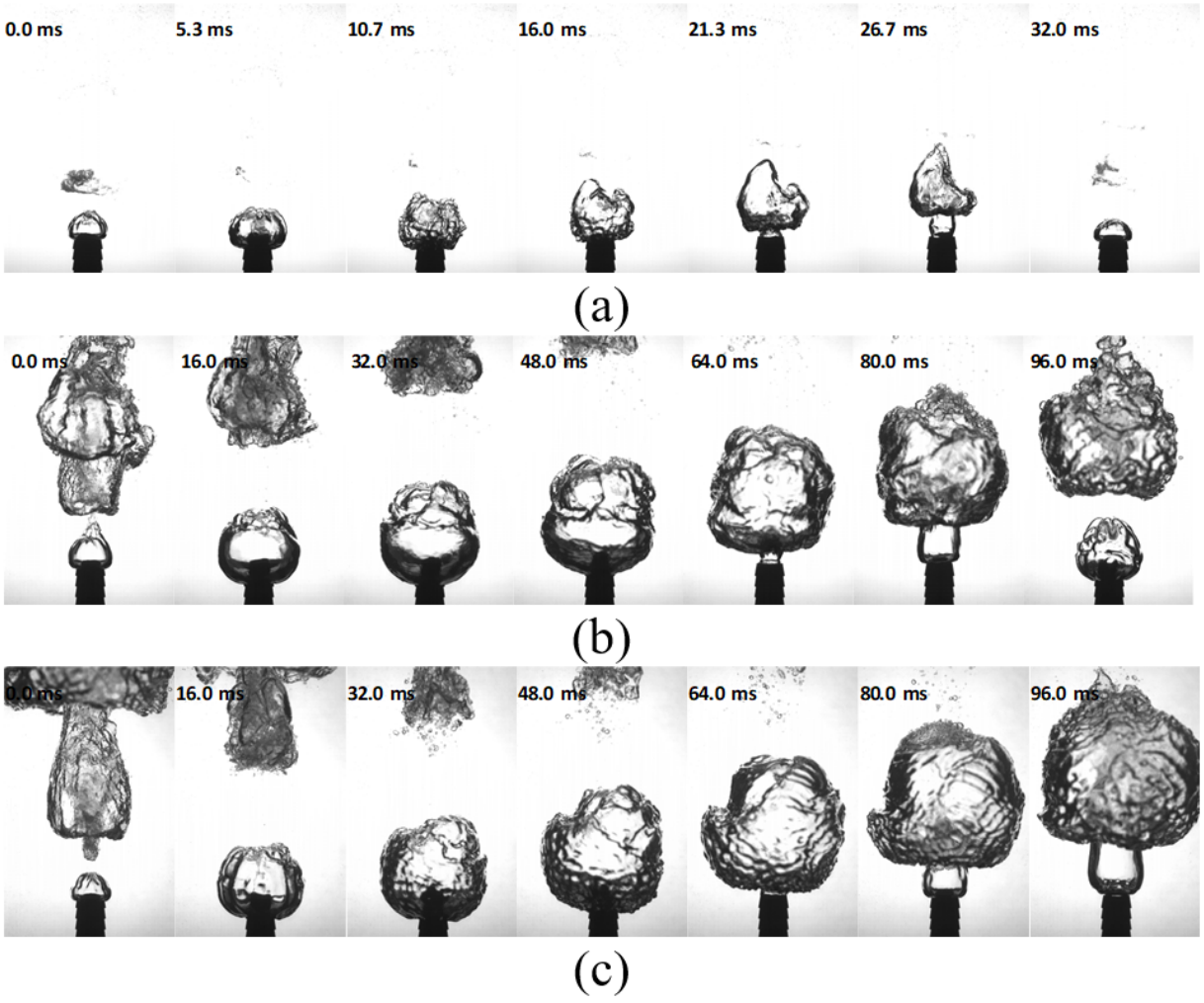

Figure 4.2: Sequent photos for a single period of unstable bubble direct contact condensation of steam/air mixture in subcooled water at pool temperature of 75°C and total gas flow rate of 2.0 g/s with different air ratio: (a) steam 100 %, (b) steam 90 % and air 10 %, (c) steam 25 % and air 75 %.

As shown in Fig. 4.2 (a), which is steam 100 %, the condensation of a single bubble was completed within the region of interest (ROI) in 32.0 ms. However, condensation of the detached bubble was only partially captured within the ROI in the steam/air mixture case as shown in Fig. 4.2 (b) and (c), and the bubble detachment periods were increased. It implies that even a 10 % of the air mixed in steam has a huge effect on the bubble dynamics and condensing pattern. Also, comparing (b) and (c), the difference of the projected non-condensing bubble area is not large, even though the amount of the air is increased notably (10 % to 75 %). It can be interpreted that the influence of mixing ratio of the air may not be significant in the bubble dynamics and condensing pattern. Fig. 4.3 presents the heat transfer coefficient versus air mixing ratio plots for different pool temperatures.

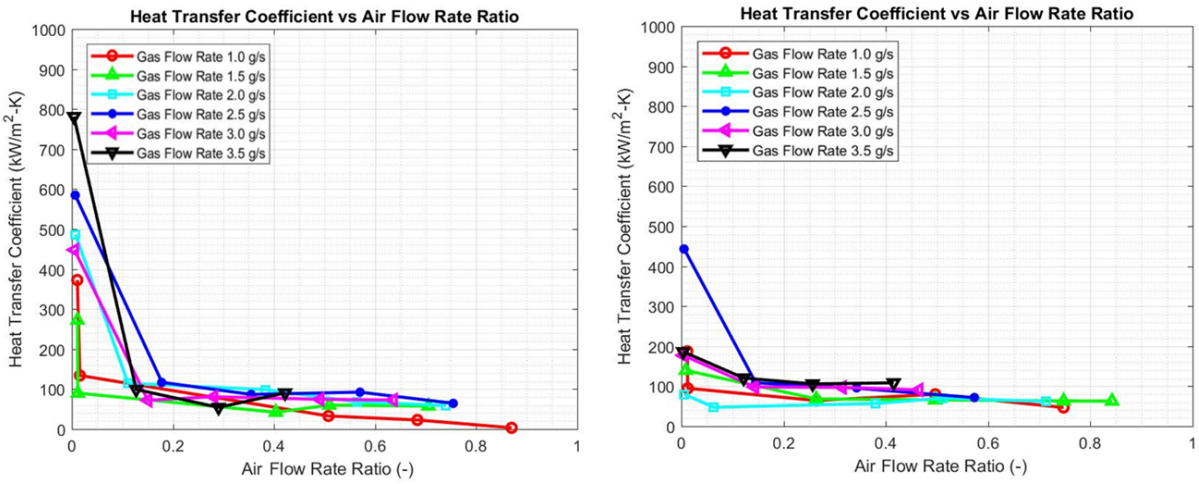

Figure 4.3: Heat transfer coefficient to air flow rate ratio: Pool temperature of (a) 75°C, (b) 85°C

As shown in Fig. 4.3 (a) and (b), decreasing trend of heat transfer coefficient can be found as the flow rate ratio of air (non-condensable gas) increases. The results imply that even with the small amount of non-condensable gas may reduce the heat transfer coefficient significantly. Also, regardless of the total gas flow rate, heat transfer coefficient converged to about 100 kW/m^2-K after the ratio of air mass flow rate exceeds 20 in this unstable condensation regime. As shown in this

preliminary result, non-condensable gas effect on unstable bubbling direct contact condensation seems to be predictable. Further investigation is required to quantify the effect.

5. CONCLUSION

5.1 Part I. Helium-air Binary Gas Mixture Flow: NGNP HTGR Reactor Building Response to Depressurization Event

In Part I, a 1/28 down-scaled simplified RB model was developed to investigate the transient gas flow responses of NGNP HTGR VLPCs during a D-LOFC accident experimentally. Scaling analysis was conducted based on the distinctive thermal-hydraulic phenomena expected during the air refill phase, including vertical stratification and mixing, horizontal stratification (gravity current), gas thermal expansion and contraction, and molecular diffusion of the binary gas mixture (air-helium). A non-dimensional similarity approach was employed for scaling analysis. The experimental facility was fabricated and calibrated based on the scaling parameters and NGNP HTGR design criteria.

The experimental study on the RB response to hypothetical moderate breaks in the HPB of the reactor cavity and the steam generator cavity was presented where air was assumed to be forced out and helium was released continuously. To investigate the dynamic response of the system because of depressurization and air refill for the scaled experimental facility, three experiments with test IDs P3-A(1), P3-A(2), and P3-F were designed and conducted with different flow path configurations. Pressure and oxygen concentration responses were obtained throughout the tests. Furthermore, qualitative analysis was performed on the experimental results.

- The P3-A(1) test simulated a hypothetical moderate-sized break from the upper region of the steam generator cavity with a vent path configured at the top of the steam generator cavity. The oxygen concentration in the RB compartments maintained its value as the atmospheric condition (21%), which means that air ingress into the RPV through the break site can occur immediately following a depressurization event by diffusion and natural convection. The results imply that the vent path configuration for P3-A(1) should be modified to defer air ingress into the RPV.

- The P3-A(2) test simulated a hypothetical moderate-sized break from the upper region of the steam generator cavity with a vent path configured at the bottom of the steam generator cavity and then at the top of the equipment shaft. The oxygen concentration results indicate a lowest peak of 2% due to the purging of air by the helium depressurization process. The results suggest that the vent path should be placed at the bottom of the compartments. The oxygen concentration at the CV6 bottom exhibited a slower change rate than that of the CV6 top because of the trapped air at the bottom of CV6.

- The P3-F test simulated a hypothetical moderate-sized break from the upper region of the reactor cavity with a vent path configured at the bottom of the reactor cavity and steam generator cavity, and then at the top of the equipment shaft. The oxygen concentration results indicate a lowest peak of 3% due to the purging of air by the helium depressurization process. The oxygen concentration at the CV6 bottom exhibited a similar change rate to that of the CV6 top, which means that there was no trapped air at the bottom of CV6.

The results of this study can provide reference data for validation of system codes, such as GOTHIC, RELAP, and MELCOR. A numerical study of GOTHIC simulation modeling and validation was performed based on present study, and showed good agreement with the experimental results (Mustafa *et al.*, 2018). The validity of the system code for the scaled facility could then provide a basis for system code analysis for a full-scale plant in various LOFC accident scenarios. A combination of CFD simulation with a system code may provide an improved understanding of the phenomena related to an LOFC event.

5.2 Part II. Steam-air Mixture Flow in Subcooled Water Pool: Direct Contact Condensation of Steam-air Mixture Jet in a Subcooled Water

In Part II, an experimental study on the steam-water direct contact condensation in the unstable bubbling regime was conducted to investigate the thermal hydraulic characteristics of these phenomena. Given the boundary conditions of mass flow rate and pool temperature, the parameters for both the thermal and hydraulic dynamics were measured. The bubbling frequency was intro-

duced and analyzed as a new concept that can explain the unstable characteristic at the tip of the nozzle. Through the thermal hydraulic analysis, the following results were found in accordance to the following:

- The correlation of the bubbling frequency was suggested to be a function of the boundary conditions, steam mass flux, and pool temperature, and was modeled with the use of the Jakob and Bond numbers.
- A relationship between the bubbling frequency, bubble diameter, and rising velocity in the low-flow rate for the unstable direct contact condensation of steam yielded a reasonable agreement with the correlations suggested by previous researchers derived for the pool boiling cases.
- The correlation of the averaged heat-transfer coefficient was suggested to be a function of the bubbling frequency, and the predicted heat-transfer coefficients were generally within $\pm 30\%$ bounds.
- A novel technique for backlight-aided planar laser-induced fluorescence thermometry for two-phase flows was developed.
- The developed thermometry showed significant improvements compared to conventional laser-induced fluorescence.
- Instantaneous and averaged temperature fields were reported.
- In combination with particle image velocimetry and the developed thermometry, a simultaneous velocity and temperature measurement for unstable bubbling direct contact condensation of steam in subcooled water was performed
- Instantaneous temperature and velocity with the averaged fields were reported.
- Turbulence statistic information was provided

Given the finding that the bubbling frequency can be correlated with the thermal hydraulic dimensionless numbers obtained from the fluid properties and the experimental boundary conditions, and given that the frequency can directly model the heat-transfer coefficient of direct contact condensation in the unstable bubbling regime of the present study, the heat-transfer coefficient was able to be determined with the given boundary conditions.

A spatiotemporally resolved temperature field measurement of unstable direct contact condensation of steam in subcooled water was performed as an example of the developed PLIF thermometry for two-phase flows. Rhodamine B was used as the fluorescent dye and a 532 nm laser sheet was applied to the test section to excite the fluorescence. A spatially resolved in situ calibration was performed to obtain the correlation between emitted light intensity and temperature. The temperature field was evaluated using the intensity-temperature correlation from the high-speed camera images.

The results show various instantaneous temperature field characteristics, including bubble dynamics while the phase change was occurring. Time averaging the results showed a distinctive pattern of the average temperature gradient on the single-phase and condensation regions.

Also, a spatiotemporally resolved velocity and temperature field measurement of unstable direct contact condensation of steam in subcooled water was performed as an example of the developed simultaneous velocity and temperature measurement for two-phase flow. Analysis of the results will give us a better understanding of the effects of temperature and velocity on specific condensation processes. The detailed temperature and velocity field results obtained from this study can be extended to further experimental or computational fluid dynamics investigations on about thermal-hydraulic bubble dynamic models for this specific condensation process.

The scientific merit of this work is to provide the case specific benchmark data sets for the multifluid, multiphase flow phenomena for computer code validation. Not only validating the computer code, it can also provide an insight, or be directly applied to develop a new mathematical closure models. For example, a new closure model for CFD simulation of unstable bubbling direct contact condensation process is expected to be developed utilizing the field data in combination

with the heat transfer coefficient modeling based on the frequency analysis discussed in section 3.4. Thus,the application of the current study is not limited to the nuclear thermal-hydraulics computer code validation, but can be extended to general research of multifluid, multiphase flow phenomena.

REFERENCES

Alliance Limited, NGNP Industry. (2017) Final Project Report - Evaluation And Testing Of HTGR Reactor Building Response To Depressurization Accidents. United States,
Web. https://doi.org/10.2172/1398376

Aya, I., Nariai, H. and Kobayashi, M. (1980). Pressure and Fluid Oscillations in Vent System due to Steam Condensation, (I). Journal of Nuclear Science and Technology, 17(7), 499-515.
Web. https://doi.org/10.1080/18811248.1980.9732617

Aya, I., Nariai, H. and Kobayashi, M. (1983). Pressure and Fluid Oscillations in Vent System due to Steam Condensation, (II). Journal of Nuclear Science and Technology, 20(3), 213-227.
Web. https://doi.org/10.1080/18811248.1983.9733383

Aya, I., and Nariai, H. (1991). Evaluation of heat-transfer coefficient at direct-contact condensation of cold water and steam. Nuclear Engineering and Design, 131(1), 17-24.
Web. https://doi.org/10.1016/0029-5493(91)90314-8

Ball, S. (2004). Sensitivity studies of modular high-temperature gas-cooled reactor postulated accidents, Proc. 2nd Int'l Topical Meeting on HTR Technology (HTR '04), Beijing, China, September 22-24, 2004, Nucl. Eng. Des.

Ball, S., Matt Richards, Sergey Shepelev (2008). Sensitivity studies of air ingress accidents in modular HTGRs, Nucl. Eng. Des., 238 2935-2942

Barnert, H., Singh, J., Design evaluation of a small high-temperature reactor for process heat applications, Nucl. Eng. Des. 109 245-251 (1988).

Bruchhausen, M., Guillard, F., and Lemoine, F. (2004). Instantaneous measurement of two-dimensional temperature distributions by means of two-color planar laser induced fluorescence (PLIF), Experiments in Fluids, 38(1), 123-131.
Web. http://doi.org/10.1007/s00348-004-0911-2.

Brucker, G. G., and Sparrow, E. M. (1977). Direct contact condensation of steam bubbles in water at high pressure. International Journal of Heat and Mass Transfer, 20(4), 371-381.

Web. https://doi.org/10.1016/0017-9310(77)90158-2

Castanet, G., Lavieille, P., Lebouché, M., and Lemoine, F. (2003). Measurement of the temperature distribution within monodisperse combusting droplets in linear streams using two-color laser-induced fluorescence, Experiments in Fluids, 35(6), pp. 563-571.

Web. http://doi.org/10.1007/s00348-003-0702-1

Chen, L.-D., and Faeth, G. M. (1982). Condensation of Submerged Vapor Jets in Subcooled Liquids. Journal of Heat Transfer, 104(4), 774.

Web. https://doi.org/10.1115/1.3245199

Chen, Z., Chen, X., Zheng, Y. Sun J., Chen, F., Shi L., Li F., Dong, Y., Zhang, Z. (2017). Air ingress analysis of chimney effect in the 200MWe pebble-bed modular high temperature gas-cooled reactor, Annals of Nuclear Energy, Volume 106, Pages 143-153

Cho, S., Song, C.-H., Park, C. K., Yang, S. K., and Chung, M. K. (1998). "Experimental Study on Dynamic Pressure Pulse in Direct Contact Condensation of Steam Discharging into Subcooled Water," Proceedings of 1st Korea-Japan Symposium on Nuclear Thermal Hydraulics and Safety (NTHAS1), Pusan, Korea, 291-298.

Chun, M., KIM, Y., and PARK, J. (1996). "An Investigation of Direct Condensation of Steam Jet in Subcooled Water," Int. Comm. Heat Mass Transfer, Vol. 23, No. 7, pp. 947-918

Cole, R. (1960). A Photographic Study of Pool Boiling in the Region of the Critical Heat Flux. American Institute of Chemical Engineers Journal, 6(4), 533-538.

Web. https://doi.org/10.1002/aic.690060405

Coolen, M. C. J., Kieft, R. N., Rindt, C. C. M., van Steenhoven, A. A. (1999). Application of 2-D LIF temperature measurements in water using a Nd: YAG laser, Experiments in Fluids, 27(5), 420-426.

Web. http://doi.org/10.1007/s003480050367

Coppeta, J., and Rogers, C. (1998). Dual emission laser induced fluorescence for direct planar scalar behavior measurements, Experiments in Fluids, 25(1), pp. 1-15.

Web. https://doi.org/10.1007/s003480050202

Corradini, Michael, and Dale Klein. (2012) Fukushima Daiichi-ANS Committee Report. The American Nuclear Society Special Committee on Fukushima.
Web. http://fukushima.ans.org/report/Fukushima_report.pdf

De With, A., Calay, R., Holdo, A., de With, G. (2007). "Regimes of direct contact condensation of steam injected into water." International Journal of Multiphysics. 1. 271-282.

Eckstein A., Vlachos PP. (2009a). Assessment of advanced windowing techniques for digital particle image velocimetry (DPIV). Meas. Sci. Technol. 20(7):075402

Eckstein A., Vlachos PP. (2009b). Digital particle image velocimetry (DPIV) robust phase correlation. Meas. Sci. Technol. 20(5):055401

Estrada-Pérez, C. E., Hassan, Y. A., Tan, S. (2011). Experimental characterization of temperature sensitive dyes for laser induced fluorescence thermometry. Review of Scientific Instruments, 82(7), 074901.
Web. https://doi.org/10.1063/1.3590929

Estrada-Pérez, C. E., Tan, S., Hassan, Y. A. (2011). Whole-Field Temperature and Velocity Measurements for Two-Phase Flow Using PIV/LIF. ASME/JSME 2011 8th Thermal Engineering Joint Conference.
Web. https://doi.org/10.1115/ajtec2011-44507

Fukuda, S. (1981). Pressure Variations due to Vapor Condensation in Liquid, (II) Phenomena at Large Vapor Mass Flow Flux. Nippon Genshiryoku Gakkai-Shi (Japanese), 24(6), 466-474.

Funatani, S., Fujisawa, N., and Ikeda, H. (2004). Simultaneous measurement of temperature and velocity using twocolour LIF combined with PIV with a colour CCD camera and its application to the turbulent buoyant plume, Measurement Science and Technology, 15(5), pp. 983-990.
Web. https://doi.org/10.1088/0957-0233/15/5/030

GA Technologies Inc., (1988) Probabilistic Risk Assessment for the Standard Modular High Temperature Gas-Cooled Reactor, DOE-HTGR-86011, Rev. 5, General Atomics, San Diego, CA

GA Technologies Inc., (2011) Next Generation Nuclear Plant (NGNP) Prismatic HTGR Conceptual Design Project, Conceptual Design Report - Steam Cycle Modular Helium Reactor (SC-

MHR) Demonstration Plant, NGNP-R00016, Revision 1, General Atomics, San Diego, CA

Gould, D., Franken, D., Bindra, H., Kawaji, M. (2017). Transition from molecular diffusion to natural circulation mode air-ingress in high temperature helium loop, Annals of Nuclear Energy, Volume 107, Pages 103-109

Gulawani, S. S., Dahikar, S. K., Mathpati, C. S., Joshi, J. B., Shah, M. S., RamaPrasad, C. S., and Shukla, D. S. (2009). Analysis of flow pattern and heat transfer in direct contact condensation. Chemical Engineering Science, 64(8), 1719-1738.
Web. https://doi.org/10.1016/j.ces.2008.12.020

Gulawani, S. S., Joshi, J. B., Shah, M. S., RamaPrasad, C. S., and Shukla, D. S. (2006). CFD analysis of flow pattern and heat transfer in direct contact steam condensation. Chemical Engineering Science, 61(16), 5204-5220.
Web. https://doi.org/10.1016/j.ces.2006.03.032

Haque, H., (2008) Consequences of delayed air ingress following a depressurization accident in a high temperature reactor, Nucl. Eng. Des. 238 3041-3046

Hishida, K., and Sakakibara, J. (2000). Combined Planar laser-induced fluorescence-particle image velocimetry technique for velocity and temperature fields, Experiments in Fluids, 29, pp. 129-140.
Web. https://doi.org/10.1007/s003480070015

Hishida, M. and Takada, K. (1999) Study on Air Ingress during an Early Stage of a Primary-Pipe Rupture Accident of a HTGR, Nuclear Engineering and Design 126, 175-187

Ivey, H. J. (1967). Relationships between bubble frequency, departure diameter and rise velocity in nucleate boiling. International Journal of Heat and Mass Transfer, 10, 1023-1040.

Ju, S. H., No, H. C., and Mayinger, F. (2000). Measurement of heat transfer coefficients for direct contact condensation in core makeup tanks using holographic interferometer, 199, 75-83.

Kar, S., Chen, X. D., and Nelson, M. I. (2007). Direct-contact heat transfer coefficient for condensing vapour bubble in stagnant liquid pool. Chemical Engineering Research and Design, 85(3 A), 320-328.

Web. https://doi.org/10.1205/cherd06030

Kerney, P. J., Faeth, G. M., and Olson, D. R. (1972). Penetration Characteristics of a Submerged Steam Jet. American Institute of Chemical Engineers Journal, 18(3), 548-553.

Khan, A., Haq, N. U., Chughtai, I. R., Shah, A., and Sanaullah, K. (2014). Experimental investigations of the interface between steam and water two phase flows. International Journal of Heat and Mass Transfer, 73, 521-532.

Web. https://doi.org/10.1016/j.ijheatmasstransfer.2014.02.035

Kim, H., Kihm, K., and Allen, J. (2003). Examination of ratiometric laser induced fluorescence thermometry for microscale spatial measurement resolution, International Journal of Heat and Mass Transfer, 46(21), pp. 3967- 3974.

Web. https://doi.org/10.1016/S0017-9310(03)00243-6

Kim, J. S., Hwang, J.-S., Kim, E. S., Kim, B. J., Oh, C. H. (2016) Experimental study on fundamental phenomena in HTGR small break air-ingress accident, Annals of Nuclear Energy, Volume 87, Pages 145-156

Kim, Y. S., and Youn, Y. J. (2008). Experimental study of turbulent jet induced by steam jet condensation through a hole in a water tank. International Communications in Heat and Mass Transfer, 35(1), 21-29.

Web. https://doi.org/10.1016/j.icheatmasstransfer.2007.05.014

Lavieille, P., Lemoine, F., Lavergne, G., Virepinte, J. F., Lebouché, M. (2000). Temperature measurements on droplets in monodisperse stream using laser-induced fluorescence, Experiments in Fluids, 29(5), 429-437.

Web. http://doi.org/10.1007/s003480000109

Lavieille, P., Lemoine, F., Lavergne, G., and Lebouché M. (2001). Evaporating and combusting droplet temperature measurements using two-color laser-induced fluorescence, Experiments in fluids, 31(1), pp. 45-55.

Web. http://doi.org/10.1007/s003480000257

Lavieille, P., Lemoine, F., and Lebouché, M. (2002). Investigation on temperature of evaporat-

ing droplets in linear stream using two-color laser-induced fluorescence, Combustion science and technology, 174(4), pp. 117-142.
Web. http://dx.doi.org/10.1080/713713017

Lemoine, F., Antoine, Y., Wolff, M., and Lebouche, M. (1999). Simultaneous temperature and 2D velocity measurements in a turbulent heated jet using combined laser induced fluorescence and LDA, Experiments in Fluids, 26(4), pp. 315-323.
Web. http://doi.org/10.1007/s003480050294

Liang, K. S., and Griffith, P. (1994). Experimental and analytical study of direct contact condensation of steam in water. Nuclear Engineering and Design, 147(3), 425-435.
Web. https://doi.org/10.1016/0029-5493(94)90225-9

Loflin, L., Containment versus confinement for High-Tmeprature Gas Reactors: Regulatory, Design Basis, Siting, and Cost/Economic Consideration., EPRI Technical update 1011948, CA, Palo Alto (2005).

Moon, Y. T., Lee, H. D., and Park, G. C. (2009). CFD simulation of steam jet-induced thermal mixing in subcooled water pool. Nuclear Engineering and Design, 239(12), 2849-2863.
Web. https://doi.org/10.1016/j.nucengdes.2009.08.003

Natrajan, V., and Christensen, K. (2009). Two-Color Fluorescent Thermometry for Microfluidic Systems, Measurement Science and Technology, 20, p. 015401.
Web. https://doi.org/10.1088/0957-0233/20/1/015401

Nguyen, T. D., Petrov, V., Manera, A. (2014). Design of a scaled experimental facility for the NGNP Reactor Cavity Cooling System, Proc. 2014 American Nuclear Society Winter Meeting and Nuclear Technology Expo, Anaheim, California, November 9-13, 2014, American Nuclear Society

Nguyen, T., Kappes, E., King, S., Hassan, Y., Ugaz, V. (2018). Time-resolved PIV measurements in a low-aspect ratio facility of randomly packed spheres and flow analysis using modal decomposition, Exp Fluids, 59, 127.
Web. https://doi.org/10.1007/s00348-018-2583-3

Petrovic de With, A., Calay, R. K., and de With, G. (2007). Three-dimensional condensation regime diagram for direct contact condensation of steam injected into water. International Journal of Heat and Mass Transfer, 50(9-10), 1762-1770.
Web. https://doi.org/10.1016/j.ijheatmasstransfer.2006.10.017

Piskunov, M. V., Strizhak, P. A. (2018). Using Planar Laser Induced Fluorescence to explain the mechanism of heterogeneous water droplet boiling and explosive breakup. Experimental Thermal and Fluid Science, 91, 103-116.
Web. https://doi.org/10.1016/j.expthermflusci.2017.10.018

Qu, X., Sui, H. and Tian, M. (2016). CFD simulation of steam-air jet condensation. Nuclear Engineering and Design, 297, 44-53.
Web. https://doi.org/10.1016/j.nucengdes.2015.11.011

Reyes Jr., J. N., Groome, J. T., Woods, B. G., Jackson, B., Marshall, T. D. (2010). Scaling analysis for the high temperature Gas Reactor Test Section (GRTS), Nucl. Eng. Des. 240 397-404

Richards M., Baxter A., Ellis C., Gutierrez O., Crozier J. (2012) Conceptual Design of the NGNP Reactor System, Proc. Intl' Conf. on Nucl. Eng. 2012 American Society of Mechanical Engineering, Anaheim, California

Ross, D., Gaitan, M., and Locascio, L. E. (2001). Temperature Measurement in Microfluidic Systems Using a Temperature-Dependent Fluorescent Dye, Analytical Chemistry, 73(17), 4117-4123.
Web. http://doi.org/10.1021/ac010370l

Sakakibara, J., Adrian, R. J. (1997). Measurement of whole-field temperature using two-color LIF. J. Visualization Soc. Japan 17: 333-336 (in Japanese)

Sakakibara, J., and Adrian, R. (1999). Whole field measurement of temperature in water using two-color laser induced fluorescence, Experiments in Fluids, 26(1), pp. 7- 15.
Web. https://doi.org/10.1007/s003480050260

Sakakibara, J., and Adrian, R. (2004). Measurement of temperature field of a Rayleigh-Bénard convection using two-color laser-induced fluorescence, Experiments in fluids, 37(3), pp. 331-340.

Web. https://doi.org/10.1007/s00348-004-0821-3

Sakakibara, J., Hishida, K., and Maeda, M. (1997). Vortex structure and heat transfer in the stagnation region of an impinging plane jet (simultaneous measurements of velocity and temperature fields by digital particle image velocimetry and laser-induced fluorescence), International Journal of Heat and Mass Transfer, 40(13), pp. 3163-3176.

Web. http://doi.org/10.1016/s0017-9310(96)00367-5

Saurwein, John. Next Generation Nuclear Plant (NGNP) Prismatic HTGR Conceptual Design Project - Final Technical Report. United States, 2011.

Web. http://doi:10.2172/1019034

Seitzman, J. M., Kychakoff, G., and Hanson, R. K. (1985). Instantaneous temperature field measurements using planar laser-induced fluorescence. Optics Letters, 10(9), 439.

Web. https://doi.org/10.1364/ol.10.000439

Seuntiëns, H. J., Kieft, R. N., Rindt, C. C. M., van Steenhoven, A. A. (2001). 2D temperature measurements in the wake of a heated cylinder using LIF, Experiments in Fluids, 31(5), 588-595.

Web. http://doi.org/10.1007/s003480100338

Simpson, M. E., and Chan, C. K. (1982). Hydrodynamics of a Subsonic Vapor Jet in Subcooled Liquid. Journal of Heat Transfer, 104(May 1982), 271.

Web. https://doi.org/10.1115/1.3245083

Song, C.-H., Cho, S., and Kang, H.-S. (2012). Steam Jet Condensation in a Pool: From Fundamental Understanding to Engineering Scale Analysis. Journal of Heat Transfer, 134(3), 31004.

Web. https://doi.org/10.1115/1.4005144

Tan, S., Estrada-Perez, C. E., Dominguez-Ontiveros, E. E., Hassan, Y. A. (2010). Experimental Study of Temperature Sensitive Dyes for Planar Laser Induced Fluorescence Thermometer. 18th International Conference on Nuclear Engineering: Volume 4, Parts A and B.

Web. https://doi.org/10.1115/icone18-29328

Tzanos, P., Farmer, M. T. (2006). Feasibility Study for Use of the Natural Convection Shutdown Heat Removal Test Facility (NSTF) for Initial VHTR Water-Cooled RCCS Shutdown, ANL-

GenIV-079, Argonne National Laboratory

USNRC. (2018). "Computer Codes:
Web. https://www.nrc.gov/about-nrc/regulatory/research/safetycodes.html," USNRC

USNRC. (1981) "Suppression Pool Temperature Limits for BWR Containments," NUREG-0783, USNRC

Vaghetto, R., Hassan, Y. A. (2014). Experimental Study of a Scaled Water-Cooled Reactor Cavity Cooling System, Nucl. Technol., 187, 282-293

Volkov, R. S., Strizhak, P. A. (2018). Research of temperature fields and convection velocities in evaporating water droplets using Planar Laser-Induced Fluorescence and Particle Image Velocimetry. Experimental Thermal and Fluid Science, 97, 392-407.
Web. https://doi.org/10.1016/j.expthermflusci.2018.05.00

Volkov, R.S., Strizhak, P.A. (2019). Measuring the temperature of a rapidly evaporating water droplet by Planar Laser Induced Fluorescence, Measurement, 135, 231-243.
Web. https://doi.org/10.1016/j.measurement.2018.11.047

Voytkov, I. S., Volkov, R. S., Strizhak, P. A. (2018). Temperature and Velocity of the Gas-Vapor Mixture in the Trace of Several Evaporating Water Droplets. Journal of Heat Transfer, 141(1), 011502.
Web. https://doi.org/10.1115/1.4041556

Wilson Jr., T. L., Ball, S. J., Wood, R. T., Cetiner, M. S., Poore, W. P. (2012) Advanced Control and Protection System Design Methods for Modular HTGRs, ORNL/TM-2012/170, Oak Ridge National Laboratory.

Xu, Q., and Guo, L. (2016). Direct contact condensation of steam jet in crossflow of water in a vertical pipe. Experimental investigation on condensation regime diagram and jet penetration length. International Journal of Heat and Mass Transfer, 94, 528-538.
Web. https://doi.org/10.1016/j.ijheatmasstransfer.2015.02.036

Yang, S. R., Silberberg, M., Fullerton, C., Nguyen, T., Vaghetto, R., Hassan, Y., (2016). Experimental study on a simplified facility of HTGR reactor building response to depressurization

accidental scenarios, Proc. Int'l Topical Meeting on HTR Technology (HTR '16), Las Vegas, Nevada

Yang, S. R., Kappes, E., Nguyen, T., Vaghetto, R., Hassan, Y. (2018). "Experimental study on 1/28 scaled NGNP HTGR reactor building test facility response to depressurization event," Annals of Nuclear Energy, Vol. 114, pp. 154-164
Web. https://doi.org/10.1016/j.anucene.2017.12.023

Yang, S. R., Seo, J., Hassan, Y. (2019). "Thermal hydraulic characteristics of unstable bubbling of direct contact condensation of steam in subcooled water," International Journal of Heat and Mass Transfer, Vol. 138, pp. 580–596
Web. https://doi.org/10.1016/j.ijheatmasstransfer.2019.04.065

Yildiz., M. A., Yang, S. R., Vaghetto, R., Hassan, Y. (2018). "Numerical analysis of 1/28 scaled NGNP HTGR reactor building test facility response to depressurization event using GOTHIC," Annals of Nuclear Energy, Vol. 119, pp. 46-65
Web. https://doi.org/10.1016/j.anucene.2018.04.030

Zhao, Q., and Hibiki, T. (2018). Progress in Nuclear Energy Review: Condensation regime maps of steam submerged jet condensation, 107(August 2017), 31-47.
Web. https://doi.org/10.1016/j.pnucene.2017.12.014

Zuber, N. (1959). Hydrodynamic Aspects of Boiling Heat Transfer (thesis).
Web. https://doi.org/10.2172/4175511

Zuber, N. (1964). Recent trends in boiling heat transfer research Part I: nucleate pool boiling, Applied Mechanics Reviews, 17, 663-672.